BULGARIAN CHEMICAL COMMUNICATIONS

EDITORIAL
National conference "Sofia Electrochemical Days'2017" (SED'2017)
10-13 May, 2017, Sofia, Bulgaria

The current issue of the Bulgarian Chemical Communications consists the papers, presented as lectures and posters at the 6th national conference "Sofia Electrochemical Days'2017" (SED'2017 held in Sofia from 10 to 13 May 2017.

The forum dedicated to the 50th anniversary of the "Academician Evgeni Budevski Institute of Electrochemistry and Energy Systems", Bulgarian Academy of Sciences gathered more than 80 participants from 12 countries - young and experienced scientists, representatives of various academic institutions and companies. For the first time the conference was sponsored by the International Electrochemical Society (ISE).

During the conference a jubilee session was held, attended by The President of Bulgarian Academy of Science, directors of scientific institutes, and representatives of many partner organizations. On the occasion of the jubilee, IEES was awarded with the honorary plaque of BAS "Marin Drinov" for merits in the development of electrochemistry in Bulgaria and globally.

The organizers would like to express their gratitude to the SED'2017 participants for their contribution to the conference success as well for the warm and collaborative atmosphere they created. We express our sincere thanks to the authors for their incentive presentations, to the referees for their efforts in reviewing the submitted manuscripts and to the Editorial Board of the Bulgarian Chemical Communications for the publications in this issue.

Guest editor:
Antonia Stoyanova,
Academician Evgeni Budevski Institute of Electrochemistry and Energy Systems, Bulgarian Academy of Sciences

Durability of anodic aluminum oxide (AAO) films formed on technically pure AA1050 alloy against corrosion

Ch. A. Girginov*, S. V. Kozhukharov, M. J. Milanes

University of Chemical Technology and Metallurgy, 8 St. Kliment Ohridski blvd., 1756 Sofia, Bulgaria

The present research provides data about the remarkable durability of Anodized Aluminum Oxide (AAO) film grown on technically pure AA1050 alloy during and after extended exposure to 3.5% NaCl model corrosive medium. The samples were cut from thick aluminum foil with approximate dimensions 30 x 30 mm. The anodization was performed for 48 min in 15%wt. H_2SO_4 in galvanostatic (15 mA cm^{-2}) and isothermal (20 °C) regime. This process was carried out in a two electrode cell with continuous stirring. The obtained AAO films were submitted to regular weekly electrochemical measurements via Electrochemical Impedance Spectroscopy (EIS) and Linear Sweep Voltammetry (LSV). The EIS spectra have shown almost pure capacitive behavior of the investigated samples. This fact is an indication for the well-expressed insulating capability of the obtained AAO films. Furthermore, the specimens kept their capacitance during the entire exposure period, showing remarkable AAO durability. Only gradual EIS spectra shape evolution was registered, without any abrupt changes. The obtained spectra were further submitted to quantitative data fitting analysis to suitable equivalent circuits. The EIS results were further confirmed by the LSV measurements. The registered currents were in the range of the equipment minimum detection threshold, confirming the assumption for the purely capacitive AAO behavior. The obtained data reveal that the formed AAO films efficiently protect the metallic substrates even after 5208 hours of exposure without any indication for corrosion damage.

Keywords: Anodization, Alumina films, EIS, LSV

INTRODUCTION

Pure aluminum and its low doped alloys find various applications in both mass production and hi-tech industrial sectors. One of the widest fields of use of this metal is the packaging of various nutrition products and soft drinks [1-4]. However, reliable packaging requires additional surface protection of the Al-based packaging materials, prior to contact with whatever nutrition product. This requirement has arisen because Al-ions resorption was recently evinced from such packaging products [5-7], which can be dangerous for the human health [8, 9]. The specific conjunction of electrical conductivity with the strength to weight ratio [10-12] makes aluminum an indispensable material for high voltage, long distance electricity distribution [13-16]. Aluminum rolls with precisely textured AAO surfaces are widely used for ink-printing on paper and plastic packaging materials [17-20], and even for production of flexible solar cells by printing [21].

Anodization is a relatively simple process, which at defined conditions enables the formation of highly ordered oxide layers with various possible applications in the hi-tech industrial branch. The AAO films are representative for the so called "self-assembled monolayers" (SAM) [22]. Besides, both the porous and barrier AAO layers can be successfully used for large series of Metal Oxide Semiconductor (MOS), Metal Dielectric Semiconductor (MDS) and Metal Oxide Semiconductor Field Effect (MOSFE) high performance transistors and integral micro-schemes, based on these electronic elements [23-25]. The capabilities of the anodized aluminum self-assembled layers have recently been investigated for fuel cell electrodes [26] and even for gas analysis sensors [27] and biosensors [28].

The aim of the present research work is to provide information regarding the durability of porous AAO layers on AA1050 substrates in a conventional 3.5% NaCl model corrosive medium. The experiments were performed by regular (once per week) electrochemical measurements via Electrochemical Impedance Spectroscopy (EIS) and Linear Sweep Voltammetry (LSV) for extended exposure times, up to 5208 hours.

EXPERIMENTAL

A set of samples of technically pure aluminum (AA1050) were submitted to anodization and subsequent electrochemical measurements. The samples were preliminary etched in 50 g dm^{-3} NaOH solution at 60°C and then activated in diluted (1:1 v/v) HNO$_3$ at room temperature. Both operations were performed for two minutes. The

anodization was performed for 48 min. in 15%wt. H_2SO_4 in galvanostatic (15 mA cm^{-2}) and isothermal (20 °C) regime, after vigorous cleaning by tap and distilled water. This process was carried out in a two electrode cell (250 ml) with continuous stirring. The actual working zones, submitted to anodization were with a diameter of 24.5 mm for all samples.

The already anodized samples were then put through electrochemical characterizations, using Electrochemical Impedance Spectroscopy (EIS) and Linear Sweep Voltammetry (LSV) as measurement techniques. The respective measurements were carried out regularly (once per week), until 5208 hours of exposure to 3.5% NaCl (100 ml) model corrosive medium. The sample exposure was carried out in three electrode cells with Ag/AgCl/3M KCl reference electrode and a platinum cylindrical counter-electrode. Only part of the anodized zones (diam. 16 mm) was exposed to the electrolyte, in order to avoid any edge effects.

The EIS data acquisition was performed in the frequency range from 10^4 to 10^{-2} Hz, distributed in 50 steps at 120 mV, according to the Open Circuit Potential (OCP). This excitation signal amplitude was selected in order to overcome the high oxide layer resistance. After each EIS spectrum recording, individual LSV curves were recorded from +30 to -500 mV (in cathodic direction) and from -30 to +600 mV (in anodic direction),

respectively. The cathodic curves were acquired immediately after the EIS spectra acquisition, whereas the anodic ones were recorded after several hours of retention at OCP. This measurement cycle organization was selected for avoiding any polarization effects from the cathodic curves, on the shape of the anodic ones. The LSV curves in both directions were recorded with a potential sweep rate of 10 mV s^{-1}, in order to avoid any electrode damage due to excessive polarization.

RESULTS AND DISCUSSION

The visual inspection of the investigated samples (after 5208 hours of exposure to model corrosive medium) has shown lack of any notable features of localized corrosion attack whatsoever.

Since all specimens revealed absence of any corrosion activity, the possible AAO deterioration caused by the corrosive medium was evaluated by precise data analysis of the performed electrochemical measurements.

Electrochemical impedance spectroscopy
Initial EIS spectra acquisition

The EIS spectra, acquired after 168 hours of exposure resemble capacitors, due to the well-defined barrier properties of the formed AAO layers. An example for the EIS spectra of three samples is shown in Fig. 1.
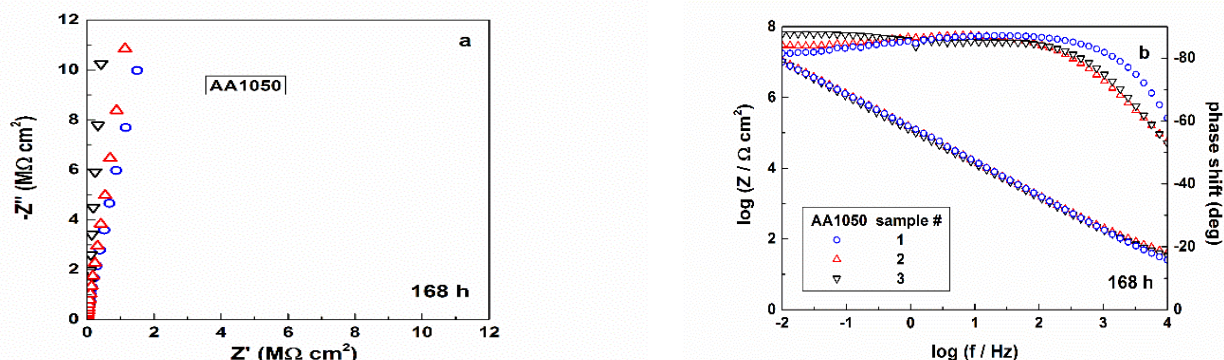

Fig.1. EIS spectra of three samples, recorded after 168 hours of exposure: Nyquist (a) and Bode (b) plots.

Besides, obviously the spectra in Fig. 1 almost completely overlap, indicating the remarkable reproducibility of the obtained AAO films. In order to determine the AAO durability, the experiments have been extended for larger exposure times, up to 5208 hours. The obtained results are shown below.

EIS spectra shape evolution within the exposure to the model corrosive medium

Fig. 2 illustrates the typical EIS evolution trends during the sample exposure to the corrosive medium. The Nyquist plots (Fig. 2a) acquired after

336 hours, until 5208 hours of exposure, remain unchanged, being almost straight vertical lines. Since such lines are typical for electronic capacitors, it can be inferred that the AAO films grown on AA1050 substrates possess definitely insulating properties which do not suffer significant changes during the entire period of exposure.
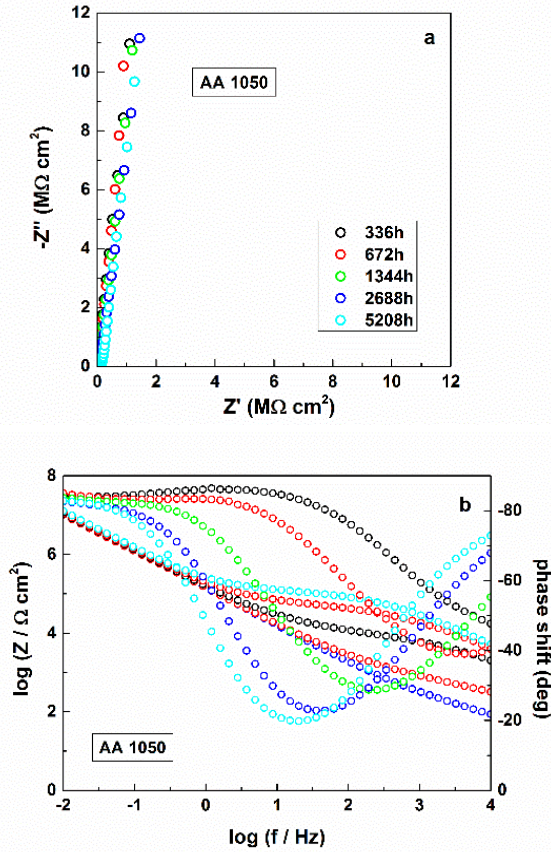
Fig. 2. Nyquist (a) and Bode (b) plots of typical EIS spectra, acquired after different exposure durations

The Bode plots (Fig. 2b) recorded after the same periods of time look more distinguishable from each other. The maxima of the φ/log(f) lines displace towards the lower frequency range and at the high frequency range minima appear. Simultaneously, additional inflexions of the log|Z|/log(f) curves appear, revealing an increase of the electrical resistance. This gradual change of the EIS spectra during the exposure, reveal coincident increase of the capacitive and the resistive components of the spectra. Both these trends reveal an AAO thickness decrease, combined with obstruction of the AAO pores and possible defects by insoluble corrosion products. These effects are probably result of the following reactions proceeding during the exposure of the AAO coated AA1050 samples to the model corrosive medium [29]:

$$Al_2O_3 + 6H^+ + 6Cl^- \leftrightarrow 2AlCl_3 + 3H_2O \tag{1}$$
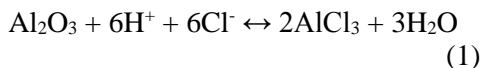
Although the corrosive medium provides a neutral environment (pH $\approx$ 7), local acidification appears near the metallic surface, according to [30]:

$$Al^{3+} + H_2O \rightarrow Al(OH)^{2+} + H^+ \tag{2}$$
$$Al^{3+} + 3H_2O \rightarrow Al(OH)_3 + 3H^+ \tag{3}$$
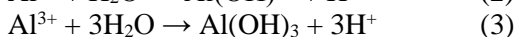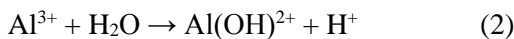
Alternatively, because the model corrosive medium was left to natural aeration, it contains dissolved oxygen and it can cause localized alkalization, following the reactions [30]:

$$O_2 + 2H_2O + 4e^- \rightarrow 4OH^- \tag{4}$$
$$2H_2O + 2e^- \rightarrow 2OH^- \tag{5}$$

The hydroxide anion generation causes additional attack against the AAO layer:

$$Al_2O_3 + OH^- \rightarrow Al(OH)_3 \tag{6}$$

Both proposed chemical mechanisms result in AAO thickness decrease, combined by obstruction of the AAO pores and possible defects by insoluble corrosion products. The occurrence of such insoluble products with Keggin type cluster structures was proposed in previous works [31, 32]. This concept has served as a basis for the equivalent circuit description, commented below.

EIS modeling and quantitative data analysis

In order to obtain quantitative data, the acquired EIS spectra were fitted to suitable equivalent circuits, following the basic circuit description code (CDC) rules, proposed by Boukamp [33]. There, the capacitance elements are being used for description of charge transfer across interfaces, whereas the ohmic elements describe the charge transport through homogeneous medium. The spectra acquired after 168 hours of exposure were appropriate for fitting to an equivalent circuit, composed by two parallel RC-units, connected in series. However, after 336 hours of exposure, an additional constant phase element (CPE$_{diff}$) was necessary for data fitting. The need for this supplemental element is a consequence of the already occured notable obstruction of the AAO pores by corrosion products, commented above. Consequently, the equivalent circuit suitable for EIS data fitting after 336 hours of exposure was composed by two time constants (i.e. parallel RC-units), with additional CPE, as illustrated in Fig. 3. The first element of the equivalent circuit is the model corrosive medium (electrolyte) resistance (R_{el}), which is consecutively connected with the first time constant (C_{oxy}, R_{oxy}). It is composed by the capacitance of the interface between the model corrosive medium and AAO (C_{oxy}) and the resistance of the electrolyte, within the pores of the oxide layer (R_{oxy}). The second time constant (C_{edl}, R_{ct}) can be ascribed to the interface between AAO and the metallic substrate. It comprises the electric double layer capacitance (C_{edl}) and the charge transfer resistance (R_{ct}). Finally, the additional constant phase element (CPE$_{diff}$) describes the

diffusion limitations caused by the corrosion product obstruction.

The quantitative data acquired by the fitting of the spectra shown in Fig. 2, to the equivalent circuits, illustrated in Fig.3 are summarized in Table 1 (for three of the investigated samples). It shows only the numerical values determined at 336 and 5208 hours of exposure, since it would be onerous to represent the obtained data from all recorded spectra (all exposure times).
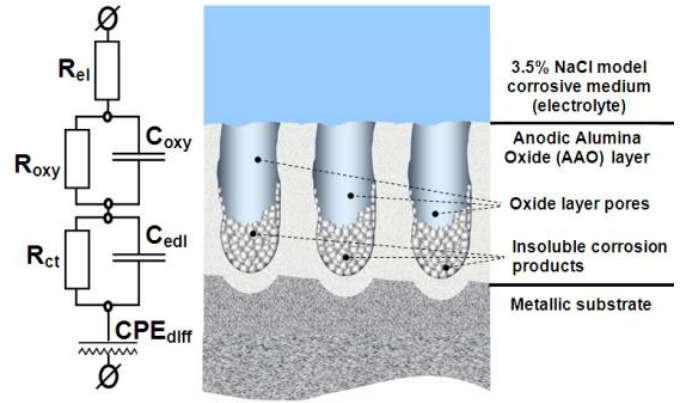

Fig. 3. Illustration of the equivalent circuit, suitable for EIS data fitting for extended exposure durations and the respective conceptual model.

Table 1. EIS data fitting results for the corrosion process kinetics

336 hours of exposure

Element	Unit		Sample **1**	Sample **2**	Sample **3**
R_{el}	Ω cm^2		29.94 ± 2.03	95.40 ± 6.12	30.7 ± 6.32
C_{oxy}	F cm^{-2}	10^{-7}	2.67 ± 0.21	2.97 ± 0.03	3.19 ± 0.26
R_{oxy}	Ω cm^2	10^3	0.49 ± 0.04	0.204 ± 0.002	0.48 ± 0.01
C_{edl}	F cm^{-2}	10^{-7}	1.16 ± 0.01	1.36 ± 0.06	1.44 ± 0.01
R_{ct}	Ω cm^2	10^3	0.17 ± 0.03	0.46 ± 0.02	0.24 ± 0.01
Q_{diff}	s^n Ω^{-1} cm^{-2}	10^{-7}	5.91 ± 0.31	6.36 ± 0.05	6.04 ± 0.89
n	-----		0.71 ± 0.02	0.82 ± 0.03	0.84 ± 0.02

5208 hours of exposure

Element	Unit		Sample **1**	Sample **2**	Sample **3**
R_{el}	Ω cm^2	10^3	2.44 ± 0.43	3.00 ± 0.63	2.80 ± 0.56
C_{oxy}	F cm^{-2}	10^{-9}	12.55 ± 2.88	11.78 ± 1.62	13.16 ± 1.69
R_{oxy}	Ω cm^2	10^3	163.40 ± 3.58	122.80 ± 8.65	131.40 ± 7.00
C_{edl}	F cm^{-2}	10^{-9}	3.34 ± 0.16	2.34 ± 0.10	2.58 ± 0.12
R_{ct}	Ω cm^2	10^3	63.60 ± 2.47	73.60 ± 7.21	60.80 ± 5.33
Q_{diff}	s^n Ω^{-1} cm^{-2}	10^{-7}	5.06 ± 0.10	4.88 ± 0.11	5.46 ± 0.12
n	-----		0.90 ± 0.01	0.88 ± 0.01	0.89 ± 0.01

The comparison of the data, represented in Table 1 shows that both C_{oxy} and C_{edl}, decrease by three orders of magnitude from 10^{-6} to 10^{-9} F cm^{-2}. The diffusion related constant phase element (CPE$_{diff}$), follows the same trend. However its coefficient (n) retains its value (around 1). This fact indicates that the CPE$_{diff}$ resembles pure capacitance, resulting from the obstruction effect, caused by the insoluble corrosion products. Simultaneously, all the resistance elements: R_{el}, R_{oxy} and R_{ct}, increase in value, due to corrosion products accumulation. Consequently, the accumulation of polynuclear Keggin type $Al_x(OH)_{3x-z}Cl_z$ corrosion products suppresses the Al-oxide layer thinning, by hindering the access of corrosive species to the surface.

The impedance spectra components do not follow similar trends of evolution (Fig. 4).

The R_{el}, initially increases progressively, and afterwards remains unchanged at about 3 kΩ cm^2. The rest resistance components R_{oxy} and R_{edl} tend to increase linearly. This difference of the resistance evolution kinetics can be explained, having in mind that R_{el} corresponds to the total accumulation of corrosion products on the entire sample surface, whereas R_{oxy} and R_{edl} are rather related only to the corrosion product accumulation inside the AAO pores and defects.

The capacitance elements show similar trends. Initially, C_{oxy} shows a sharp decrease, followed by reaching of almost steady state at about 2 nF cm^{-2}. The C_{edl} and CPE$_{diff}$ suffer weak linear decrease with insignificant slope.
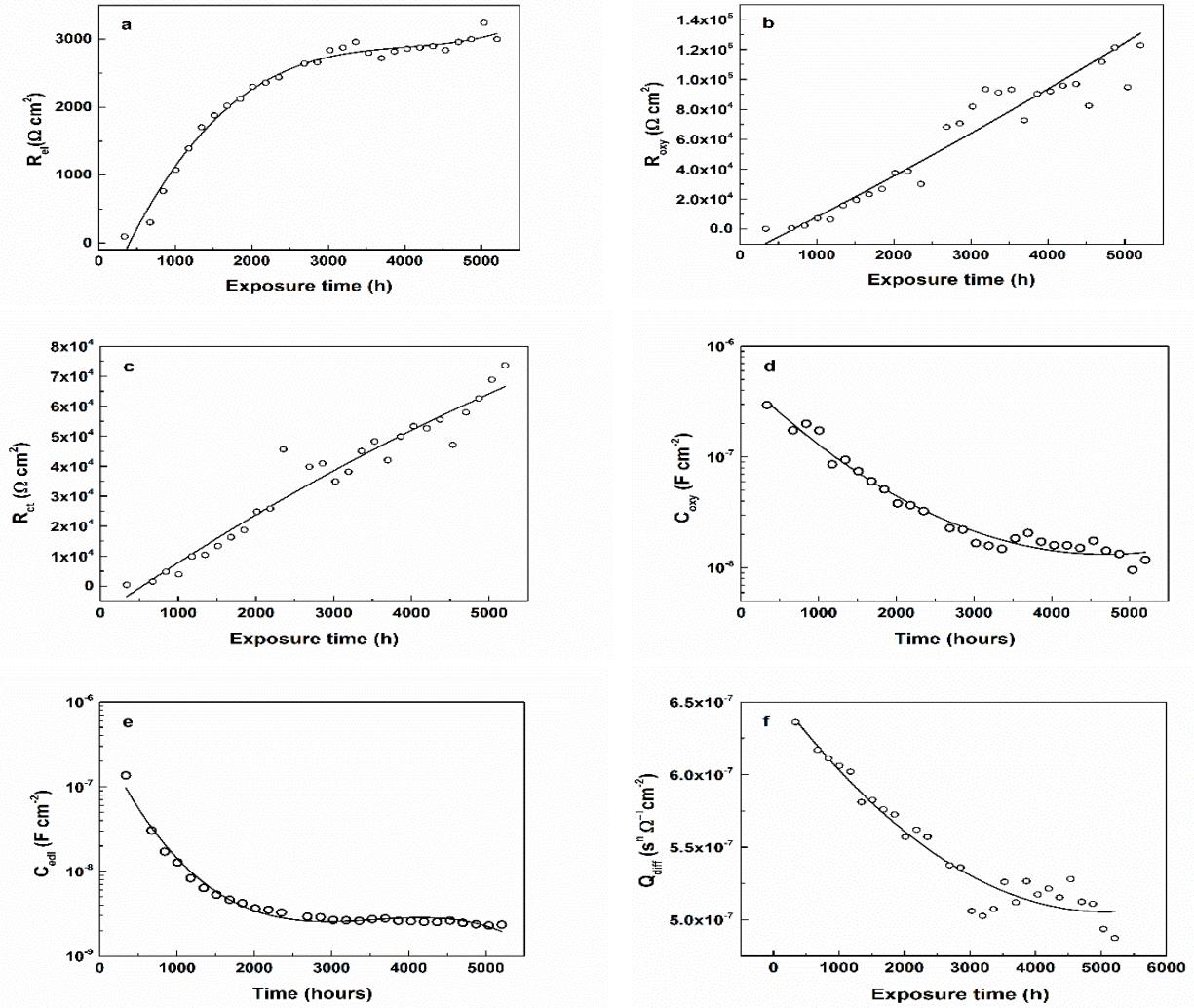
Fig. 4. Resistance (a - c), capacitance and CPE (d - f) values evolution during the exposure to the model corrosive medium

Linear sweep voltammetry

This method was used, because any eventual AAO breakdowns could easily be determined by the sharp changes of the respective LSV curves. Besides, this method enables the detection of localized corrosion activities [34], by the occurrence of sharp inflexions in the anodic LSV branches.

In the present case the LSV curves acquired even after 5208 hours of exposure to the model corrosive medium, remain at the equipment minimal current detection threshold (Fig. 5).

This fact obviously evinces the lack of any oxide film breakdowns for the entire period of exposure (5208 hours), confirming the inferences done for the EIS measurements. The LSV curves are horizontal, revealing the passivation role of the AAO formed during anodization.

Summarizing the data obtained by both electrochemical methods, it can be concluded that the corrosion process of anodized AA1050 alloy in stationary hydrodynamic conditions is a self-inhibiting process, due to the insoluble corrosion products accumulation and the consequent pore obstruction. These processes suppress the corrosion process, because of the corrosive species hindering the inside of AAO pores and defects.
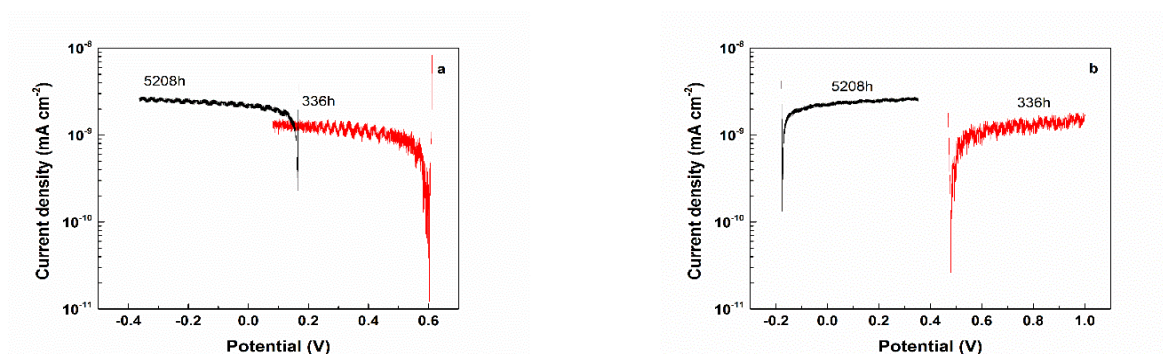
Fig. 5. Cathodic (a) and anodic (b) LSV curves, recorded for two exposure durations (336 and 5208 h)

CONCLUSIONS

The remarkable durability of Anodized Aluminum Oxide (AAO) layer grown on technically pure aluminum substrates in conventional 3.5% NaCl model corrosive medium was evaluated. The specimens did not show any remarkable indications for corrosion even after 5208 hours of exposure.

The acquired EIS spectra have shown almost pure capacitance, revealing the well-defined insulation properties of the obtained AAOs. Indeed, the phase shift approached 90 degrees. Besides, the spectra shapes changed gradually, due to lack of any film breakdowns for the entire exposure period.

A quantitative numerical analysis was applied to the acquired EIS spectra by fitting to appropriate equivalent circuits. The successful data fitting required pure capacitances (C), instead of Constant Phase Elements (CPE). This fact confirms the purely capacitive properties of the obtained AAO films. The equivalent circuit data fitting has shown that additional CPE was necessary for the data fitting of the spectra, acquired after 336 hours of exposure. This element was ascribed to pore obstruction by $Al_x(OH)_{3x-y}Cl_y$ products. The further data fitting analysis has shown gradual decrease of the capacitances, coupled by simultaneous resistance increment.

On the basis of all data, it was established that the AAO suffer gradual deterioration which decelerates with time. The reason for this deceleration is the access suppression of corrosive species, due to the pore obstruction commented above.

The LSV curves have undoubtedly confirmed the inferences done for the EIS data analysis. All the curves, acquired for the entire period of 5208 hours of exposure were at insignificant currents, approaching the equipment minimum current detection threshold. This fact confirms the statement that the AAO films are able to resist and do not suffer any breakdowns for the entire exposure period.

REFERENCES

1. M. Lamberti, F. Escher, *Food Rev. Internat.*, **23**, 407 (2007).
2. O. Ayalon, Y. Avnimelech, M. Shechter, *Envir. Sci. Pol.*, **3**, 135 (2000).
3. C. C. Huang, H. W. Ma, *Sci. Total Env.*, **324**, 161 (2004).
4. K. Marsh, B. Bugusu, *Mater. Envir. Iss.*, **72**, R39 (2007).
5. S. P. Joshi, R. B. Toma, N. Medora, K. O'Connor, *Food Chemistry*, **83**, 383 (2003).
6. M. Šeruga, J. Grgić, M. Mandić, *Z. Lebensm. Unters.Forch.*, **198**, 313 (1994).
7. F. Bianchi, M. Careri, M. Maffini, A. Mangia, C. Mucchino, *Rapid Commun. Mass Spectr.*, **17**, 251 (2003).
8. A. Becaria, A. Campbell, S. C. Bondy, *Toxicol. Ind. Health*, **18**, 309 (2002).
9. J. Kandiah, C. Kies, *Biometals*, **7**, 57 (1994).
10. S. S. Golru, M. M. Attar, B. Ramezanzadeh, *Appl. Surf. Sci.*, **345**, 360 (2015).
11. S. S. Golru, M.M. Attar, B. Ramezanzadeh, *Prog. Org. Coat.*, **87**, 52 (2015).
12. S. S. Golru, M.M. Attar, B. Ramezanzadeh, *J. Ind. Eng. Chem.*, **24**, 233 (2015).
13. D. E. Johnson, T. L. Anderson, US patent, US6559385B1 (2003).
14. C. McCullough, A. Mortensen, P. S. Werner, H. E. Deve, T. L. Anderson, US patent US6180232B1 (1995).
15. X. Y. Huang, P. K. Jiang, J. Appl. Phys., 102, 124103 (2016).
16. C. Hiel, G. Korzeniowski, D. Bryant, US Patent US7179522B2 (2004).
17. J. Crahay, US Patent, US4322600A (1979).
18. T. M. Smith, US Patent, US3987897A (1975).
19. C. Ralph E., US Patent, US2114072A (1938).

20. J. Curt, US Patent, US2780253A (1950).
21. F. C. Chen, M. K. Chuang, S. C. Chien, J. H. Fang, C. W. Chu, *J. Mater. Chem*., **21**, 11378 (2011).
22. R. Abdel-Karim, S. M. El-Raghy, Chapter 7 in: Nanofabrication using Nanomaterials, J. Ebothé, W. Ahmed (Eds.) One Central Press (Manchester U.K.) 2016, p. 197 - 218
23. P. Vachkov, D.Ivanov, Gov. Ed. "Tekhnicka" Sofia, 15 (1990).
24. S. Iwauchi, T. Tanaka, *Jpn. J. Appl. Phys*., **10**, 260 (1971).
25. H. Klauk, *Nature Materials,* **8**, 853 (2009).
26. P. Bocchetta, M. Santamaria, F. Di Quarto, *J. Mater. Sci. Nanotehnol*., **1**, 1 (2014).
27. T. Kumeria, A. Santos, D. Losic, *Sensors*, **14**, 11878 (2014).
28. A.Santos, T. Kumeria, D. Losic, *Materials*, **7**, 4297 (2014).
29. H. Kaesche, Corrosion of the Metals, "Metallurgy" Gov. Ed., Moscow, 219 (1984).
30. M. Machkova, E.A. Matter., S. Kozhukharov, V. Kozhukharov, Corros. Sci. 69, 396 (2013).
31. S. Kozhukharov, V. Kozhukharov, M. Wittmar, M. Schem, M. Aslan, H.Caparrotti, M.Veith, *Prog. Org. Coat.,* **71**, 198 (2011).
32. A. A. Salve, S. Kozhukharov, J. E. Pernas, E. Matter, M. Machkova, *J. Univ. Chem.Technol. Metal.,* **47**, 319 (2012).
33. B. A. Boukamp, *Solid State Ionics*, **18/19**, 136 (1986).
34. M. Bethencourt, F. J. Botana, J. J. Calvino, M. Marcos, M. A. Rodriguez-Chacon, *Corros. Sci.,* **40**, 1803 (1998).

КОРОЗИОННА УСТОЙЧИВОСТ НА АНОДНИ ОКСИДНИ СЛОЕВЕ (АОС) ОТЛОЖЕНИ ВЪРХУ ТЕХНИЧЕСКИ ЧИСТА СПЛАВ АА1050

К. А. Гиргинов, С. В. Кожухаров, М. Х. Миланес

Химикотехнологичен и металургичен университет, бул. Климент Охридски№8,1756 София,България

(Резюме)

Представени са данни за значителната корозионна устойчивост на анодни оксидни слоеве (АОС), формирани върху техническата алуминиева сплав АА1050. Формирането на оксидните филми е проведено галваностатично (15 mAcm^{-2}) и изотермично (20 °C) в 15% H$_2$SO$_4$, в продължениена 48 min. Процесът е провеждан с образци от АА1050 (30x30 mm) в двуелектродна електролизна клетка, при непрекъснато разбъркване на електролита. Изследванията на АОС са проведени след продължително (до 5208 часа) експониране на образците в моделна корозионна среда (3.5% NaCl). Чрез Електрохимична Импедансна Спектроскопия (ЕИС) и Линейна Волтамперометрия (ЛВА) оксидните слоеве са подлагани на регулярни (ежеседмични) електрохимични измервания. Анализът на импедансните спектри показва почти чисто капацитивно поведение на изследваните образци, което се дължи на добре изразената изолаторна способност на оксидните слоеве. Оксидните слоеве запазват своите капацитивни свойства през целия период на експозиция, демонстрирайки много добра корозионна устойчивост. Получените импедансни спектри са подложени на количествен анализ при използване на подходящи еквивалентни схеми. Резултатите получени чрез импедансните спектри за свойствата на АОС са потвърдени и от проведените волтамперометрични измервания. Регистрираните токови плътности (в анодна и катодна посока) потвърждават заключенията за почти чистото капацитивно поведение на формираните АОС. Получените данни показват, че дори след 5208 часово излагане в корозионна среда не се наблюдават забележими корозионни поражения. Това е убедително доказателство, че формираните оксидни слоеве могат ефективно да защитават алуминиевата АА1050 сплав.

Ключови думи: Анодиране, Анодни филми върху алуминий, ЕИС, ЛСВ

Comparative electrochemical and topographical elucidation of Anodic Aluminum Oxide (AAO) layers formed on technically pure aluminum (TPA) and AA2024-T3 aircraft alloy

S. V. Kozhukharov*, Ch. A. Girginov

University of Chemical Technology and Metallurgy, 8 St. Kliment Ohridski blvd. 1756 Sofia, Bulgaria

The remarkable difference between the mechanical properties of pure aluminum and its industrial alloys predetermines significant variations in their chemical comportment. This fact imposes more detailed investigations on the correlation between the alloy's chemical composition and its behavior during the preliminary chemical treatments and further exposure to corrosive media. In this sense, the present research is devoted to the comparison of Anodic Aluminum Oxide (AAO) films, formed at the same conditions on technically pure aluminum (TPA) and the highly doped (AA2024-T3) aircraft alloy. The anodization process was performed galvanostatically with simultaneous in-situ chrono-potentiometric curve recording. The electrochemical behavior of the investigated anodized specimens in 3.5 %NaCl medium was elucidated by Electrochemical Impedance Spectroscopy (EIS) and Linear Voltammetry (LVA). The topology of the obtained AAO films was observed by Scanning Electron Microscopy (SEM) and Atomic Force Microscopy (AFM). Remarkable differences between the AAO films formed on TPA and AA2024-T3 were registered by all analytical techniques used in the present research. The electrochemical methods used have shown completely different curve shapes and the further numerical analysis confirmed the observed significant dissimilarities. The SEM and AFM surface observations also revealed entirely different surface morphologies, for both investigated aluminum compositions. The remarkably distinguishable morphologies were observed in both cases: prior to and after anodization. Summarizing the results of both types of electrochemical measurements and the topological observations, it can be inferred that the TPA forms uniform barrier AAO film, whereas the oxide layer on AA2024-T3 is rather cracked and possesses lower durability in the model corrosive medium.

Keywords: Aluminum anodization, AA2024-T3, EIS, LVA, SEM, AFM

INTRODUCTION

Although the anodization process has been intensively studied [1-13] and well described in the literature [14], its impact on Al-based industrial alloys is not sufficiently investigated. On the other hand, the industrial branch requires highly doped alloys with extended mechanical strength and reliable exploitation characteristics [15, 16]. The alloying dopants promote chemical and structural heterogeneity, which enhances the resulting alloys' susceptibility to localized corrosion [17-22]. Especially, the Cu-Mg-doped AA2024 type of alloys contains a large variety of intermetallic inclusions, which precipitate during the finishing metallurgical thermal post-treatments [23, 24]. These inclusions initiate considerable deviations of the alloy surface behavior from the expected for pure aluminum. In a previous work [25], it was established that the AA2024-T3 alloy has different behavior than a clad alloy with the same composition, during both coating primer deposition and subsequent corrosion tests. In addition, only a few papers on the AA2024-T3 anodization were found [26-28], but the results reported in these works are not compared to pure aluminum.

All these facts have predetermined the aim of the present research: to compare the electrochemical characteristics and topological features of Anodized Aluminum Oxide (AAO) films, obtained at the same conditions on technically pure aluminum and AA2024-T3 aircraft alloy.

EXPERIMENTAL

Two sets by three samples of (Al 99.5%) technically pure aluminum (signed as TPA) and AA2024-T3 were submitted to anodization, followed by subsequent electrochemical measurements and morphological observations. Prior to anodizing, all samples underwent preliminary treatment by etching in 50 g dm^{-3} NaOH solution at 60 °C and activation in diluted HNO$_3$ (1:1 v/v) at room temperature. Both procedures were performed for two minute, followed by vigorous cleaning with tap and distilled water.

The anodization was performed at galvanostatic (15 mA cm^{-2}) and isothermal (20 °C)

* To whom all correspondence should be sent.
E-mail: stephko1980@abv.bg

conditions for 48 minutes with simultaneous in-situ chrono-potentiometric curves acquisition. The curve recording enabled to determine the AAO formation voltage (U_f) with anodization time (t). A two electrode cell, with 250 ml of 15%wt. of H_2SO_4 with continuous stirring was used. The zones submitted to anodization were circular with 24.5 mm diameter for all samples.

The electrochemical measurements were performed after 24 and 168 hours of exposure to 100 ml 3.5% NaCl model corrosive medium in three electrode cells. The exposed areas from the anodized zones were 16 mm in diameter and served as working electrodes. This lower surface area was selected, in order to avoid any edge effects. The signal acquisition was performed against Ag/AgCl/3M KCl reference electrode and cylindrical platinum mesh, serving as a counter electrode.

The measurements were performed using Electrochemical Impedance spectroscopy (EIS), followed by Linear Voltammetry (LVA) in cathodic and anodic directions. The former was performed from 10 kHz to 10 mHz, with 50 frequency steps at 20 to 120 mV, according to the Open Circuit Potential (OCP). This relatively high excitation signal amplitude interval was selected because of the high oxide layer resistance (corresponding to definitely insulating properties in the case of pure aluminum). After each EIS spectrum acquisition, individual cathodic (from 30 to -500 mV) and anodic (from -30 to 500 mV) LVA curves were acquired, respectively. The anodic curves were recorded at least 3 hours after the respective cathodic ones, in order to restore the initial OCP values. The potential sweep in both cases was 10 mVs^{-1}, in order to avoid any significant polarization and electrode damage.

The AAO morphology of some of the samples was additively observed by Scanning Electron Microscopy (SEM), using a TESCAN SEM/FIB LYRA I XMU device. The respective Atomic Force Microscopy (AFM) observations were performed on both cases of technically pure aluminum and AA2024-T3 alloy. These observations were done in dynamic regime by Eayscan 2, "Nanosurf" (Switzerland) on square zones with linear size of 49.5 μm from both the anodized and bare areas, at 256 points per line of resolution. The AFM device was equipped by TAP 190-G cantilever, produced by Budgetsensors (Bulgaria).

RESULTS AND DISCUSSION
In-situ data acquisition

In general terms, all the curves look quite similar, being composed of a sharp vertical slope at the beginning and horizontal line until the end of the anodization process (Fig. 1).
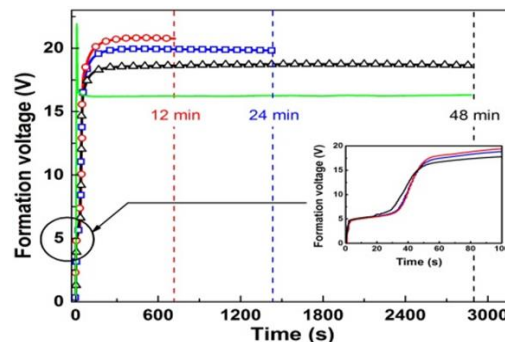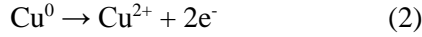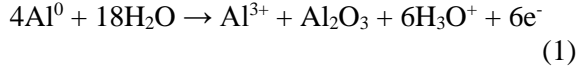

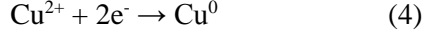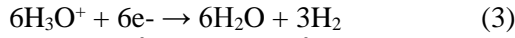**Fig. 1.** In-situ chronopotentiometric curves, acquired during the anodization process

However, the more detailed analysis of the $U_f(t)$-curves reveals a sharp initial rise (until 22.5 V) in the case of TPA, whereas for AA2024-T3 alloy, there is a retention at about 30 - 40 s at 5 V. This fact is related to the differences in the initial oxide layers, formed on Al-foil and AA2024-T3 alloy during the preliminary treatment procedures. In the former case, the oxide layer is more uniform and has specific resistance of 1.5 kΩ cm^2, whereas in the latter case the potential barrier at 5 Volts is somehow related to the thinner oxide layer, corresponding to a resistance of about 0.3 kΩ cm^2. The occurrence of the potential retention at 5 V is related either to copper oxidation or oxide layer growth on the Al matrix adjacent and beneath the intermetallic inclusions, after their dissolution.

Another difference between the in-situ $U_f(t)$-curves is that the horizontal part in the case of TPA is situated at 16.3 V, whereas the curves of the AA2024-T3 alloy are positioned at 18.75 V. This difference is related to the larger specific surface area provided by the alloy. It is a consequence of the higher roughness (commented in the next sections), resulting from the intermetallics' selective dissolution, during both the preliminary treatment procedures and the anodization process itself. Finally, it is worth mentioning that the horizontal parts of the chrono-potentiometric curves correspond to gradual proceeding of Al-oxidation conjugated with reduction of H_3O^+ ions to H_2 on the cathode. In the case of AA2024-T3, these processes are coincided with metallic Cu deposition on the counter electrode. Thus, in the case of AA2024-T3, besides reactions 1 and 3, additional reactions 2 and 4 proceed:

On the anode:

$$4Al^0 + 18H_2O \rightarrow Al^{3+} + Al_2O_3 + 6H_3O^+ + 6e^-$$
$$\text{(1)}$$

$$Cu^0 \rightarrow Cu^{2+} + 2e^- \quad \text{(2)}$$

On the cathode:

$$6H_3O^+ + 6e^- \rightarrow 6H_2O + 3H_2 \quad \text{(3)}$$
$$Cu^{2+} + 2e^- \rightarrow Cu^0 \quad \text{(4)}$$

The additional reactions (2 and 4) require higher voltage, in order to achieve 15 mA cm^{-2}, which is the reason for the higher U_f values for the alloy.

Electrochemical measurements

The already anodized TPA and AA2024-T3 samples were submitted to systematical electrochemical measurements during exposure to 3.5% NaCl model corrosive medium. These measurements were performed by two electrochemical analytical methods.

Electrochemical Impedance Spectroscopy

The impedance spectra acquired at the initial 24 hours of exposure were not sufficiently representative, probably due to intensive adsorption and penetration of the corrosive medium species across the oxide layers. Well-ordered impedance spectra were acquired after 168 hours of exposure. As it was mentioned in the experimental section, the TPA samples needed EIS data acquisition at much higher amplitudes (120 mV versus OCP), in order to obtain readable spectra.

The rather distinguishable shapes of the EIS spectra for the investigated types of aluminum reveal clear structural differences of the AAO film properties, as consequence of the respective substrate compositions. An example of typical EIS spectra acquired for both the investigated compositions (i.e. TPA and AA2024) is represented in Fig. 2.

The dependence of the phase shift (φ) on the excitation signal frequency (f) (i.e. $\varphi(f)$- curves) for TPA show almost completely pure capacitance from 1 kHz to 10 mHz, tending to 90° angular. For comparison, the respective curves for AA2024-T3 in the Bode plots (position b) show two maxima at the high and middle frequency ranges, combined with indistinguishable inflexion at the lowest frequencies.
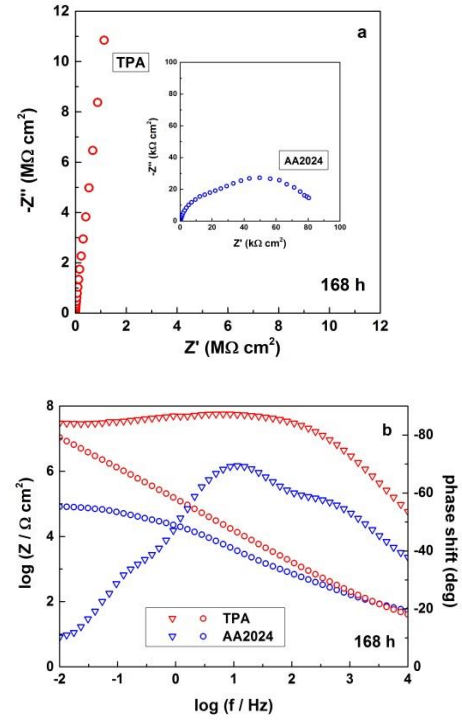

Fig.2. EIS spectra for AAO films after 168 hours of exposure to the model corrosive medium

The Nyquist plots recorded for both types of samples look rather different, as well. In the former case (TPA) almost vertical arcs are obtained, whereas in the alloy case, overlapped semi-circles are observable. It is noteworthy, that pure capacitors give vertical lines and consequently the pure aluminum AAO films behave as almost pure capacitors. Such behavior can be explained assuming dense dielectric film, formed on TPA. Another reason for the occurrence of almost completely pure capacitance might be the higher surface smoothness in the case of the technically pure aluminum.

The rather different spectra shapes required different equivalent circuits (EC) for quantitative data fitting analysis (Fig. 3).
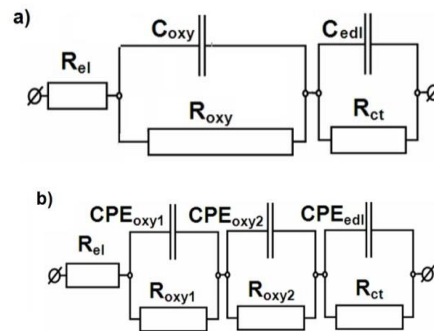

Fig. 3. Equivalent circuits used for EIS data fitting: (a) technically pure Al (TPA) and (b) AA2024-T3 aircraft alloy

The spectra acquired for TPA are composed by only two time constants (i.e. parallel RC units), whereas the data for AA2024-T3 were successfully fitted to circuits, composed by three time constants, connected in series.

Another, rather interesting feature of the equivalent circuit, appropriate for the pure Al spectra fitting was that the use of capacitors (C) was more suitable instead of constant phase elements (CPEs). This fact is an additional evidence for the purely capacitive behavior of the AAO films in this case.

The necessity for description of the AAO formed on the AA2024-T3 alloys by surface CPEs reveals structural and topological irregularity of the oxide layer in this case. This irregularity is an obvious consequence of the variation of the oxide layer growth kinetics on the intermetallic inclusion locations and the basic alloys' Al-matrix. During the anodization process, copper deposition was observed on the cathode, according to reaction (4). This fact is an evidence for Cu-dissolution from the AA 2024-T3 alloy (reaction 2), coinciding the AAO growth. Initially, it was suggested, that the occurrence of two time constants in the case of AA2024-T3 is a result of the simultaneous AAO growth on the basic Al-matrix (with higher rate) and under the actively dissolving Cu-intermetallics (with lower rate, hindered by reactions 2 and 4). However, this assumption is not consistent, because otherwise the oxide layer time constants (CPE_{oxy1} R_{oxy1}) and (CPE_{oxy2} R_{oxy2}) should be connected in parallel, but the data fitting to such equivalent circuit was not successful. The consecutive connection of both time constants reveals occurrence of an interface inside the oxide layer. Thus, distinguishable exterior and interior AAO composing layers are obviously formed. The outer electrolyte/outer oxide interface (CPE_{oxy1}) and the resistance (R_{oxy1}) of the electrolyte penetrated in its defects belong to the upper irregular film. Beneath this outer layer, another, inner layer is formed with a well-defined intermediate interface. This interphase is characterized by its own constant phase element (CPE_{oxy2}) and ohmic resistance (R_{oxy2}). This resistance is probably related to electrolyte penetration towards the metallic surface or Al^{3+} ion transport resistance, as proposed in [1].

The last time constant for both equivalent circuits (C_{edl} or CPE_{edl} and R_{ct}) is related to the chemical reactions of the corrosion process (i.e. oxygen reduction and Al-oxidation) of the already formed AAO films.

In order to evaluate the data dissipation, the numerical data of all the investigated samples obtained by the data fitting of the EIS the spectra by the equivalent circuits (Fig 3) are summarized in Table 1.

The R_{ct} value of sample 3 of TPA group has shown 96.85% deviation. The same trend has been shown by the rest pure aluminum samples after larger exposure times. Probably, the equivalent circuit undergoes changes, due to corrosion product accumulation.

Linear voltammetry

The averaged LVA curves in Fig. 4, acquired after 168 hours of exposure show even more remarkable differences between the typical behavior possessed by the AAO layers on TPA and the alloy, respectively. The LVA results confirm the statements done for the EIS spectra. Indeed, both the cathodic (position a) and anodic (position b) types of curves show significant differences.

The cathodic curves for TPA are almost horizontal, due to the barrier passivation of AAO film, whereas the curves acquired for the AA2024-T3 alloy are smooth and reveal clear occurrence of corrosion processes, being positioned at much higher current densities.
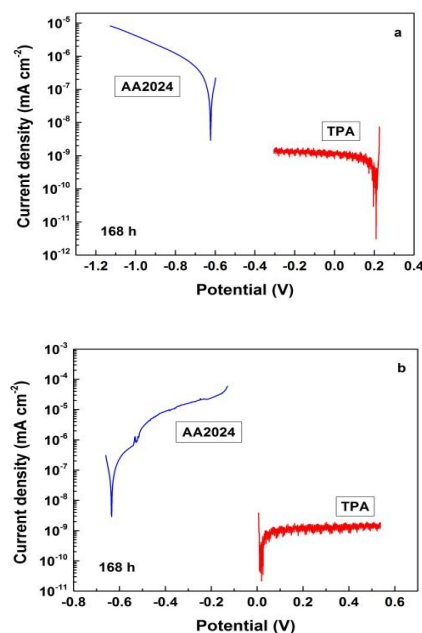

Fig. 4. Cathodic (a) and anodic (b) polarization curves acquired after 168 hour of exposure of the investigated specimens.

Similar trends are observable for the respective anodic curves. Besides, the anodic curves of the alloy possess inflexions, revealing localized corrosion activities [34]. The registered current densities for TPA approach the equipment detection minimum threshold, due to the strong insulating properties of its AAO film.

16

All differences between the curves' shapes described above evince the aptitude of TPA to form dense and uniform AAO with well-expressed barrier properties, whereas the AA2024-T3 forms an oxide layer which does not protect the alloy efficiently.

The LVA curves, acquired after 168 hours of exposure for all investigated samples were submitted to further Tafel slope analysis and the results are shown in Table 2.

The corrosion potential (E_{corr}) values of the alloy samples are in a very narrow interval between -618 and -634 mV, (measured vs. Ag/AgCl/3M KCl), whereas a great E_{corr} dissipation was registered for the pure aluminum. The mentioned E_{corr} deviations for TPA are a result of the insignificant current densities (approaching the equipment detection minimum threshold). The R_p values for TPA are by two orders of magnitude higher than those for AA2024-T3. This fact is an additional evidence for the superior barrier properties of the AAO, formed on the technically pure aluminum.

Table 1. EIS data fitting results from the spectra acquired after 168 hours of exposure

Element	Unit		Sample **1**	Sample **2**	Sample **3**
Anodized TPA samples					
R_{el}	Ω cm^2		28.24 ± 3.08	50.74 ± 6.78	50.04 ± 4.90
C_{oxy}	μF cm^{-2}		1.50 ± 0.12	0.760 ± 0.10	1.40 ± 1.40
R_{oxy}	Ω cm^2	10^3	1.568 ± 0.76	0.29 ± 0.06	3.08 ± 0.80
C_{edl}	μF cm^{-2}		0.685 ± 0.01	0.570 ± 0.01	0.70 ± 0.01
R_{ct}	Ω cm^2	10^6	102.80 ± 28.26	120.40 ± 38.44	286.40 ± 274.54
Anodized AA2024-T3 alloy					
R_{el}	Ω cm^2		16.04 ± 0.73	40.38 ± 2.85	14.42 ± 0.76
Q_{oxy1}	s$^n\Omega^{-1}$cm^{-2}	10^{-6}	4.23 ± 0.49	27.78 ± 6.00	48.04 ± 1.84
n	-		0.88 ± 0.03	1.00 ± 0.09	0.96 ± 0.02
R_{oxy1}	Ω cm^2	10^3	0.85 ± 0.13	51.78 ± 12.32	12.16 ± 1.34
Q_{oxy2}	s$^n\Omega^{-1}$cm^{-2}	10^{-6}	7.78 ± 0.51	4.31 ± 0.19	7.30 ± 1.22
n	-		0.77 ± 0.01	1.00 ± 0.03	0.95 ± 0.04
R_{oxy2}	Ω cm^2	10^3	71.00 ± 15.14	31.50 ± 5.05	0.48 ± 0.06
Q_{edl}	s$^n\Omega^{-1}$cm^{-2}	10^{-6}	14.78 ± 2.50	19.62 ± 3.10	27.25 ± 2.28
n	-		0.96 ± 0.03	0.60 ± 0.15	0.65 ± 0.07
R_{ct}	Ω cm^2	10^3	161.00 ± 16.09	109.60 ± 14.61	40.80 ± 1.08

Table 2. Tafel plot analysis of the polarization curves acquired after 168 hours of exposure

	Cathodic curves		Anodic curves	
	R_p (kΩ cm^2)		R_p (kΩ cm^2)	
Sample	**TPA**	**AA 2024**	**TPA**	**AA 2024**
S 1	22.90×10^3	192.08	26.76×10^3	192.26
S 2	23.32×10^3	161.90	40.14×10^3	157.30
S 3	51.10×10^3	41.72	37.60×10^3	45.90

The corrosion potential (E_{corr}) values of the alloy samples are in a very narrow interval between -618 and -634 mV, (measured vs. Ag/AgCl/3M KCl), whereas a great E_{corr} dissipation was registered for the pure aluminum. The mentioned E_{corr} deviations for TPA are a result of the insignificant current densities (approaching the equipment detection minimum threshold). The R_p values for TPA are by two orders of magnitude higher than those for AA2024-T3. This fact is an additional evidence for the superior barrier properties of the AAO, formed on the technically pure aluminum.

Impact of the anodization process on the surface morphology
Scanning Electron Microscopy

The SEM images (Fig. 5) reveal that the impact of the anodization process for the technically pure aluminum and the highly doped

AA2024-T3 differs. In the former case, the AAO film repeats the substrate's topology. It can be described as laminar surface (inset of position (a)) with multitude of pits (position (a) basic image). The laminar surface is obtained during the Al-foil rolling, whereas the pits are formed during the preliminary etching and acid activation.
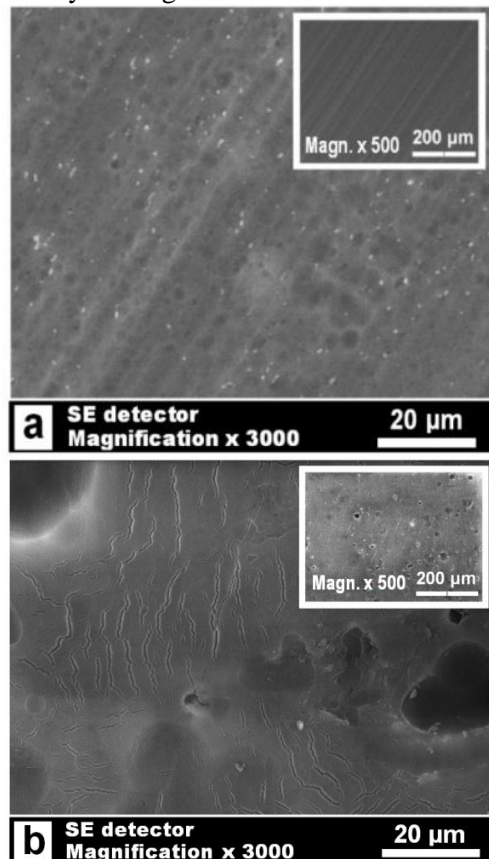

Fig. 5. SEM images of the investigated samples: (a) TPA and (b) AA2024-T3

The AAO layer, formed on AA2024-T3 is covered by multitude of cracks and ruptures. In addition, in the inset of position (b) a large number of wide caverns (not pits) are observable. The results of previous research works dedicated on the preliminary treatment of this alloy [31-33] lead to the inference that these concavities are rather result of the sample etching and acidic activation than to be consequence of the anodization process. These observations completely correlate with the EIS data analysis results. Probably, the cracks and ruptures, together with the entrapped electrolyte correspond to (CPE_{oxy1} R_{oxy1}), whereas the time constant (CPE_{oxy2} R_{oxy2}) shows that these defects do not reach the metallic surface, hence a denser inner oxide layer is present.

Atomic Force Microscopy

The AFM images (Fig. 6) reveal that in the case of TPA, the AAO film repeats the substrate's

topology. Consequently, the anodization of the technically pure aluminum results in only slight smoothening of the laminas and increase of the pits' number and depth.

For comparison, the AA2024-T3 surface looks rather different from the above described even prior to anodization. Besides the cracks commented above (regarding the SEM images), wide caverns instead of pits are observable for the alloy samples. Also, coarse formations are observable, probably due to occurrence of large-sized intermetallics, which are formed during the thermal treatment of the alloy.

The formation of pits and caverns during the preliminary treatments (etching and acidic activation) can be ascribed to selective dissolution phenomena. These phenomena involve the smaller grains in the case of TPA and adjacent Al-matrix surrounding the cathodic intermetallics of the AA2024-T3 alloy, respectively.
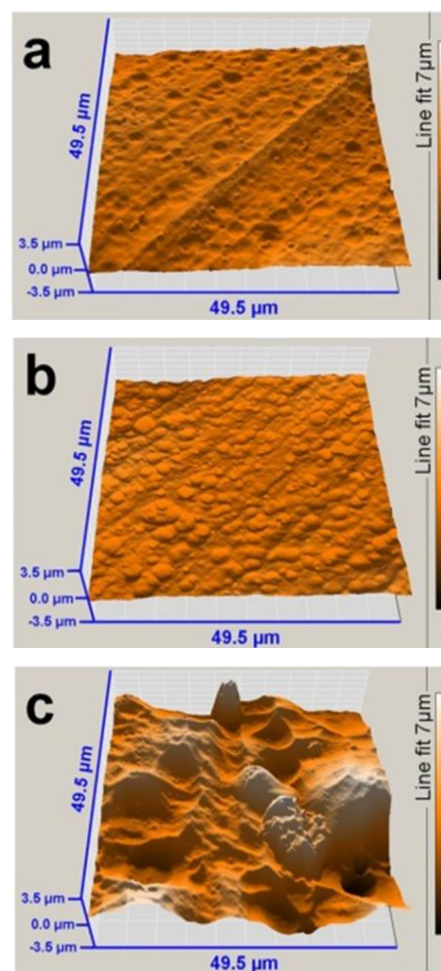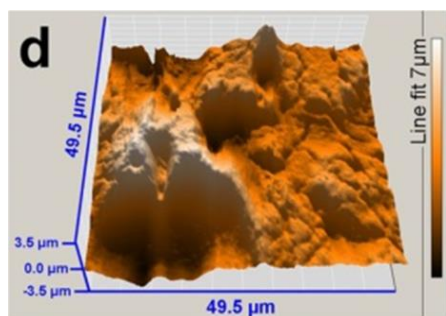
Fig. 6. AFM images of reference (a, c) and anodized (b, d) samples of TPA (a, b) and AA2024-T3 (c, d)

The quantitative AFM data analysis for TPA causes surface roughness increment, regarding the roughness mean (S_m) from 0.4 to 31.2 pm. This S_m increase (of almost 80 times) confirms the inference for pit depth and number increase during the anodization.

For comparison, the anodization of AA2024 leads to greater topological changes than in the case of TPA. The AAO film formed on the alloy shows that the anodization results in twice rougher topology (S_m values from 62.8 pm for TPA up to 190.1 pm for AA2024). This difference can be explained, considering the coincidence of Al-oxide film growth and selective dissolution around the intermetallics.

The maximal distance between the highest and the lowest points (S_y) for TPA changes from S_y = 1.50 to 1.31 μm, due to the anodization process. This S_y decrement with about 0.30 μm is consequence of the smoothening of the laminar ridges, which cannot be compensated by the pitting proliferation, discussed above. For comparison, the AA2024-T3 samples preserve their topology with negligible decrease of S_y from 6.40 to 6.14 μm, regarding the total roughness.

CONCLUSIONS

The in-situ chronopotentiometric curves of TPA possess a sharp initial rise (until 22.5 V), whereas for AA2024-T3 alloy, there is retention of about 30-40 s at 5 V. This phenomenon is related to the differences of the initial oxide layers, formed on TPA foil and AA2024-T3 alloy during the preliminary treatment procedures. The occurrence of the potential retention at 5 V is probably related either to Cu-intermetallics oxidation, or to adjacent Al matrix oxide layer growth, coinciding the intermetallics dissolution. Besides, the horizontal parts of TPA are slightly lower, compared to those for the alloy. This fact is a result of the higher roughness, resulting from the intermetallics selective dissolution during the preliminary treatment procedures.

The TPA samples needed EIS data acquisition at a much higher excitation signal amplitude, in order to obtain readable spectra. The rather distinguishable EIS spectra shapes for the pure aluminum and the alloy reveal clear structural differences of the AAO films, as consequence of the respective substrate compositions. These rather different spectra shapes required different equivalent circuits for quantitative data fitting analysis. The analysis results have shown purely capacitive properties of the AAO formed on TPA, whereas the alloy showed irregular oxide layer, due to intermetallic occurrence.

The cathodic curves for TPA are almost horizontal, due to the barrier passivation of AAO film, whereas the respective curves acquired for the AA2024-T3 alloy are smooth and reveal clear occurrence of corrosion processes. Similar trends are observable for the respective anodic curves. Besides, the anodic curves of the alloy possess inflexions, revealing localized corrosion activity. The polarization resistance (R_p) values for TPA are by two orders of magnitude higher than those for AA2024-T3, because of the superior barrier properties of the AAO, formed on the technically pure aluminum. The corrosion potential (E_{corr}) values of the alloy samples are in a very narrow interval, but a great E_{corr} dissipation was registered for TPA as a result of the random pit distribution, as well as the insignificant current densities, near to the equipment detection minimum threshold.

The SEM and AFM images reveal that the impact of the anodization process for the technically pure Al and the highly doped AA2024-T3 is quite different. In the former case, the anodization results in only slight smoothening of the laminas and increase of the pits' number and depth. The AA2024-T3 surface looks rather different from the above described even prior to anodization. Wide caverns instead of pits are observable for the alloy samples. Besides, coarse formations are also observable, probably due to occurrence of large size intermetallics, which are formed during the thermal treatment of the alloy. The formation of pits and caverns during the preliminary treatments can be ascribed to selective dissolution of smaller grains of the TPA, and adjacent Al-matrix surrounding the cathodic intermetallics of the AA2024-T3 alloy, respectively. Its AAO film has a more distinguishable topology, compared to the respective bare alloy. The quantitative AFM data analysis shows that the AAO film is twice smoother for TPA, than the bare AA2024-T3 alloy (with S_m values of 190.10 to 62.8 pm), because of

coincidence of Al-oxide film growth and selective dissolution.

Summarizing the results of the electrochemical measurements and the topological observations, it can be inferred that the TPA forms uniform AAO, whereas the oxide layer on AA2024-T3 is composed by a cracked outer layer and an underlayer.

REFERENCES

1. J. Siejka, C. Orteg, *J. Electrochem. Soc*. **124**, 883 (1977).
2. V.P. Parkhutik, J. M. Albella, Yu. E. Makushok, I. Montero, J.M. Martinez-Duart, V.I. Shershulskii, *Electrochim. Acta*, **35**, 955 (1990).
3. V.P. Parkhutik, V.T. Belov, M.A. Chernyckh, *Electrochim. Acta*, **35**, 961 (1990).
4. Ch. Girginov, S. Kozhukharov, *Internat. J. Electrochem.* (2011), Article ID 126726; doi:10.4061/2011/126726
5. V. Surganov. C. Jansson. J.G. Nielsen. P. Morgen, *Electrochim. Acta*, **33**, 517 (1988).
6. K.V. Heber, Electrochim. Acta 23, 127 (1978).
7. K.V. Heber, *Electrochim. Acta*, **23**, 135 (1978).
8. F. Nasirpouri, M. Abdollahzadeh, M.J. Almasi, N. Parvini-Ahmadi, *Current Appl. Phys.,* **9**, S91 (2009).
9. A. Bai, C-C.Hu, Y-F.Yang, C-C. Lin, *Electrochim. Acta*, **53**, 2258 (2008).
10. C-U. Yu, C-C.Hu, A. Bai, Y-F. Yang, *Surf. Coat. Tech.,* **201**, 7259 (2007).
11. J.M. Montero-Moreno, M. Sarret, C. Müller, *Surf. Coat. Tech.,* **201**, 6352 (2007).
12. S. Ono, M. Saito, H. Asoh, *Electrochim. Acta,* **51**, 827 (2005).
13. M. Ghorbani, F. Nasirpour , A. Iraji-zad, A. Saedi, *Materials & Design*, **27**, 983 (2006).
14. W. J. Stępniowski, M. Salerno, Chapter 12. Fabrication of nanowires and nanotubes by anodic alumina template-assisted electrodeposition, Manufacturing Nanostructures (Eds. Waqar Ahmed, Nasar Ali), One Central Press (2014) pp. 321-357.
15. E. A. Starke, Jr., J. T. Staley, Prog. Aerospace Sci., 32, 131 (1996).
16. S. V. Kozhukharov, Deposition of Environmentally Compliant Cerium-Containing Coatings and Primers on Copper-Containing Aluminium Aircraft Alloys, Biobased and Environmental Benign Coatings (eds A. Tiwari, A. Galanis and M. D. Soucek), John Wiley & Sons, Inc. (2016), Hoboken, NJ, USA. p. 20
17. F.M. Queiroz, M. Magnani, I. Costa, H.G. de Melo, *Corr. Sci.,* **50**, 2646 (2008).
18. Ch. Blanc, G. Mankowski*, Corr. Sci*., **40**, 411 (1998).
19. J.A. DeRose, T. Suter, A. Bałkowiec, J. Michalski, K.J. Kurzydlowski, P. Schmutz, *Corr. Sci.*, **55**, 313 (2012).
20. A. Aballe, M. Bethencourt, FJ. Botana, M. Marcos, M.A. Rodríguez-Chacón, *Rev. Metal.*, **34**, 42 (1998).
21. V. Guillaumin, G. Mankowski, *Corr. Sci.* **41**, 421 (1998).
22. A. Boag, R.J. Taylor, T.H. Muster, N. Goodman, D. McCulloch, C. Ryan, B. Rout, D. Jamieson, A.E. Hughes*, Corr. Sci.*, **52**, 90 (2010).
23. A. E. Hughes, C. MacRae, N. Wilson, A. Torpy, H. T. Muster, A. M. Glenn, Surf. *Int. Anal.*, **42**, 334 (2010).
24. C. Blanc, B. Lavelle, G. Mankowski, *Corr. Sci.,* **39**, 495 (1997).
25. S. Kozhukharov, M. Milanes, C. Girginov, M. Machkova, *Materials and Corrosion*, DOI: 10.1002/maco.201508635
26. M. Zaki-Mubarok, W. Sutarno, S. Wahyudi, *J. Min. Mater. Char. Eng*., **3**, 154 (2015).
27. G. Boisier, N. Pébère,a, C. Druez, M. Villatte, S. Suelb, *J. Electrochem. Soc.*, **155**, C521 (2008).
28. M. Xiangfeng, W. Guoying, G. Hongliang, Y. Yundan, C. Ying, H. Dettinger, *Int. J. Electrochem. Sci.*, **8**, 10660 (2013).
29. S. Kozhukharov, Ch. Girginov, I. Avramov, M. Machkova, *Mat. Chem. Phys.*, **180**, 301 (2016).
30. M. Curioni, P. Skeldon, E. Koroleva, G. E. Thompson, J. Ferguson, *J. Electrochem. Soc.*, **156**, C147 (2009).
31. E. A. Matter, S. Kozhukharov, M. Machkova, V. Kozhukharov, *J. Chem. Tech. Metall*., **50**, 52 (2015).
32. E. A. Matter, S. V. Kozhukharov, M. S. Machkova, *Bul. Chem. Comm.*, **43**, 23 (2011).
33. E. Matter, S. Kozhukharov, *Ann. proceed. Univ. Rousse (Bulgaria),* **49**, 14 (2010).
34. M. Bethencourt, F.J. Botana, J.J. Calvino, M. Marcos, M.A. Rodriguez-Chacon*, Corr. Sci.*, **40**, 1803 (1998).

СРАВНИТЕЛНО ЕЛЕКТРОХИМИЧНО И ТОПОЛОГИЧНО ИЗСЛЕДВАНЕ НА АНОДНИ ОКСИДНИ ФИЛМИ ФОРМИРАНИ ВЪРХУ ТЕХНИЧЕСКИ ЧИСТ АЛУМИНИЙ И САМОЛЕТНА AA2024-T3 СПЛАВ

С. В. Кожухаров, К. А. Гиргинов

Химикотехнологичен и металургичен университет, бул. Климент Охридски № 8,
1756 София (България)

(Резюме)

Големите разлики в механичните свойства на чистия алуминий и неговите индустриални сплави предопределя значителни вариации на тяхното химично и електрохимично поведение. Този факт налага по-подробно изследване на връзката между състава на сплавта и нейното отнасяне при предварителните химични обработки, както и при излагане в корозионни среди. Настоящото изследване е посветено на сравнението на анодните оксидни филми (AAO), формирани при еднакви условия върху технически алуминий (TPA) и високо легирана сплав (AA2024-T3). Анодирането е провеждано в галваностатично-изотермичен режим, като са регистрирани in-situ хроно-потенциометрични кинетични криви. Електрохимичното поведение на анодираните образци в 3.5% NaCl среда е изследвано чрез електрохимична импедансна спектроскопия (EIS) и линейна волтаметрия (LVA). Топологията на формираните AAO филми е наблюдавана чрез сканираща електронна микроскопия (SEM) и атомно-силова микроскопия (AFM). Чрез използваните аналитични техники е установена забележима разлика в отнасянията на AAO-филмите, образувани върху TPA и тези върху AA2024-T3. Използваните електрохимични методи показаха напълно различни отнасяния, което е потвърдено и от извършения допълнителният цифров анализ на експерименталните данни. Повърхностните наблюдения (SEM и AFM) разкриха напълно различна топологична картина на повърхността за двата изследвани алуминиеви състава. От обобщението на резултатите от електрохимичните измервания и топологичните наблюдения, може да се заключи, че TPA образува равномерен AAO филм, докато оксидният слой върху AA2024-T3 е по-скоро напукан и притежава по-малка трайност в моделната корозивна среда.

Ключови думи: анодиране на алуминий, AA2024-T3, EIS, LVA, SEM, AFM

Application of electro-Fenton process for the treatment of Methylene Blue

D. Clematis[1], N. Klidi[2], A. Barbucci[1], M.P. Carpanese[1], M. Delucchi[1], G. Cerisola[1], M. Panizza[1,*]

[1]*Department of Civil, Chemical and Environmental Engineering, University of Genoa, P.le J.F. Kennedy 1, 16129 Genoa, Italy.*

[2]*Unité de Recherche Electrochimie, Matériaux et Environnement (UREME), Faculté des Sciences de Gabès, Université de Gabès, Cité Erriadh, 6072 Gabès, Tunisie*

The electrochemical removal of an aqueous solution containing 0.25 mM of methylene blue (MB), one of the most important thiazine dye, has been investigated by electro-Fenton process using a graphite-felt cathode to electrogenerate in situ hydrogen peroxide and regenerate ferrous ions as catalyst. The effect of operating conditions such as applied current, catalyst concentration, and initial dye content on MB degradation has been studied. MB removal and mineralization were monitored during the electrolysis by UV–Vis analysis and TOC measurements. The experimental results showed that MB was completely removed by the reaction with •OH radicals generated from electrochemically assisted Fenton's reaction, and in any conditions the decay kinetic always follows a pseudo-first-order reaction. The faster MB oxidation rate was obtained applying a current of 300 mA, with 0.3 mM Fe^{2+} at T=35 °C. In these conditions, 0.25 mM MB was completely removed in 45 min and the initial TOC was removed in 90 min of electrolysis, meaning the almost complete mineralization of the organic content of the treated solution.

Keywords: Methylene Blue, electro-Fenton, graphite felt, dye oxidation.

INTRODUCTION

Synthetic dyes usually contain aromatic rings and consequently they are toxic and bio-recalcitrant and cause serious environmental problems. Therefore, there is a widespread consideration on the development of efficient and cost effective methods for the removal of such hazardous pollutants from industrial effluents. Conventional methods for the removal of synthetic dyes, such as coagulation and filtration generate large volume of sludge to be disposed and/or need the regularly regeneration of adsorbent materials, resulting in an increase in the operational costs [1-3]. Many papers reported that Advanced Oxidation Processes (AOPs) such as Fenton's reagent, ozonation and photochemical oxidation provide effective colour removal and complete destruction of dyes molecules avoiding the potential formation of wastes [4-6].

Among the AOPs, the Electrochemical Advanced Oxidation Processes (EAOPs) are a promising alternative because they are environmentally clean and can produce large amount of hydroxyl radicals (•OH) on demand, under control of applied current [7-12]. In these processes, heterogeneous •OH generated by anodic oxidation (AO) of water using high O_2 overvoltage anodes such as boron-doped diamond (BDD) [13-21] or PbO_2 [22-27] anodes:

$$H_2O \rightarrow {}^\bullet OH + e^- + H^+ \qquad (1)$$
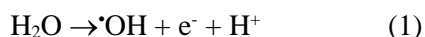
Recently, a new EAOP was proposed for synthetic dye removal and it is based on the production of homogeneous •OH in solution bulk through electrochemically assisted Fenton's reaction (EF), where hydrogen peroxide is generated in situ from the two-electron reduction of O_2:

$$O_2 + 2H^+ + 2e^- \rightarrow H_2O_2 \qquad (2)$$
$$Fe^{2+} + H_2O_2 \rightarrow Fe(OH)^{2+} + {}^\bullet OH \qquad (3)$$
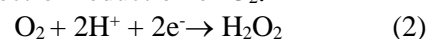
These reactions occur with high yield and satisfactory rate only at gas diffusion cathodes (GDE) [28-32] and three-dimensional carbon-based cathodes, such as RVC [33] and graphite felt [34-38].

Reaction (3) is propagated thorough the continuous regeneration of ferrous iron at the cathode (reaction 4) thus avoiding Fe3+ accumulation in the medium and consequently eliminating the production of iron sludge:

$$Fe^{3+} + e^- \rightarrow Fe^{2+} \qquad (4)$$

In this study we report a detailed discussion on the degradation of methylene blue (MB), a thiazine dye selected as model compound, by electro-Fenton process using commercial graphite-felt as cathode for the production in situ of hydrogen peroxide.

EXPERIMENTAL

Chemicals and analytical procedures

The synthetic solution was prepared by dissolving 0.25 mM of MB (C16H18ClN3S, inset of Figure 1 (a)) (Carlo Erba reagents, 92% purity) used

---

* To whom all correspondence should be sent.
E-mail: marco.panizza@unige.it

without further purification, in bi-distilled water, in 50 mM Na_2SO_4 (Sigma Aldrich). Analytical grade H_2SO_4 (Sigma Aldrich) were used to adjust the initial pH of the solution at the value of 3 using a Schott Gerate CG822 pH-meter. This value of pH was chosen because many literature studies reported to be the optimum for electro-Fenton process [39].

A JascoV-570 UV/VIS spectrophotometer using silica cells of path length 1 cm was used for the determination of MB concentration. A Lambert–Beer diagram was established to correlate the absorbance at 664 nm to MB concentration.

The evolution of TOC was analyzed by using a Hach-Lange reagent Set and the spectrophotometer Dr. Lange LASA50.

Electrochemical system

The experiments were performed using an undivided cell with a volume of 300 mL, supplied with a heat exchanger and a magnetic stirrer under galvanostatic conditions using an AMEL 2055 potentiostat/galvanostat. The cathode was a 70 cm^2 (10 cm x 7 cm) carbon-felt piece (Carbone Loraine) with a thickness of 0.5 cm, and the anode was a 4.5 cm height cylindrical grid (i.d = 3.1 cm). The anode was a Ti/RuO_2 net centered in the electrolytic cell, surrounded by the cathode, which covered the inner wall of the cell. The distance between the electrodes was 1.6 cm. H_2O_2 was produced from reduction of O_2 dissolved in the solution, from reaction (2). Continuous saturation of the solution by O2 at atmospheric pressure was ensured by bubbling of compressed air having passed through a frit at about 1 dm^3 min^{-1}, starting 10 min before electrolysis. Solutions were vigorously stirred using a cylindrical with a magnetic bar (length: 25 mm, diameter: 6 mm) with a rotation rate of about 700 rpm to allow mass transfer.

RESULTS AND DISCUSSIONS

For each experiment, the removal of MB and the effectiveness of electro-Fenton process has been followed using UV-vis spectrophotometry. The absorption spectra of MB at room temperature present two absorption bands at about 664 and 611 nm which are directly related to the colour of the solution. The more well-defined peak at 611 nm was chosen for the determination of the concentration of MB using Lambert–Beer correlation. Figure 1(a) shows an example of UV-spectra evolution for 0.25 mM MB during electrolysis with an applied current of 200 mA and iron concentration of 0.3 mM. During the electrolysis the absorbance bands decreas continuously until disappearing meaning that the MB is almost completely removed by the reaction with •OH radicals electrogenerated (Eq. 3). Figure

1(b) shows that 98% of MB was removed in 90 min and its oxidation can be satisfactory described by a pseudo-first order reaction kinetic.
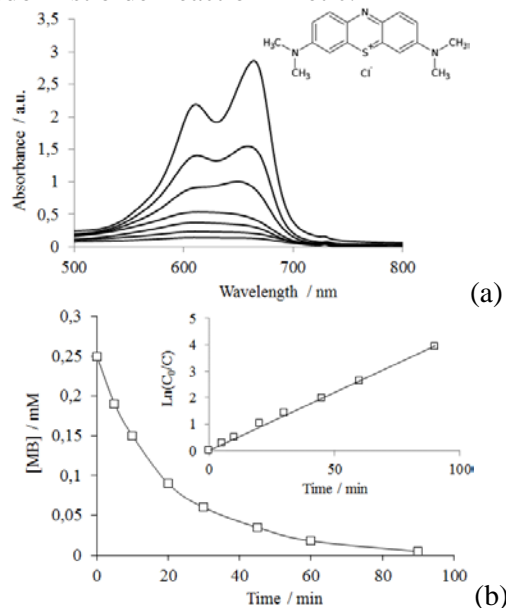

Fig.1. Evolution of (a) UV–visible spectra; (b) MB concentration and corresponding kinetic analysis (inset) as a function of time during electrolysis of 0.25 mM MB. Experimental conditions: $[Fe^{2+}] = 0.3$ mM, I = 200 mA, T = 20 °C, pH = 3.

The effect of several operational parameters including applied current, initial iron concentration and temperature on MB removal was studied during the electro-Fenton treatment of 0.25 mM of MB at pH=3. In the electro-Fenton process the applied current is an important parameter that have to be optimised because both the production rate of H_2O_2 and the regeneration of Fe^{2+} is affected by the applied current [40, 41]. The effect of this parameter on the decay kinetics of MB was investigated performing electrolysis at different current values, i.e., 100, 200, and 300 mA in the presence of 0.3 mM of Fe^{2+} as catalyst and the results are reported in Figure 2.
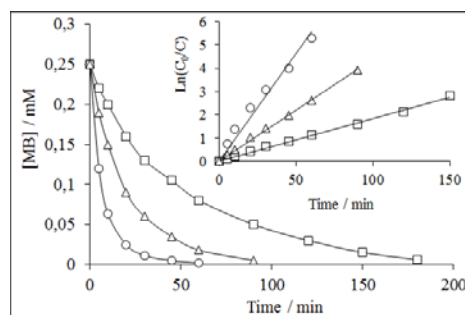

Fig. 2. Effect of applied current on the evolution of MB concentration during the electrolysis of 0.25 MB solution at applied current of: (□) 100 mA; (Δ) 200 mA; and (o) 300 mA. Conditions: pH = 3; T = 20 °C; $[Fe^{2+}] = 0.2$ mM. The inset presents the corresponding kinetics analysis assuming a pseudo first-order reaction.

As can be seen, an increase of the applied current resulted in a higher oxidation rate and in less time required for the complete oxidation of MB. In fact, the time necessary for 96% removal of MB was 180, 90 and 60 minutes at a current of 100, 200 and 300 mA, respectively.

This enhancement of the oxidation rate with the applied current can be related to a greater production of H_2O_2 (Eq. 2) and regeneration of Fe^{2+} (Eq. 4) leading to the generation of higher amount of hydroxyl radicals from Fenton's reaction (Eq. 3).

It can be also seen from Figure 2 that the concentration of MB decreases exponentially for all current values and it can be satisfactory described by a pseudo-first order reaction kinetic (inset of Figure 2). Apparent rate constants for oxidative degradation of MB, obtained from the slop of straight lines of the inset of Fig. 1 were reported in Table 1. The values of the apparent rate constant increased almost linearly with the applied current.

The Fe^{2+} concentration is another important parameter in the electro-Fenton process. in an attempt to optimise reaction conditions on the EF system, degradation of 0.25 mM MB was investigated in the presence of different Fe^{2+} concentrations at pH 3 applying a constant current of 300 mA. The effect of Fe^{2+} concentration on the degradation of MB was shown in Figure 3.

The MB removal rate increases with increasing Fe^{2+} concentration from 0.1 to 0.3 mM, and after this value the degradation rate decreases by increasing Fe^{2+} concentration. The negative effect of the higher catalyst concentration on the degradation kinetic can be explained by increase of the rate of the waste reaction occurring between the hydroxyl radicals and the excess of ferrous ions [39, 42-44]:

$$Fe^{2+} + {}^{\bullet}OH \rightarrow Fe^{3+} + OH^{-} \qquad (5)$$
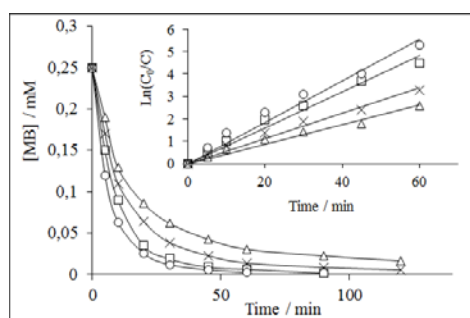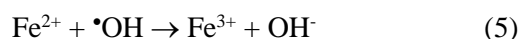
Fig. 3. Effect of Fe^{2+} concentration on the oxidation kinetics of MB during its degradation electro-Fenton treatment. Conditions: pH = 3; T = 20 °C; applied current = 300 mA; [Fe^{2+}] = (□) 0.1 mM. (o) 0.3 mM, (×) 0.5 mM, (Δ) 1.0 mM, the inset presents the corresponding kinetics analysis assuming a pseudo first-order reaction.

The inset of the panel of Figure 3 presents the excellent correlation decay considering a pseudo-first-order reaction rate. The values of the apparent rate constants obtained from the kinetic analyses of the plots in Figure 4 are reported in Table 1.

Table 1. Effect of applied current on the of the relative pseudo-first-order rate constant under conditions given in Figs 2-6

Run	I (mA)	[Fe^{2+}] (mmol dm^{-3})	T (°C)	k_{app} (min^{-1})
1	100	0.3	20	0.0184
2	200	0.3	20	0.0441
3	300	0.3	20	0.0928
4	300	0.1	20	0.0568
5	300	0.5	20	0.0823
6	300	1.0	20	0.0436
7	300	0.3	35	0.1177

Figure 4 reports the effect of temperature on the removal of MB in the range 20 – 35 °C. As can be observed, there are no significant differences between the two temperatures, but higher oxidation rate was obtained at higher temperature because the reaction of hydroxyl radicals oxidizing the dye molecules could be accelerated by increasing the temperature, according to Arrhenius law. Temperature above 35 °C was not considered because it is not convenient, from economic point of view, to further heat the solution.
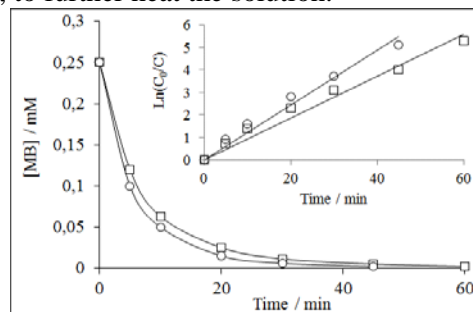

Fig. 4. Effect of temperature on the evolution of MB concentration during the electrolysis of 0.25 mM MB solution. Conditions: pH = 3; applied current 300 mA; [Fe^{2+}] = 0.2 mM, T = (□) 20 °C; (o) 35 °C. The inset presents the corresponding kinetics analysis assuming a pseudo first-order reaction.

The complete oxidation of MB is not an indication that all the organic compounds presents in the solution oxidation have been degraded because of formation of oxidation reaction intermediates. Thus, the mineralization of MB was monitored measuring the TOC of the solution during the electrolysis under best conditions found previously (i.e. applied current 300 mA and Fe2+ concentration 0.3 mM and temperature of 35 °C) and the results are presented in Figure 5.
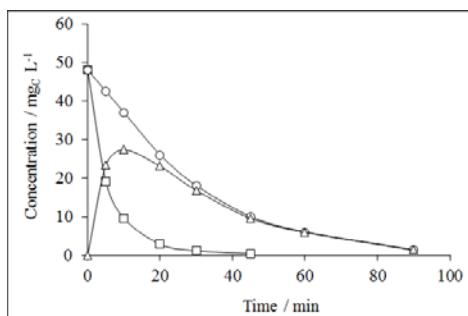
Fig. 5. Evolution of the (o) TOC, (□) MB concentration and (Δ) intermediates expressed as mg/L of carbon, during electro-Fenton treatment of MB aqueous solution. Experimental conditions: pH = 3; applied current 300 mA; $[Fe^{2+}] = 0.2$ mM, T = 35 °C; [MB] = 0.25 mM

After 90 min of treatment, more than 96% of TOC was removed, meaning that almost all the organic compounds (i.e. MB and its oxidation intermediates) are completely mineralised to CO2 and water. However, the faster decrease of MB concentration (expressed in term of mg dm-3 carbon) compared to the removal of TOC indicates that some intermediates are produced during the oxidation. The concentration of this intermediates, obtained by difference between TOC and MB concentration, increased in the first 10 min and then it progressively decreased up to zero.

CONCLUSIONS

The oxidative degradation of MB, one of the most important thiazine dye, by electro-Fenton process has been studied under different experimental conditions. Results show that it is possible to attain a complete removal of the dye and the TOC. This fact is due to the generation of hydroxyl radicals, from Fenton's reagent, that attack to the organic matter present in wastewater, favoring its complete degradation.

In any applied conditions the decay kinetic of MB follows a pseudo-first-order reaction and the oxidation rate largely depends on applied current, Fe^{2+} concentration, while temperature has only a slightly effect. With our cell design the higher oxidation rate was obtained for applied current of 300 mA, catalyst (Fe^{2+}) concentration of 0.3 mM and T = 35 °C.

In these conditions, 0.25 mM MB was completely removed in 45 min and the initial TOC was removed in 90 min of electrolysis, meaning the almost complete mineralization of the organic content of the treated solution.

REFERENCES

1. H. Issa Hamoud, G. Finqueneisel, B. Azambre, *J. Environ. Manage*, **195,** 195 (2017).
2. H. Li, S. Liu, J. Zhao, N. Feng, *Colloids Surf., A*, **494**, 222 (2016).
3. N. Nikooe, E. Saljoughi, *Appl. Surf. Sci.*, **413**, 41 (2017).
4. A. Yasar, N. Ahmad, A. A. A. Khan, A. Yousaf, *J. Environ. Sci.*, **19**, 1183 (2007).
5. M. Aleksić, H. Kušić, N. Koprivanac, D. Leszczynska, A. L. Božić, *Desalination*, **257**, 22 (2010).
6. J. Saien, A. R. Soleymani, J. H. Sun, *Desalination*, **279**, 298 (2011).
7. E. Brillas, I. Sirés and M. A. Oturan, Chem. Rev., **109**, 6570 (2009).
8. C. A. Martínez-Huitle, E. Brillas, *Appl. Catal. B-Environ.*, **87**, 105 (2009).
9. M. Panizza, G. Cerisola, *Electrochim. Acta*, **51**, 191 (2005).
10. M. Panizza, G. Cerisola, *Chem. Rev.*, **109**, 6541 (2009).
11. M. A. Rodrigo, N. Oturan, M. A. Oturan, *Chem. Rev.*, **114**, 8720 (2014).
12. I. Sires, E. Brillas, M. A. Oturan, M. A. Rodrigo and M. Panizza, *Environ. Sci. Pollut. Res.*, **21**, 8336 (2014).
13. D. Clematis, G. Cerisola, M. Panizza, *Electrochem. Commun.,* **75**, 21 (2017).
14. J. Rodriguez, M. A. Rodrigo, M. Panizza, G. Cerisola, *J. Appl. Electrochem.*, **39**, 2285 (2009).
15. M. Panizza, G. Cerisola, *J. Hazard. Mater.*, **153**, 83 (2008).
16. C. Saez, M. Panizza, M. A. Rodrigo, G. Cerisola, *J. Chem. Technol. Biotechnol.*, **82**, 575 (2007).
17. J. M. Aquino, M. A. Rodrigo, R. C. Rocha-Filho, C. Sáez, P. Cañizares, *Chem. Eng. J.*, **184**, 221 (2012).
18. D. M. d. Araújo, C. Sáez, C. A. Martínez-Huitle, P. Cañizares, M. A. Rodrigo, *Appl. Catal. B-Environ.*, **166–167**, 454 (2015).
19. A. Raschitor, C. M. Fernandez, I. Cretescu, M. A. Rodrigo, P. Cañizares, *Sep. Purif. Technol.*, **135**, 110 (2014).
20. J. Sun, H. Lu, L. Du, H. Lin, H. Li, *Appl. Surf. Sci.*, **257**, 6667 (2011).
21. A. Cruz-Rizo, S. Gutiérrez-Granados, R. Salazar, J. M. Peralta-Hernández, *Sep. Purif. Technol.*, **172**, 296 (2017).
22. L. Labiadh, A. Barbucci, M. P. Carpanese, A. Gadri, S. Ammar, M. Panizza, *J. Electroanal. Chem.*, **766**, 94 (2016).
23. M. Panizza, G. Cerisola, *Ind. Eng. Chem. Res.*, **47**, 6816 (2008).

24. G. Ramírez, F. J. Recio, P. Herrasti, C. Ponce-de-León, I. Sirés, *Electrochim. Acta*, **204**, 9 (2016).

25. S. Song, J. Fan, Z. He, L. Zhan, Z. Liu, J. Chen, X. Xu, *Electrochim. Acta*, **55**, 3606 (2010).

26. J. M. Aquino, R. C. Rocha-Filho, N. Bocchi and S. R. Biaggio, *J. Environ. Chem. Eng.*, **1**, 954 (2013).

27. K. Irikura, N. Bocchi, R. C. Rocha-Filho, S. R. Biaggio, J. Iniesta and V. Montiel, *J. Environ. Manage.*, **183, Part 1**, 306 (2016).

28. M. Panizza and G. Cerisola, *Water Res.*, **43**, 339 (2009).

29. L. C. Almeida, S. Garcia-Segura, C. Arias, N. Bocchi and E. Brillas, *Chemosphere*, **89**, 751 (2012).

30. K. Cruz-González, O. Torres-Lopez, A. M. García-León, E. Brillas, A. Hernández-Ramírez and J. M. Peralta-Hernández, *Desalination*, **286**, 63 (2012).

31. X. Florenza, A. M. S. Solano, F. Centellas, C. A. Martínez-Huitle, E. Brillas, S. Garcia-Segura, *Electrochim. Acta*, **142,** 276 (2014).

32. S. Garcia-Segura, E. Brillas, *Electrochim. Acta*, **140**, 384 (2014).

33. A. Özcan, Y. Şahin, A. Savaş Koparal, M. A. Oturan, *J. Electroanal. Chem.*, **616**, 71 (2008).

34. M. Panizza, M. A. Oturan, *Electrochim. Acta,* **56**, 7084 (2011).

35. M. Panizza, A. Barbucci, M. Delucchi, M. P. Carpanese, A. Giuliano, M. Cataldo-Hernández, G. Cerisola, *Sep. Purif. Technol.*, **118,** 394 (2013).

36. S. Bouafia-Chergui, N. Oturan, H. Khalaf, M. A. Oturan, *Procedia Eng.,* **33**, 181 (2012).

37. S. Hammami, N. Oturan, N. Bellakhal, M. Dachraoui, M. A. Oturan, *J. Electroanal. Chem.*, **610**, 75 (2007).

38. I. Sirés, E. Guivarch, N. Oturan, M. A. Oturan, *Chemosphere*, **72**, 592 (2008).

39. M. Panizza, G. Cerisola, *Water Res.*, **35**, 3987 (2001).

40. A. Özcan, M. A. Oturan, N. Oturan, Y. Şahin, *J. Hazard. Mater.*, **163**, 1213 (2009).

41. N. Oturan, S. Trajkovska, M. A. Oturan, M. Couderchet, J.-J. Aaron, *Chemosphere*, **73**, 1550 (2008).

42. M. Zhou, Q. Yu, L. Lei, *Dyes Pigments*, **77**, 129 (2008).

43. E. Brillas, M. Á. Baños, M. Skoumal, P. L. Cabot, J. A. Garrido, R. M. Rodríguez, *Chemosphere*, **68**, 199 (2007).

44. Y. Sun, J. J. Pignatello, *Environ. Sci. Technol.*, **27**, 304 (1993).

ПРИЛОЖЕНИЕ НА ЕЛЕКТРО-FENTON ПРОЦЕСА ЗА ТРЕТИРАНЕ НА МЕТИЛЕНОВО СИНЬО

Д. Клематис[1], Н. Клиди[2], А. Барбучи[1], М.П. Карпанезе[1], М. Делуки[1], Г. Керизола[1], М. Паница[1]

[1]*Катедра по строително, химическо и екологично инженерство (DICCA), Университет Генуа, 16129 Генуа, Италия*

[2]*Изследователско звено „Електрохимия, материали и околна среда" (UREME), Научен факултет, Университет в Габе, 6072 Габе, Тунис*

(Резюме)

Електрохимичното отстраняване на метиленово синьо (MB) от воден разтвор, съдържащ 0.25 mM MB, едно от най-важните тиазинови багрила, е изследвано чрез електро-Fenton процес, като се използва графитно кече за катод, за да се генерира *in situ* по електричен път водороден пероксид и да се регенерират железните йони като катализатор. Изследван е ефектът на условията на работа, като например приложен ток, концентрация на катализатора и първоначално съдържание върху разграждането на MB. Отстраняването на MB и минерализирането бяха наблюдавани по време на електролизата чрез UV-Vis анализ и TOC измервания. Експерименталните резултати показват, че MB е напълно отстранен чрез реакцията с • OH радикали, генерирани от електрохимично подпомогната реакция на Fenton и при всички условия кинетиката на разпад винаги следва реакция от псевдо-първи ред. По-бързата скорост на окисление на MB се получава при прилагане на ток от 300 mA с 0,3 mM Fe^{2+}при T = 35°C. При тези условия 0.25 mM MB се отстранява напълно за 45 минути и първоначалният TOC се отстранява за 90 минути електролиза, което означава почти пълната минерализация на органичното съдържание на третирания разтвор.

Ключови думи: метиленово синьо, електро-Fenton, графитово кече, окисляване на багрилото

Electrochemical studies of two pyrrolo[1,2-c]pyrimidines

M.-L. Tatu[1], F. Harja[1], E.-M. Ungureanu[1]*, E. Georgescu[2], L. Birzan[3], M.-M. Popa[3]

[1]Department of Inorganic Chemistry, Physiscal Chemistry and Electrochemistry, University "Politehnica" of Bucharest, Gh. Polizu 1-7, 011061, Romania

[2]Research Center Oltchim, Uzinei Street 1, 240050, Ramnicu Valcea, Romania,

[3]Romanian Academy, Institute of Organic Chemistry "C. D. Nenitzescu", Spl. Independentei, 202B, 060023-Bucharest, 35 P.O. Box 108, Romania

The electrochemical characterization of two pyrrolo[1,2-c]pyrimidines has been performed by cyclic voltammetry (CV), differential pulse voltammetry, and rotating disk electrode voltammetry. Their diffusion coefficients were determined from the scan rate influence on CV anodic currents. Modified electrodes were prepared in pyrrolo[1,2-c]pyrimidines solutions in acetonitrile containing tetrabutylammonium perchlorate by cycling the potential or by controlled potential electrolysis at different anodic potentials and charges.

INTRODUCTION

The pyrrolo[1,2-*c*]pyrimidine type structures are present in many natural products [1-6], and these compounds have been studied for their bioactivity. Some compounds of this class have antioxidant, antifungal and antimicrobial properties, or are used in cancer treatments. Pyrrolopyrimidine derivatives are used for their PI3Ka kinase inhibitory activity, for the treatment of MDR pathogens [6-10].

Pyrrolo[1,2-*c*]pyrimidine is an N-bridgehead heterocyclic compound obtained by formal condensation of a pyrrole with a pyrimidine [9]. Different procedures for the synthesis of pyrrolo[1,2-*c*]pyrimidines starting from suitable substituted pyrroles [10-11] or pyrimidines [12-15] are described. The reactions starting from different pyrrole structures such as pyrrole-2-carboxaldehyde with tosylmethyl isocyanide gives pyrrolo[1,2-*c*]pyrimidine derivatives with a good `yield, but they use the hazardous isocyanide derivative, and the tosyl group cannot be removed so easy. Thus, the most efficient and environmentally friendly method to obtain pyrrolo[1,2-*c*]pyrimidines is by 1,3-dipolar cycloaddition reaction of the pyrimidinum *N*-ylides in 1,2-epoxybutane as reaction medium. The use of the epoxide as a reaction medium and acid scavenger has the advantage of direct formation of the final compound avoiding the generation of the inactivated product [9, 16-21].

There are several studies on the electrochemical characterization of pyrrolo[1,2-*c*]pyrimidine derivatives reported by our group [22]. Their characterization has been done by cycling voltammetry (CV), and differential pulse voltammetry (DPV). The present paper is focused on the electrochemical characterization of two other related pyrrolo[1,2-*c*]pyrimidines. The electrochemical study is important as it offers the simplest method to estimate HOMO and LUMO energies of a molecule [23], which is essential for organic light-emitting diode (OLED) applications.
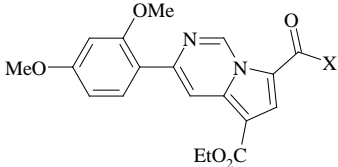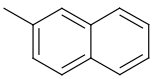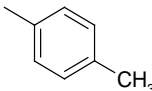
The two compounds are ethyl3-(2,4-dimethoxyphenyl)-pyrrolo[1,2-*c*]pyrimidine-5-carboxylates substituted at position 7 of the pyrrole ring either with 2-naphthoyl (**P1**) or with 4-methylphenylcarbonyl (**P2**). CV, DPV and also rotating disk electrode (RDE) voltammetry have been used for their characterization. Modified electrodes have been obtained by potentiodynamic or potentiostatic methods in order to future applications.

EXPERIMENTAL

The pyrrolo[1,2-*c*]pyrimidines were synthesized as previously described [20-22]. The structure and melting point (m.p.) of compounds considered in the present study are given in Table 1. Their electrochemical study was performed in acetonitrile (CH₃CN) in the presence of tetrabutylammonium perchlorate (TBAP), both from F1uka.

---

* To whom all correspondence should be sent.
E-mail: ungureanu2000@yahoo.com

Table 1. Investigated pyrrolo[1,2-*c*]pyrimidines

Formula	Entry	X	m.p. (ºC)
	P1		163-164
	P2		230-231

PGSTAT 12 AUTOLAB potentiostat connected to a three-electrode cell was used for electrochemical investigation. A glassy carbon electrode disk (3 mm diameter) from Metrohm was used as working electrode. Its active surface was polished with diamond paste (2 μm) and cleaned with the acetonitrile before each experiment. Ag/10 mM $AgNO_3$ in 0.1 M TBAP/CH_3CN was used as reference electrode. The auxiliary electrode was a platinum wire. The experiments were performed at room temperature (25ºC) under argon atmosphere. All potentials were referred to the potential of ferrocene/ ferrocenium redox couple (Fc/Fc$^+$) which in our experimental conditions was +0.07 V. CV curves were usually recorded at 0.1 V·s^{-1} or at various scan rates (0.1 – 1 V·s^{-1}), DPV curves at 0.01 V·s^{-1} with a pulse height of 0.025 V and a step time of 0.2 s, and RDE curves at 0.01 V·s^{-1}

RESULTS AND DISCUSSIONS

The electrochemical characterization was performed in millimolar solutions of each .

pyrrolo[1,2-*c*]pyrimidine by CV, DPV, and RDE at different concentrations in 0.1 M TBAP/CH_3CN. All anodic and cathodic curves were recorded starting from the stationary potential. In all cases, the processes put in evidence by DPV were denoted in the order of their apparition in DPV curves in anodic (a1, a2, …) or cathodic (c1, c2, ..) scans, and this notation was kept for the corresponding processes recorded by other methods (CV or RDE).

Study of *P1*

DPV and CV curves at different concentrations (0 – 0.75 mM) of **P1** are presented in Figure 2. The DPV curves show four anodic (a1 – a4), and four cathodic peaks (c1 – c4). They highlight, respectively, 4 oxidation and 4 reduction processes which can occur during the potential scans. The peaks are also seen in CV curves. CV anodic peaks are less prominent, due to the superposition to the background oxidation process (dotted line). The peak currents increase with concentrations for CV and DPV curves.
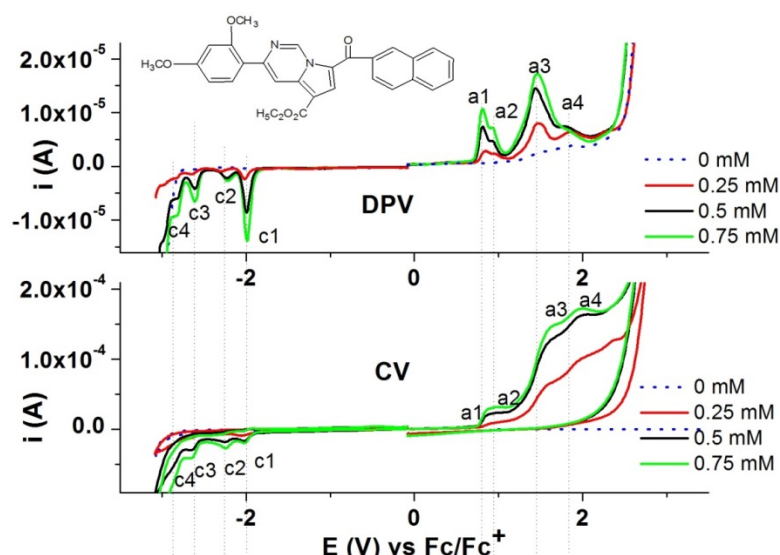
Fig.2. CV (0.1 V·s^{-1}) and DPV (0.01 V·s^{-1}) curves on glassy carbon electrode (diameter 3 mm) at different concentrations for **P1** in 0.1 M TBAP/CH_3CN

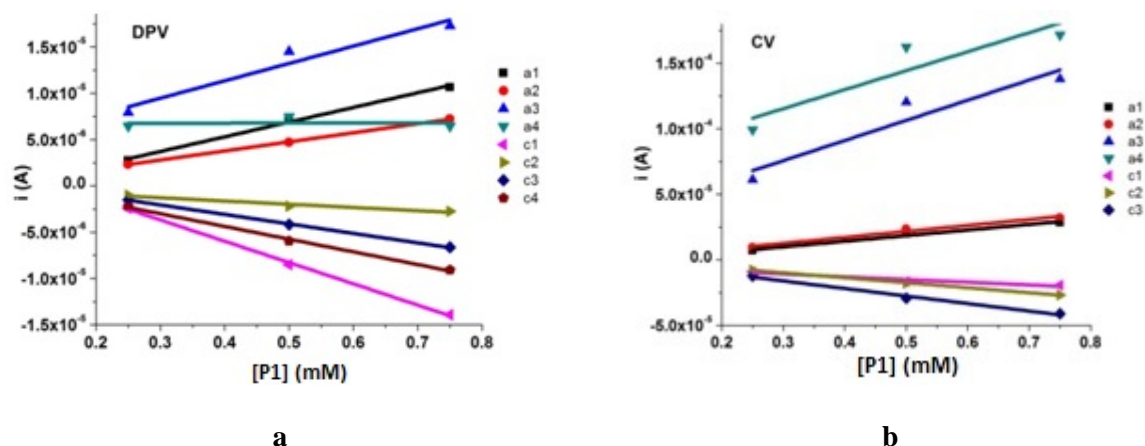**a**   **b**

Fig. 3. Linear dependences of the peak currents on concentration from DPV (0.01 V·s⁻¹) (a) and CV
(0.1 V·s⁻¹) (b) curves from Fig. 2

Table 2. Equations and the correlation coefficients of the linear peak currents dependences on **P1** concentration* from
CV (0.1 V·s⁻¹) and DPV (0.01 V·s⁻¹) curves from Fig. 3

Method	Equation	Correlation coefficient
DPV	$i_{peak\ a1} = -1.03 + 15.86 \cdot [\mathbf{P1}]$	0.984
	$i_{peak\ a2} = -0.14 + 9.81 \cdot [\mathbf{P1}]$	0.998
	$i_{peak\ a3} = 3.86 + 18.75 \cdot [\mathbf{P1}]$	0.896
	$i_{peak\ c1} = 3.22 - 22.99 \cdot [\mathbf{P1}]$	0.997
	$i_{peak\ c2} = -0.22 - 3.49 \cdot [\mathbf{P1}]$	0.905
	$i_{peak\ c3} = 1.02 - 10.24 \cdot [\mathbf{P1}]$	0.999
	$i_{peak\ c4} = 1.11 - 13.72 \cdot [\mathbf{P1}]$	0.994
CV	$i_{peak\ a1} = -3.02 + 42.94 \cdot [\mathbf{P1}]$	0.972
	$i_{peak\ a2} = -1.05 + 45.48 \cdot [\mathbf{P1}]$	0.960
	$i_{peak\ a3} = 29.53 + 153.78 \cdot [\mathbf{P1}]$	0.821
	$i_{peak\ c1} = 1.83 - 24.58 \cdot [\mathbf{P1}]$	0.971
	$i_{peak\ c2} = 1.57 - 38.07 \cdot [\mathbf{P1}]$	0.997
	$i_{peak\ c3} = 1.15 - 57.46 \cdot [\mathbf{P1}]$	0.979

*i_{peak} is expressed in μA, and [**P1**] in mmol.l⁻¹

The linear dependences of the total currents *vs* concentration for DPV and CV curves are presented in Figure 3a and 3b, respectively. Table 2 shows the equations and the correlation coefficients for these linear dependences of all peak currents on **P1** concentration. The slopes in Table 2 show the increase in peak height with the **P1** concentration. It occurs with different slopes for the investigated peaks, indicating a complexity of the involved processes. It can be seen that peak a3 has a correlation coefficient less than 0.9, both in DPV and in CV. The peak potentials from DPV and CV curves for **P1** are given in Table 3.

RDE anodic and cathodic curves at various concentrations (0.25 – 0.75mM) are given in Fig. 4 for a constant rotation rate (1000 rpm) and in Fig. 5 for different rotation rates (500 – 2000 rpm) at constant concentration (0.5 mM) of **P1**. The DPV curves for this concentration are presented

underneath, in order to allow their parallel evaluation.

From Figs. 4 and 5 it can be seen that RDE cathodic currents have regular behaviour (increasing with **P1** concentration and rotation rate of the electrode). Conversely, the anodic currents have particular variation: they are increasing with concentration for RDE anodic wave corresponding to a1 process, while in the range of a2 DPV peak, the current promptly decreases to the background value and it increases again in the range of a3 process, but not proportionally. The isosbestic point is situated at about 1.53 V. There is no wave corresponding to a4 DPV peak on RDE curves.

The anodic curves for **P1** could be explained by the processes given in Table 3. After **P1** oxidation to the radical cation (peak a1), there is an irreversible process of film formation in the range of a2 peak, which continues at more positive potentials. In the

29

range of a3, there is another oxidation process, which competes with the film formation started in a2. It has the highest current at the smallest concentration of **P1.** These aspects are in agreement with the RDE curves in Fig. 5. When increasing the rotation rate of RDE, only the currents for anodic a1 and a4 peaks are increasing. The currents for a2 are constant, while those for a3 are decreasing. This means these processes (a1, a4) are not involved in the film formation, as it is the case for a2. The currents for a3 are inversely proportional to the imposed rotation rate. At low rotation rates, the current in the domain of a3 is higher, as the intermediates for the film formation can stay close to the electrode and keep on the polymerization process. Two isosbestic points which delimitates the change between processes can be noticed at 1.299 V (I1) and 1.627 V (I2), respectively.
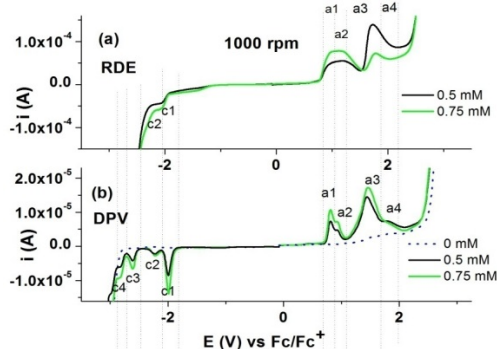
Fig. 4. RDE curves (0.01 V·s⁻¹) on glassy carbon electrodes (3 mm diameter) at different concentrations in **P1** solution in 0.1 M TBAP/CH$_3$CN at 1000 rpm (a), DPV curves (0.01V·s⁻¹) obtained for **P1** on glassy carbon electrode (3 mm diameter) in 0.1 M TBAP/CH$_3$CN (b)

Figure 6 presents the CV curves in the range of the first anodic and cathodic peaks for **P1** (0.5 mM) at different scan rates, and the dependences of the total peak currents for a1 and c1 peaks *vs* the scan rate. It can be seen that the total currents linearly increase with the square root of the scan rate (with good correlation coefficients for a1 and c1). It can be seen also from Fig. 6a that a1 is an irreversible process, while c1 is a quasi-reversible process, having a corresponding peak in the reverse scan c1' situated at about 100 mV *vs* c1.

In figure 7 are given the CV curves for **P1** (0.5 mM) on different scan domains. From these curves, the reversibility of each process in the anodic and cathodic domains has been estimated. Processes obtained in the anodic domains are irreversible, while the cathodic ones are reversible or quasi-reversible (Table 3), the last mentioned showing corresponding peaks situated at potentials of less than 100 mV in respect with the peaks in the direct scans.
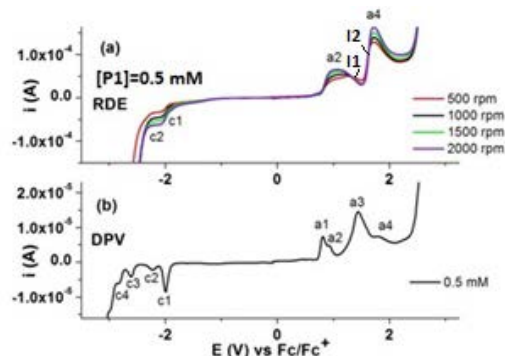
Fig. 5. RDE curves on glassy carbon electrode (3 mm diameter) in **P1** solution (0.5 mM) in 0.1 M TBAP/CH$_3$CN at different rotation rates (500 – 2000 rpm) (a), and DPV curve (0.01V·s⁻¹) for **P1** (0.5 mM) on glassy carbon electrode in 0.1 M TBAP/CH$_3$CN (b)
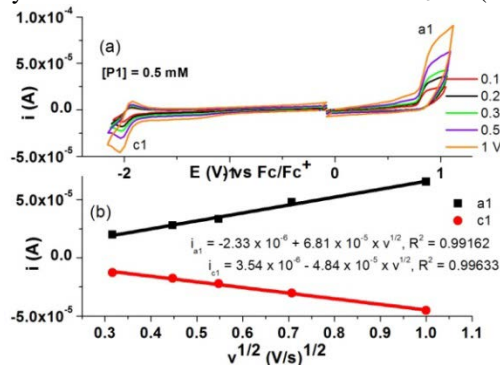

Fig.6. CV curves in 0.1 M TBAP/CH$_3$CN on glassy carbon electrode (3 mm diameter) for **P1** (0.5 mM) at different scan rates (0.1 – 1 V·s⁻¹) (a) and dependences of the peak currents on the square root of the scan rate (b)
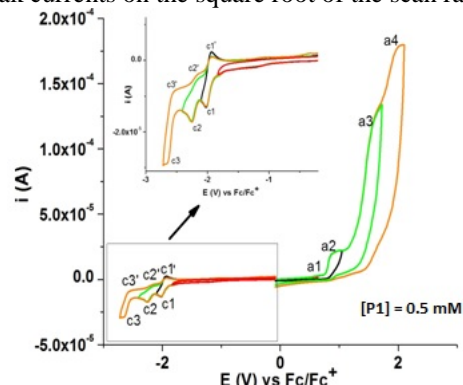

Fig.7. CV curves (0.1 V·s⁻¹) at different scan domains on glassy carbon electrode (3mm diameter) for **P1** (0.5 mM) in 0.1 M TBAP/CH$_3$CN; inset A: detail of the cathodic domain

Modified electrodes based on P1

Chemical modified electrodes (CME) based on electrode coverage with compound **P1** were obtained either by potentiodynamic (successive scans) or potentiostatic (controlled potential electrolysis) methods in solutions of **P1**(0.5 mM) in the domain of the anodic processes a1, a2, a3, and a4.

Table 3. Peak potential values (V) *vs* Fc/Fc$^+$ for **P1** from DPV and CV curves

Peak	Method		Process characteristic
	DPV	CV	
a1	0.81	0.86	irreversible
a2	0.93	0.97	irreversible
a3	1.44	1.57	irreversible
a4	1.80	1.98	irreversible
c1	-1.99	-2.03	reversible
c2	-2.23	-2.26	quasi-reversible
c3	-2.61	-2.65	quasi-reversible
c4	-2.82	-	quasi-reversible

a

b

c

d
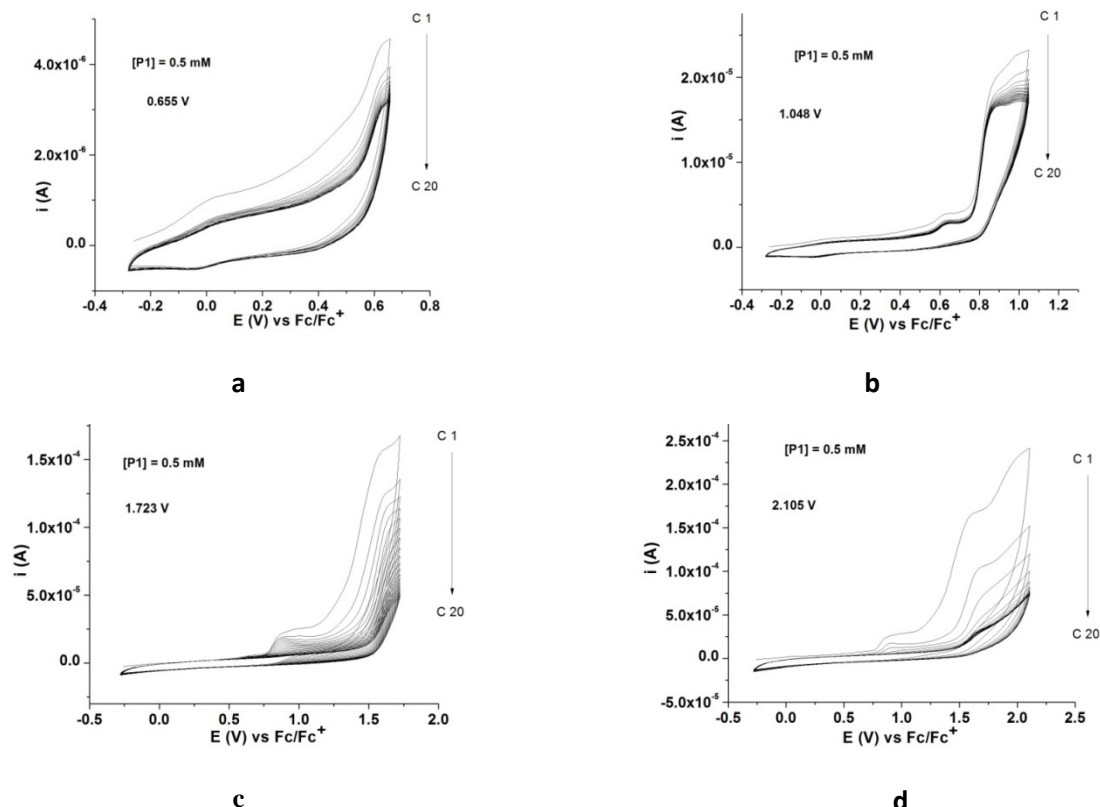
Fig. 8 . CV curves (0.1 V·s^{-1}) during the preparation of CME by successive scans in 0.5 mM solution of **P1** in 0.1 M TBAP/CH$_3$CN between -0.3 V and different anodic limits: +0.655 V (a); +1.048 V (b); +1.723 V (c); +2.105 V (d)

Figure 8 presents the CV curves during the preparation of CME by potentiodynamic method. Figure 9 shows the CV curves obtained after the transfer of the modified electrodes obtained by successive potential scans between -0.3 V and different anodic potentials (+0.655 V (Fig. 8a); +1.048 V (Fig. 8b); +1.723 V (Fig. 8c); +2.105 V (Fig. 8d)) in 1 mM ferrocene solution in 0.1 M TBAP/CH$_3$CN. The ferrocene CV curves obtained on CMEs are different than the CV curve obtained for the bare electrode. In the inset A are the dependences of the anodic and cathodic peak potentials for ferrocene (Fc) on the anodic limit scan, that show important variations starting at potentials more positive than 1.5 V. In the inset B are shown the corresponding anodic and cathodic currents dependencies, which have the same behavior as those shown by inset A. It can be seen

that the ferrocene signal is the most diminished for the potential scan limit of +2.105 V, where it can be assumed that the most compact coverage of the electrode is attained
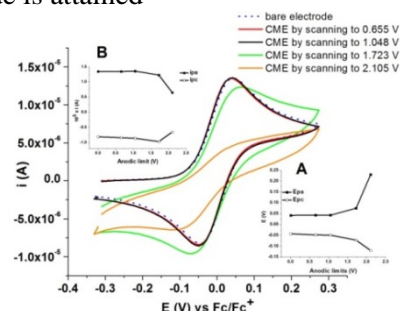
Fig. 9. CV curves (0.1V/s) for CME prepared by successive scans (in 0.5 mM solution of P1 in 0.1 M TBAP/CH$_3$CN) after the transfer of CME in 1mM Fc solution in 0.1 M TBAP, CH$_3$CN; dependences of the anodic and cathodic Fc peak potentials (inset A) and currents (inset B) on the anodic limit
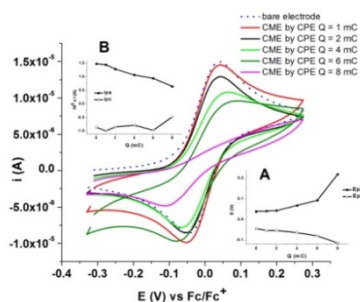
31

Fig. 10. CV curves (0.1V/s) for CME prepared by CPE (at +2.105 V in 0.5 mM solution of **P1** in 0.1 M TBAP/CH₃CN) after the transfer of CME in 1mM Fc solution in 0.1 M TBAP, CH₃CN; dependences of the anodic and cathodic Fc peak potentials (inset A) and currents (inset B) on electropolymerization charge (Q)

Films based on **P1** have been also prepared by CPE at different potentials: 0.655V, 1.048 V, 1.723 V, 2.105 V using a charge of 1 mC. The CV curves of the CMEs in transfer ferrocene solution have very small changes in respect with the bare electrode, indicating a weak coverage of the electrode. However, the CPE performed at 2.105 V led to evident changes which occur continuously when the charge increases from 1 mC to 8 mC. In Fig. 10 are given the CV curves after the transfer in ferrocene solution of the CMEs obtained at 2.105 V, indicating the continuous increase of the coverage of the electrode. For the potential of +2.105 V the most insulating film is obtained at 8 mC, for which the ferrocene curve has the smallest anodic peak, and the most shifted potential to positive values, as shown in the inset A, which presents the dependences of the anodic and cathodic potentials on the applied charge (Q). The current for anodic and cathodic peaks for ferrocene are almost linearly decreasing with Q, as it can be seen in the inset B. This evolution is in agreement with the thickness of the film.

Study of **P2**

Experiments were carried out to characterize compound **P2**, similarly to the assays performed to characterize the compound **P1**. The CV and DPV curves have been recorded in **P2** solutions in 0.1 M TBAP, CH₃CN. They are shown in Figure 11 for different concentrations (0 – 0.5 mM). DPV curves show five oxidation peaks (a1 – a5) and three reduction peaks (c1– c3). One anodic peak (a1) and three cathodic peaks (c1, c2, c3) are seen in CV, denoted in agreement with processes notation from DPV curves. The peak currents are increasing with the concentration for both CV and DPV curves. In Figure 11 and Table 4 are given the linear plots of the peak currents on **P2** concentration for the main

peaks, and their equations and correlation coefficients, respectively. Good correlation coefficients have been obtained. The slopes in Table 4 indicate an increase of the peak height with **P2** concentration, with different slopes for the investigated peaks, as in the case of **P1**. The peak potentials from DPV and CV curves for **P2** are given in Table 5.
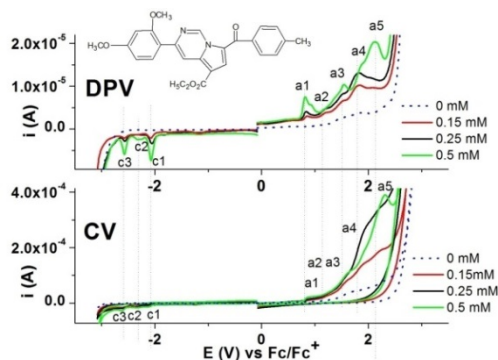

Fig. 11. CV (0.1 V·s⁻¹) and DPV (0.01 V·s⁻¹) curves on glassy carbon electrode (diameter 3 mm) at different concentrations for P2 in 0.1 M TBAP/CH₃CN
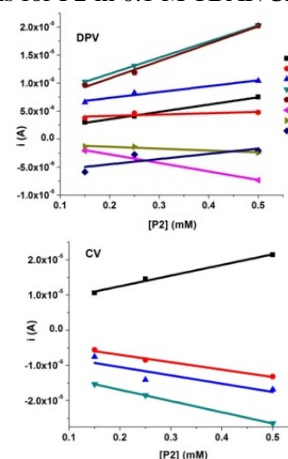

Fig. 12. Linear dependences of the peak currents on **P2** concentration from (a) DPV (0.01 V·s⁻¹) and (b) CV (0.1 V·s⁻¹) curves from Fig. 11

RDE anodic and cathodic curves at different rotation rates (500 - 2000 rpm) recorded for [**P2**] = 0.5 mM and the corresponding DPV curve are given in Fig.13. The curves present the isosbestic point (I1) situated at about 1.45 V. In the range of a2 DPV peak, RDE currents have constant values, and they increase again in the range of a3 process. These anodic RDE curves could be explained by the processes given in Table 5. The currents in the potential domain of a3 are inversely proportional to the rotation rate, while those in the domains of a4 and a5 are almost not influenced by the rotation rate.

Table 4. Equations and the correlation coefficients of the linear peak currents dependences on concentration* from CV (0.1 V·s^{-1}) and DPV (0.01 V·s^{-1}) curves from Fig. 11

Method	Equation*	Correlation coefficient
DPV	$i_{peak\ a1} = 0.95 + 13.1 \cdot$ [**P2**]	0.994
	$i_{peak\ a3} = 5.26 + 10.6 \cdot$ [**P2**]	0.941
	$i_{peak\ a4} = 5.89 + 28.8 \cdot$ [**P2**]	0.999
	$i_{peak\ a5} = 4.65 + 30.92 \cdot$ [**P2**]	0.986
	$i_{peak\ c1} = 0.31 - 15.2 \cdot$ [**P2**]	0.996
	$i_{peak\ c2} = -0.71 - 3.33 \cdot$ [**P2**]	0.894
	$i_{peak\ c3} = -0.27 - 11.06 \cdot$ [**P2**]	0.978
CV	$i_{peak\ a1} = 6.41 + 30.2 \cdot$ [**P2**]	0.984
	$i_{peak\ c1} = -2.81 - 21.0 \cdot$ [**P2**]	0.978
	$i_{peak\ c3} = -10.6 - 31.8 \cdot$ [**P2**]	0.999

*i_{peak} is expressed in μA, and [**P2**] in mmol/L

In Fig.14 are given the CV curves at different scan rates for the first anodic and cathodic peaks, and the linear dependences of their currents on the square root of the scan rate. High values of correlation coefficients have been obtained (Fig. 14b).
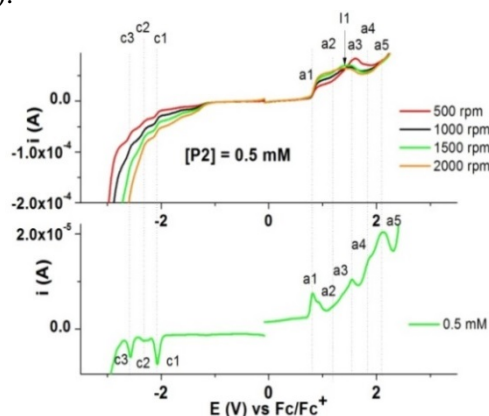
Fig.13. RDE curves (0.01 V·s^{-1}) on glassy carbon electrode (3 mm diameter) at different rotation rates (500 – 2000 rpm) in 0.5 mM **P2** solution in 0.1 M TBAP/CH$_3$CN (a); DPV curve obtained for 0.5 mM solution of **P2** on glassy carbon electrode (3 mm diameter) in 0.1 M TBAP/CH$_3$CN (b)

In figure 15 are shown the CV curves of **P2** on different scan domains. The reversibility of each process has been estimated from these curves (Table 5). Processes obtained in the anodic domain are irreversible. Those from the cathodic domain are irreversible (c1) or quasi-reversible (c2, c3), with corresponding peaks situated at potentials shifted of 70 mV (for c2') and 100 mV (for c3') in respect with the peaks in the direct scans.
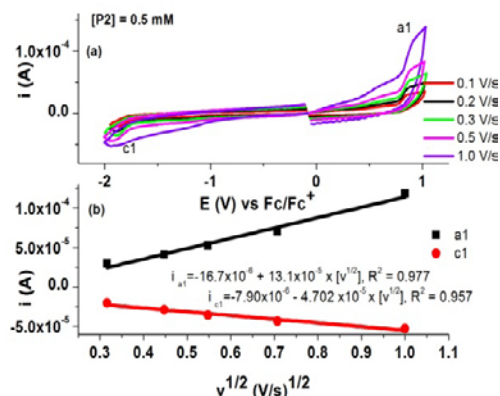

Fig. 14. CV curves in 0.1 M TBAP/CH$_3$CN on glassy carbon electrode (3 mm diameter) for P2 (0.5 mM) at different scan rates (0.1 – 1 V·s^{-1}) (a) and dependences of the peak currents on the square root of the scan rate (b)
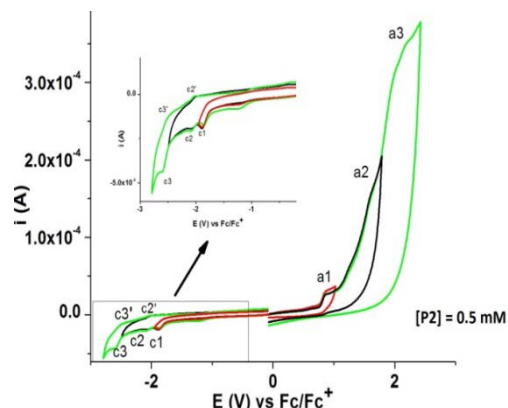

Fig. 15. CV curves (0.1 V·s^{-1}) on glassy carbon electrode (3mm diameter) on different scan domains for **P2** (0.5 mM) in 0.1 M TBAP/CH$_3$CN; inset: detail of the cathodic domain
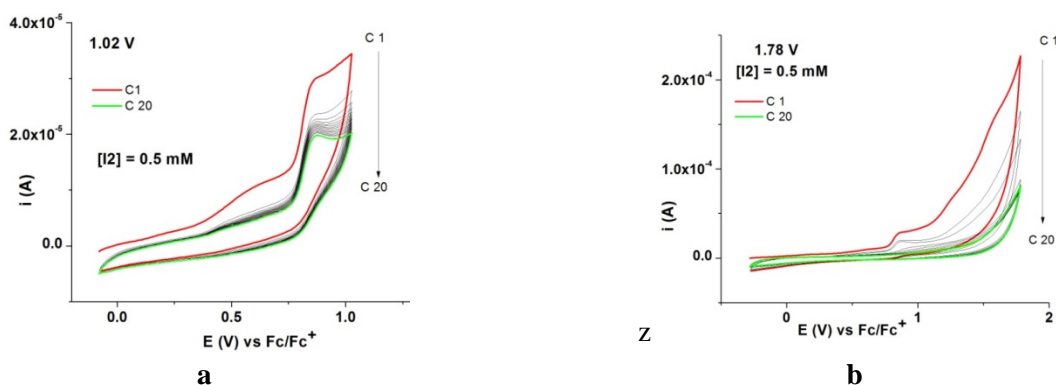
Table 5. Peak potentials values (V) *vs* Fc/Fc$^+$ from DPV and CV curves for **P2**

Peak	Method		Process characteristic
	DPV	CV	
a1	0.82	0.87	irreversible
a2	1.19	-	irreversible
a3	1.54	1.57	irreversible
a4	1.81	2.17	ireversible
a5	2.12		-
c1	-2.08	-2.12	irreversible
c2	-2.33	-2.33	quasi-reversible
c3	-2.57	-2.62	quasi-reversible

Fig. 16. CV curves (0.1 V·s^{-1}) during the preparation of CMEs by successive scans in 0.5mM solution of **P2** in 0.1 M TBAP, CH$_3$CN between -0.3 V and different anodic limits: +1.02 V (a); +1.78 V (b)
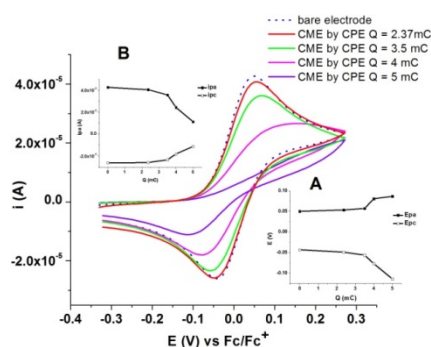

Fig. 17. CV curves (0.1 V/s) in 1 mM ferrocene solutions in 0.1 M TBAP, CH$_3$CN for the CME prepared in 0.5 mM **P2** solution in 0.1 M TBAP/CH$_3$CN by CPE at +1.78 V at different charges Q; dependences on Q of the anodic and cathodic Fc peak potentials (inset A) and currents (inset B)

Modified electrodes with *P2*

Chemical modified electrodes based on **P2** were obtained either by potentiodynamic or potentiostatic methods in solutions of **P2** (0.5 mM) in the domain of the anodic processes a1 and a2. In order to test that the electrode is covered, the modified electrodes were transferred in 1 mM ferrocene solution in 0.1 M TBAP, CH$_3$CN.

The modified electrodes were prepared by successive scans (20 cycles) between -0.3V and different anodic limits: 1.02 V (Figure 16 a); 1.78 V (Figure 16 b). The curves obtained after the transfer in ferrocene solution for anodic limits of 1.02 V, and 1.78 V are presented in Fig. 17. It can be seen that the ferrocene signal is much more flat in comparison to the bare electrode when the potential limit is more positive. The dependencies of the anodic and cathodic peak potentials for ferrocene (Fc) on the selected anodic limit scan are seen in Fig. 17 inset A; they show important changes starting at potentials more positive than 1 V. The corresponding anodic and cathodic currents dependencies, which indicate a sharp decrease after 1 V, are shown in Fig. 17 inset B.

Films based on **P2** have been also prepared by CPE at different potentials (1.02 V and 1.78 V); there were no important changes in ferrocene CV for charges of 2.37 mC or 3.5 mC. However, if CPE has been performed at 1.78 V evident changes occur continuously when the charge increases from 2.37 mC to 5 mC. In Fig. 17 are given the CV curves after the transfer in 1 mM ferrocene solution of the CMEs obtained at 1.78 V at different charges, indicating an increase with charge of the electrode coverage. Fig. 17 insets A and B show the dependences of ferrocene anodic and cathodic peak potentials and currents, respectively, on charge (Q); after Q = 3.5 mC, the anodic and cathodic potentials are sharply increasing with Q, while the currents are decreasing with Q.

Comparison between *P1* and *P2*

The diffusion coefficients for **P1** and **P2** have been calculated from the slopes of a1 peaks given in Figure 6 (b) and Figure 14 (b) using Randles–Sevcik equation (1), taking into account that the CV curves have been obtained at room temperature (298 K). In (1), i$_p$ = peak current (A), n = number of electrons transferred in the redox process (n=1), A = electrode area (cm^2), D = diffusion coefficient (cm^2/s), C = concentration of **P1** or **P2** (mol/cm^3), and ν = scan rate (V/s). Compound **P2** has a higher diffusion coefficient (Table 6) than **P1**, in agreement with his small molecular volume.

$$i_p = 268600 \cdot n^{3/2} \cdot A \cdot C \cdot D^{1/2} \cdot v^{1/2} \qquad (1)$$

Table 6. Diffusion coefficients for compounds **P1** and **P2**

Comp.	X	Slope	$10^5 \times D$ (cm^2/s)
P1		0.000068	10.2
P2		0.000131	19.1

It can be noticed from Figure 18 and Table 7 that compounds **P1** and **P2** have very close potentials for a1 and c1 peaks, as expected taking into account their similar structure.
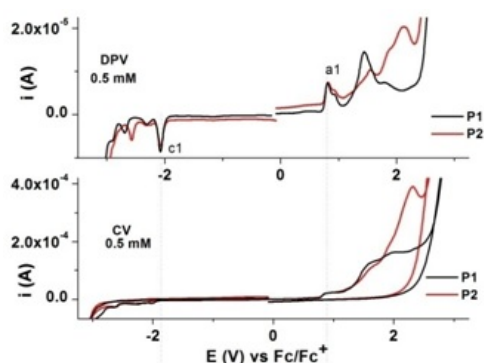

Fig.18. Comparison of DPV and CV curves in 0.1 M TBAP, CH$_3$CN for **P1** (0.5 mM) and **P2** (0.5 mM)

Table 7. Peak potentials (V) from DPV curves (0.5 mM) and the assessed processes for **P1** and **P2**

Compound Peak	P1	P2	Functional group/process
a1	0.81	0.82	Py→Py$^{+\cdot}$/oxidation 1*
a2	0.93	1.19	Ph / oxidation 2
a3	1.44	1.54	Py/oxidation 3
a4	1.80	1.81	Py/oxidation 4
a5	-	2.12	Py/oxidation 5
c1	-1.99	-2.08	CO→CO$^{-\cdot}$→CHOH/reduction 1
c2	-2.23	-2.33	Pyrrole double bonds/reduction 2
c3	-2.61	-2.57	Ester/reduction 3
c4	-2.82	-	Pyrimidine/reduction 4

*= pyrrolo[1,2-c]pyrimidine moiety
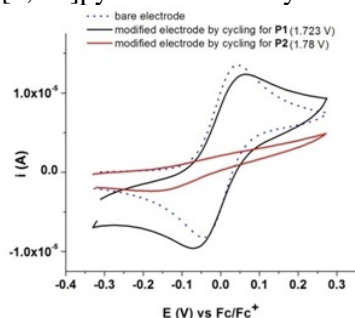
Fig. 19. CV curves (0.1 V·s^{-1}) in 1mM ferrocene solutions in 0.1 M TBAP, CH$_3$CN on modified electrodes prepared by 20 scans between -0.3 V and 1.723 V for **P1** and 1.78 V for **P2**, and on bare electrode (dotted line), respectively

CONCLUSIONS

The electrochemical characterization of ethyl 3-(2,4-dimethoxyphenyl)-7-(2-naphthoyl)pyrrolo [1,2-*c*]pyrimidine-5-carboxylate (**P1**) and ethyl 3-(4-methylphenyl)-7-(4-methylbenzoyl)pyrrolo [1,2-c]pyrimidine-5-carboxylate (**P2**) was performed by cyclic voltammetry, differential pulse voltammetry and rotating disk electrode methods.

The pyrrolo[1,2-*c*]pyrimidines present similar peaks in the anodic and cathodic domain. Modified electrodes were obtained by successive scanning or by controlled potential electrolysis at different anodic peaks and charges. The coverage of the electrode surface was confirmed by the transfer of the modified electrodes in ferrocene solutions, when the CV signal for ferrocene was found attenuated in intensity and distorted (with an increased gap between the peak potentials). **P2** gave the best electrode coverage by electrooxidation. The modified electrodes investigation is in progress in view of OLED applications.

Pyrrolo[1,2-*c*]pyrimidine has a low aromatic character, which confers a high reactivity in comparison to the common aryls. The difficulty of peak assessment is increased by the presence of stabilizing functional groups, which have redox potentials close to the aromatic moiety. The potentials of DPV peaks and the assessed processes for the compounds **P1** and **P2** are presented in Table 7.

The transfer in ferrocene solution (Figure 19) of the modified electrodes based on **P1** and **P2**, obtained by successive cycling between -0.3 V and about 1.7 V, lead to more distorted curves in case of **P2**, indicating that **P2** covers better the electrode surface, probably due to the formation of a more compact film.

REFERENCES

1. F. Rise, H. Wikstroem, S. Ugland, D. Dijkstra, L.L. Gundersen, P. De Boer, A. Bast, G. Haenen, O.G. Antonsen, WO 9621662 A1 (1996).
2. M. Ono, L. Sun, Z.Q. Xia, E. Kostik, K. Koya, Y. Wu, M. Nagai, Fused pyrrole compounds, WO 2004082606 A2 (2004).
3. G. Mangalagiu, M. Ungureanu, G. Grosu, I.I. Mangalagiu, M. Petrovanu, *Ann. Pharm. Fr.*, **59**, 139 (2001).
4. S. Kristafor, T.G. Kraljevic, S.M. Ametamey, M. Cetinac, I. Ratkajd, R.T. Haceke, S. K. Pavelic, S. R. Malic, Chem. *Biodivers.*, **8**, 1455 (2011).
5. J.T. Kim, A.D. Hamilton, C.M. Bailey, R.A. Domoal, L. Wang, K.S. Anderson, W.L. Jorgensen, *J. Am. Chem. Soc.*, **128**, 15372 (2006).
6. M.A. Ibrahim, S.M. Abou-Seri, M.M. Hanna, M.M. Abdalla, N.A.E. Sayed, *European Journal of Medicinal Chemistry*, **99**, 1 (2015).
7. M. Ono, L. Sun, Z.Q. Xia, E. Kostik, K. Koya, Y. Wu, M. Nagai, Intl. Pat. WO 2004/082606.
8. G. Mangalagiu, M. Ungureanu, G. Grosu, I.I. Mangalagiu, M. Petrovanu, *Annales pharmaceutiques françaises*, **59**,139 (2001).
9. E. Georgescu, F. Georgescu, P. C. Iuhas, C. Draghici, M. G. Danila, P. I. Filip, *Arkivoc*, **381,** 242 (2007).
10. J.M. Minguez, J.J. Vaquero, J.L. Garcia-Navio, J. Alvarez-Builla, *Tetrahedron Lett.*, **37**, 4263 (1996).
11. M. Alvarez, D. Fernandez, J.A. Joule, *J. Chem. Soc. Perkin Trans.*, **1**, 249 (1999).
12. V. B. Ivanov, V. S. Reznik, B. E. Ivanov, A. A. Musina, Efremov, Yu. Ya., *Izv. Akad. Nauk. SSSR, Seriya Khim.*, 2428 (1980).
13. C.H. Weidner, F.-M. Michaels, D. J. Beltman, C.J. Montgomery, D.H. Wadsworth, B. T. Briggs, L.M. Picone, *J. Org. Chem.*, **56**, 5594 (1991).
14. A. Copar, B. Stanovnik, M. Tisler, *J. Heterocycl. Chem.*, **30**, 1577 (1993).
15. Y. N. Romashin, M.T.H. Liu, S.S. Nijjar, O. Attanasi, *Chem. Commun.*, 1147 (2000).
16. A. De la Hoz, J.L.G. De Paz, E. Diez-Barra, J. Elguero, C. Pardo, *Heterocycles*, **24**, 3473 (1986).
17. G.C. Mangalagiu, I.I. Mangalagiu, R.I. Olariu, M. Petrovanu, *Synthesis*, **14,** 2047 (2000).
18. C.C. Moldoveanu, I.I. Mangalagiu, *Helv. Chim. Acta*, **88**, 2747 (2005).
19. I.I. Mangalagiu, G.C. Mangalagiu, C. Deleanu, G. Drochioiu, M.G. Petrovanu, *Tetrahedron*, **59**, 111 (2003).
20. E. Georgescu, F. Georgescu, M.M. Popa, C. Draghici, L. Tarko, F. Dumitrascu, *ACS Combi Sci.*, **14**, 101 (2012).
21. E. Georgescu, F. Georgescu, C. Draghici, L. Cristian, M.M. Popa, F. Dumitrascu, Comb Chem High T Scr,16, 851 (2013).
22. L. Soare, E.-M. Ungureanu, E. Georgescu, L. Birzan, *REV. CHIM. (Bucharest)*, **63**, 1451 (2012).
23. B. W. D. Andrade, S. Datta, S. R. Forrest, P. Djurovich, E. Polikarpov, M. E. Thompson, *Organic Electronics*, **6**, 11 (2005).

ЕЛЕКТРОХИМИЧНИ ИЗСЛЕДВАНИЯ НА ДВА ПИРОЛ [1,2-c] ПИРАМИДИНИ

М.-Л. Тату[1], Ф. Харя[1], Е.-М. Унгуреану[1]*, Е. Джорджеску[2], Л. Бирзан[3], М.-М. Попа[3]

[1]*Катедра по неорганична химия, физикохимия и електрохимия, Университет "Политехника" на Букурещ, 011061, Румъния*
[2] *Научен център Олтхим, 240050, Ramnicu Valcea, Румъния,*
[3]*Румънска академия, Институт по органична химия "С. Д. Ненитческо", 060023-Букурещ, Румъния*

(Резюме)

Електрохимичното охарактеризиране на два пирол [1,2-c] пиримидини е извършена чрез циклична волтаметрия (CV), диференциална импулсна волтамперометрия и волтамперометрия с ротиращ дисков електрод. Техните дифузионни коефициенти са определени на основа влиянието, което оказва скоростта на сканиране на потенциала върху CV анодните токове. Модифицираните електроди са приготвени в пирол [1,2-c] пиримидинови разтвори в ацетонитрил, съдържащ тетрабутиламониев перхлорат чрез циклиране на потенциала или чрез контролирана потенциална електролиза при различни анодни потенциали и заряди.

Ключови думи: пирол [1,2-c] пиримидини, циклична волтамперометрия, диференциална импулсна волтамперометрия, дифузионни коефициенти, модифицирани електроди, ротиращ дисков електрод

Electrodeposition and structure of Ni-Co-P alloy coatings in stationary and pulse potentiostatic mode

K. N. Ignatova[1*], Y. S. Marcheva[2], S. A. Vladimirova[3], G. V. Avdeev[3], D. S. Lilova[1]

[1]*University of Chemical Technology and Metallurgy – Sofia, 8 Kl. Ohridsky blv.*

[2]*Technical University of Sofia, 8 Kl. Ohridsky blv., Sofia 1000*
[3]*Bulgarian Academy of Sciences, Institute of Physical Chemistry "Acad. Rostislav Kaishev"- Bulgarian Academy of Sciences, "Acad. G. Bonchev" str., bl.11, Sofia 1113*

The rate of growth, composition, morphology and microstructure of Ni-Co-P coatings, deposited at Constant Potential Mode (CPM) and at Pulse Potential Mode (PPM) were investigated depending on the content of NaH_2PO_2 in the electrolyte, temperature, cathodic polarization and the pulse frequencies.

It was established, that with the rising of NaH_2PO_2 content (from 0.189 M up to 0.5 M), the rate of growth and the phosphorous content in the Ni-Co-P coatings in both modes of deposition increase. Maximum phosphorous content in the coatings are received in pulse mode at pulse frequencies 100 Hz at a temperature of the electrolyte 20°C (9.7 mass.% P) and at 80°C (14.8 mass. % P) at cathodic polarization ΔE = -1.15 V. With the raising of pulse frequencies the rate of growth of the coating and the phosphorous content decrease. The pulse potential mode (PPM) of deposition results in weaker manifestation of the phenomenon "anomalous" deposition of cobalt in the alloy and this being explained by stabilizing the pH of the solution in the pulse mode. The different conditions of electrocrystallization in the both mode of deposition reflect in formation of different type structures. Ni-Co-P coatings, deposited at stationary mode are monophasic and polycrystalline. The identified phase of the type NiCoP has a hexagonal symmetry. The coatings, deposited at pulse mode (PPM) are typical amorphous.

Key words: Ni-Co-P coatings, electrodeposition, pulse mode, alloy coatings, morphology, phase structure

INTRODUCTION

The ternary Ni-Co-P alloy coatings combine by unique way the high wear- resistance, corrosion resistivity and hardness of Ni-P alloys with the magnetic and lubricant properties of Co-reach Ni-Co coatings [1]. That is why they are used as anticorrosion coating (as alternative of the hard chromium coatings) [1-3] and as layers in magnetic recorders [4, 5].

The deposition of Ni-P and Ni-Co-P coatings can be carried out by two methods: electroless deposition [6] and electrodeposition [3, 7-12] using sulphate electrolytes [10], modified Watts electrolytes [11, 12], chloride [7] and sulphamate solutions [8].

It was established, that Co-P [12] and Ni-P [13] alloys are possible to be deposited at room temperature, which is an important contribution to the searching of the ways for the raising of the efficiency of the electrodeposition method.

Recently, a bigger attention is payd to the pulse methods of electrodeposition, and the most common being square-wave pulsed direct current and pulsed reverse current [14-19]. The possibility to receive fine-crystal and nano-structured coatings by pulse mode of deposition can be explain by creating of conditions of electrocrystallization in thinner diffusion layer [14-17]. According to [18], applying the pulse mode give Ni-P coatings with higher phosphorous content and higher cathodic current efficiency. This effect of the pulse electrodeposition is strongly manifested at lower pulse filling (θ = 0.1), which is explained by the mechanism of deposition of Ni-P coating. The mechanism of deposition can be direct [11, 12] or indirect [22], and the possible reactionsare given in Table 1. In the case of deposition of Ni-Co-P coatingto the reactions for Ni-P have to be added two other possible reactions: (5) and (10) [1, 21].

Independent of the mechanism of deposition, the presence of the high concentrations of H^+ and the formation of conditions for adsorbtion of atomic hydrogen on the surface of the rising coating (which is observed at bigger pauses) are the necessity condition for phosphorous incorporation [1,3,18]. pH of the solution is an important factor not only for the mechanism of Ni-P deposition [18], but also for the appearance of the phenomenon of "anomalous" deposition of cobalt in Ni-Co [15-17] and in Ni-Co-P alloys [1, 3].

* To whom all correspondence should be sent.
E-mail: katya59inatova@gmail.com

Table 1. Possible reactions during the deposition of Ni-P and Ni-Co-P coatings by direct and indirect mechanism

Direct mechanism	Indirect mechanism
(1) $Ni^{2+} + 2e^- \rightarrow Ni$	(6) $6H^+ + 6e^- \rightarrow 6H_{ads}$
(2) $H^+ + e^- \rightarrow H_{ads}$ and $H_{ads} + H_{ads} \rightarrow H_2$	(7) $H_3PO_3 + 6H_{ads} \rightarrow PH_3 + 3H_2O$
(3) $H_3PO_3 + 3H^+ + 3e^- \rightarrow P(wh) + 3H_2O$	(8) $2PH_3 + 3Ni^{2+} \rightarrow 3Ni + 3P + 6H^+$
(4) $H_2PO_2^- + 2H^+ + e^- \rightarrow P(red) + 2H_2O$	(9) $H_2PO_2^- + 5H^+ + 4e^- \rightarrow PH_3(g) + 2H_2O$
(5) $Co^{2+} + 2e^- \rightarrow Co$	(10) $2PH_3 + 3Co^{2+} \rightarrow 3Co + 3P + 6H^+$

In the case of electroless deposition of Ni-P, the most commonly used phosphorus-producing agent is NaH_2PO_2 and the main reaction in this case is as follows [6]:

$$Me^{2+} + 2H_2PO_2^- + 2H_2O \rightarrow Me + 2H_2PO_3^- + 2H^+ + H_2 \quad (11)$$
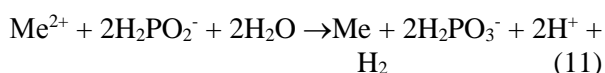
There is not a common opinion in the literature about what phosphorous – producing agent to be used in electrolytes for electrodeposition of Ni-P [11], Co-P [5] or Ni-Co-P coatings [1, 6]. According to most of the authors, most frequently this is only sodium hypophosphite [1]. Its influence on the phosphorous content and on the structure of Ni-Co-P alloy coating in the presence of the two phosphorous oxyacids (H_3PO_4, H_3PO_3) is not sufficiently discussed in the literature. Data about the use of pulse potentiostatic mode for deposition of Ni-Co-P alloy coating was not found.

The aim of the presented paper was to investigate the influence of the sodium hypophosphite during the stationary and pulse potentiostatic mode of deposition, as well as the effect of the pulse frequency and electrolyte temperature on the rate of growth, composition, morphology and microstructure of Ni-Co-P coatings.

EXPERIMENTAL

The electrolyte for Ni-Co-P alloy deposition was with composition: 0.2M $NiSO_4.6H_2O$; 0.1M $CoSO_4.7H_2O$; 0.1M KCl; 0.125M H_3PO_4; 0.2M H_3PO_3; 0.32 M H_3BO_3 and NaH_2PO_2 (0.189 M ÷ 0.5 M) with pH = 2. The pH correction was done using diluted solutions of NaOH and H_2SO_4. The potentiodynamic voltammograms (sweep rate 30 mV s^{-1}) and coating deposition at constant potentiostatic mode (CPM) were realized using Potentioscan type Wenking (Germany).

Tree-electrode thermostated electrochemical cell was used with total volume 150 dm^3. The working electrode for the voltammograms was cylindrical, disk-shaped with surface area 1 cm^2, made from copper foil (Merck, 99.97%).The counter electrode was Pt foil with surface, ten times bigger than this one of the working electrode(=>10 cm^2). The reference electrode was commercial saturated calomel electrode (SCE). The alloy coatings were deposited on copper foil (Merck, 99.97%) with work area 4 cm^2 (2x2 cm). Before the deposition, the work electrode was etched, rinsed with distilled water and drying [19]. The mass of the coating was calculated by the difference of the cathodic masse before and after the deposition, using analytical balance (accuracy 0.0001g). By calculation, the masse of the coating, deposited on the unity of surface during the unity of time (i.e. the rate of growth), G [mgcm^{-2} h^{-1}], was determined.

The realization of the pulse potentiostatic mode (PPM) with rectangular form of pulses of the potential is described in details in [20]. The frequency of pulses are changed from 100 up to 500 Hz at constant pulse filling $\theta = 0,5$. The theoretical relation between the average and amplitude value of the polarization ΔE_m (calculated as difference between the potential at a given current and the equilibrium potential), and the amplitude value (ΔE_p) of the polarization is $\Delta E_m = \theta . \Delta E_p$. The coatings are deposited with the aim of comparison at the same value of the cathodic polarization in both modes of deposition (ΔE for CPM and ΔE_m for PPM).

The morphology and the elemental composition of the coatings were investigated through SEM and Energy Dispersive Spectral Analysis (EDSA) methods using equipment of Oxford Instruments, JSM-6390- Jeol. The phases, presented in the deposited coatings, were identified by XRD analysis using vertical automatic diffractometer Philips PW 1050 with secondary graphitemonochromator, operating with CuKα radiation and scintillation counter. The diffraction curves were recorded in angular interval from 10 to 100 degrees, 2θ with step 0.04 degrees and exposure 1 sec.

RESULTS AND DISCUSSIONS

At Fig. 1 are compared the cathodic voltammograms in electrolytes for deposition of Ni-Co-P alloys without (curve 1) and with 0.5M NaH_2PO_2(curve 2) at room temperature (20^0C) at constant composition of the rest of solution.

As can be seen, in the presence only of the phosphorous – containing acids (cv.1),

the current reach to very high values at high cathodic polarizations and at the potential of E = -1.75V (SCE) passes through maximum.
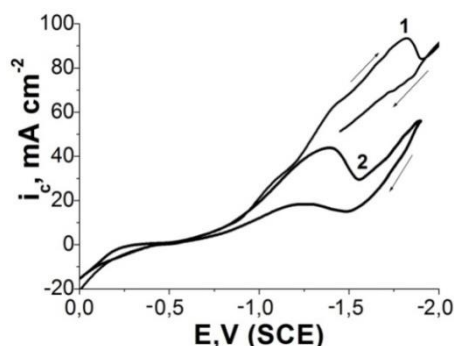

Fig. 1 Cathodic voltammograms in electrolytes for deposition of Ni-Co-P coating without NaH_2PO_2 (curve 1) and with 0.5M NaH_2PO_2 (curve 2) in the bath at 20^0C.

Supplementing to the bath of 0.5M NaH_2PO_2 (curve 2) results in strong decrease of the current and to displacement of the potential, corresponding to the maximum, in a more positive direction.

The two opposite effects, observed in the presence of NaH_2PO_2 – its depolarization effect and the lowering of the rate of the process of deposition, could be explained using the chemical mechanism of deposition. According to this mechanism, NaH_2PO_2 is a reducing agent regarding to nickel and cobalt ions and its presence at high concentrations can result in reduction of these ions not only by the electrochemical but also by chemical mechanism [6, 19] according to the reaction (11).

Data about the rate of grow of the mass G (Fig. 2a) and the phosphorous content in the coating (Fig. 2b) depending on NaH_2PO_2 content in the solution at stationary (curve 1) and pulse (curves 2-4) mode of deposition at pulse frequencies 100 up to 500 Hz is presented at Fig. 2.

The coatings of Ni-Co-P are deposited at room temperature at the same cathodic polarization in CPM and PPM at -1.15V (ΔE and ΔE_m resp.).

Data, presented in Fig. 2 show, that when stationary mode is applied, with the rise of NaH_2PO_2 content up to 0.4 M the coating mass rise with bigger rate, almost linearly. At bigger concentration the rate decrease (Fig. 2a, cv. 1). Applying the pulse mode, the mass of the coating rise slowly with the increasing of NaH_2PO_2 concentration (Fig. 2a, cvs 2-

4) compared to the stationary mode (Fig. 2a, cv. 1) especially at frequencies, higher than 500 Hz (Fig. 2a, cv. 4). At a given average value of the polarization, according to the relation $\Delta E_m = \theta.\Delta E_p$, during the pulse time, almost twice bigger values of the amplitude values of the polarization (respectively of the current density) are achieved. It can be assumed, that at this conditions, the part of the current, used for hydrogen evolution is bigger, compared to the stationary conditions [18]. At pulse frequencies, higher than 250 Hz, the time for nuclei creation and growth, as well as for the recovery of the concentration gradient of the deposited ions, is smaller than this one at lower frequencies, which results in lowering of the rate of coating deposition (Fig. 2a, cv. 4).
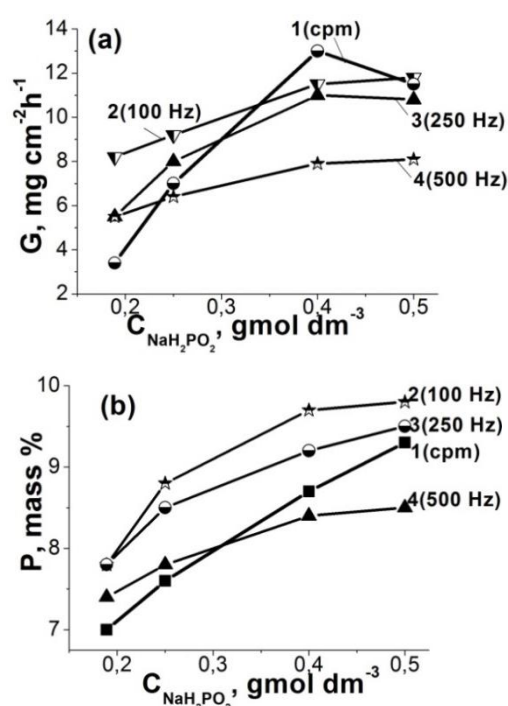

Fig. 2. Effect of NaH_2PO_2 concentration in the solution on the rate of growth G of the coating (a) and the content of P, mass.% (b) of the Ni-Co-P alloys in CPM (curve 1) and in PPM (curves 2-4); ΔE, resp. ΔE_m = - 1.15V (SCE)): (2) 100 Hz; (3) 250 Hz and (4) 500 Hz, $\theta = 0.5$.

At stationary mode, with the growing of NaH_2PO_2 content, the phosphorous content in Ni-Co-P coatings also grow (Fig. 2b, cv. 1), but it stay lower compared to this one at pulse mode at pulse frequencies from 100 up to 250 Hz (Fig. 2b, cvs 2,3). The maximum phosphorous content (up to about 9.7%) is achieved at pulse frequency 100 Hz and maximum NaH_2PO_2 content in the solution 0.5M. With the raising of pulse frequencies (Fig. 2b, cv. 4), the phosphorous content in the alloys going down under this one in stationary mode. The fact, that at lower pulse frequencies (100 and 250 Hz) the phosphorous content in the alloy is higher, can be

explained with the time of pauses between the pulses, which in these conditions is higher. This give a possibility for adsorbtion of hydrogen ad-atoms on the cathodic surface, which facilitate the reactions (7) and (8) and (10) from Table 1, all chemical by nature, and resulting in producing of P, Ni and Co, combined in the ternary Ni-Co-P alloy.

Table 2 presents data from EDSA analysis about the composition of the coatings. It can be seen,

that at all studied concentrations of NaH_2PO_2, the phenomenon of "anomalous" high cobalt concentration in the coatings (compared to this one in the solution in respect to the nickel concentration) is observed.The cobalt content, compared to this of the nickel, decrease notably at pulse mode (for example by 0.189 M NaH_2PO_2 from 70,6% at CPM to 66.3% in PPM).

Table 2 Chemical composition of Ni-Co-P coatings (in mass %), deposited in stationary mode (CPM) and in pulse mode at 250 Hz (PPM)depending on the NaH_2PO_2 content in the solution;Cathodic polarization ΔE, resp. ΔE_m= -1.15V (20° C)

Content, mass % →	% P	% Ni	% Co	% P	% Ni	% Co
$C_{NaH_2PO_2}$, M ↓	**CPM**	**CPM**	**CPM**	*PPM*	*PPM*	*PPM*
0.189	7.0	22.4	70.6	7.8	25.9	66.3
0.250	7.6	25.9	66.5	8.8	28.1	63.1
0.400	8.7	27.8	63.5	9.7	31.5	58.8
0.500	9.3	29.3	61.4	9.8	33.1	57.1

In pulse mode a supplementary rise of the phosphorous content (up to 14.8 % at 100 Hz) in the coatings and decreasing of the manifestation of the "anomalous" deposition is observed at rising the electrolyte temperature up to 80ºC at lower pulse frequencies (Table 3). The explanation can be related to the change in pH of the solution close to the electrode and its raising as a result of hydrogen evolution simultaneously with the main reactions (Table 1). According to many authors, the hydrogen evolution from Watts and sulphamate electrolytes begins at potentials, close to the potentials of deposition of nickel and cobalt [15, 16, 18].

With increase of the pH of the solution in the cathodic range, the appearance of hydroxide

complex ions of the metals is observed. The constant of stability of $Co(OH)^+$ are lower than this of $Ni(OH)^+$ which means, that at conditions where the first ones are formed and adsorbed easier, a preferential deposition of Co in Ni-Co alloys is observed [15, 16]. As it is shown in [18] during the pulse mode of deposition the pH of the solution is stabilized, i.e. the low values of pH are supported, as a consequence of restoring of the concentration gradient, created during the pulses at hydrogen evolution. That is why at lower and middle pulse frequencies the possibility for formation of metal-hydroxide complex ions decreases and as a result the effect of "anomalous" Co deposition decrease.

Table 3. Composition of Ni-Co-P alloys depending on the parameters of the applied mode (ΔE for CPM and frenquency, ffor PPM, ΔE_m = -1.15 V) at 80ºC and 0.189 M NaH_2PO_2

CPM ΔE, V	% P	% Ni	% Co	PPM f, Hz	% P	% Ni	% Co
- 0.95	10.3	33.6	56.1	100	14.8	36.7	48.5
-1.15	9.5	31.1	59.4	250	13.7	34.2	52.1
-1.25	8.7	29.3	62.0	500	12.3	34.4	53.3

Morphology

At the Fig. 3, the SEM images are shown of the surfaces of the Ni-Co-P alloys, deposited at room temperature at stationary (Fig. 3 a,b) and pulse (Fig. 3 c,d) potentiostatic mode (ΔE и ΔE_m = -1.15V) and different content of NaH_2PO_2 in the solution: 0.189 M NaH_2PO_2 (a, c); 0.5 M NaH_2PO_2 (b, d). The SEM images show, that the mode of deposition has a strong effect on the character of the formed crystals.

The deposited at stationary mode coatings have a columnar structure. At lower concentration of NaH_2PO_2 the coatings are nano-dimensioned (Fig. 3a), and at higher concentration of NaH_2PO_2 simultaneously with the predominate nano-dimensional crystals, crystals with dimensions about and over 500 nm are formed (Fig. 3b).
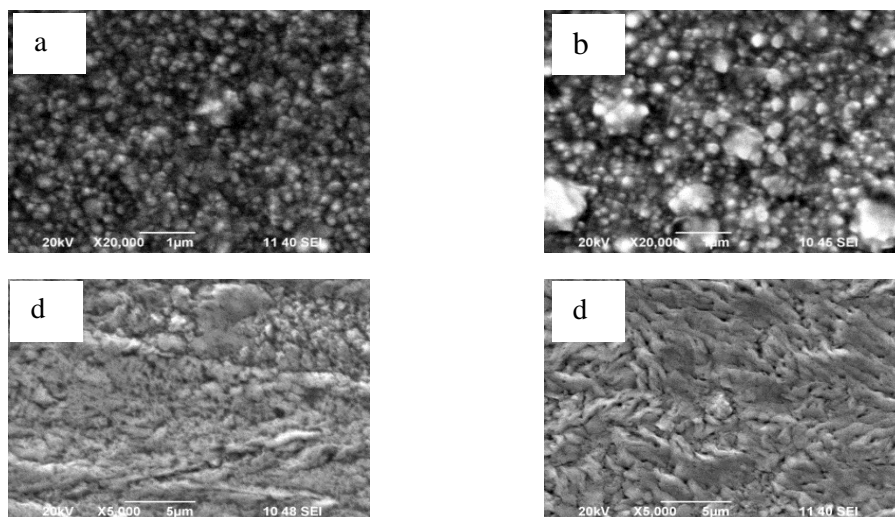
Fig.3. SEM images of Ni-Co-P alloys, deposited in CPM (a, b) and in PPM (c, d) (ΔE, resp. ΔE_m = -1.15V) at different content of NaH_2PO_2 in the solution: 0.189 M NaH_2PO_2 (a, c); 0.5 M NaH_2PO_2 (b, d)

At pulse mode of deposition, the dimensions and the form of the crystals are changed (Fig. 3c,d), which prove, that during this mode the conditions of electrocrystallization are changed. The coatings have prolonged crystals, arranged in networked structure, peculiar to the higher concentration of NaH_2PO_2 (Fig. 3d). In the both modes of deposition, the coating at lower content of NaH_2PO_2 have more fine-crystal structure (Fig. 3a,c).
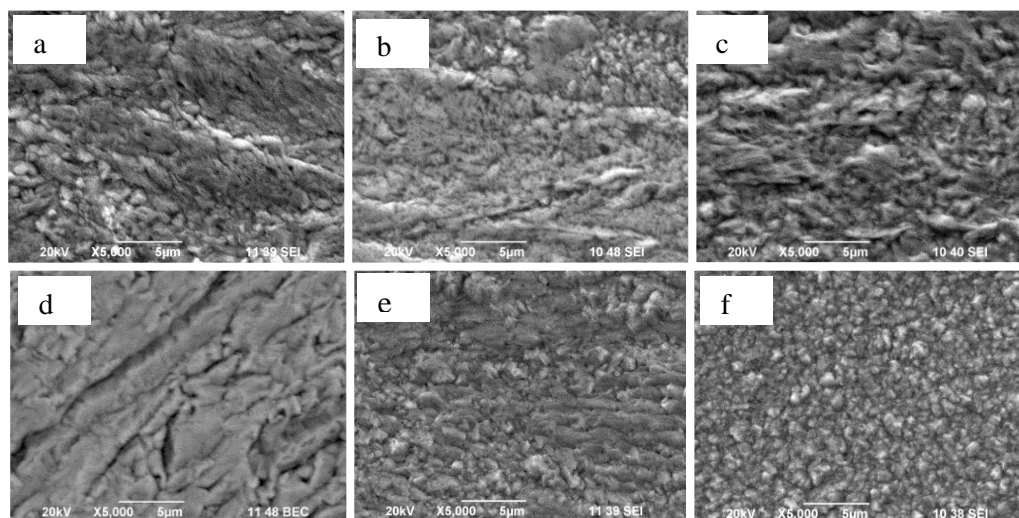
Fig. 4. SEM images of Ni-Co-P alloys, deposited in pulse mode at pulse frequencies 100 Hz (a, d); 250 Hz (b, e); 500 Hz (c, f) at 20ºC (a-c) and 80ºC (d-e); 0,189 M NaH_2PO_2 (ΔE, resp. ΔE_m = -1.15V).

Fig.4 shows the influence of the pulse frequencies and the temperature on the morphology of the Ni-Co-P alloys in pulse mode. The increase of the pulse frequency at room temperature does not change importantly the morphology of the coatings (Fig.4 a-c). The coatings are build up from crystals with filiform structure. In the coatings, deposited in pulse mode, at a temperature of the electrolyte 80ºC, the morphology of the Ni-Co-P coatings is changed (Fig.4, d-f). At low pulse frequency (100 Hz) a layered structure is seen with a maximum smoothing compared to other coatings (Fig. 4d). With the rising of pulse frequencies up to 500 Hz, the structure of the coatings begins to look like this one in stationary conditions (for comparison Fig.4 f and Fig. 4a) – it is fine-crystal, composed by separate grains. The established higher phosphorous content for the coatings, deposited at lower pulse frequency compared to these, deposited at 500 Hz (Fig. 2b) is a possible reason for the smoother structure at 100 Hz.

Phase composition

41

Fig.5 (a, b) show the diffractograms of the deposited at stationary and at pulse mode Ni-Co-P alloys at temperature 80ºC at the same cathodic polarization and the same content of NaH_2PO_2 (0.189 M) in the solution. In the stationary mode of deposition a monophasic polycrystalline Ni-Co-P coating is forming. The compound is of the type NiCoP and it is well distinguished by the diffraction peaks. It has a hexagonal symmetry (according ICSDref 98-062-4449).

The Ni-Co-P coating, deposited in pulse mode at frequency about 250 Hz, is amorphous. The deposited coating is thin (under 10 μm), as the peaks of the substrate is seen (Fig.5, b).
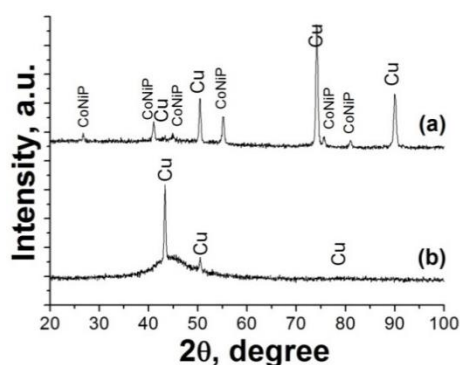
Fig. 5. Diffractograms of Ni-Co-P alloy coatings, deposited at temperature 80ºC in stationary, CPM (a) and pulse mode, PPM (250 Hz) (b) at the same cathodic polarization ΔE (CPM), resp. ΔE_m (PPM) = -1.15V.

CONCLUSIONS

1. With the increase of the NaH_2PO_2 content in the solution the mass of the deposited Ni-Co-P coating and the phosphorous content grow up faster in stationary mode compared to the pulse mode. Using the pulse mode with frequencies between 100 and 250 Hz results in higher phosphorous content in the coatings;

2. When the temperature of the electrolyte rise and the polarization is lower, in stationary mode and at lower pulse frequencies in pulse, the content of phosphorous in the coatings grow (up to 14.8% P at 100 Hz, 80^{0}C); the manifestation of the phenomenon of "anomalous" cobalt deposition and of the fine-crystal structure going down.

3.Ni-Co-P coatings, deposited in stationary mode, are monophasic and polycrystalline and the identified phase has hexagonal symmetry. The coatings, deposited in pulse mode are typical amorphous.

REFERENCES

1. C. Ma, S. Wang, F. C. Walsh, *Transactions of the IME*, **93**, 275 (2015)
2. N. M. Alanazi, A. M. El-Sherik, S. H. Alamar, S. Shen, *Int. J. Electrochem. Sci*., **8**, 10350 (2013)
3. M. M. V. Parente, O. R. Mattos, S. L. Diaz, P. L. Neto, F. J. F. Miranda, *J. Appl. Electrochem*., **31**, 677 (2001)
4. Lucas, L. Perez, C. Aroca, P. Sanchez, E. Lopez, M. C. Sanchez, *J. of Magnetism and Magnetic Materials,* **290-291**, 1513, (2005)
5. L. Perez, O de Abril, M. C. Sanchez, C. Aroca, E. Lopez, P. Sanchez, *J. of Magn. Materials,* **215-216**, 337 (2000)
6. N. Rakitevitch, PhD Thesis, University of Pristina, (1994) (in Serbian)
7. G. Pattanaik, D. M. Kirkwood, X. Xu, G. Zangari, *Electrochim. Acta*, **52**, 2755 (2007)
8. W. T. Chang, C. H. Chen, H. Fang, J. Electrochem. Soc., D57-D61, 155 (2008)
9. USA Patent No.4786390, MKI S 25 B 9/00, NKI 204/242, (1988)
10. S. J. Splinter, R. Rofangha, N. S. McIntyre, U. Erb, *Surface and Interface Analysis,* **24**, 181 (1996)
11. T. Morikawa, T. Nakade, M. Yokoi, Y. Fukumoto, C. Iwakura, *Electrochim. Acta*, **42**, 115 (1997)
12. S. S. Djokic, *J. Electrochem. Soc*., **146**, 1824 (1999)
13. Y. Suzuki, S. Arai, I. Shohji, E. Kobayashi, *J. Electrochem. Soc*., **156**, D283 (2009)
14. F. C. Walsh, C. Ponce de Leon, D. V. Bavykin, C. T. J. Low, S. C. Wang, C. Larson, *Transactions of the IMF*, **93**, 209 (2015)
15. J. C. Puippe, F. Leaman (Eds.), Theory and Practice of Pulse Plating, *Amer. Electroplaters and Surface Finishers Soc*., (1986)
16. J. V. Arenas, T. Treeratanaphitak, M. Pritzker, *Electrochim. Acta*, **62**, 63 (2012)
17. C. K. Chung, W. T. Chang, *Thin Solid Films*, **517**, 4800 (2009)
18. C. S. Lin, C. Y. Lee, F. J. Chen, C. T. Chien, P. L. Lin, W. C. Chung, J. *Electrochem. Soc*., **153**, C387 (2006)
19. K. N. Ignatova, Y. S. Marcheva, *Journal of UCTM*, (2017), in press
20. K. N. Ignatova, *Bulg. Chem. Comm*., **45**, 357 (2013).
21. Handbook of Chemistry and Physics, Table of Common Standard Reduction Potentials at 25ºC, 89th Edition, CRC Press (2008)
22. M. Ratzker, D. S. Lashmore, K. W. Pratt, *Plat. Surf. Finish*, **9**, 74, (1986).

ЕЛЕКТРООТЛАГАНЕ И СТРУКТУРА НА NI-Co-P СПЛАВНИ ПОКРИТИЯ В СТАЦИОНАРЕН И ИМПУЛСЕН ПОТЕНЦИОСТАТИЧЕН РЕЖИМ

Катя Н. Игнатова[1], Йорданка С. Марчева[2], Стела Ат. Владимирова[3], Георги В. Авдеев[3], Даниела С. Лилова[1]

[1]Химикотехнологичен и Металургичен Университет, бул. Кл.Охридски 8,1756 София
[2]Технически университет Софияа, бул. Кл. Охридски 8,1000 София
[3]Институт по Физикохимия „Акад. Ростислав Каишев"- Българска академия на науките, ул. Акад. Г. Бончев бл. 11, София 1113

(Резюме)

Изследвани са скоростта на нарастване, състава, морфологията и микростуктурата на Ni-Co-P покрития, отложени в стационарен и в импулсен потенциостатичен режим в зависимост от съдържанието на NaH_2PO_2 в електролита, температурата, катодния потенциал и честотата на импулсите. Установено е, че с нарастване на съдържанието на NaH_2PO_2 (от 0.189 М до 0.5 М), скоростта на нарастване на масата на покритието и съдържанието на фосфор в Ni-Co-P покрития и при двата токови режима нараства. Максимално съдържание на фосфор в покритията е получено при честота на импулсите 100 Hz при температура на разтвора 20℃ (9.7 mass.% Р) и при 80ºC (14.8 mass. % Р) при катодна поляризация ΔE = -1.15 V. С нарастване на честотата на импулсите скоростта на нарастване на масата на покритието и съдържанието на фосфор намаляват. В импулсен потенциостатичен режим се наблюдава по-слабо проявление на феномена „аномално" отлагане на кобалт в сплавта и това е обяснено със стабилизиране на рНна разтвора в този режим. Различните условия на електрокристализация в двата режима се отразяват във формиране на различни типове структури. Ni-Co-P покрития, отложени в стационарен режим, са еднофазни и поликистални. Идентифицираната фаза е от типа NiCoP с хексагонална симетрия. Покритията, отложени при импулсен режим са типично аморфни.

Ключови думи: електроотлагане, импулсен режим, сплавни покрития, морфология, фазова структура

Anomalous electrodeposition of gold-indium alloys

B.-K. Choi[1], F. Sauer[1], G. Beck[1,2], R. Stauber[3], Ts. Dobrovolska[4*]

[1]Fraunhofer Applied Research Center for Resource Efficiency, Alzenau, Germany
[2]Aschaffenburg University of Applied Sciences, Aschaffenburg, Germany
[3]Fraunhofer Project Group Materials Recycling and Resource Strategies, Alzenau, Germany
[4]Institute of Physical Chemistry, Bulgarian Academy of Sciences, Sofia, Bulgaria

The process of anomalous deposition of gold–indium alloys from different electrolytes on the basis of ammonium sulphate (with addition of oxalic, malonic and lactic acid, and glycine) was investigated. The oscillations, observed at some current densities from the first three mentioned electrolytes were investigated in galvanostatic regime. By linear sweep voltammetry technique, besides the methods of cyclic voltammetry and conventional X-ray analysis the phase composition of the deposited alloys from glycine electrolytes were determined.

Keywords: glycine electrolytes, gold-indium alloys, oscillations, spatio-temporal structures

INTRODUCTION

In our previous investigations, the electrodeposition of gold-indium alloys was studied from several electrolytes - cyanide, citrate, acetate and glycine and some brief literature review on the deposition and properties of the alloy were presented elsewhere [1]. The morphology and the phase composition of the coatings from the mentioned electrolytes were determined, with particular attention being paid to the cathodic processes during electrodeposition of the alloy coatings from glycine electrolyte. Instabilities and oscillations of the potential during electrodeposition from the above mentioned electrolytes, namely the presence of oscillations at almost the same current densities (respectively reaching a similar coating composition) were observed. This behaviour of different indium electrolytes and the modes for the passivation/re-passivation are well-known [2], but the information about deposition of indium alloys in the literature is scarce [3].The present study aims to show the processes of deposition of gold-indium alloys in more details.

It was also recognized that the process of electrodeposition of gold-indium alloy from glycine electrolytes is a very promising one because of the possibility to obtain a variety of spatio-temporal structures on the surface of the electrode which would allow comparison with other known indium alloy systems with similar nature [4-6]. The content of indium in alloys deposited from glycine electrolytes even at low current densities is more than 40 wt. %. This leads to the suggestion that the electrodeposition of the alloy is if anomalous type, where the more noble metal does not deposit preferentially [7]. The second aim of our study was to apply anodic linear sweep voltammetry technique [8], besides the methods of cyclic voltammetry and conventional X-ray analysis [8] in order to determine the phase composition of the deposited alloys from glycine electrolytes.

EXPERIMENTAL

The Au-In alloy coatings were deposited from the electrolytes with the compositions presented in table 1.

Table 1: Chemical compositions of the electrolytes

Compounds, gdm^{-3}	Electrolytes			
	A	**B**	**C**	**D**
Au as KAu(CN)$_2$	1	1	1	1
In as InCl$_3$	6	6	6	6
Ammonium sulphate	40	40	40	40
Oxalic acid	40			
Malonic acid		40		
Lactic acid			40	
Glycine				40
pH	3.2	3.3	3.4	3.0

All solutions were made with *p. a.* purity chemicals and distilled water.

The experiments were performed in a 100 cm^3 tri-electrode glass cell at room temperature. The vertical working electrode (area 2 cm^2) and the two counter electrodes were made from gold. An Ag|AgCl reference electrode ($E_{Ag|AgCl}$= 0.197 V vs. SHE) was used.

The experiments were carried out at room temperature by means of a computerized PAR 273 A potentiostat/galvanostat using the software Power Suite.

The Au, In and alloy coatings were dissolved in the tri-electrode cell for anodic linear sweep voltammetry (ALSV) experiments with platinum counter electrode and the Ag|AgCl reference electrode in a solution containing 12 M LiCl. Before each experiment the gold electrode was cleaned by cyclic CV curves in the 0.1 N solution of sulfuric acid to remove traces of undissolved hydroxides and chlorides. The In or Au distribution on the surface of the coatings was examined by energy-dispersive analysis (EDAX).

Additionally, the galvanostatic deposition was performed onto brass substrates (2x1 cm) in order to investigate elemental composition of the obtained alloy coatings. The In percentage in the coatings depending on the electrolysis conditions was determined in experiments by X-ray fluorescence analysis (Fischerscope X-RAY XDAL).

The phase analysis was performed by means of a Bruker D8 Advance diffractometer at 2θ-angles from 15 to 90° with Cu-K$_\alpha$ irradiation and Sol X detector.

RESULTS AND DISCUSSIONS

Figure 1 (a-d) shows the chronopotentiometric curves obtained during electroplating of gold-indium alloys from electrolytes A, B, C and D (see Table 1). To the basic electrolyte containing ammonium sulphate four different organic ligands were added using oxalic, malonic and lactic acids and glycine. Thus, the galvanostatic curves obtained in the first three (A, B, C) investigated solutions show features associated with the occurrence of oscillations at the current density of 0.6 A dm^{-2}. In the glycine electrolyte single oscillations but at all investigated current densities were observed.

Oscillations with amplitude close to and above 300 mV are clearly visible (Figure 1A-C, insets). There is no trend in the behaviour with regard to the quantity of carbon atoms (in the order of oxalic, malonic and lactic ligands).
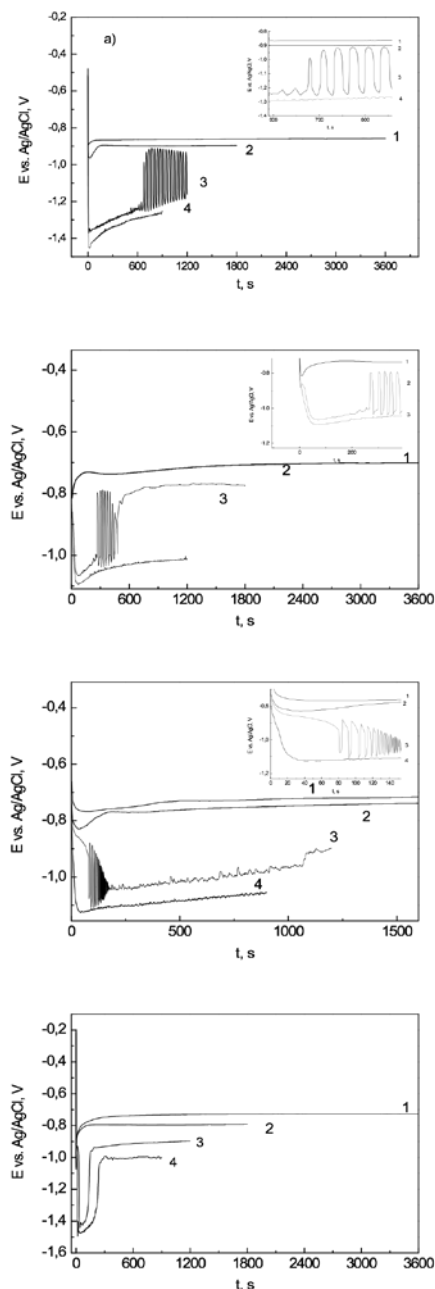
Fig. 1. Chronopotentiometric curves, obtained at different current densities: Curve 1 -0.2 A dm^{-2}; curve 2 - 0.4 A dm^{-2}; curve 3 -0.6 A dm^{-2}; curve 4 -0.8 A dm^{-2} in the electrolytes (see Table 1): a) A; b) B; c) C; d) D

Certainly, it can be supposed that the beginning of the oscillations is performed after process of nucleation, i.e. when the thickness of the coatings is more than 0.3 µm (in the electrolyte with an oxalic acid the oscillations start after the 600th second (Figure 1, inset 1a) after the beginning of the process, while with the malonic acid (Figure 1, inset 1b) they start markedly earlier - after the 80th second and in the case of using lactic acid – after about 180 seconds from the beginning of the reduction process (Figure 1, inset 1c).

Additionally, in all four investigated electrolytes the composition of the obtained coatings is similar and practically the same between 50 and 60 wt. %. The dependence of the composition on the current density is shown in Figure 2.
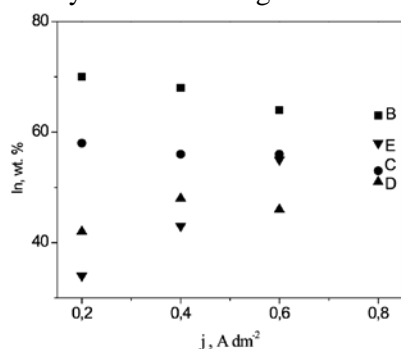

Fig. 2. Content of indium in dependence of the current density in the alloys deposited in the electrolytes A-D onto brass substrates.

In fact, it could be assumed that the potential oscillations are not related to the phase formation but more likely they could be associated with an alkalization in the vicinity of the electrode and formation/destruction of passive layers. There is no evidence in the literature about the formation of indium complexes with the indicated organic acids (oxalic, lactic, malonic and glycine), but with ammonia ions and hydroxyl ions its complexes are strong enough (the instability constant of the complex of indium with two ligands of ammonium is about 10^{-9} and that with the hydroxide group, with four ligands reaches the value of 10^{-28} [9]). However, it should be noted that oscillations in the process of indium deposition in absence of gold (as well as of gold in absence of indium) are not observed.

It is known that at pH values higher than 3.4 some passive indium-hydroxide and indium-cyanide layers are formed [10]. Most probably the conditions to form these layers are favoured at 0.6 A dm^{-2}. The glycine electrolyte is more acid than the others and that could be the reason that the oscillations cannot appear. This phenomenon of formation/destruction of the oscillations is not new and has been observed and described by de Levie [2], developed and modelled by M. T. M. Koper et al. [11-15] in case of the reduction of In^{3+} to In^0 in the thiocyanate electrolyte. It could be a reason to state that the appeared oscillations are a result from the chemical formation/destruction of some passive layer of indium oxide/hydroxide layer formed due to the increased alkalinity around vicinity of the electrode/electrolyte interface and may be a further option or could play a role for detecting pH changes in the vicinity of the electrode.

As previously mentioned, the composition of the alloy coatings from the different electrolytes

obtained in the region of indicated current densities is similar and it could be stated that the alloy deposition is anomalous, i.e. even at the lowest current density some indium-containing alloy phase starts to form. The study of this phenomenon continued with the work of glycine electrolyte, where structure formation is observed.
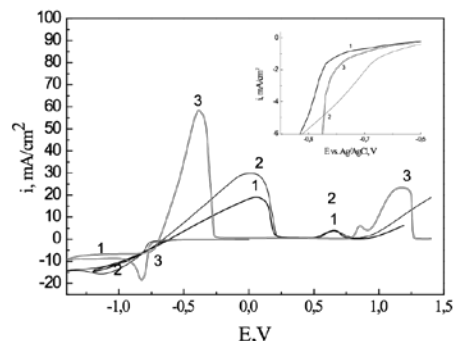
Fig. 3. Cyclic voltammetry curves, registered at v = 20 mV s^{-1} in the water solution of: 1) InCl$_3$ (curve 1); 2) InCl$_3$ + glycine (curve 2); 3) InCl$_3$ + glycine + (NH$_4$)$_2$SO$_4$ (curve 3), Inset: Part of the same curves, in the potential region -0.6 to -0.7 V.

Figure 3 presents cyclic voltammetry curves, obtained in the alloy electrolyte, without gold ions. The addition of the glycine depolarized the cathodic process and addition of the ammonium sulphate polarized the process of reduction of indium (with a presence of glycine) which starts at -0.8 V. (Figure 3, inset).

The anodic part of the CV curves seems to be more interesting. The dissolution of indium deposited from aqueous solution of indium chloride as well as in the presence of glycine goes through two peaks – one wide, with a maximum at 0 V and a second, small one with a maximum at 0.7 V (Figure 3, curves 1 and 2). These two peaks are divided by region of passivity about 250 mV. Most probably, the first peak belongs to the dissolution of indium and the second one to the dissolution of the passive layer, formed at the beginning of the deposition process, where some oxide – hydroxide layer is formed [10]. Also, it cannot be excluded, that the second anodic peak could also be a result of dissolution at a more positive potential of similar layers formed by the dissolution of indium at the first anodic maximum. The addition of ammonium sulphate (curve 3), which does not affect markedly the cathodic process or accelerates the first anodic process and a big anodic peak with a maximum around -0.5 V could be registered. The second peak with a maximum around 1.25 V most probably is connected with the dissolution of the passive layer formed at the beginning of the indium reduction process.
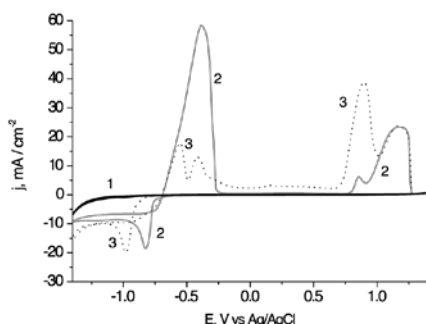
Fig. 4. Cyclic voltammetry curves, registered at v = 20 mV s^{-1} in aqueous solution of: a) KAu(CN)$_2$ + Glycine + (NH$_4$)$_2$SO$_4$ (curve 1), b) InCl$_3$ + glycine + (NH$_4$)$_2$SO$_4$ (curve 2), c) KAu(CN)$_2$ + Glycine + (NH$_4$)$_2$SO$_4$+ InCl$_3$ (curve 3)

Figure 4 shows cyclic voltammetry curves in the alloy electrolyte with the metals present separately and together. At this scale there are no visible peaks onto the CV curve (curve 1), obtained in the alloy electrolyte containing gold ions (in absence of indium). Curve 2, registered in the presence only of indium in the alloy electrolyte shows the already commented (in Figure 3) two well defined peaks with maximums around -0.4 V and 1.2 V (the last one is accompanied with a small bump at 0.85 V). The alloy electrolyte (curve 3) shows polarization of the cathodic reaction of about 200 mV, which is connected with a fact that indium reduction process proceed at the more negative potential onto already formed gold-indium alloy layer.

To clarify the nature of the peaks and the correspondence between cathodic and anodic processes, CVA curves reaching different vertex potentials in the cathodic period were recorded (Figure 5).
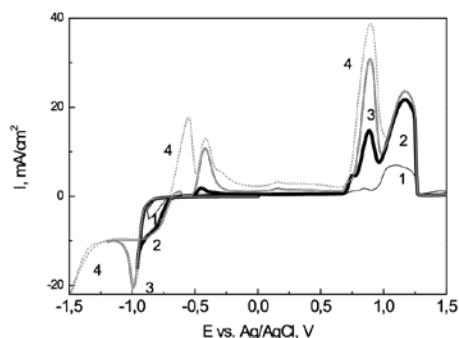
Fig. 5. Effect of the scan reversal potential on the anodic part at the CV curves, obtained in the electrolyte D (with glycine) registered at a scan rate of 20 mV s^{-1}, 1) -0.8 V; 2) -0.95 V; 3) -1.2 V; 4) -1.5 V

The different vertex potentials are chosen as follows: Firstly – just after beginning of some visible reduction process (curve 1), at the middle of the

process of reduction (curve 2), at the end of first peak (curve 3) and up to the appearance of a hydrogen evolution reaction (curve 4).

It could be seen, that the beginning of the deposition process corresponds to the appearance of the anodic peak with a maximum about 1.2 V (curve 1), connected with the dissolution of the passive hydroxide indium layer, formed at the beginning of the cathodic process (i.e. only indium products are the players in the beginning of the process). Next run shows that during the first cathodic well-visible process the gold-containing phase appears (peak with a maximum around 0.87 V) together with increased peak. Small peak also appears at the potentials about -0.4 V, which belongs to the indium-rich phase dissolution. Running the curve until vertex potential after the end of the cathodic peak at about -1 V (curve 3) leads to the growing of all anodic peaks, which were registered in the previous run. With a vertex potential, where the hydrogen evolution reaction takes place the appearance of the most negative anodic peak (left part of the split peak) appears, which should be assigned to the dissolution of the pure indium.

The phase analysis of the deposited coatings at different current densities, with different metal content shows almost similar diffractograms with peaks of AuIn$_2$-and In-phases.
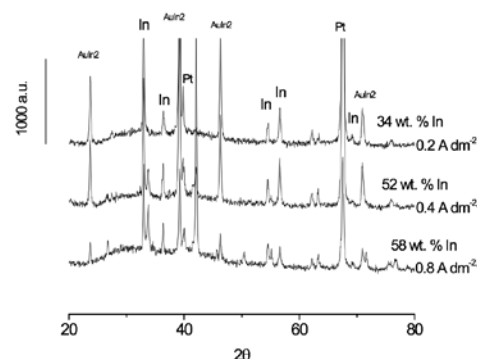

Fig. 6. XRD pattern of the coatings, obtained at 0.2 A dm^{-2}, 0.4 A dm^{-2} and 0.8 A dm^{-2} from the electrolyte D

From the performed experiments it is not possible to clarify the phenomena of anomalous deposition of the gold-indium alloy. The anodic linear sweep voltammetry technique is an appropriate tool to investigate the phase composition. The technique is described in [8] and the most important requirement is that during dissolution in the different electrolytes the re-precipitation is avoided which simplifies the "anodic" picture. So, the complicated nature of the anodic peaks directed the experiments to the anodic linear sweep experiments, performed on coatings

deposited at the 3 current densities parallel to the XRD experiments.

Similarly to the already by ALSV technique investigated silver-indium electrodeposited alloys [8] the electrolyte for the dissolution of the alloy was chosen to be lithium chloride, which is appropriate for the investigated gold-indium system as well.

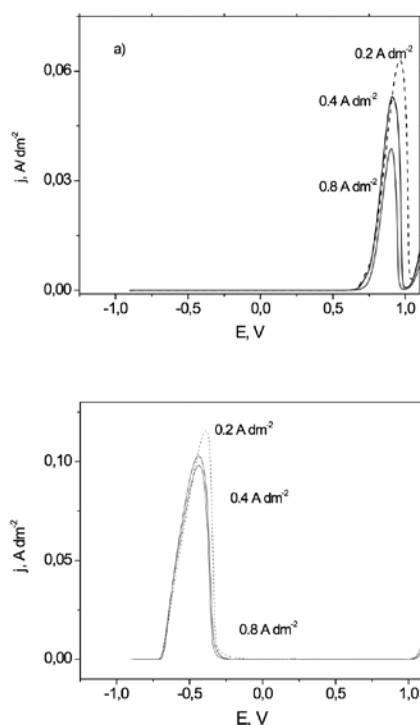The dissolution curves of the at 0.2, 0.4 and 0.8 A dm^{-2} deposited gold and indium layers are presented in Figure 7 a, b.

Fig. 7. ALSVs of gold and-indium coatings (v = 1 mV s^{-1}) deposited with a constant charge of electricity Q = 1.25 C cm^{-2} at different current densities: Dashed line – 0.2 A dm^{-2}; black solid line – 0.4 A dm^{-2}; grey solid line – 0.8 A dm^{-2}, dissolution of gold coatings, dissolution of indium coatings

The dissolution of indium in the lithium chloride takes place at -0.5 V, and that of gold at +1 V. The small difference in the area under peaks depends on the different cathodic efficiency during deposition of the coatings.

The dissolution of the alloy coatings was performed in the solution of LiCl and the obtained anodic linear sweep voltammetry curves are presented in Figure 8. For the coatings deposited at different current densities all peaks exists, but the content range of the elements is different. This fact corresponds to our previously obtained results [8].
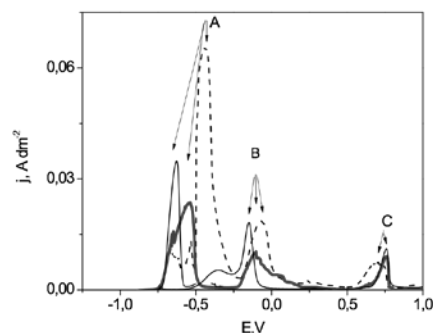
Fig. 8. ALSVs of gold-indium alloy coatings (v = 1 mV s^{-1}) deposited with a constant charge of electricity Q = 1.25 C cm^{-2} with different current densities: Dashed line - 0.2 A dm^{-2}; black solid line -0.4 A dm^{-2}; grey solid line - 0.8 A dm^{-2}

Considering the XRD pattern of the alloy system Au–In (Figure 6) it appears that each phase exists in a very broad range of percentages in the alloy. The potential range of each phase registered by ALSV technique depends on the weight percentage range of its appearance. Taking into account that the distribution of indium in the coating is non-homogeneous, the observed change of the position of some peaks on the ALSV is reasonable.

According the ALSV curves shown in Figures 7 and 8 together with the results of the X-ray analysis presented in Figure 6 it could be stated that:
- the peak A corresponds to the pure In;
- the peak B corresponds to the phase AuIn$_2$;
- the peak C corresponds to the pure Au and/or to the alpha phase of the system.

CONCLUSIONS

The electrodeposition of gold–indium alloys from different electrolytes on the basis of ammonium sulphate (with addition of oxalic, malonic and lactic acid, and glycine) belongs to the anomalous electrodeposition due to the fact that the gold-indium phases deposit preferentially than the gold, as a more noble metal. The oscillations, observed at some current densities from the first three mentioned electrolytes depend on the pH value near to the electrode/electrolyte interface where the formation/destruction of passive layers takes place. The dissolution potentials of gold, indium and gold-indium alloys depend on the deposition current density, respectively on the percentage of the alloy.

Each ALSV peak is ascribed to a corresponding phase and there is a very good agreement between the alloy characterization by the ALSV technique and by the X-ray technique.

REFERENCES

1 Ts. Dobrovolska, M. Georgiev, I. Krastev, *Transactions of the IMF*, **93**, 321(2015).
2. L. Pospisil, R. De Levie, *Journal of Electroanalytical Chemistry and Interfacial Electrochemistry*, **25**, 245 (1970).
3. T. Dobrovolska, I. Krastev, M. Georgiev, in M.Aliofkhazraei (Ed.), Comprehensive Guide for Nanocoatings Technology, Volume 1: Deposition and Mechanism, M. Aliofkhazraei (eds), NOVA publisher, 2015, ch. 1 p. 269
4. N. Dimitrova, T. Dobrovolska, I. Krastev, *Arch. Metall. Mater.*, **58**, 255 (2013).
5. T. Dobrovolska, L. Veleva, I. Krastev, A. Zielonka, *J Electrochem Soc*, **152**, C137 (2005).
6. I. Krastev, T. Dobrovolska, U. La-Injevac, S. Nineva, *J. Solid State Electrochem.*, **16**, 3449 (2012).
7. A. Brenner, Electrodeposition of alloys: principles and practice, Academic Press, New York and London, 1963, p.41.
8. T. Dobrovolska, V. D. Jovic, B. M. Jovic, I. Krastev, *J Electroanal Chem.*, **611**, 232 (2007).
9. J. A. Dean, Lange's handbook of chemistry, University of Tennessee, Knoxville: McGrawHill, Inc, 1999.
10. T. Dobrovolska, I. Krastev, A. Zielonka, *Galvanotechnik*, **95**, 872 (2004).
11. M. T. M. Koper, J. H. Sluyters, *Journal of Electroanalytical Chemistry and Interfacial Electrochemistry*, **303**, 65 (1991).
12. M. T. Koper, P. Gaspard, *The Journal of Physical Chemistry*, **95**, 4945 (1991).
13. M. T. Koper, P. Gaspard, J. H. Sluyters, *The Journal of Physical Chemistry*, **96**, 5674 (1992).
14. M. T. Koper, *Electrochim. Acta*, **37**, 1771 (1992).
15. M. T. M. Koper, J. H. Sluyters, *J. Electroanal. Chem*, **347**, 31 (1993).

АНОМАЛНО ЕЛЕКТРООТЛАГАНЕ НА СПЛАВ ЗЛАТО –ИНДИЙ

Б.-К. Чой[1], Ф. Зауер[1], Г. Бек[1,2], Р. Щаубер[3], Цв. Доброволска[4*]

[1]*Фраунхофер център за приложни изследвания по ресурсна ефективност, Алценау, Германия*
[2]*Университет по приложни науки в Ашафенбург, Ашафенбург, Германия*
[3]*Фраунхофер* проектна група по рециклиране на материали и ресурсни стратегии, Алценау, Германия
[4]*Институт по физикохимия, Българска академия на науките, София, България*

(Резюме)

Изследван е процесът на аномално отлагане на сплав злато-индий от различни електролити на базата на амониев сулфат (с добавянето на оксалова, малонова и млечна киселини, както и глицин). При галваностатичен режим на работа с първите три горепосочени електролити се наблюдават осцилации на потенциала. При електроотлагане на сплавта от глицинов електролит се наблюдава структурообразуване на повърхността на електрода. Фазовият състав на хетерогенните покрития, получени от глицинов електролит, са изследвани с анодна линейна волтамперометрия и резултатите са сравнени с данните от конвенционалния рентгеноструктурен анализ.

Ключови думи: глицинов електролит, сплав злато-индий, осцилации, периодични пространствено-времеви структури

Network modification of phosphate materials by transition metals doping

O. Kostadinova[1*], D. Kochnitcharova[1], E. Lefterova[1], M. Shipochka[2], P.Angelov[1], T.Petkova[1]

[1] Section Solid State Electrolytes, Institute of Electrochemistry and Energy systems "Acad. EvgeniBudevsky", Bulgarian Academy of Sciences, Acad. G. Bonchev Str., bld. 10, 1113 Sofia, Bulgaria
[2] Institute of General and Inorganic Chemistry, Bulgarian Academy of Sciences, "Acad. GeorgiBonchev" Str. bld.11, 1113 Sofia, Bulgaria

This work is focused on structural modification of phosphate materials by doping with transition metal oxides. The structure of $(TiO_2)_x(V_2O_5)_y(P_2O_5)_{100-x-y}$ composites is discussed in terms of composition, structural units and valence variations. XRD diffraction, IR and XPS spectroscopic techniques are used to analyze the materials. The addition of V_2O_5 and TiO_2 destroys P-O-P bridge structure, generates mixed P-O-V bonds and non-bridged oxygen atoms leading to the appearance of isolated PO_4^{3-} units.

INTRODUCTION

The need of urgent development of alternative energy sources continuously increases. The solid oxide fuel cells (SOFCs) are a promising response since they can operate reversibly, storing excess of renewable electricity in electrolysis mode, and then converting the fuel back to electricity in fuel cell mode [1]. The most favourable approach in SOFCs optimization is to lower the operating temperatures (200-600 ºC). Composite materials with charge imbalance caused by the cation non-stoichiometry compensated by protons (cation off-stoichiometric materials) are among the promising candidates for SOFC electrolytes. The non-stoichiometry is a typical behaviour of the transition metals that can influence the materials properties. With incorporation of transition metal ions, one may introduce non-stoichiometry and create new pathways for proton mobility due to structure reformation [2, 3]. In this respect, the phosphate materials like phosphate glasses, metal pyrophosphates and metal phosphates with NASICON type structure are an interesting subject of scientific work [4-6].

The present study discusses structural modification of $(TiO_2)_x(V_2O_5)_y(P_2O_5)_{100-x-y}$, composites with x = 10, 20 mol % and y = 45, 50, 60 mol % after doping with transition metal.

EXPERIMENTAL

Bulk samples from $(TiO_2)_x(V_2O_5)_y(P_2O_5)_{100-x-y}$ system were synthesized by melt quenching method. The initial compounds of TiO_2 and V_2O_5 powders and orthophosphoric acid (H_3PO_4) were homogenized and melted at 1100 ºC to obtain samples with compositions:

$(TiO_2)_{10}(V_2O_5)_{45}(P_2O_5)_{45}$ (N1),
$(TiO_2)_{10}(V_2O_5)_{50}(P_2O_5)_{40}$ (N2),
$(TiO_2)_{10}(V_2O_5)_{60}(P_2O_5)_{30}$ (N3),
$(TiO_2)_{20}(V_2O_5)_{50}(P_2O_5)_{30}$ (N4).

The structure of the samples was studied by X-ray diffractometer Philips APD-15 using CuK_α radiation. The IR spectra are recorded by FTIR spectrometer VARIAN 660-IR in the frequency range between 400 - 1400 cm^{-1} with a resolution of 2 cm^{-1}. X-ray photoelectron spectroscopy (XPS) measurements were carried out by spectrometer VG ESCALAB II using $AlK\alpha$ radiation with energy of 1486.6.eV. The binding energies were determined with an accuracy of ±0.1 eV utilizing the C_{1s} line at 285.0eV (from adventitious carbon) as a reference.

RESULTS AND DISCUSSIONS

Structural background

The studied materials are composed of three oxides: vanadium, titanium and phosphorus oxides, connected and forming various groups and units.

The phosphate atoms usually form a network consisting of PO_4 units linked with neighbouring PO_4 tetrahedra trough one-, two- or three P-O-P bridges (Bridging Oxygen BO), denoted as Q^i, where*i* is the number of the BO (n = 0, 1, 2 or 3) [7]. Linkage by two BO (Q^2 units) can be considered as PO_2^- middle groups in phosphate chains, while (Q^1) corresponds to PO_3^{2-} terminal units. Q^0 represents an isolated PO_4^{3-} tetrahedron known as orthophosphate unit. The vitreous P_2O_5 consists of Q^3 phosphate tetrahedra that form a three dimensional network. The addition of metal oxides results in "depolymerisation" of this network due to breaking of P-O-P bonds and

---

creation of negatively charged non-bridging oxygen (NBO). The Q^i species change according to Kirkpatrick and Brow model [7, 8] in consecution $Q^3 \rightarrow Q^2 \rightarrow Q^1 \rightarrow Q^0$ with increasing of the amount of modifying oxide.

The vanadium atoms could be present in different oxygen environments forming various types of polyhedra as VO_6 octahedra, VO_5 groups (square pyramids or trigonal bi-pyramids) and VO_4 tetrahedra in the crystalline and amorphous vanadates [9-12]. In vanadate-phosphate systems mixed units are formed composed of VO_x and PO_4 polyhedra [12].

The TiO_2 in all polymorph forms is built from TiO_6 octahedra [13]. TiO_6 is the main structural unit in the titanium-phosphates as pyrophosphates [14], and NASICON (Na Super Ionic Conductor) like phosphates [15]. In the phosphate glasses Ti atoms are in six-, five- or fourfold coordination [16-18].

X-ray Diffraction

The broad halo in XRD patterns reveals the amorphous character of samples N1 and N2 with higher phosphate content (Fig. 1). The samples N3 and N4 are glassy-crystalline as defined from the diffraction peaks and the halo on diffractograms. The higher TiO_2 content (20 mol.%) is accountable for the appearance of pure rutile phase observed in the sample N4. An empty NASICON-type crystal structure was identified for crystalline part of sample N3 - $(TiO_2)_{10}(V_2O_5)_{60}(P_2O_5)_{30}$ as described in previous work [19]. The structural formula of NASICON-type vanadyl (V) titanium(IV) phosphate proposed by S. Titlbach et. al. [20] is $(V^VO)Ti^{IV}_6(PO_4)_9$.
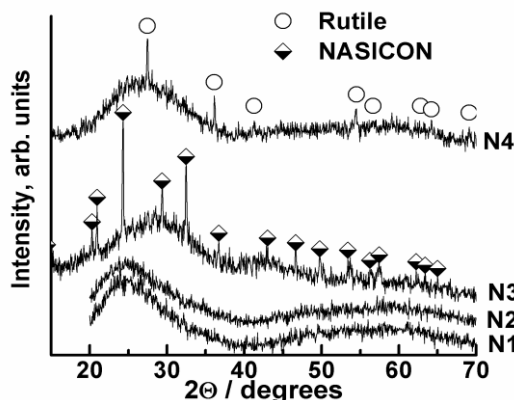
Fig. 1. XRD patterns of samples from $(TiO_2)_x(V_2O_5)_y(P_2O_5)_{100-x-y}$ system.

Infrared study

The infrared spectra of $(TiO_2)_x(V_2O_5)_y(P_2O_5)_{100-x-y}$ samples are presented in fig. 2. The absorption above 1200 cm^{-1} and the weak band at 1180cm^{-1} on the spectrum of sample N1 are connected with asymmetric and symmetric

stretching of PO_2^- (Q^2) middle groups in phosphate chains [21]. The absence of a pronounced absorption peak at ~1250 cm^{-1} however demonstrates the formation of short chains. The bands at 1130cm^{-1} and 1064 cm^{-1} are due to vibrations of PO^- in PO_3^{2-} (Q^1) terminal groups in the phosphate chains and pyrophosphate units $P_2O_7^{4-}$, respectively [22, 23]. The P-O-P bridges absorb at ν_{as} ~ 900 cm^{-1} and ν_s ~ 740 cm^{-1}. The bands at the 940 cm^{-1} and 870-850 cm^{-1} are due to the symmetric and anti-symmetric stretching vibration of the VO_2 groups in the VO_4-polyhedra [9, 10]. The absorption at 1010 cm^{-1} might arise from stretching vibration of V=O vanadyl bond in VO_5-groups or/and normal mode of PO_4^{3-} (Q^0) isolated phosphate groups [24]. In the glass N1 probability to detect PO_4^{3-} unit is small, therefore more likely VO_5 and VO_4 units are present. With the increasing of the V_2O_5 content the absorption band at ~940 cm^{-1} disappeared and VO_4 units is not registered on IR spectrum of glass N2. The spectra of N3 and N4 are comparable: the absorption above ~1200 cm^{-1}, related to the PO_2^- phosphate groups, disappears and the band at 900 cm^{-1} shifts to lower (860 cm^{-1}) wavenumber due to mixed P-O-V bridge formation. This indicates that no phosphate chains in these samples exist and they are built of Q^1 and Q^0 species.

The IR spectrum of the glassy-crystalline sample N3 is similar to this of crystalline $NaTi_2(PO_4)_3$ [25,26] NASICON structure. The structure consists of TiO_6 octahedra which share corners with six PO_4 tetrahedra while each PO_4 tetrahedron is connected by the corner with four TiO_6 octahedra [15]. As a results, isolated phosphate group PO_4^{3-} (Q^0), located at ~996 cm^{-1} and bending at 576 cm^{-1}, as well as normal vibration of TiO_6 octahedra ~at 640 cm^{-1} are identified in N3 spectrum. The band at 1020 cm^{-1} is due to V=O in VO_5 trigonal bipyramid.
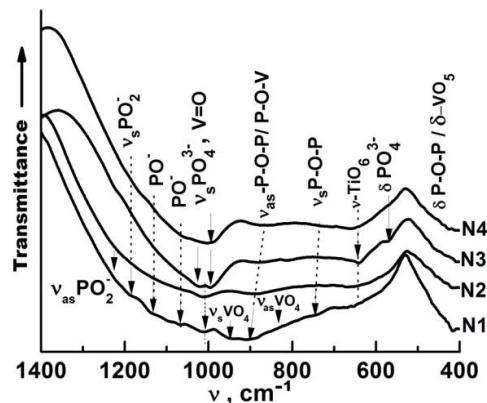

Fig. 2. Infrared spectra of samples $(TiO_2)_x(V_2O_5)_y(P_2O_5)_{100-x-y}$ system

The formation of TiO_2 Rutile phase leads to the higher concentration of P_2O_5 in amorphous matrix, which reflect on the IR spectrum of sample N4 as shoulder located at 1060 cm^{-1} because of the appearance of additional PO_3^{2-} (Q^1) groups.

The bands in the 400 – 500 cm^{-1} range are due to the lattice vibrations in vanadium oxide network and deformation of PO_4 units.

X-ray Photoelectron spectroscopy investigation

The XPS spectra shown in Fig 3 (a-d) validate the existence of different structure units. The broad P2p high resolution spectra are deconvoluted in three $P2p_{3/2}$-$P2p_{1/2}$ doublets which correspond to Q^0 tetrahedra (PO_4^{3-}) at ~132.5 eV, Q^1 (PO_3^{2-}) at ~133.5 eV and (PO_2^-) Q^2 with binding energy (BE) around 134.5 eV [27, 28]. The dominance of pyrophosphate groups $P_2O_7^{4-}$ is clearly visible. The number of isolated PO_4^{3-} phosphate group increases when the P_2O_5 content decreases (grow of component Q^o) whereas more PO_2^- units (Q^2) are detected at higher phosphate content.

O1s peak was deconvoluted in three components (Fig 3b): O1 with BE around 259-530.5 eV correspond to non-bridging oxygen (NBO) which forms oxygen bonds with titanium or vanadium and V-O-V bridges; O2 peak with BE=531-532 eV is assigned to mixed bridging bonds V-O-P and component O3 with BE of 533-534 eV associated with bridged oxygen in P-O-P bond or oxygen from adsorbed water [28].

The peak position of $Vp_{3/2}$ at ~517.6 eV (fig.3c) is evidence for predominantly V^{5+} valence of vanadium. The deconvolution with two components reveals weak asymmetry towards the lower energies due to the presence of V^{4+} with BE $\approx$ 516.5 eV.

Ti2p spectra on fig. 3(d) indicates the existence of Ti^{4+} valence state with $BE(Ti2p_{3/2}) \approx$ 459.3 eV in the crystalline samples corresponding to Anatase/Rutile BE [29]. The BE of Ti in the glassy samples is shifted to higher values at 459.85 eV.
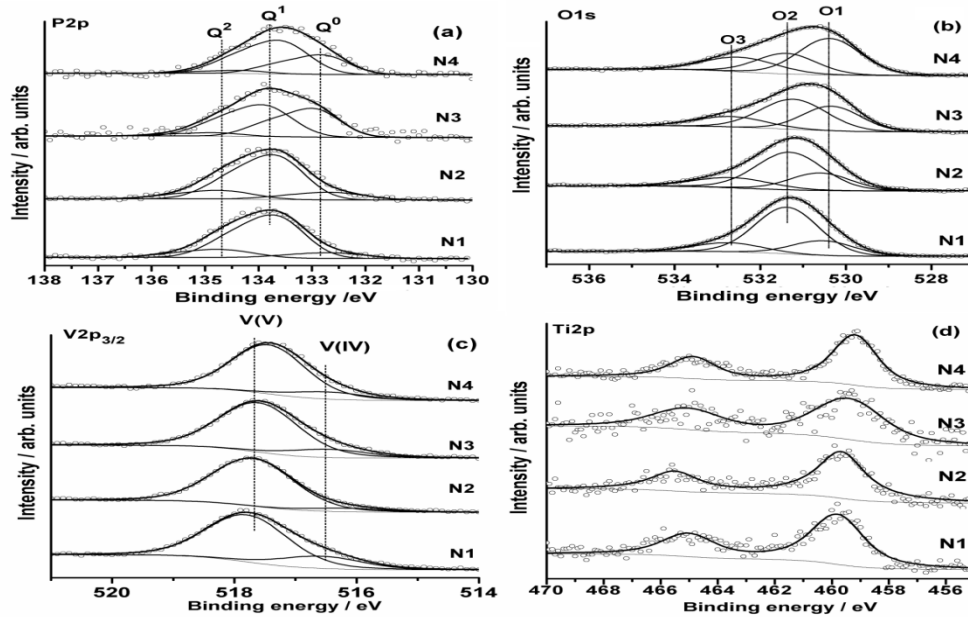
Fig. 3. High resolution X-ray photoelectron spectra of the $(TiO_2)_x(V_2O_5)_y(P_2O_5)_{100-x-y}$ samples: (a) P2p ; (b) O1s; (c) $V2p_{1/2}$; (d) Ti2p.

FTIR and XPS investigations show that pyrophosphate $(P_2O_7)^{4-}$ units are the major group in the samples under study. The units, however, are partially displaced by isolated PO_4^{3-} when the phosphorus content decreases or by PO_2^- units when the phosphate content grows.

The samples N3 and N4 are based on both: Q^1 with a two PO_3^{2-} tetrahedra connected in pyrophosphate units and Q^0, i.e. isolated PO_4^{3-} tetrahedra. The vanadium pentoxide plays role of the second glass former. Addition of V_2O_5 and/or

TiO_2 leads to destroying P-O-P bridge structure introducing mixed P-O-V bridges and new NBOs. The titanium atoms possess stable fourth valence and octahedral coordination in all samples.

CONCLUSIONS

The study of materials from $(TiO_2)_x(V_2O_5)_y(P_2O_5)_{100-x-y}$ system reveals that the structure is characterized by different oxygen environment. The addition of V_2O_5 and TiO_2 leads to destroying P-O-P bridge structure introducing mixed P-O-V bridges and new NBOs. The

pyrophosphate ($P_2O_7^{4-}$) groups are the main structural units in the samples partially displaced by isolated PO_4^{3-} groups when the V_2O_5 and/or TiO_2 content increases or by PO_2^- units when the content of the transition metals decreases. The glass-crystalline samples with NASICON or Rutile type-structure possess lower P_2O_5 content.

The vanadium exist in two valence states V^{5+} and V^{4+}. The presence of VO_5 groups and TiO_6-octahedra is typical to all studied samples.

REFERENCES

1. D. Vladikova, Z. Stoynov, G. Raikova, A. Thorel, A. Chesnaud, J. Abreu, M. Viviani, A. Barbucci, S. Presto, P. Carpanese, *Electrochim. Acta*, **56**, 7955 (2011).
2. R. V. Barde, S. A. Waghuley, J Advanced Ceramics, 2, 246 (2013).
3. B. Zhu, *Solid State Ionics*, **145**, 371 (2001).
4. Y. Daiko, *Journal of the Ceramic Society of Japan (JCS-Japan)*, **121**, 539 (2013)
5. Y. Jin, Y. Shen and Takashi Hibino, *Mater. Chem.*, **20**, 6214 (2010).
6. M.A. Moshareva, S.A. Novikova, A.B. Yaroslavtsev, *Inorg. Mater.*, **52**, 1283 (2016).
7. R. K. Brow, *J. Non-Cryst. Solids*, **263&264**, 1 (2000).
8. R.K. Brow, C.A. Click, T.M. Alam, *J. Non-Cryst. Solids*, **274**, 9 (2000).
9. V.Dimitrov, *J. Non-Cryst. Solids*, **192&193**, 183 (1995).
10. Y. Dimitriev, V. Dimitrov, M. Arnaudov, and D. Topalov, *J. Non-Cryst. Solids*, **57**, 147 (1983).
11. M. Willinger, N. Pinna, D. S. Su, R. Schlögl, *Physical Review B*, **69**, 155114 (2004).
12. S. Boudin, A. Guesdon, A. Leclaire, M.-M.Borel, *Int. J. Inorg.Materials*, **2**, 561 (2000).
13. M. Matsui, M. Akaogi, *Molecular Simulation*, **6**, 239 (1991).
14. S. T. Norberg, G. È. Svensson and J. È. Albertsson, *Acta Cryst.*, **C57**, 225 (2001).
15. S. Benmokhtar, A. El Jazouli, A. Aatiq, J.P. Chaminade, P. Gravereau, A. Wattiaux, L. Fourne`s, J.C. Grenier, *J. Solid St. Chem.*, **180**, 2004 (2007).
16. A. Tang, T. Hashimoto, T. Nishida, H. Nasu, K. Kamiya, *Journal of Ceramic Society of Japan*, **112**, 496 (2004).
17. B. Tiwari, A. Dixit, G. P. Kothiyal, M. Pandey, S. K. Deb, *BARC Newsletter*, **285**, 167 (2007).
18. S. Lee, H. Maeda, A. Obata, K. Ueda, T. Narushima, T. Kasuga, *J. Non-Cryst. Solids*, **426**, 35 (2015).
19. D. V. Blaskova-Kochnitcharova, T. Petkova , L. Fachikov, E. Lefterova , I. Kanazirski, P. Angelov, S. Vassilev, *Bulg. Chem. Commun.*, **45:A**, 159 (2013).
20. S. Titlbach, W. Hoffbauer, R. Glaum, *J. Solid State Chem.*, **196**, 565 (2012).
21. L. L. Velli, C. P. E. Varsamis, E. I. Kamitsos, D. Möncke& D. Ehrt, *Phys. Chem. Glasses*, **46**, 178 (2005).
22. A. Shaim, M. Et-tabirou, *Materials Chemistry and Physics*, **80**, 63 (2003).
23. K. Nakamoto, Infrared and Raman Spectra of Inorganic and Coordination Compounds: Part A: Theory and Applications in Inorganic Chemistry, Sixth Edition John Wiley & Sons, Inc., 2009
24. H-K Roh, M-S Kim, K. Chung, M. Ulaganathan, V. Aravindan, S. Madhavi, K. Roh, K-B Kim, *Journal of Materials Chemistry A*, **5**, 17506 (2017).
25. P. Tarte, A. RulmontAnd C. Merckaert-Ansay, *Spectrochimica Acta*, **42A**, 1009 (1986).
26. R. Gresch, W. Muller-Warmuth, H. Dutz, *J. Non-Cryst. Solids*, **34**, 127 (1979).
27. A. V. Naumkin, A. Kraut-Vass, S. W. Gaarenstroom, C. J. Powell, NIST Standard Reference Database 20, Version 4.1 (2013), http://srdata.nist.gov/xps
28. A. Majjane, A.Chahine, M. Et-tabirou, B. Echchahed, T. Do, P. Mc Breen, *Mater. Chem. Phys.*, **143**, 779 (2014).
29. U. Diebold, T. E. Madey, *Surf. Sci. Spectra*, **4**, 227 (1996).

МОДИФИЦИРАНЕ НА МРЕЖАТА НА ФОСФАТНИ МАТЕРИАЛИ ЧРЕЗ ДОТИРАНЕ С ПРЕХОДНИ МЕТАЛИ

О. Костадинова[1], Д. Кошничарова[1,2], Е. Лефтерова[1], М. Шипочка[3], П. Ангелов[1], Т. Петкова[1]

[1]*Институт по електрохимия и енергийни системи "Акад. Евгени Будевски ", Българска академия на науките, ул." Акад. Г. Бончев ", бл. 10, 1113 София, България*

[2]*Химикотехнологичен и металургичен университет, бул. "Климент Охридски" 8, 1756 София, България*

[3]*Институт по обща и неорганична химия, Българска академия на науките, ул. "Акад. Георги Бончев" бул. 11, 1113 София, България*

(Резюме)

Тази работа се фокусира върху изследването на структурните промени на фосфатните материали при дотиране с оксиди на преходните метали. Структурата на новите композити $(TiO_2)_x(V_2O_5)_y(P_2O_5)_{100-x-y}$ се разглежда по отношение на състава, структурните единици и валентността. За анализ на материалите се използват Ренгенова дифракция, ИЧ и фотоелектронна спектроскопия. Добавянето на V_2O_5 и TiO_2 разрушава P-O-P мостовата структура и води до образуване на смесени и немостови кислородни връзки, както и до появата на изолирани PO_4^{3-} единици. При високо съдържание на преходните метали са получени стъклокристални образци.

Ключови думи: оксиди на преходни метали, структурни изследвания, IR, XPS

Thin phosphate films on aluminum surfaces

G. P. Ilieva, D. I. Ivanova, L. B. Fachikov*,

University of Chemical Technology and Metallurgy, 8 "Kliment Ohridski" Blvd., 1756 Sofia, Bulgaria

The effects of different factors such as concentration (2.0÷11 vol. %) and temperature (20÷70ºC) on formations, compositions and morphologies of coatings obtained by treatment of aluminum (Al – 99.5 %) surfaces in solutions containing ammonium and sodium phosphates, MoO_4^{2-} promoting ions, buffers, softeners, inorganic activators, as well as surfactants, have been investigated. Gravimetric and electrochemical methods, optical microscopy, scanning electron microscopy with EDX-analysis and X-ray photoelectron spectroscopy have been used. The optimal operating conditions (concentration 4 – 7 vol. % and temperature range 50 – 70ºC), under which dense and homogeneous coatings with thickness of about 1 μm can be produced have been estimated. The coating contents include phosphorus, oxygen, molybdenum and nickel, and consequently a conjecture about probable chemical compounds

Keywords: aluminum, aluminum alloys, conversion coatings, phosphating.

INTRODUCTION

Aluminum and its alloys are extensively encountered in materials used in aerospace, automotive, electronic, architectural and other industries due to their important properties such as low density, high ductility, high thermal and electrical conductivity, high mechanical strength as well as good corrosion resistance in neutral media [1-2]. Contacting solutions containing special complexing agents the aluminum undergoes to localized corrosion which invokes different protection methods against degradation processes of the metal and its alloys, to be developed.

Chemical conversion coatings are commonly produced on various engineering alloys, to improve paint adhesion and as adequate corrosion protection. Treatment in chromate [3-6] or chromate-phosphate [7-8] solutions has frequently been used to modify aluminum alloy surfaces in the past. However, chromate solutions have been widely associated with carcino – genesis [9-10], and its removal as a waste is a problem that should be resolved. Current environmental legislations are moving toward total bans on chromate-based treatments. Additionally, such treatments are not adaptable to the mixed steel-aluminum components frequently encountered in car body parts [2].

There is a strong incentive to explore and evaluate alternative treatments for aluminum surface modification. Recent studies [11-14] have shown that chemical conversion treatments in chromate-free phosphate baths are promising alternatives for the surface modifications of iron-aluminum components. It has long been recognized that phosphated metals exhibit substantially greater corrosion resistances and paint adhesions. More importantly, this technique has advantages over chromate-phosphate treatment in terms of environmental effects [15].

Among these methods, the polymeric coatings with Zr or Ti metal addition and amorphous phosphate coatings should be mentioned. The amorphous phosphate coatings are widely used for steel and zinc-plated steel [16-17], but this method is insufficiently studied when applied to aluminum alloys [18-19].

The primary aim of this report is present results from studies where the characteristics of amorphous phosphate coatings on the aluminum surfaces, obtained in aqueous solutions of a newly developed process (KAF-50 FA) were examined.

EXPERIMENTAL

Materials and samples

Disk shaped samples (26 mm, thickness 0.5 mm and working surface area 0.1 dm^2) cutted from an aluminum sheet (Al – 99.5 %) were tested. The electrochemical experiments were carried out with plate-shaped specimens prepared in accordance with ISO/FDIS 17475 (ISO 17475:2005) and a fixed working surface area of 1 cm^2. In addition, square plates (10x10 mm) were used as specimens in case of all physical methods applied in the study.

Solutions

The working media represented aqueous solutions as follows:
- solution for cleaning;
- solution for brightening of Al surfaces on the basis of organic acids;

---

* To whom all correspondence should be sent.
E-mail: fachikov@uctm.edu

- solution for phosphating, containing ammonium and sodium phosphates, MoO_4^{2-} promoting ions, buffers, softeners, inorganic activators, as well as surfactants, pH=4.0.

The working conditions for gravimetric method referred to:

Concentration values of 2.0 vol.%, 4.0 vol.%, 7.0 vol.% and 11.0 vol.%;

Temperature values of 20.0 °C, 30.0 °C, 40.0 °C, 50.0 °C, 60.0 °C and 70.0 °C;

Process duration: 1.0 min, 4.0 min, 8.0 min, 10.0 min and 15.0 min.

The working/model media used for the corrosion experiments is 0.6 M NaCl.

Methods of investigation
Gravimetric method

The Gravimetric method was used for studying kinetics of forming and determining conditions of the processes for increasing of the coating's thicknesses depending on the influence of different factors. The method allows determining mass alteration of experimental samples after forming and removing coatings:

$$M = \frac{m_1 - m_2}{S} \ ,$$

where: M, $g \ m^2$ is mass or as accepted to call a thickness of the obtained coating,; m_1 and m_2 are the sample mass before and after coating, g; S is the sample surface area, m^2.

Electrochemical methods
Open circuit potential determination

Metals immersed in liquid electrolytes media resulted in establishment of non-equilibrium, i.e. the so-called corrosion potentials. The corrosion potentials are not indicative with respect to the resistance attained but their values and time variations provide enough information about the character of the corrosion process, the behavior of both the metal and metal coating in different media under various conditions.

Potentiodynamic polarization method

The polarization curves recorded potentiostatically or potentio- dynamically allow determination of various corrosion characteristics such as corrosion rate, corrosion potential, etc.

The experiments were carried out with EG&G Princeton Applied Research, *Potentiostat/ Galvanostat, Model 263A*, provided with the specialized software package PowerCORR®.

Physical methods
Optical microscopy (OM)

The microstructure of aluminum and the type of the corrosion attack were determined by optical microscopy, using a microscope OPTIKA® *Model:* B-500Bi.

Scanning electron microscopy (SEM)

The morphology and structure of the coatings were examined by scanning electron microscopy, using a *SEM/FIB LYRA I XMU, TESCAN* electron microscope, equipped with ultrahigh resolution scanning system secondary electron image (SEI).

Energy dispersive X-ray spectroscopy (EDX)

The energy dispersive spectroscopy is a local X-ray spectral analysis which permits qualitative and quantitative determination of surface micro volume contents of the order of several μm^3. Apparatus Quantax 200, BRUKER with spectroscopic resolution at Mn-Ka and 1 kcps 126 eV is used.

X-ray photoelectron spectroscopy (XPS)

The chemical composition and the oxidation state of the elements on the surface being formed were studied using X-ray photoelectron spectroscopy (XPS). The XPS studies were performed in an Escalab II system with Al K_α radiation with energy of 1486.6 eV and total instrumental resolution of ~1 eV. The elemental concentrations were evaluated from the integrated peak areas after linear background subtraction using theoretical cross-sections.

RESULTS AND DISCUSSIONS

The data summarized in Table 1 shows the most important characteristics of the solution used in the phosphating experiments with aluminum specimens: density, ρ; pH; conductivity, σ and total, K_O acidity.

Table 1. Phosphating solution characteristics

Solution	ρ	pH	σ	Ko
	$g \ cm^{-3}$		$mS \ sm^{-1}$	
KAF-50 FA	1.23	4.29	64.3	208

Gravimetric investigations

The method was used to elucidate the effect of the operating conditions (concentration and temperature of the phosphating solution as well the duration of the process) on the coating thickness M_1. The plots in Figure 1 are the relationships $M_1 = f(\tau)$ in 2 (1a), 4 (1b), 7 (1c) and 11 (1d) vol.% aqueous solution of the KAF-50 FA agent under various conditions imposed by variations in the temperature

and duration of the sample treatment. These conditions were selected after preliminary tests.
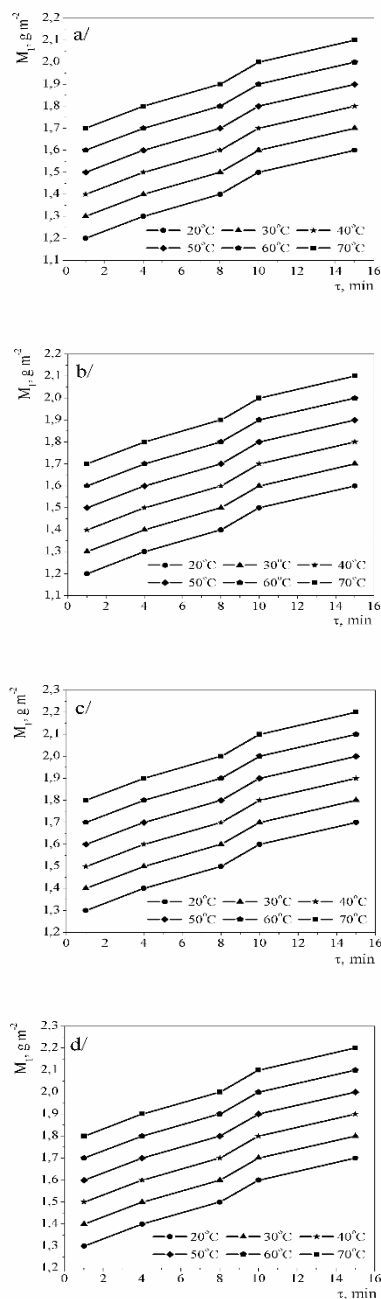

Fig. 1. Effect of the phosphating duration, τ, min on the thickness/mass of the phosphate coating obtained in KAF-50 FA, M_1, g m^{-2}: a/ 2 %; b/ 4 %; c/ 7 %; d/ 11 %.

The curve behaviours reveal that the thickness/mass on films formed on the aluminum surfaces grows in time. The increase in the solution temperature from 20.0 to 70.0°C results in increased thickness/mass where the maxima are attained at 70.0°C. The similarities between the curves and the small differences in the values of M_1 indicate that the solution concentration does not affect significantly both the mechanism and the rate of the phosphate film formations. The weak increase in M_1 with

increase in the concentration reveals, actually, that it is more reasonable solutions with moderate concentrations to be used, that also have an economic impact, rather than film formations in high concentration solutions.

The phosphate coatings obtained are from pale to dark yellowish colors. The coatings with better distribution of thickness and color over the entire sample area were obtained at about 60°C and solution concentrations in the range 4÷7 vol.%.

Electrode potentials measurement

The electrode potentials of the phosphate aluminum specimens were measured in the course of the coatings formation in the phosphating bath and after that they were tested in a model aqueous media 0.6 M NaCl.

The electrode potentials shown in Figure 2 are relevant to the process of amorphous phosphate coating formation by submerging of the samples in solutions with 7 vol.% (at 20.0, 30.0, 40.0, 50.0, 60.0 and 70.0°C) lasting 10 min. It is obvious that at all temperatures used the potentials shift in the positive direction: at the beginning approximately linearly and then followed by almost parabolic behaviour up to the moment when stabilization is attained.
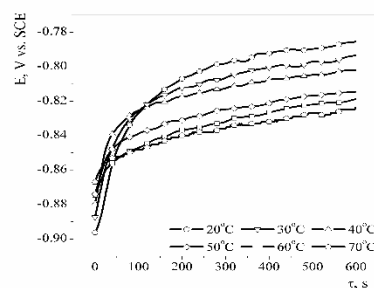
Fig. 2. Relationships potential-time during formation of the coating (open circuit): 7 vol.%; 10 min and different temperatures of obtaining

The corrosion resistance of the amorphous phosphate coatings was determined in model aqueous solutions of NaCl with 0.6 M concentration. The tests itself includes a submerging procedure for about 1 h of all samples in the NaCl solutions. The coating was determined as resistant if for 1 h (an empirically chosen time interval) no changes in the surface as color spots or colorization of the solutions occur. Meanwhile, in parallel to these tests the corrosion potential of the samples were measured that allowed to compare the behaviour with that of uncoated aluminum samples.

The potential behaviour shown in Figure 3 is relevant to the corrosion resistance of amorphous phosphate coatings in 0.6 M aqueous solutions of NaCl. The plots reveal that just after the sample

submergement in the corrosion medium the potentials shift sharply in the negative directions and after a certain accommodation time interval (about 500 seconds) a stable state is attained. In additions, with increase in the temperature of the phosphate coatings the potentials move in the positive direction. The corrosion potential of an uncoated aluminum sample is more positive than the phosphate coated ones at 20 and 30°C.
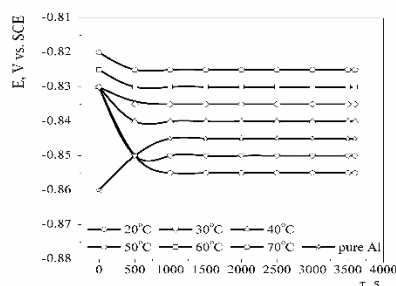

Fig. 3 Relationships potential-time in 0.6 M NaCl (open circuit): 7 vol.%; 10 min and different temperatures of obtaining.

Potentiodynamic polarization investigations

The potentiodynamic polarization studies of the phosphate coatings were carried out at 20°C in model aqueous solutions of 0.6 M NaCl. The scanning rate of 10 mV s^{-1} was chosen based on preliminary test runs. The target of these experiments was to obtain information about the corrosion resistance of the phosphate coatings formed in the corresponding model media in course of their cathodic and anodic polarization and consequently to compare them.

The potentiodynamic polarization relationships of the phosphate coatings (see Figure 4) obtained in the model solutions of 0.6 NaCl allow estimating both the corrosion potentials and the corresponding currents, summarized in Table 2. It is obvious that in 0.6 M NaCl solutions the potentials shift in the positive direction with increase in the temperature and the corrosion current (it slightly varies) is the lowest in the range 40-60°C.
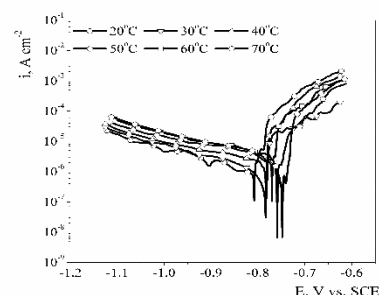
Fig. 4. Potentiodynamic polarization relationships of the phosphate coatings in 0.6 M NaCl: 7 vol. %; 10 min, scan rate 10 mV s^{-1} and different temperatures of obtaining

Table 2. Corrosion parameters of the coatings in 0.6M NaCl

Corrosion parameters	Temperatures, °C					
	20°C	30°C	40°C	50°C	60°C	70°C
E_{corr}, mV (SCE)	-808	-785	-784	-760	-771	-749
i_{corr}, A cm^{-2}	8.3x10^{-7}	3.5 x10^{-7}	1.4 x10^{-6}	1.6x10^{-6}	2.2x10^{-6}	7.3x10^{-7}

Optical microscopy

The micrographic picture in Figure 5 demonstrates surface of amorphous phosphate coating on an aluminum sample. The surface is almost homogeneous with dense fine film coating of gray bluish color.
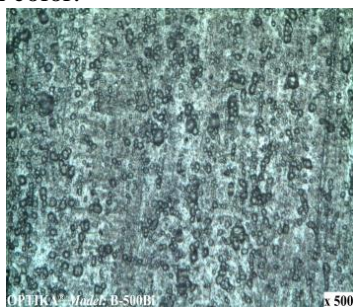
Fig. 5. Optical microscopy of the phosphate coating: 7 vol. %; 60°C; 10 min.

Scanning electron microscopy

The microphotography in Figure 6a demonstrates an amorphous phosphate coating obtained on aluminum samples. The surface is covered with dense fine film with some small areas where spherical formations with white color emerge. The surface shown in Figure 6b and Figure 6c, in different colors, show the distribution of the elements in the coating content.
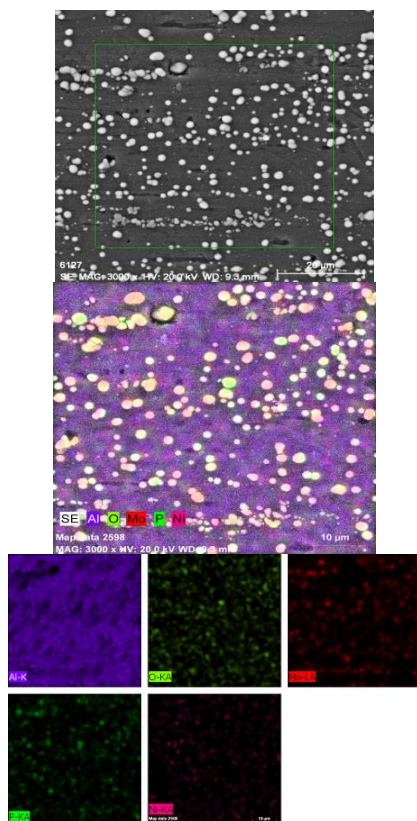
Fig. 6. SEM – microphotograph of the obtained coating: 7 vol.% 60°C; 10 min.

Energy dispersive X-ray spectroscopy, EDX

The EDX-analysis is performed on specimens treated in phosphate solutions again at 7 vol.%; 60°C; 10 min (see Figure 7). The basic elements contained in the coating determined by means of this analysis are Al, P, O, Mo and a little bit quantity of Ni. The results of EDX-analysis are presented in Table 3.
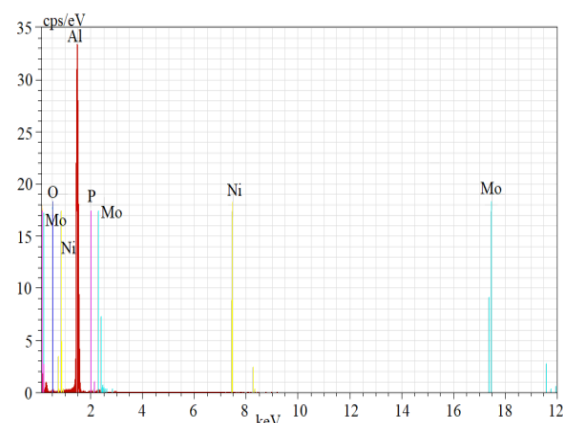

Fig. 7. EDX – spectrums of the elements in the coating: 7 vol.%; 60oC; 10 min.

X-ray photoelectron spectroscopy, XPS

XPS was used for determination of the chemical content of the coatings. Figure 8 presents the photoelectron spectra of Al2s, P2p, O1s and Mo3d, registered in the analysis of the phosphate coatings. The value of bonding energy of Al2s is 120.5 eV and it corresponds to the typical rage related to Al_2O_3. The bonding energy of P is 133.7 eV and this value indicates that it is (V) valent state as PO_4^{-3}. The obtained spectrum of O1s is characterized with wide half-wide and asymmetric shape in the direction of the higher bonding energy which may be attributed to formation of various oxides as well as hydroxides and phosphates.

Table 3. EDX analyse of the elements in the coating at the film surface

Concen-tration	Elements				
	Al	O	Mo	P	Ni
Atomic,%	84.91	10.70	3.24	0.78	0.37
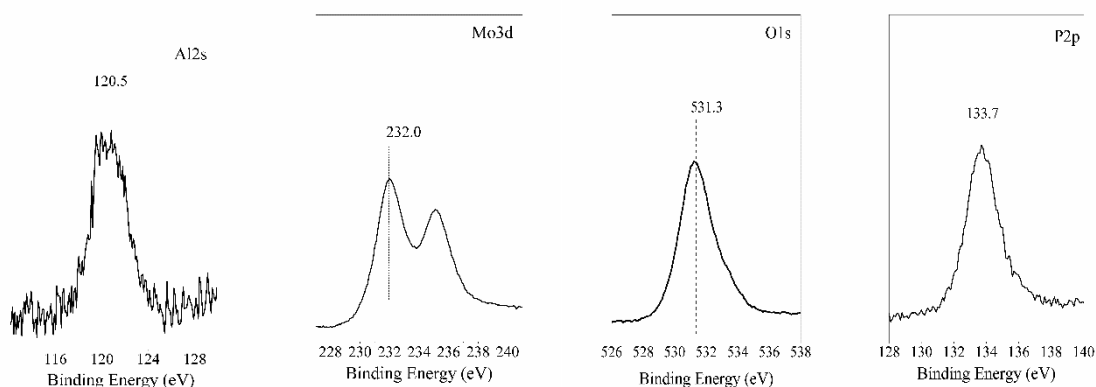
Fig. 8. XPS – spectra of the elements in the phosphate coating: 7 vol.%; 60°C; 10 min.

The maximum value of the bonding energy of Mo3d is 232.0 eV. The shape and the large half-wide of the registered peak suggest existence of Mo in various valent states at the coating surface.

Table 4 presents the quantity of the elements included in coatings determined by X-ray photoelectron spectroscopy in atomic percentages.

Table 4. XPS-analyse of the elements in the coating

Concentration	Elements			
	Al	O	Mo	P
Atomic %	4.9	76.0	12.0	7.1

CONCLUSIONS

The effects of the operating conditions (concentration, temperature) on the thickness, content and morphology of coatings formed at aluminum surfaces in solutions containing ammonium and natrium phosphates (as well as molybdate, softeners and inorganic activators and surfactants) have been investigated by gravimetric, electrochemical polarizing methods X-ray and microscopic analyzes.

The studies carried out reveal that:

1. The mass/thickness of the coatings increases with increase in the temperature in all cases of the concentration variations.

2. SEM and optical analyzes reveal that the surfaces of the treated aluminum samples are coated by homogenous dense films and the better results were obtained with phosphating baths with concentrations 4-7 vol.% and temperature of about 60ºC.

3. The coatings obtained are X-ray amorphous and the contents include phosphorous, oxygen, molybdenum, and nickel, forming chemical compounds in the structure of the coatings such as oxides, hydroxides and phosphates of aluminum, molybdenum and nickel.

REFERENCES

1. P.G. Sheasby, R. Pinner. The surface treatment and finishing of aluminum and its alloys, 6th edition, Redwood Books, Trowbridge, Wilts BA14 8RB, UK, 2001.
2. S. Wernic, R. Pinner. Surface treatment and finishing of aluminum and its alloys, Teddington (Middlesex, England): Robert Deaper, 1996.
3. S.M. Cohen, *Corrosion*, **51**, 71 (1995).
4. F.W. Lytle, R.B. Greegor, G.L. Bibbins, K.Y. Blohowiak, R.E. Smith, G.D. Tuss, *Corros. Sci.*, **37,** 349 (1995).
5. G.M. Brown, K. Shimizu, K. Kobayashi, G.E. Thompson, G.C. Wood, *Corros. Sci.*, **33**, 1371 (1992).
6. J.A. Treverton, M.P. Amor, A. Bosland, *Corros. Sci.*, **33**, 1411 (1992).
7. B. Shadzi, *Metal Finish.*, **87,** 41 (1989).
8. P.A. Schweitzer, Corrosion and Corrosion Protection Handbook, Marcel Dekker, 1988, Ch.. 4.
9. J.W. Bibber, *Metal Finish.*, **91**, 46 (1993).
10. T. Foster, G.N. Blenkinsop, P. Blattler, M. Szandorowski, *J. Coat. Technol.*, **63**, 101 (1991).
11. H. Ishii, O. Furuyama, S. Tanaka, *Metal Finish.*, **91**, 7 1993).
12. Ying J. F., M. Y. Zhou, B.J. Flinn, P.C. Wong, K. A. R. Mitchell, T. Foster, *J. Mater. Sci.*, **31**, 565 (1996).
13. B. Cheng, S. Ramamurthy, N.S. McIntyre, *J. Mater. Eng. Performance*, **6**, 405 (1997).
14. W. Rausch, The phosphating of metals, Finishing Publications Ltd., London, 1990
15. L. Fachikov, D. Ivanova, *Appl. Surface Sci.*, **258,** 10160 (2012).
16. L. Fachikov, Y. Tumbaleva, D. Ivanova, B. Tzaneva, *Trans. Inst.Metal Finish.*, **90,** 330 (2012).
17. V. Burokas, A. Martushene, A. Ruchinskene, A. Sudavichyus, G. Bikul'chyus, *Protection of Metals,* **42,** 339 (2006).
18. V. Burokas, A. Martušienè, O. Girčienè, *Surface & Coating Technol.*, **202**, 239 (2007).

ТЪНКИ ФОСФАТНИ ФИЛМИ ВЪРХУ АЛУМИНИЕВИ ПОВЪРХНОСТИ

Г. П. Илиева, Д. И. Иванова, Л. Б. Фачиков

Химикотехнологичен и металургичен университет, бул. „Кл. Охридски" 8, София 1756, България

(Резюме)

Изследвано е влиянието на различни фактори като концентрация (2.0÷11 vol. %) и температура (20÷70ºC), върху формирането, състава и морфологията на покрития, получени при третиране на алуминиеви повърхности (Al – 99.5 %) в разтвори, съдържащи амониеви и натриеви фосфати, MoO_4^{2-} промотиращи йони, буфери, омекотители, неорганични активатори и ПАВ. Използвани са гравиметричен и електрохимичен методи, оптична микроскопия, сканираща електронна микроскопия с EDX-анализ, и рентгенова фотоелектронна спектроскопия (XPS). Определени са оптималните експериментални условия (концентрация 4 – 7 vol.% и температура 50 – 70ºC), при които се получават хомогенни покрития с дебелина около 1 μm. В състава на покритията се съдържат фосфор, кислород, молибден и никел, които са под формата на фосфатни и оксидни съединения.

Structure and corrosion resistance of Ni-P, Co-P and Ni-Co-P alloy coatings

K. N. Ignatova[1]*, St. V. Kozhukharov[1], G. V. Avdeev[2], I. A. Piroeva[2]

[1] University of Chemical Technology and Metallurgy – 8, Kl. Ohridski Blvd, Sofia 1756, Bulgaria

[2]Bulgarian Academy of Sciences, Institute of Physical Chemistry "Acad. Rostislav Kaishev",Acad. G.Bonchev" St., Bl.11, Sofia 1113, Bulgaria

The present research work reports the results acquired from the systematical characterization regarding the morphology, the phase composition, the barrier properties and the corrosion resistance, possessed by Ni-P, Co-P and Ni-Co-P coatings on copper substrates. The investigated coatings were galvanostatically deposited at similar conditions from sulfate-chloride electrolytes, with pH = 2, at 80°C. The XRD analysis results have revealed that the Ni-P alloy coating possesses typically amorphous structure, whereas the Co-P coatings are with homogeneous polycrystalline structures, composed by orthorhombic Co_2P phase. The Ni-Co-P coating hasnano-sized structure and possesses variable composition consisted by series of solid solution Ni_2P -Co_2P depending on the content of the main elements. The results obtained from Electrochemical Impedance Spectroscopy (EIS) and Linear Sweep Voltammetry (LSV) for the barrier ability and the corrosion durability reveal clear corelation between themselves. The quantitative data aqcuired by both EIS and LVA methods applied during exposure from 24 to 672 hours to 3.5% NaCl have shown that the superior corrosion protective characteristsics belong to the Ni-Co-P three-component layer. Besides, both Ni-Co-P and Ni-P alloy coatings preserve their barrier properties during the entire 672 h exposure cycle. For comparison, the Co-P coating was completely broken after 168 hours of exposure to the model corrosive medium.

Key words: nickel-cobalt-phosphorus coatings, morphology, phase composition, corrosion resistance, impedance analysis

INTRODUCTION

The Ni-P based alloy coatings are being largely used in various industrial branches due to their significant mechanical strength, low friction coefficient, and remarkable durability in corrosive media [1, 2]. The main application fields of these coatings are the automobile and the aircraft industry [2]. Furtheremore, these materials are used as electrocatalytic material for hydrogen production by water splitting [3]. The Co-P based compositions are also interesting for potential industrial application, because of their superplastic extensibility [4], superior wear resistance [5, 6], high saturation magnetization and considerable thermal stability [7, 8].

Recently, the Ni-Co-P ternary alloyed coatings became object of intensive research activities [9, 10], because these compositions combine the extended protective capabilities, typical for Ni-P alloys and the specific tribological and magnetic properties owed by the cobalt enriched Co-Ni based materials [9]. In adition, the ternary alloys with 70% of Ni content (15-20%Co, 10-15%P), appear to be a promising alternative of the hard chromate coatings [11, 12].

The electrochemical deposition of all the three types of Ni-P, Co-P and Ni-Co-P coatings could be performed from sulphate [13], modified Watts [10, 14, 15], chloride [14], citrate [16] and sulfamate [2] electrolytes on copper or low carbon steel substrates, predominantly at high temperatures (80-90°C). The correlation between the component composition, the morphological and structural features, possessed by Ni-P, Co-P and Ni-Co-P films by one side, and their resulting protective abilities on the other side, was object of various researchers [1, 6, 10, 13]. Parente [10] has performed an extended research on the thermal treatment impact on the corrosion protective ability of Ni-P and Ni-Co-P, by systematical EIS and LSV measurements. According to various authors [10, 17, 18], the amorphous state enhances the durability of these coatings against corrosion attack. Moreover, the amorphisation in these cases is favoured by the increase of phosphorous content from 7 to 10% [9, 10, 17]. The superior corrosion protective abilities of the amorphous alloys can be explained by the lower interatomic distances (i.e. closed structural packaging), resulting in low density of grain boundaries, dislocations and other surface

---

defects [9, 17]. In this sense, the comparison of Ni-P, Co-P and Ni-Co-P alloy films, deposited at identical conditions (i.e. current density, temperature, pH, etc.) appears as an actual task of considerable interest. Its decision should enable to clarify the role of each coating ingredient on the corrosion protective ability of the resulting ternary Ni-Co-P composition.

The present research aims to compare the characteristics of Ni-P, Co-P and Ni-Co-P, deposited on copper substrates from sulfate-chloride electrolyte, at identical conditions. For this purpose, inherent phase composition, morphology, as well as the resulting barrier ability and durability against corrosion were submitted to elucidation and further analysis.

EXPERIMENTAL

The deposition kinetcs was studied in three-electrode electrochemical cell with 150 dm^3 of volume at thermostatic conditions (80^0C). The working electrode was copper (MERK, 99.97%) disc with surface area of 1 cm^2, insulated by epoxide rubber in plexiglass holder. The counter electrode was a platinum sheet with at least ten times larger surface area. The potentiostatic recording of the polarization dependencies was performed with saturated calomel electrode ($E_{SCE} = 0.241 \div 0.244$ V) as reference, placed in a separate space connected to the cell by Lugin capillary.

The depositions were done in two electrode configuration cell against a platinum electrode in galvanoistatic regime for 40 min. at current density of 65 mA cm^{-2} on copper foil (MERK, 99.97%) electrodes with 2x2 cm of size (4 cm^2). Ni-P, Co-P and Ni-Co-P alloy deposits were obtained by electrodeposition from solution with a similar composition as in [10] at 80^0C, but by replacement of the H_3PO_4 with H_3PO_3 (Table 1) and in the absence of Na_2CO_3, which makes the solution more stable.

Table 1. Basic electrolytes composition (pH = 2)

Coating type	Electrolyte content (in [gmol dm^{-3}])				
	$NiSO_4.6H_2O$	$NiCl_2.H_2O$	$CoSO_4.7H_2O$	NaH_2PO_2	H_3PO_3
Ni-P	0.66	0.20	---------	0.60	0.60
Co-P	---------	---------	0.35	0.60	0.60
Ni-Co-P	0.66	0.20	0.35	0.60	0.60

The respective pH values (pH ≈ 2) were corrected by diluted NaOH or H_2SO_4 aqueous solutions. Immediately prior to these electrochemical procedures, the copper substrates were always submitted to cleaning procedures involving washing with distilled water, etching in a solution containing 40% H_2SO_4 and 30% HNO_3 in a ratio 1:1 (40°C), followed by twice washing in double distilled water. The thickness of the coatings was measured by a non-destructive magnetic-induction method with a caliper of type BB20 of the company BioEviBul.

The coating formation kinetics was evaluated by obtaining of voltammograms, by Wenking (Germany) potentiostat at potential sweep rate of 30 mV s^{-1}. The same device was used for the coating depositions, performed at stationary potentiostatic regime.

The corrosion protective properties of the investigated films were evaluated by two electrochemical methods, independent between themselves: Electrochemical Impedance Spectroscopy (EIS) and Linear Sweep Voltammetry (LSV). These measurements were performed by PG-stat Autolab 30 universal potentiostat/ galvanostat, combined with FRA-2 frequency response analyzer. The samples were mounted in standard (ISO 16773)

three-electrode "flat" cells, which provided exposition of 2 cm^2 working surface of the investigated samples in 100 ml of naturally aerated 3.5% NaCl model corrosive medium. Cylindric platinum net was used as counter electrode and "Metrohm" Ag/AgCl/3M KCl electrode served as reference. The impedance spectra and the LSV polarization curves were recorded after defined time intervals: 24, 168, 336, 504 and 672 hours of exposure to the 3.5% NaCl aqueous solution. The spectra were acquired in frequency range between 10 kHz and 10 mHz, distributed into 50 measuring steps at 10 mV, regarding the Open Circuit Potential (OCP). The anodic LSV curves were recorded in Tafel semi-logarithmic coordinates for the newly deposited coatings. The potential interval was selected to be between -270 до 350 mV in respect to Ag/AgCl/3M KCl electrode, at potential scan rate of 5 mV s^{-1}, so that the measurements included the corrosion potential (E_{corr}) value.

The coating morphology and element composition were defined by Scanning Electron Microscopy (SEM) and Energy Dispersive Spectral Analysis (EDSA), using "Jeol JSM-6390- Oxford Instruments" device. The identification of the crystalline phases was done by X-Ray diffraction analysis (XRD). The respective diffracttograms

were acquired by Philips PW 1050, coupled by secondary graphite monochromator. The acquisitions were performed at Cu Kα radiation source, at 2θ interval, between 10 and 100 angular degrees, at 0.04° scanning step and 1 s. of exposition per step.

RESULTS AND DISCUSSIONS
Deposition kinetics

The film formation kinetics was determined by voltammograms acquisition during deposition of coatings from the electrolytes descrtibed in Table 1, at 80 ℃ (Fig. 1). The figure shows that the Ni-P deposition proceeds at higher polarization (Fig.1, curve 1) compared to this of the Co-P deposition (Fig.1, curve 2). The current densities reached in the case of Co-P deposition were superior to these of Ni-P and Ni-Co-P. This fact is consequence of both of facilitation of cobalt deposition and porous Co-P film formation. The latter fact was evinced by the morphological analysis, commented in the next paragraph.
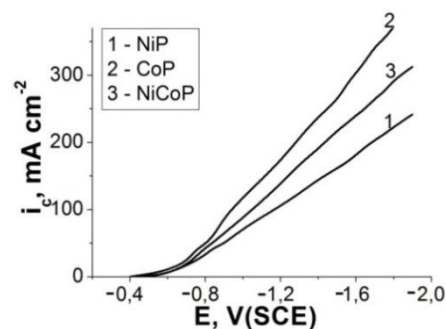
Fig.1. Kinetic curves acquired during deposition of Ni-P (1); Co-P (2) and Ni-Co-P (3) coatings at 80^0C.

Coating morphology and microstructural analysis

The Scanning Electron Microscopy (SEM) has enabled to obtain data about the morphology of the alloy films (Fig.2) deposited galvanostatically at identical conditions of 65 mAcm^{-2} of current density and 40 min. of electrolysis.

(a) 17.5%P - 82.5%Ni   b) 12.6% P – 87.4%Co   (c) 26.1%P – 24.7%Co- 49.2%Ni
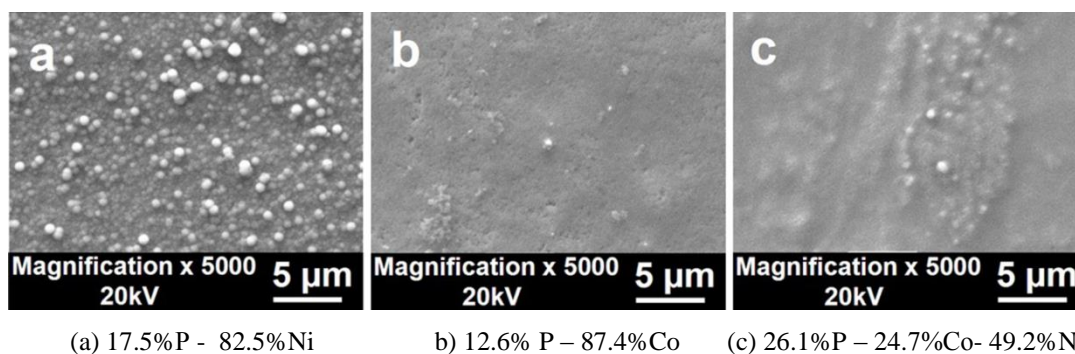
Fig. 2. SEMimagesofNi-P (a), Co-P (b) и Ni-Co-P (c) alloyed coatings, deposited at i = 65 mA cm^{-2} for 40 min, from the electrolytes described in Table 1. (the EDSA data are represented in mass.%).

The SEM images in Fig. 2 reveal that all the coatings possess fine grain crystalline configurations. The Ni-P (Fig. 2a) coatings possess a globular structure, composed by spherical crystals with maximal diameter under 1 μm. The Co-P (Fig. 2b) layers are thin (under 1.2 μm, measured with caliper), fine-crystalline and do not cover completely the entire substrate surface. Their incomplete coverage, as it shown by the data of the EIS and LVA methods, commented in the next section, had generally negative effect on their corrosion protective properties. This effect was also confirmed by the polarization curves, commented in the next section. The ternary Ni-Co-P (Fig. 2c) alloy has fine-crystalline structure, with randomly distributed spherical inclusions. The measured thickness of the coatings was about 6 μm for Ni-P and about 4.5 μm for Ni-Co-P.

The morphological and compositional differences among the investigated double and ternary alloy layers have led to distinguishable phase compositions, as well. It is demonstrated by the XRD patterns, shown in Fig. 3.
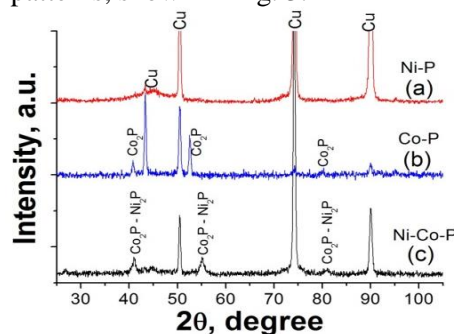
Fig. 3 X-Ray diffractograms of Ni-P (a), Co-P (b) and Ni-Co-P coatings (c).

The peaks of the copper substrate are distinguishable on all the diffractograms, confirming that the obtained coatings are relatively thin (below 10 μm). The resulting diffraction peaks are relatively low and wide but with a clearly identifiable location that was used for identification. The estimated average crystallite size of the individual phases

ranged from 35-40 nm. This gave us reason to explain the resulting coating as a nanosized matrix incorporating very few single crystals with an average crystallite size under 1 μm. This finding is also confirmed by the SEM images taken.

The Ni-P coatings are with definitely amorphous structure observable by the diffusion halo (Fig. 3a). In contrary, the Co-P layers (Fig. 3b), deposited at the conditions, and applied in the present research possess homogeneous, polycrystalline structure, consisted by orthorhombic Co_2P phase, regarding the Inorganic Crystal Structure Database (ICSD ref. code: 98-004-3685). The Ni-Co-P coating (Fig. 3c) is the most interesting one. Practically, this coating possesses variable composition consisted by series of solid solution Ni_2P - Co_2P depending on the content of the main elements. However, the diffractions peaks of both Ni_2P and Co_2P phases are indistinguishable due to the overlapping between them. These peaks were determined according to the reference ICSD data values for: Co_2P ref. code: 98-004-3685; and for Ni_2P - ref. code: 98-002-7162, respectively

Barrier ability and durability evaluation

The use of two electrochemical methods EIS and LSV, which are independent between themselves, has enabled to evaluate both the barrier ability and durability of the investigated Ni-P, Co-P and Ni-Co-P alloyed coatings, deposited on copper substrates. These corrosion protective abilities were additionally determined for Ni-Co alloy film, deposited from the same electrolyte (Table 1), but without phosphorous containing ingredients. This coating was deposited at the same conditions (I = 65 $mAcm^{-2}$ for 40 min.), as the rest ones.

The EIS and LSV electrochemical measurements were performed for extended period – from 24 to 672 hours of exposure to 3.5% NaCl model corrosive medium. Figure 4 represents the Bode and Nyquist plots of the EIS spectra, acquired respectively for: Ni-P (Fig. 4a), Co-P (Fig.4b), Ni-Co-P (Fig. 4c) and Ni-Co (Fig. 4d), during the entire 672 hours of exposure.
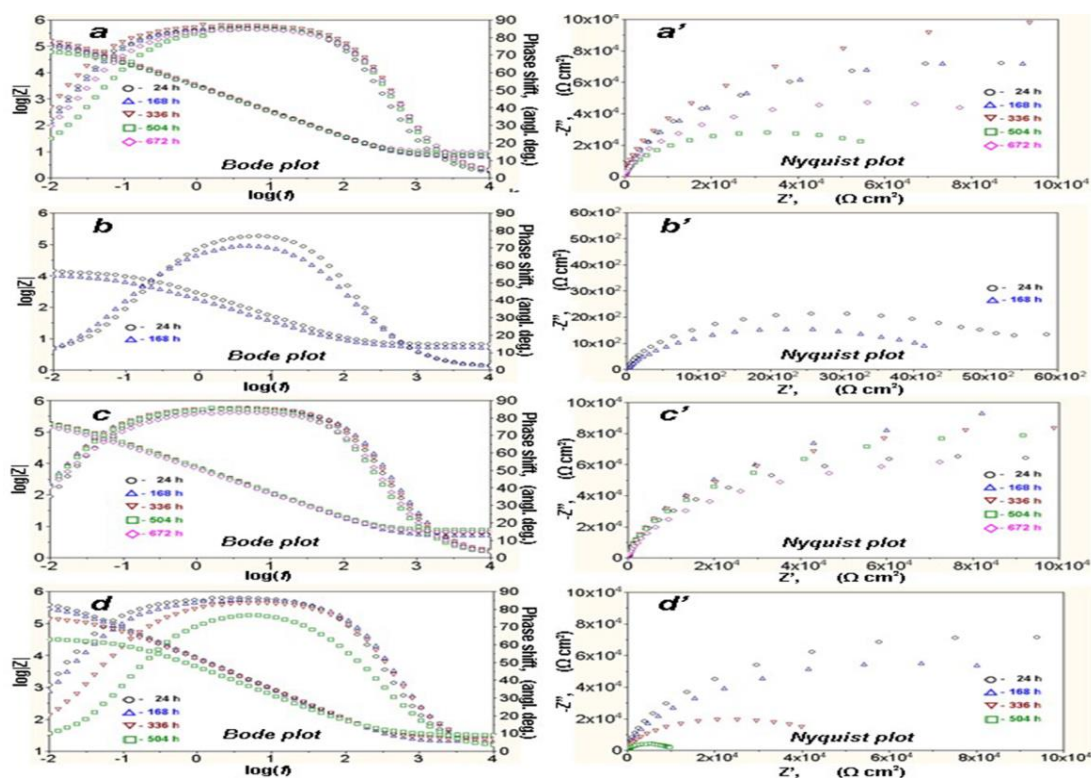
Fig. 4. EIS spectra recorded after different exposure times for: Ni-P (a), Co-P (b), Ni-Co-P (c) and NiCo - (d), represented in Bode (left side) and Nyquist (right side) plots.

On the basis of the comparizon among the Bode plots of the impedance spectra in Fig. 4, recorded for each one of the investigated samples it could be inferred that the Ni-P and Ni-Co-P compositions possess remarkably higher barrier ability than Co-P and Ni-Co ones. The entire orders of magnitude higher impedance modulus at 0.01 Hz, equal to |Z| = $10^{5.5}$ and 10^5 Ω cm^2 for Ni-P and Ni-Co-P, compared

to $|Z| = 10^{3,5}$ Ω cm^2 for Co-P, is indication for the rather superior barrier ability of the former Ni-containing compositions. The Ni-Co coating occupies an intermediate position with $|Z| = 10^{4.5} \div 10^5 \, \Omega$ cm^2.

The phase shift (φ) between the sinusoides of the applied potential and the resulting current density for the Ni-P, Ni-Co-P and Ni-Co reaches 90°, corresponding to almost pure capacitance, whereas for Co-P film, it decreases down to $\varphi \sim 70^0$. This fact is an evidence for the almost pure capacitive character of the electric double layer (EDL) between the model corrosive medium and the Ni-P, Ni-Co-P and Ni-Co coatings, being undoubted evidence for theit nano-sized structures. The exponent „n" values in their cases tend to unit (i.e. 100%) (Table 2). These facts conceive that the EDL resembles the behaviour of almost ideal flat capacitor and consequently, the Ni-P, Ni-Co-P and Ni-Co coatings are smooth and with high crystal distribution homogeneity. The indistinguishable deviations between the real EIS spectra recorded and the respective equivalent circuit serves as an additional evidence for the coating uniformity of the Ni-P, Ni-Co-P and Ni-Co coatings

The Nyquist coordinates presentation of the EIS spectra renders even clearer image for the differences for each specimen and the deterioration of their barrier ability after the respective exposure periods. The highest real (corresponding to the Ohmic resistance), and imaginary (related to the capacitive resistance) impedance values, acquired after 24 hour of exposure [19] belong to the Ni-P coating, followed subsequently by Ni-Co, Ni-Co-P and Co-P. The fitting of the real electrochemical impedance spectra of the investigated samples to spectra of suitable equivalent circuits has allowed defining all the resistances and capacitances occurring in the electrolyte/coating/substrate system. In the present case, the selected equivalent circuit comprised 3.5% NaCl, electrolyte resistance R_{el}, electric charge transfer resistance R_{ct} (including all the cathodic and anodic reactions of the corrosion process), and Constant Phase element CPE (i.e. pseudocapacitance) of the electric double layer on the interface between the coating surface and the 3.5% NaCl solution. The equivalent circuit is shown in Figure 5.

The values determined by the quantitative analysis of the impedance spectra, recorded after 24 hours of exposition (Table 2) reveal that the highest barrier ability is owed by Ni-P and Ni-Co alloys, followed by Ni-Co-P composition, corresponding to

R_{ct} = 300.80, 295.00 and 271.40 kΩ cm^{-2}, respectively. For comparison, the R_{ct} obtained from the Co-P film is by entire order of magnitude lower, reaching 10.82 kΩ cm^{-2}, which results from the incomplete coverage of the surface.
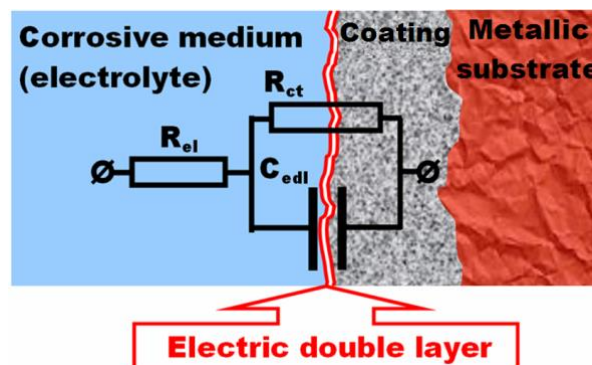
Fig. 5. Equivalent circuit used for EIS data fitting: R_{el} − MCM electrolyte resistance; C_{edl}− electric double layer capacitance; R_{ct}− charge transfer reactions resistance

The comparison of the spectra for Ni-P, Ni-Co-P and Ni-Co coatings, especially in Nyquist coordinates (Fig. 4 a, c, d)) and the R_{ct} data summarized in Table 2 for the respective exposure periods shows that the ternary Ni-Co-P coating possesses the highest durability of the barrier properties, compared to these of Ni-P and Ni-Co coatings. Indeed, both the real and the imaginary impedance components recorded for the entire 672 hours of exposure for Ni-P and especially for Ni-Co decrease more rapidly than for the Ni-Co-P composition. From the R_{ct} data in Table 2, it can be seen that R_{ct} of Ni-Co-P decreases to a lesser degree than for the Ni-P coating. On the other hand, the most remarkable barrier properties deterioration belongs to Ni-Co and Co-P coatings. The former, Ni-Co reaches very low R_{ct} value, equal to only $R_{ct} = 19.36$ kΩ cm^{-2} (Table 2), whereas the latter Co-P layer was completely destroyed after the initial 168 hours of exposure. Negligible R_{ct} increase was detected for the Ni-Co-P, and Ni-P compositions after respectively the 168th and the 336th hour of exposure, instead of the expected decrease. It could be explained assuming corrosion products accumulation, which disturbs the access of the corrosive species towards the coating surfaces [10]. Another explanation for the observed effect is the reported by some authors [9, 10] increase of the phosphorus content of the coating by increasing its thickness. This fact is reflected so in the impedance spectra shapes, so in the respective R_{ct} values.

Table 2. Values of the electrolyte Ohmic resistance R_{el}, the electric double layer pseudocapacitance CPE_{edl} and the charge transfer resistance R_{ct} acquired by the impedance modeling for Ni-P, Co-P, Ni-Co-P and Ni-Co coatings.

SAMPLE: NiP (A)

Hours of exposure	Rel [$\Omega.cm^2$]		CPE_{edl} ($\times 10^{-5}$) [$s^n.\Omega^{-1}.cm^{-2}$]		n [-]		$R_{ct}(\times 10^3)$ [$\Omega.cm^2$]	
	v	E %	v	E %	v	E %	v	E %
24h	19.50	1.07	2.73	0.82	0.96	0.19	300.80	2.13
168h	13.68	0.83	2.66	0.60	0.96	0.14	302.20	1.56
336h	13.44	0.77	2.73	0.54	0.96	0.12	404.40	1.71
504h	14.38	1.43	12.76	1.17	0.95	0.26	121.00	2.04
672h	13.08	1.09	12.82	0.81	0.94	0.19	200.20	1.88

SAMPLE: CoP (B)

Hours of exposure	Rel [$\Omega.cm^2$]		CPE_{edl} ($\times 10^{-5}$) [$s^n.\Omega^{-1}.cm^{-2}$]		n [-]		$R_{ct}(\times 10^3)$ [$\Omega.cm^2$]	
	v	E %	v	E %	v	E %	v	E %
24h	16.06	1.43	11.57	1.78	0.88	0.47	10.82	1.88
168h	7.51	0.99	20.78	1.14	0.84	0.33	8.52	1.45

SAMPLE: NiCoP (C)

Hours of exposure	Rel [$\Omega.cm^2$]		CPE_{edl} ($\times 10^{-6}$) [$s^n.\Omega^{-1}.cm^{-2}$]		n [-]		$R_{ct}(\times 10^3)$ [$\Omega.cm^2$]	
	v	E %	v	E %	v	E %	v	E %
24h	17.16	0.91	31.34	0.69	0.95	0.16	271.40	1.87
168h	14.28	0.82	30.71	0.57	0.95	0.13	390.00	1.97
336h	15.96	0.73	31.45	0.53	0.95	0.13	346.00	1.69
504h	21.80	0.87	32.84	0.67	0.95	0.17	323.60	2.11
672h	18.74	1.28	37.47	0.97	0.93	0.24	246.80	2.85

SAMPLE: NiCo (D)

Hours of exposure	Rel [$\Omega.cm^2$]		CPE_{edl} ($\times 10^{-6}$) [$s^n.\Omega^{-1}.cm^{-2}$]		n [-]		$R_{ct}(\times 10^3)$ [$\Omega.cm^2$]	
	v	E %	v	E %	v	E %	v	E %
24h	16.78	0.73	33.60	0.56	0.96	0.13	295.00	1.65
168h	13.32	1.15	33.97	0.85	0.95	0.20	230.40	2.18
336h	14.10	1.27	40.24	1.07	0.93	0.25	86.60	1.81
504h	19.90	0.75	74.65	0.83	0.87	0.21	19.36	0.94
672h	-	-	-	-	-	-	-	-

The application of LSV as an electrochemical method, alternative to EIS and the further Tafel slope analysis data have enabled to acquire supplemental data about the corrosion protective abilities of the films on the basis of the corrosion potential E_{corr} and the polarization resistance R_p values (Table 3).

The anodic polarization curve shapes (Fig. 6, a-d) and the data in Table 3 confirm the statement for the higher barrier ability of the Ni-P (Fig. 6a) and Ni-Co-P (Fig. 6c), in comparison to this of the Ni-Co (Fig. 6d) and Co-P (Fig. 6b).

Table 3. Data for the corrosion potential, E_{corr}, [mV] vs. Ag/AgCl and the polarization resistance R_p, [kΩcm^2] determined by the anodic (Tafel) polarization curves for different periods of exposure of the investigated samples to the model corrosive medium

Exposuret ime	Ni-P (A)		Co-P (B)		Ni-Co-P (C)		Ni-Co (D)	
	E_{corr}, mV	R_p, kΩcm^2	E_{corr}, mV	R_p, kΩcm^2	E_{corr}, mV	R_p, Ωcm^2	E_{corr}, mV	R_p, kΩcm^2
24 h	-266	147.28	-208.0	10.24	-246.0	231.00	-223	372.00
168 h	-258	302.60	-189.0	9.30	-321.0	378.80	-199	224.40
336 h	-257	289.40	corrosion	corrosion	-213.0	601.00	-215	80.56
504 h	-180	101.48	corrosion	corrosion	-186.0	223.20	-169	16.30
672 h	-230	194.42	corrosion	corrosion	-173.0	267.80	corrosion	corrosion
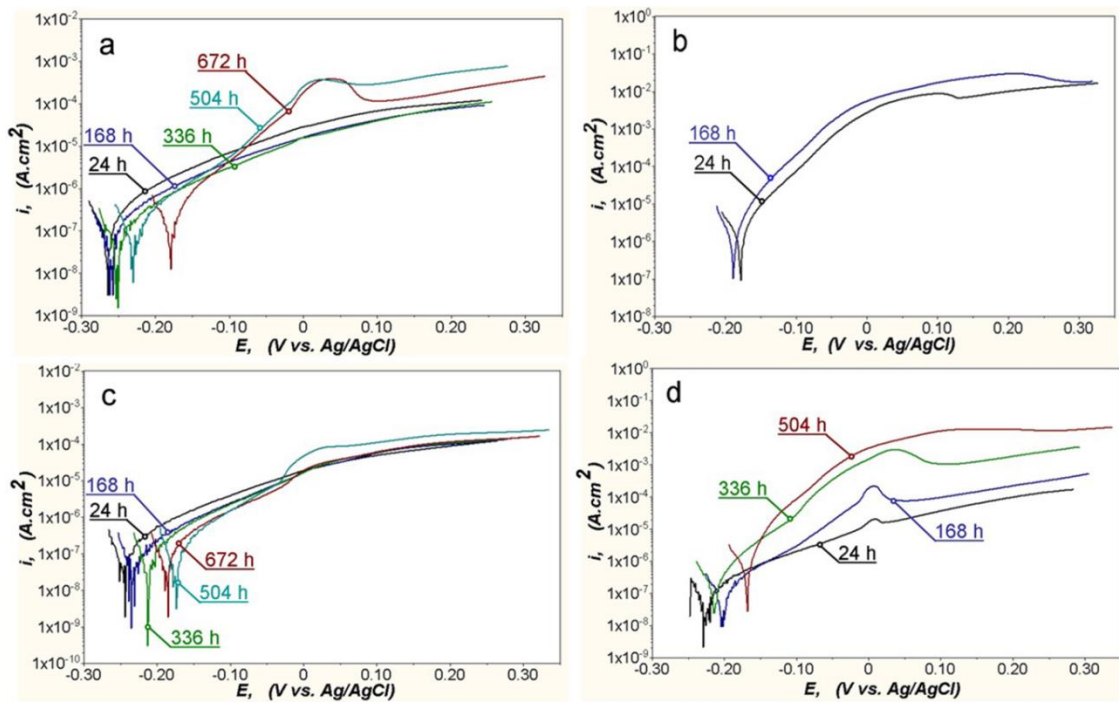
Fig. 6. Anodic polarization curves, recorded during the entire 672 hours of exposure for Ni-P (a), Co-P (b), Ni-Co-P (c) and Ni-Co (d) coatings

Weak current density change within the anodic polarization for Ni-P and Ni-Co-P was observed until the 336th hour of exposition. Afterwards, at 504 hours of exposure, the respective curves change sharply their shape. The dissolution current rises and passes through a maximum at about 0.025 V. Such current increase was observed for the Ni-Co composition after 168 hours of exposure. The occurrence of the observed maxima in the anodic curves can be explained by corrosion products accumulation. In the case of the Ni-P film, these maxima are more sharp (Fig. 6a), due probably to the denser strtucture of the respective corrosion products, compared to this of the Ni-Co-P coating (Фиг. 6c). Literature data exixst [20, 21] which report that the active Ni-P dissolution leads to phosphorous heaping, as a result of selective Ni-dissolution during anodic polarization. Simultaneously, Ni$_3$(PO$_4$)$_2$ film

formation proceeds, contributing as a barrier against further dissolution. That is why, the Ni-Co-P ternary film has revealed the highest R_p values during the entire exposure period (Table 3), compared to Ni-P and especially to Co-P. In the case of Ni-Co coating, the R_p were high only at the initial 24 hours of exposure, and afterwards, these values decrease sharply.

The R_p values measured for all the investigated compositions (Table 3) follow the same trend, as the respective R_{ct} (Table 2), obtained by the impedance modeling. Because the R_p includes both R_{ct} and the oxide layer resistance R_{oxy} (i.e. $R_p \approx R_{ct} + R_{oxy}$) [22], it could be assumed that the anomalous R_p rise for the ternary Ni-Co-P coating (Table 3) after 336 hours of exposure, up to 601.00 kΩcm^2 is a result of both increasing the phosphorus content with the thickness of the film [9,10] and the formation of an oxidation film.

CONCLUSIONS

The Ni-P, Co-P and Ni-Co-P alloy films, deposited at identical conditions at galvanostatic regime, possess different crystal structure, phase composition and corrosion resistance. It was found:

(1) The estimated from the XRD patterns average crystallite size of the individual phases for all coatings ranged from 35 to 40 nm, i.e. the resulting coatings are nanosized matrix incorporating very few single crystals with an average crystallite size under 1 μm.

(2) The Ni-P coatings (17.5%P - 82.5%Ni) are typically amorphous and possess a globular structure.

(3) The Co-P layers (12.6% P – 87.4%Co) are thin (under 1.2 μm) and do not cover completely the entire substrate surface. They consist of orthorhombic Co_2P phase.

(4) The ternary Ni-Co-P alloy (26.1%P – 24.7%Co- 49.2%Ni) possesses variable composition consisted by series of solid solution Ni_2P - Co_2P.

(5) The quantitative analysis of the impedance spectra, together with the respective anodic LSV polarization curves have revealed that the highest barrier ability and corrosion resistance belong to the Ni-Co-P three-component layer.

REFERENCES

1. M. Crobu, A. Scorciapino, B. Elsener, A. Rossi, *Electrochim. Acta*, **53**, 3364 (2008)
2. P. Cojocaru, L. Magagnin, E. Gomez, E. Valles, *J. Alloys Compd*, **503**, 454 (2010).
3. R.K. Shervedani, A. Lasia, *J. Electrochem. Soc.*, **144**, 511(1997).
4. N.M. Alanazi, A.M. El-Sherik, S. H. Alamar and Sh. Shen, *Int. J. Electrochem. Science*, **8**, 10350 (2013).
5. J.L. Crea, *Surf. Eng.*, **26**, 149 (2010).
6. H. Jung, A. Ajfanazi, *Electrochim. Acta*, **51**, 1806 (2006).
7. Lucas I., L.Perez, C. Aroca, P. Sanchez, E. Lopez, M. C. Samchez, *J. Magn. & Magnet. Mater.*, **290-291**, 1513 (2005).
8. G. Hibbard, K.T.Aust, G. Palumbo, *U. Erb, Scripta Mater.*, **44**, 513 (2001).
9. C. Ma, S. Wang, F. C. Walsh, review, Transactions of the IME, *Internat. J. Surf. Eng. Coat.*, **93**, 275 (2015).
10. M.M.V. Parente, O.R. Mattos, S.L. Diaz, P.L. Neto, F.J.F. Miranda, *J. Appl. Electrochem.*, **31**, 677 (2001).
11. R.A. Prado, D. Facchini, N. Mahalanobis, F. Gonzalez, G. Palumbo, 2009 DoD Corrosion Conference, NAVAIR Public Release 09-776, 1-13 (2009).
12. C. Ma, S. Wang, F. C. Walsh, *Transactions of the IME*, **93**, 1, 8 (2015).
13. K. S. Lew, M. Raja, S. Thanikaikarasan, T. Kim, Y. D. Kim, T. Mahalingam, *Mater. Chem. Phys.*, **112**, 249 (2008).
14. J. Ahmad, K. Asami, A. Takeuchi, D.V. Louzquine, A. Inoue, *Materials Transactions*, **44**, 911 (2003).
15. S. S. Djokic, *J. Electrochem. Soc.*, **146**, 1824 (1999).
16. T. Morikawa, T. Nakade, M. Yokoi, Y. Fukumoto and C. Iwakura, *Electrochim. Acta*, **42**,115 (1997).
17. R. Raicheff, V. Zaprjanova, *J. Mater. Sci. Lett.*, **19**, 3 (2000).
18. F. Zhaoheng, *Trans. Nonferrous Met. Soc. China*, **7**, 148 (1997).
19. B.A. Boukamp, *Solid State Ionics*, **18-19**, 136 (1986).
20. H. Habazaki, S.Q. Ding, A. Kawashima, K. Asami, K. Hashimoto, A. Inoue, T. Masumoto, *Corros. Sci.*, 29, 1319 (1989).
21. S.J. Splinter, R. Rofagha, N. S. McIntyre, U. Erb, *Surf. Interface Anal.*, **24**, 181 (1996).
22. E.A. Matter, S. Kozhukharov, M. Machkova, V. Kozhukharov, *Mater. Corros.*, **64**, 408 (2013).

СТРУКТУРА И КОРОЗИОННА УСТОЙЧИВОСТ НА Ni-P, Co-P И Ni-Co-P СПЛАВНИ ПОКРИТИЯ

Катя Н. Игнатова[1], Стефан В. Кожухаров[1], Георги В. Авдеев[2], ИскраАт. Пироева[1]

[1] *Химикотехнологичен и металургичен университет, бул. "Климент Охридски" 8, 1756 София, България*
[2] *Институт по физикохимия „Ростислав Каишев", Българска академия на науките, ул. "Акад. Георги Бончев" бул. 11, 1113 София, България*

(Резюме)

Настоящата статия докладва резултатите от систематичното охарактеризиране на морфологията, фазовия състав, бариерната способност и корозионната устойчивост на Ni-P, Co-P и Ni-Co P покрития върху мед. Изследваните покрития са отлагани галваностатично при съпоставими условия от сулфатно-хлориден електролит с pH = 2 при 80°C. SEM анализът установи, че получените покрития са наноразмерни с фино кристална структура, потвърдена и от резултатите на XRD анализа. Резултатите отXRD анализа показаха, че Ni-P сплавни покрития са с типично аморфна структура, докато Co-P покрития са с хомогенна поликристална структура, съставена от орторомбична Co 2 P фаза. Ni-Co- P покрития са с различен фазов състав в зависимост от съдържанието на основните елементи, представляващ серия от твърди разтвори Ni$_2$P –Co$_2$P. Данните от методите на импедансната спектроскопия (EIS) и на линейната волтамперометрия (LSV) за бариерната способност и корозионната устойчивост на изследваните покрития са в пълна корелация. Количествените данни от двата метода, получени за интервал на престояване на покритията от 24 до 672 часа в 3.5% NaCl показаха, че най-добри защитни характеристики има тройната сплав Ni-Co-P. Освен това Ni-Co-P и Ni-P сплавни покрития запазват бариерната си способност за цялото време от 672 h на престояване в разтвора. Co-P покрития напълно се разрушават след 168 часа престояване в моделната корозионна среда.

Ключовидуми: Ni-Co- P, сплавни покрития, морфология, фазов състав, корозия, импедансен метод

Corrosion behavior in model solutions of steels suggested as construction materials for mining industries

D. I. Ivanova*, G. P. Ilieva, L. B. Fachikov

University of Chemical Technology and Metallurgy, 8 "Kliment Ohridski" Blvd., 1756 Sofia, Bulgaria

A comparative study concerning corrosion behaviours of two steels suggested as construction materials in mining industries have been carried out. Samples of widely used carbon steel st.25 and the new conceived, low-alloyed, steel KP-355 (0.96 % Cr, 0.36 % Cu) have been tested. The tests have been held in model media containing the main aggressive components appearing in real mining waste waters. The main parameters characterizing the mechanical and corrosion-electrochemical behaviour of the tested materials have been determined by physical and electrochemical methods. It has been estimated that the steel KP-355 exhibited better mechanical strength behaviour and higher corrosion resistance in all media used in the tests.

Key words: corrosion, carbon and low-alloyed steels, mine waters.

INTRODUCTION

The working conditions in mines are characterized by high aggressive behaviour of underground waters and gases with respect to the metallic equipment used. The aggressive components in such media are mainly dissolved salts, dominantly chlorides and sulphates and to some extent nitrates and carbonates and dissolved gases (mainly oxygen). In addition, contaminants such as mechanical pollutants, animal and plant related microorganisms also are present. The quantities and type of all aforementioned contaminants is mainly dependent on the soil content, temperatures and flow rates of underground waters. The underground waters are mainly neutral or close to this state, but there are also with acid and basic reaction behaviours [1-4].

The mining atmospheres are characterized with high humidity and contain dangerous contaminants related to the corrosion aggression such as sulphur oxides, hydrogen sulphide, carbon and nitrogen oxides, etc. Moreover, solid particles (such as corrosion active salts NaCl, Na_2SO_4; various natural adsorbents; inert sands and product of blasts) are also present in both gases and waters in mining environments. Most of these contaminants are natural (depending on the soil content) whereas others are results of detonates and other mining operations [2-3].

The alloying components used in the low-alloyed steels are related to enhancement of their mechanical characteristics. In this context, replace the carbon steels when elements of equipment working under high mechanical loads are at issue or low-weight parts are needed. Moreover, carbon steels alloyed by copper (0.2-0.8 %) or by copper and chrome (1-2 %), with high corrosion resistances are of primary practical importance. They are well applicable in metal constructions with welded parts, working in environments of sea waters, high mineralized industrial wastewaters, etc. [5-9].

The corrosion of carbon and low-alloyed steels in mine waters or model solutions is intensively studied. The corrosion kinetics in aerated, neutral solutions of chlorides ($Cl^- > 1.5$ %) has been investigated by electrochemical methods [10, 11], whereas the impedance method has been applied in [12].

The corrosion behaviour of low-alloyed steels in mining waters and in в 3 % NaCl solutions (with flow rate of 2 m s^{-1} at 20-55ºC) has been studied in [13]. It has been estimated that in mining waters the main corrosion products are α-FeOOH, γ-FeOOH and Fe_3O_4, whereas in the chloride solution they are - α-FeOOH, β-FeOOH, α-Fe_2O_3 γ-FeOOH.

In this work results on corrosion behaviour of two steels suggested for metal mining propping is reported. Samples of widely used carbon steel st.25 and a newly suggested KP-355 have been tested in model solutions containing the principle components of mining waters.

EXPERIMENTAL

Materials tested

The test runs were carried out with simples prepared from channel shaped profiles of st.25 and KP-355. The chemical composition is listed in Table 1. The data summarized reveal that KP-355 has

---

* To whom all correspondence should be sent.
E-mail: dimkaivanova@uctm.edu

Table 1. Chemical composition and mechanical characteristics of steels tested

Characteristics	Steels	
	KP-355	st. 25
1. Content, %		
- C	0.19	0.23
- Mn	0.65	0.54
- Si	0.4	0.4
- Cr	0.96	0.06
- Ni	0.15	0.07
- Cu	0.36	0.13
- S	0.02	0.04
- P	0.014	0.013
2. Mechanical characteristics		
- yield strength limit $R_{e, 0.2}$, MPa	427	324
-ultimate tensile strength R_m, MPa	588	503
- relative elongation A_5, %	28	30
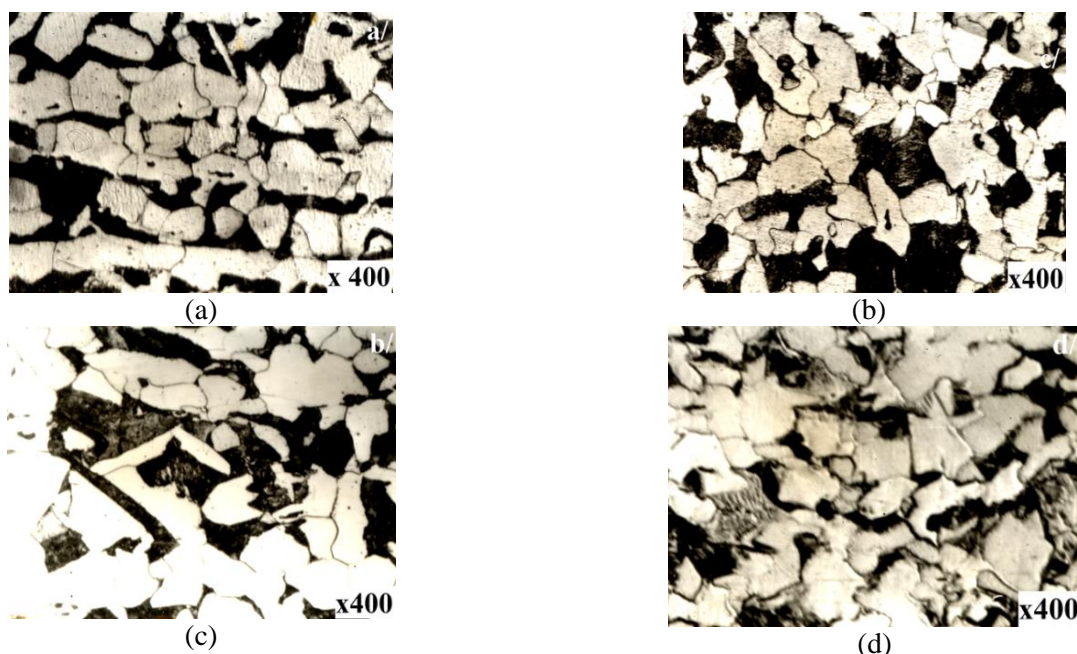
Fig. 1 Microstructures of the steels tested: a/ – st.25, c/ – KP-355: in the hot rolling state; b/ – st. 25, d/ – KP-355: in the hot rolling state and additional 10 % deformation by strain.

greater content of chrome and copper and higher tensile strength and yield strengths, then the classical steel st.25.

The microstructures of the steels have been investigated by observations of simples prepared along the direction of rolling, using a metallographic microscope NEOPHOTE-2. The photos in Fig. 1 show the microstructures of the steels tested produced by hot rolling and after 10 % additional plastic deformation by strain. The latter is almost the same as the deformation occurring during cold deformation of the beams when they are bended. The target is to obtain a material with almost equal content but with changes in the microstructure almost close to the ones of real materials. The photos reveal that the microstructure of both steels are almost identical, i.e. ferrite-perlite. The microstructure of st.25 has well defined strips along the direction of rolling but this effect commonly happens accidentally and cannot be related to a specific type of steel.

The changes after the additional plastic deformation in the steel microstructures are mainly in the elongations of the ferrite grains in the direction of the applied load but without any significant differences between both steels tested.

Methods, samples, model solutions and methodology of corrosion tests
Polarization methods

These methods use potentiostatic devices and are convenient for electrochemical and corrosion investigations. They allow studying actually all real relationships between the potential and the rate of the electrochemical reaction (the current density). The polarization curves, obtained by potentiostatic or potentiodynamic methods, allow many corrosion and electrochemical parameters such as E_{corr} and i_{corr}) to be estimated. In addition, such tests allow the parameters of the passive state to be determined, too. A potentiostat-galvanostat PAR 273 was used in this study.

The tests were carried out in a conventional three-electrode, spatially separated, electrochemical cell with a platinum plate ($S=2.5$ cm^2) as counter-electrode. In order to avoid the transport of chloride ions from the reference electrode into the cell volume, the salt bridge was filled with the working solution.

The shape of the tested samples is cylindrical with working surface area of 0.5 cm^2. The electrodes are insulated by means of polymeric material (duracryle). The preparation of the samples includes: cleaning with glass paper № 220÷600, rinsing with distilled water and drying/degreasing with alcohol-ether mixture.

Model solutions

• 5 % H$_2$SO$_4$, prepared from acid (pa) and monodistilled water;

• 5 % HCl, prepared from acid (pa) and monodistilled water;

• Artificial see water solution with the following content: NaCl – 26.52 g l^{-1}; MgCl$_2$ – 2.45 g l^{-1}; MgSO$_4$ – 3.3 g l^{-1}; CaCl$_2$ – 1.14 g l^{-1}; KCl – 0.73 g l^{-1}; NaHCO$_3$ – 0.2 g l^{-1}; NaBr – 0.08 g l^{-1}, prepared from chemicals (pa) and monodistilled water;

• Solutions with various concentrations of the sulphate ions, prepared from Na$_2$SO$_4$ (pa) and monodistilled water. The concentrations of SO$_4^{2-}$ were: 100 mg l^{-1}, 500 mg l^{-1} and 2500 mg l^{-1}. The pH of these solutions was varied within the range 3.0 – 9.0 by addition of either concentrated H$_2$SO$_4$, (pa) or NaOH, (pa).

Test protocol

The initially prepared sample (electrode) was mounted in the compartment of the working electrode in a way that the distance between it and the Haber-Luggin capillary to be about 1 mm. The counter electrode (Pt) and the bridge of the calomel reference electrode (SCE) were correctly placed in the other cell compartment.

At the beginning, prior to the records of the polarization curves, additional cathodic treatment of the sample at a potential of -1200 mV (SCE) for 1

min was carried out. After that, the potential shifts in the positive direction with a sweep rate 50 mV min^{-1}.

The polarization curves allow determining the following corrosion-electrochemical parameters, among them: corrosion potential (E_{corr}), corrosion current density (i_{corr}), Tafel slopes of the anodic (b_a) and cathodic (b_k) curves, and the parameters of passive state such as critical potential, E_{cr}; critical current density, i_{cr}; passive potential, E_p and passive current density, i_p, and the transpassive potential E_{tp}.

RESULTS AND DISCUSSIONS
Tests in 5 % H$_2$SO$_4$ solutions

The results presented in Fig. 2 are potentiodynamic polarization relation-ships E, V – lg i, A dm^{-2} of st.25 and KP-355 in 5 % H$_2$SO$_4$ solutions obtained with a potential sweep rate of 50 mV min^{-1}. The main corrosion-electrochemical parameters are summarized in Table 2. The corrosion potential E_{corr} of KP-355 steel is -520 mV, SCE and it is more positive that the one corresponding to st.25 steel (with higher carbon content), a fact that could be attributed mainly to the chrome content as alloying element.
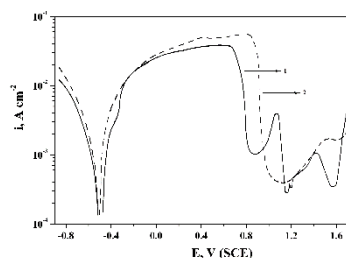
Fig. 2. Potentiodynamic polarization curves E, V – i, A cm^{-2}, developed in 5 % H$_2$SO$_4$ solutions at 25°C, and non-deformed samples: (1) – KP-355; (2) – st.25.

The corrosion rate of st.25, represented by current density (1.2×10^{-3} A cm^{-2}) is several times higher than the corrosion rate of KP-355 which could be explained by the lower carbon content and the alloyng chrome and copper in KP-355 steel.

Table 2. Corrosion-electrochemical parameters for both steels in 5 % H$_2$SO$_4$, 25°C

Parameters	KP-355	st. 25
E_{corr} (SCE), mV	-520	-540
i_{corr}, A cm^{-2}	5.6×10^{-4}	1.2×10^{-3}
b_k, mV dec^{-1}	120	125
b_a, mV dec^{-1}	50	50
E_{cr} (SCE), mV	630	790
i_{cr}, A cm^{-2}	1.6×10^{-1}	2.8×10^{-1}
E_p (SCE), mV	770	950
i_p, A cm^{-2}	2.6×10^{-3}	9.8×10^{-4}
E_{tp}, mV	1500	1690
ΔE_p, mV	740	510

The values of E_{cr} and i_{cr} characterizing the transition of the steels into the passive states indicate that these parameters are not so favorable for the st.25 samples (considering the transition into the complete passive state) due to the more-positive critical potential and higher critical current density. Both steels tested demonstrate big differences in the passive states. For the st.25 samples, the passive current i_p remained almost constant (9.8×10^{-4}A cm^{-2}), while with the KP-355 sample specific peaks were observed. The later could be related to the presence of chrome as alloying element. The Tafel slopes of the cathodic (b_k) and anodic (b_a) polarization curves are almost equal for both steels. This actually indicates that the mechanisms of the cathodic reactions (hydrogen evolution) as well as the anodic dissolution are identical for both steels.

The effect of the 10 % cold plastic deformation on the polarization relationships in 5 % H_2SO_4 solutions are shown in Fig. 3. The comparison between the corrosion-electrochemical parameters of both steels in the deformed states reveals that the 10 % cold plastic deformation does not change significantly the main parameters with respect the ones obtained with no-deformed samples. Precisely, this comment refers to: more-positive corrosion potential (E_{corr}) and lower corrosion current density (i_{corr}) for the KP-355 steel and consequently easier transition into the passive state, while the passive state of st.25 is more stable.

The most important difference observed in the characteristics of the deformed and non-deformed samples is in the pre-passive and passive states. The plastic deformation leads to more negative critical potentials E_{cr}, that is the passive states appears earlier, but the critical current densities i_c in such situations are greater. Moreover, the plastic deformation enlarges the area of complete passive state and reduces the current density i_p, A cm^{-2} (see Fig. 2 and Fig. 3).

Tests in 5 % HCl solutions

The corrosion-electrochemical characteristics of the steels tested in 5 % HCl solutions determined by means of the polarization relationships in semi-logarithmic scale E, V – lg i, A cm^{-2} are summarized in Table 3. The potentiodynamic polarization curves for both steels in the deformed states are shown in Fig. 4.
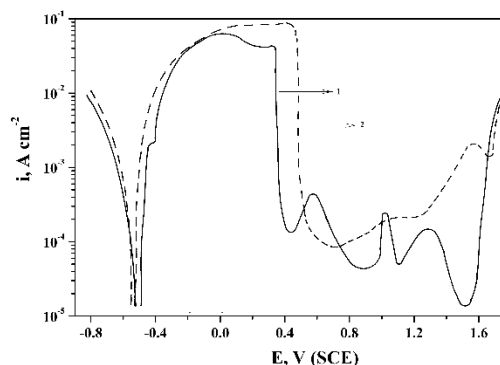
Fig. 3. Potentiodynamic polarization curves E, V – i, A cm^{-2} obtained in 5 % H_2SO_4 solutions at 25°C and 10 % elongations of the steel samples:(1) – KP-355; (2) – st.25.
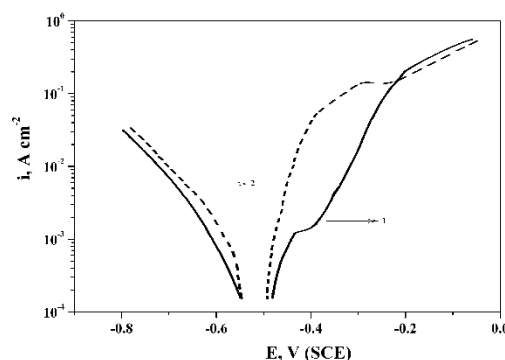
Fig. 4. Potentiodynamic polarization relationships E, V – i, A cm-2, obtained in 5 % HCl solutions at, 25oC, with 10 % elongations of the steel samples: (1) – KP-355; (2) – st.25.

The corrosion rate (i_{corr}) for st.25 in these media is of about 1.7×10^{-4}A cm^{-2} and this value is significantly higher (one order higher) than the corrosion rate of KP-355 steel. In the solutions of 5 % HCl, as well as in the model media with sulphur acid content, the corrosion potential (E_{corr}) is more-positive for the KP-355 steel that could be attributed to the copper and chrome as alloying components.

The cathodic reaction and the anodic dissolution of both steels have identical mechanisms, a standpoint supported by almost equal values of the Tafel slopes b_k and b_a.

Table 3 Corrosion-electrochemical parameters for both steels with and without 10 % cold plastic deformation, in 5 % HCl, 25°C

Parameters	Undeformed steel		10 % cold deformation	
	KP-355	*st. 25*	*KP-355*	*st. 25*
E_{corr} *(SCE), mV*	-370	-460	-450	-455
i_{corr}*, A cm^{-2}*	1.7×10^{-5}	1.7×10^{-4}	1.6×10^{-4}	3×10^{-4}
b_k*, mV dec^{-1}*	70	80	110	100
b_a*, mV dec^{-1}*	40	40	55	50

The cold plastic deformation does not change the corrosion-electrochemical parameters and their behaviour is similar to that in absence of deformation. However, the additional introduced energy and the effect on the steel heterogeneity leads to increased corrosion rates for both steels, mainly for KP-355, where the value of i_{corr} raises about 10 times.

Tests in artificial sea water solutions

In the corrosion process of both st.25 and KP-355 samples in artificial sea water oxygen depolarization take place as it well demonstrated by the polarization curves shown in Fig. 5. The parameters characterizing the corrosion behaviour are summarized in Table 6. The parameter values indicate that the dissolution rate of st.25 is higher than the one of KP-355. However, both dissolution rates are significantly lower in comparison with the ones observed in *HCl* and *H₂SO₄* media.

In this model solution the corrosion potential of KP-355 is more positive (with about 100 mV) with respect to the corrosion potential of st.25. The comparison of the corrosion-electrochemical parameters (see Table 4), reveals that the cold plastic
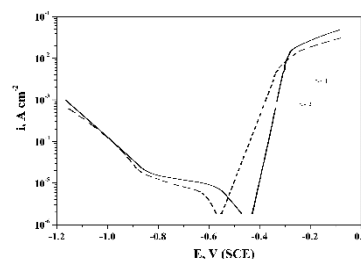
Fig. 5. Potentiodynamic polarization relationships E, V – i, A cm^{-2}, obtained in artificial sea water: (1) – KP-355; (2) – st.25.

deformation does not increase the corrosion rate in contrast to the case when the tests performed in *HCl* and *H₂SO₄* media, but significantly reduces it. Moreover, the deformation shifts the corrosion potential of st.25 in the positive direction and makes it closer to corrosion potential of KP-355.

Tests is aqueous sulphate solutions

The tests with KP-355 samples, following the same methodology, produce polarization curves shown in Fig. 6.

Table 4 Corrosion-electrochemical parameters for both steels, in artificial marine water, 25°C

Parameters	Undeformed steel		10 % cold plastic deformation	
	KP-355	*st. 25*	*KP-355*	*st. 25*
E_{corr} *(SCE), mV*	-520	-620	-510	-525
i_{corr}*, A cm^{-2}*	3_x10^{-6}	4.6_x10^{-6}	8_x10^{-8}	1.2_x10^{-7}
i_d*, A cm^{-2}*	2.2_x10^{-5}	1.8_x10^{-5}	5_x10^{-7}	5_x10^{-7}
b_a*, mV dec^{-1}*	40	45	45	50

Table 5. Corrosion-electrochemical parameters of steel KP-355 in solutions with various concentrations of sulphate ions and various pH at 25°C

[SO_4^{2-}] mg l^{-1}	pH	E_{corr}, mV (SCE)	i_{corr}, A cm^{-2}	i_d, A cm^{-2}	b_a, mV dec^{-1}
	3	-555	2_x10^{-5}	10_x10^{-5}	50
	4.5	-300	1.88_x10^{-6}	2.6_x10^{-5}	55
100	5.5	-310	2_x10^{-6}	16_x10^{-6}	60
	7.5	-340	1.3_x10^{-6}	10.2_x10^{-6}	70
	9	-400	1.1_x10^{-6}	2_x10^{-6}	90
	3	-590	1.3_x10^{-5}	7_x10^{-5}	30
	4.5	-360	9_x10^{-6}	3_x10^{-5}	55
500	5.5	-380	5_x10^{-6}	16_x10^{-6}	58
	7.5	-400	5_x10^{-6}	2.4_x10^{-5}	70
	9	-460	2.5_x10^{-6}	6_x10^{-6}	70
	3	-600	6.6_x10^{-6}	7_x10^{-5}	29
	4.5	-460	2.4_x10^{-6}	5_x10^{-6}	39
2500	5.5	-410	2_x10^{-6}	9_x10^{-6}	39
	7.5	-475	2_x10^{-6}	4.6_x10^{-6}	40
	9	-450	1.8_x10^{-6}	5.8_x10^{-6}	55

These relationships were taken at concentration $C_{SO_4^{-2}} = 100 \, mg \, l^{-1}$ and pH in the range of 3.0 – 9.0. The plots reveal that the cathodic depolarization reaction is oxygen reduction with well-shaped oxygen levels (steps). The main parameters characterizing the corrosion of the steel tested are summarized in Table 5.
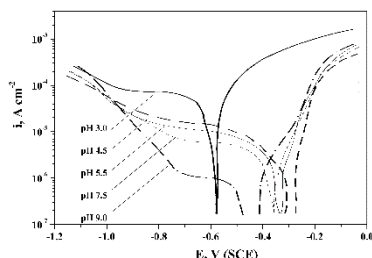
Fig. 6. Potentiodynamic polarization relationships E, V – i, A cm^{-2} of KP-355 in sulphate solutions. Concentration of SO$_4^{2-}$=100 mg l^{-1} and pH 3.0-9.0 at 25°C

The change in the corrosion potential E$_{corr}$ with variations of pH, within the rage of concentration variations are shown in Fig. 7. The values of the potentials shifts sharply from more negative (at pH=3.0) towards more positive but for pH beyond 5.0 there is a weak change in the negative direction. The plots indicate that the largest amplitude of E$_{corr}$ appears in low-concentrated solutions (100 mg l^{-1}).
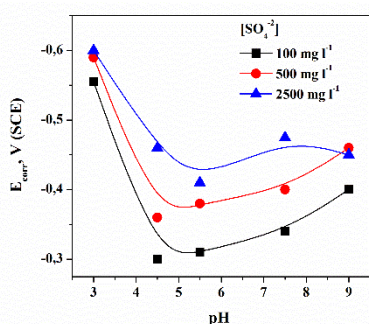
Fig. 7. Relationship E$_{corr}$=f(pH) at various concentrations of SO$_4^{2-}$ at 25°C.

Fig. 8 illustrates the relationship between the rates of the corrosion processes represented by the current density (i$_{corr}$) as a function of the solution pH as independent variable. These plots clearly demonstrate that with increase in pH the corrosion rate initially decreases rapidly from the area of the weak (low-concentrated) solutions (pH 3.0) toward the neutral and remains almost unchanged towards the range with pH 9.0. This relationship of the corrosion rate as function of pH (beyond pH 4.5) could be explained by the fact that the cathodic depolarization reaction is oxygen reduction rather than (especially at high pH) water reduction, where corrosion rate increase with increase in the value of pH.
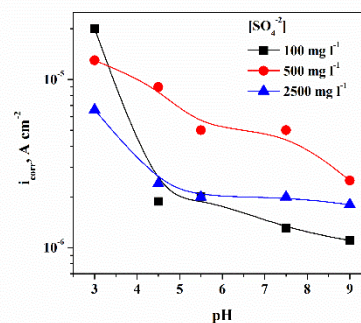
Fig.8. Relationship i$_{corr}$=f(pH) at various concentrations of SO$_4^{2-}$ at 25°C.

CONCLUSIONS

The results obtained from the corrosion test with st.25 and KP-355 samples could be outlined as:

1. In model solutions of 5 % H$_2$SO$_4$ the corrosion rate of st.25 is about two times higher than that of KP-355 alloyed by 0.96 % Cr and 0.36 % Cu. The registered more negative potential and the lower critical current density of KP-355 reveal that this steel demonstrate higher ability to be passive in sulphur acid media in comparison with the behaviour of st.25.

2. In model solutions of 5 % HCl the samples of st.25 dissolute more intensively with a rate of about one order of magnitude more (i$_{corr}$ = 1.7$_x$10^{-4} A cm^{-2}) with respect to KP-355 where i$_{corr}$ = 1.7$_x$10^{-5} A cm^{-2}.

3. The corrosion rate of KP-355 steel in artificial sea water is about two times slower than the corrosion rate of st.25.

4. The corrosion potentials (E$_{corr}$) of KP-355 steel in all model solutions are more positive with respect to the corrosion potentials of st.25 and this indicates better corrosion behaviour of KP-355 in aggressive media.

5. It was established that the dissolution rate i$_{corr}$ for both steels tested increases after additional 10 % cold plastic deformation. This effect is stronger with samples of KP-355.

6. It was estimated the effect of concentration of SO$_4^{2-}$ (100; 500 and 2500 mg l^{-1}) and pH (3.0 ÷ 9.0) of Na$_2$SO$_4$ solutions on the corrosion behaviour of KP-355 steel. The corrosion rate, irrespective of the solution concentrations, reduces rapidly from the area of weak acid solutions towards the neutral ones and remains unchanged up to pH=9.0. The shift of E$_{corr}$ in the positive direction with increase in pH is more pronounced in the weak (low-concentrated) solutions.

REFERENCES

1. Gurdeep Singh, *Int. j. of mine waters*, **5**, 21 (1986).
2. Parlapanski M., Koroziai zashtita na sarorageniata w kamenovaglenite rudnici u nas, *Nauka*, 1988.
3. Mishra B, Pak J., *ASM Handbook* Volume **13C,** *Corrosion: Environments and Industries*, 1076 (2006).
4. FarinhaP.,Biocorrosion in the miningindustry - big tanks and bigpipes, ACA Symposium on Microbial Influenced Corrosion, 10-11 August, Perth, 2011.
5. RobergeP., *Handbook of corrosion engineering, McGraw-Hill,* New York, 1999.
6. Gasior O., Farinha P., *Corrosion & Prevention*, **90**, 6 (2013).
7. Gray W., HarrisonG., Farinha P.,Risbud M., Financial benefit to a corrosion aware mine site culture, *Corrosion & Prevention*, Paper **118**, 1(2015).
8. Hassell R., Villaescusa E., Thompson A., and Kinsella B., Corrosion assessment of ground support systems, Proceedings of 5th International Symposium on Ground Support in Mining and Underground Construction, Perth, Australia, (2004).
9. Wu S., Northover M., Craig P., CanbulatI., Hagan P., Saydam, S., Environmentalinfluence on mesh corrosion in underground coal mines, Int. j. of mining, reclamation and environment, Published online: 13 Mar 2017, p. 1-17.
10. Duprat M., Bar N., Dabosi F., *J. Appl. Electrochem.,* **8**, 455 (1978).
11. Meyer D., Heinrich L., Reinhard D., *Korrosion,* **17**, 211(1968).
12. Bonel A., Dabosi F., Deslois C., Duprat M., *J. of Electrochem. Soc.,* **130**, 753 (1983).
13. Kowaka M., Ayukava M., Nagano N., *Sumitomu Kunsoki*, **21** № 2, (185) 1969.

КОРОЗИОННО ПОВЕДЕНИЕ В МОДЕЛНИ РАЗТВОРИ НА СТОМАНИ, ПРЕДНАЗНАЧЕНИ КАТО КОНСТРУКЦИОННИ МАТЕРИАЛИ ЗА МИННАТА ИНДУСТРИЯ

Д. И. Иванова*, Г. П. Илиева, Л. Б. Фачиков

Химикотехнологичен и металургичен университет,бул. „Кл. Охридски" 8, София 1756, България

(Резюме)

Извършено е сравнително изследване на корозионното поведение на две стомани, предназначени за руднично крепене: широко използваната въглеродна стомана ст.25 и новопредлаганата, нисколегирана стомана КР-355 (0.96% Cr, 0.36% Cu). Изпитванията са проведени в моделни среди, подбрани така, че да съдържат основните агресивни компоненти в повечето реални руднични води. С помощта на физични и електрохимични методи за изследване и анализ, са определени най-важните параметри, характеризиращи механичните свойства и корозионно-електрохимичното поведение на стоманите. Установено е, че стомана КР-355 е с по-добри якостни показатели и като цяло се отличава с по-висока корозионна устойчивост във всички използвани моделни среди.

Ключови думи: корозия, въглеродни и нисколегирани стомани, руднични води

Sulfite driven fuel cell for environmental purposes: optimization of the oxidation conditions

S. Stefanov*, M. Martinov, E. Razkazova-Velkova

Institute of Chemical Engineering – Bulgarian Academy of Sciences

Acad. G. Bonchev str., Bld. 103, 1113 Sofia, Bulgaria

The growing world population puts ever-increasing environmental requirements on all industries, be it construction, pharmacology or energy generation. One of the more potent and hard-to-neutralize industrial waste products are sulfites (typically sodium or calcium) generated by flue-gas desulfurization processes. Our project aims at neutralizing these dangerous compounds by oxidizing them in a fuel cell (FC) of our own design while simultaneously gaining electrical power. The present study's goal is to find suitable catalysts for the oxidation process. The experiments show that a nickel coated graphite fiber is an appropriate candidate to be used as electrode for the anode compartment of the fuel cell. A comparison of the electrochemical characteristics of the chosen fuel cell with different oxidizing agents (aerated seawater, hydrogen peroxide and ammonium chloride) is presented as well.

Key words: fuel cell, catalyst, sulfite ions, oxidation

INTRODUCTION

In our age the demand for energy, electricor other, is ever increasing. According to the International Energy Agency, [1] for 2015 over 80% of all energy gained is derived from fossil fuels. All fossil fuels contain varying quantities of sulfur that becomes a real environmental problem after the burning of the fuel when the sulfur is transformed to sulfur dioxide. Methods are developed to neutralize this hazardous product, but most of them are either too expensive for massive industrial applications or as in the cases of the lime and limestone methods require additional treatment that further complicates and increases the cost. Nevertheless all the ecological directives of the EU dictate that it is absolutely prohibited to release SO_2 in the atmosphere in high concentrations, which forces all factories and power plants to neutralize their flue gases despite the high costs.

The most economical way of scrubbing SO_2 from flue gases is via hydrated lime ($Ca(OH)_2$) or limestone ($CaCO_3$) to calcium sulfite ($CaSO_3$) and via caustic soda ($NaOH$) to sodium sulfite (Na_2SO_3).

Other industries whose wastewaters are contaminated with calcium or sodium sulfite are the pulp and paper (Kraft process), photographic (fixer), oil (oil recovery), food (preservatives), textile (dyes) and mineral processing (froth flotation).

Sulfites in wastewaters are substances that need to be oxidized to the more stable sulfates before their disposal in the environment. The oxidation process is a high energy consuming one and is accompanied with a lot of exploitation difficulties. Many studies are dedicated to the kinetics of oxidation [2-6] as well as the improvement of apparatuses equipment [7-9]. The high expenses make them inefficient for small-scale desulfurization installations.

In recent years there is increasing scientific interest for oxidation of different pollutants (including organic) in fuel cells (FC) [10-13]. This interest is due to the possibility of eliminating pollutants with minimum exploitation costs while simultaneously harvesting electrical energy.

Particularly relevant way to intensify the process of oxidation of the pollutions is the use of microorganisms in so-called microbial fuel cells (MFC). The possibilities for use of modern microbial fuel cells in our case are very limited because of the fact that sulfites are preservatives and are toxic to most bacterial strains.

Lately there are some studies [14-16] that try to improve the oxidation of sulfites by using different catalysts and electrodes.

Our project aims at improving the secondary oxidation step for both the limestone and the lime methods, as well as the caustic soda one by electrochemical oxidation in a membrane fuel cell of our own design. This way we can both reduce the cost of the neutralization steps as well as harvest the otherwise unused energy of the oxidation process. Our previous work [17] show that commercially available ion-exchange membrane Fumapem® FFA-

3-PK-75 is best suited for the fuel cell. The influence of the initial concentration, concentration of end products from the process and pH has also been investigated in the paper.

The aim of the current work is to find suitable catalysts for the oxidation process, as well as investigate alternative oxidizing agents.

EXPERIMENTAL

The preparation of the sulfite solution is done by dissolving Na_2SO_3 (analytical grade) in distilled water. The $CaSO_3$ suspension is prepared after precipitation of $CaCl_2$ and Na_2SO_3. The resulting suspension is then washed up of chloride ions. The presence of said ions is verified qualitatively with $AgNO_3$. The latter is done in order ascertain that the chloride ions won't influence the results. The concentration of the sulfites is determined by iodometric titration.

Analytical grade of sodium sulfate is dissolved in the initial solution to both increase the conductivity of the solution and to simulate accumulation of the end product.

The principal and practical scheme of the experimental installation of the fuel cell are shown in Fig. 1. It consists of two concentrically situated compartments with 200 ml volume for the anodic compartment and 75 for the cathodic one. The membrane ($S = 700$ mm^2) is placed on the bottom of the inner one. The outer volume is the anode compartment (AC) and the inner one is the cathode compartment (CC). Five standard cylindrical graphite rods (($d = 6$ mm, $L = 200$ mm, $S = 3000$ mm^2 each) are used as electrodes in the anode compartment and 30 g. (75 ml) activated carbon (Fujikasau®, Japan, 680 m^2.g^{-1}.) and one graphite rod into the cathode one. The addition of activated carbon is done in order to increase the surface area of the electrode in the cathode compartment. This approach is not done for the anode compartment due to the sorption effect of the activated carbon of the desired end products.
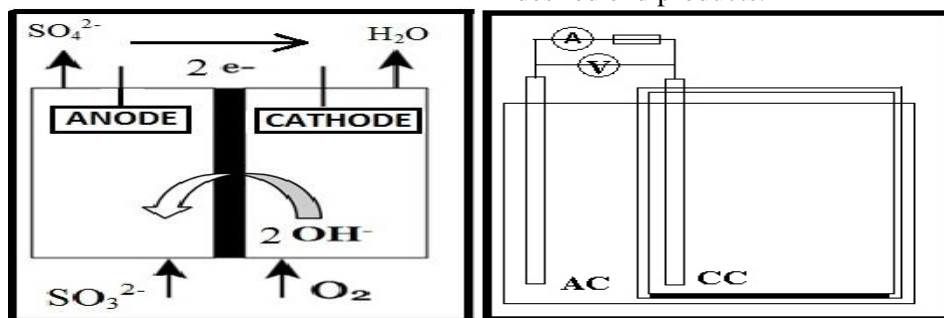
Fig. 1. Principal and practical scheme of the experimental fuel cell

The intended reactions are as follows:

Anode:
$$SO_3^{2-} + 2OH^- \rightarrow SO_4^{2-} + OH^- + H^+ + 2e^-$$

Cathode:
$$1/2\ O_2 + 2H^+ + 2e^- \rightarrow OH^- + H^+$$
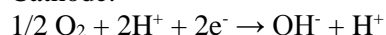
A screening is done for determining an appropriate catalyst for the process. All catalysts are molded along with binding agents into electrodes with identical surface area of 2000 mm2. The molded electrodes are as follows:
1. 3 mg Fullerenes C60/C70 (Sigma Aldrich), 40 mg manganese acetate, 60 mg Vulcan XC72 and 35 % Polytetrafluoroethylene (Teflon®) as a binder pressed over stainless steel mesh at 150°C and 150 atm. for 5 minutes;
2. 8 mg Norit®, 40 mg manganese acetate, 60 mg Vulcan XC72 and 35 % Polytetrafluoroethylene (Teflon®) as a binder pressed over stainless steel mesh at 150°C and 150 atm. for 5 minutes;
3. Ni-coated graphite fiber [18], rolled over the graphite rods with the same geometrical surface.

Roentgenography of nickel-plated graphite fiber is presented in Fig. 2. The only distinct peak is corresponding to Ni and indicates that the coating is dense and evenly distributed.
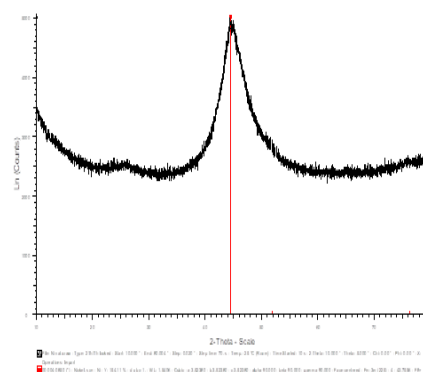
Fig. 2. Roentgenography of nickel-plated graphite fiber

RESULTS AND DISCUSSIONS
Influence of the type of pollutions

Fig. 3 shows a comparison of the electrical power output of the cell as a function of the concentration for both sodium and calcium sulfite.

It is to be expected for the calcium sulfite to have lower power output due to the fact that it is a suspension rather than a solution as is the case of the sodium sulfite. Due to the difference of one order of magnitude for further experiments we focused on the sodium sulfite and chose a concentration of 25 g.l^{-1} as it is relatively close to the real conditions [17].
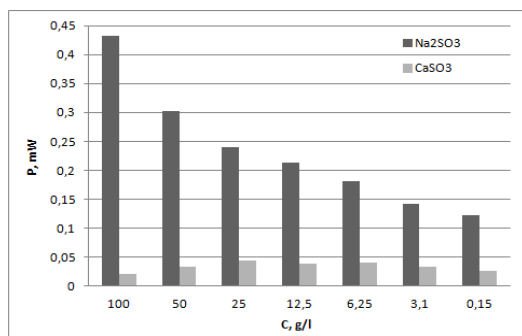
Fig. 3. Influence of the concentration of Na_2SO_3 and $CaSO_3$ on obtained electrical power

Screening for a catalyst for the process

The most common way for intensifying the oxidation process is the use of catalysts. The previously mentioned electrodes with molded catalysts are synthesized for this exact reason. Their catalytic effect is first tested in a vessel with similar volume to the fuel cell with results shown in Fig. 4. As can be seen all of them have a distinct catalytic effect (30 – 40%) compared to the experiment without catalyst. Even though the differences are within 5% by comparing the catalysts individually a distinction can be made that the Ni-coated fiber performs slightly better than the rest. For this reason this particular electrode is chosen to be used in the fuel cell as anode. In order to enhance the conductivity of the solution in the cathode compartment (saltwater with 16 g.l^{-1} NaCl) an experiment is conducted with the addition of 3% ammonium chloride with the results shown in Fig. 5. By comparing the results of both experiments as well as polarization curves we get the following:

Internal resistance of the fuel cell: when using saltwater – 40 Ω; when using saltwater with ammonium chloride – 4 Ω (an order of magnitude lower).

The power output of the fuel cell remains relatively constant between the 2^{-nd} until the 8^{-th} hour mark: when using saltwater – 0.7 mW; when using saltwater with ammonium chloride – 0.8 mW (about 15% increase).

The power output of the fuel cell at the 24^{-th} hour mark shows much greater difference: when using saltwater it is 0.45 mW while when using ammonium chloride it is 0.65 mW (about 40% increase).

A note should be made of the low wear resistance of the Ni-coating during work. After several experiments a roentgenography of the fiber (Fig. 6.) is done that shows a distinct carbon peak that is not present in the unused fiber (Fig. 2.). This indicates that portions of the Ni-coating is washed away and the underlying carbon is exposed.
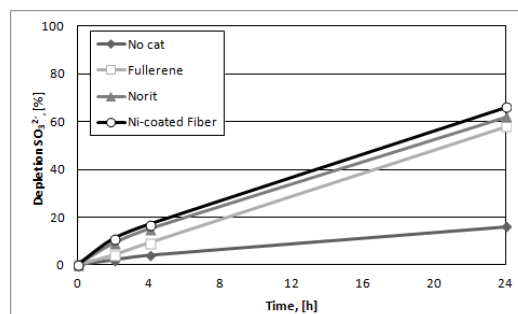
Fig. 4. Depletion of SO_3^{2-} using three different catalyst
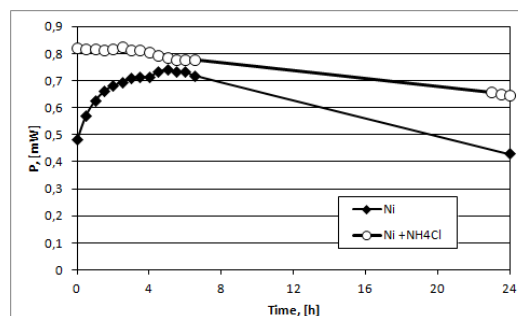
Fig. 5. Power in time using nickel-plated graphite fiber
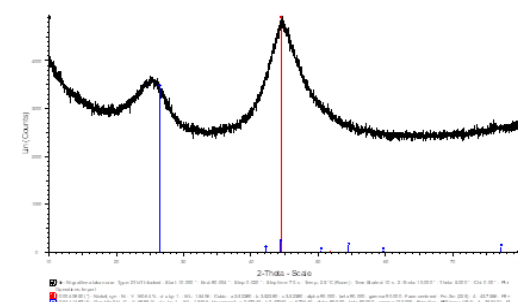
Fig. 6. Roentgenography of nickel-plated graphite fiber after 96 h

Influence of the oxidation agent

Another way for intensification of the oxidation process by using oxidizing agents. As such nitrates (with concentration of 0.5 g.l^{-1}), hydrogen peroxide (with concentration of 30 g.l^{-1}) and aerated saltwater (with atmospheric air 15 l.h^{-1}) are tested. Comparison between the power output of the cell as a function of time is shown on Fig. 7. The external resistance used is 100 Ω.
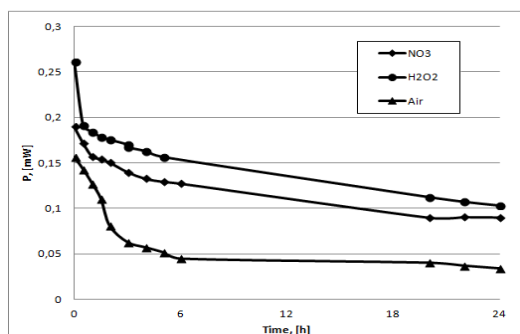
Fig. 7. Power in time using three different oxidizers

The internal resistance of the fuel cell when using nitrates, hydrogen peroxide and aerated saltwater is 50 Ω, 150 Ω and 100 Ω respectively.

The power output at the 2nd hour mark for the nitrates is 0.15 mW, for the hydrogen peroxide – 0.17 mW and for the aerated saltwater – 0.01 mW.

The power output at the 6th hour mark for the nitrates is 0.13 mW, for the hydrogen peroxide – 0.15 mW and for the aerated saltwater – 0.04 mW.

The power output at the 24th hour mark for the nitrates is 0.09 mW, for the hydrogen peroxide – 0.10 mW and for the aerated saltwater – 0.04 mW.

It should be noted that even though the aerated saltwater shows lowest power output it remains constant for the time interval $6^{th} – 24^{th}$ hour unlike the nitrates and the hydrogen peroxide. An explanation of this phenomenon can be derived from the rate of the depletion of the sulfite ions in Fig. 8 which shows that the concentration of sulfite ions remains higher for longer periods of time compared to the other oxidizing agents.
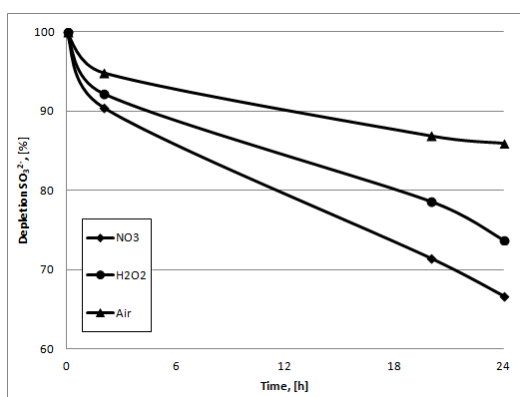
Fig. 8. Depletion of SO_3^{2-} using three different oxidizers

As shown in Fig. 8. the sulfite depletion rate is highest when using nitrates as an oxidant (about 10% higher than the peroxide and about 20% more than the aerated saltwater). Comparing with the power graph (Fig. 7.) the peroxide fuel cell that has the highest power output does not have the highest oxidation rate. Perhaps the use of hydrogen peroxide initiates other secondary reactions besides the

desired, respectively produce more power. This may be the reason for the higher electrical resistance in that case.

CONCLUSIONS

• The use of a fuel cell for sulfite ion neutralization is more effective in the case of sodium sulfite compared to calcium sulfite;

• The use of catalysts intensifies the oxidation rate of the sulfite ions in the fuel cell;

• All the investigated catalysts show definite catalytic effects on the oxidation of Na_2SO_3. Nickel-plated graphite fiber shows both best oxidation rate as well as lowest production cost but it also has very low wear resistance;

• Using more potent oxidizing agent enhances the oxidation rate of the sulfite ions and correspondingly the power gained;

• Of the studied oxidizing agents the nitrates show best results at increasing the oxidation rate of sulfite ions.

REFERENCES

1. IEA, http://www.iea.org/t&c
2. D. Karatza, M. Prisciandaro, A. Lancia, D. Musmarra, *Ind. Eng. Chem. Res.,* **43,** 4876 (2004).
3. D. Karatza, M. Prisciandaro, A. Lancia, D. Musmarra, *Chemi. Eng. J.,* **145,** 285 (2008).
4. A. Lancia, D. Musmarra, F. Pepe, M. Prisciandaro, *Chem. Eng. J.,* **66,** 123 (1997).
5. A. Lancia, D. Musmarra, *Environ. Sci. Technol.*, **33,** 1931(1999).
6. M. Pisu, A. Cincotti, G. Cao, F. Pepe, *Chem. Eng. Res. Design*, **82 (A7),** 927 (2004).
7. F.G. Wadie, S.Feeney, US Patent 4 494 614 Feb. 27 (1996).
8. Zheng Y., S. Kiil, J. E. Johnsson, Q. Zhong, *Fuel,* **81,** 1899 (2002).
9. Zheng Y., S. Kiil, J. E. Johnsson, *Chem. Eng. Sci..,* **58,** 4695 (2003).
10. K. Kwiyong, H. Jong-In, *Int. J. Hydrogen Energy,* **39,** 7142 (2014).
11. E. Razkazova-Velkova, M. Martinov, L. Ljutzkanov, N. Dermendzhieva, V. Beschkov, *J. Int. Scientific Publications: Materials, Methods &Technologies,* **7,** 456 (2013).
12. E. Razkazova-Velkova, M. Martinov, S. Stefanov, V. Beschkov, *Scientific works of University of Food Technologies – Plovdiv*, **LXI,** 485 (2014).
13. Zhai Lin-Feng, Wei Song, Zhong-Hua Tong, Min Sun, *J. Hazard. Mater.,* **243,** 350 (2012).
14. A. Enache, N. Vaszilcsin, L. Dan, *Analele Universităţii din Oradea, Fascicula Protecţia Mediului,* **XXV,** 185 (2015).

15. M.L. Dan, N. Vaszilcsin, A.F. Enache, *Chem. Bull. "POLITEHNICA"*, Univ. Timisoara, **61**, 1 (2016).
16. N. Dermendzhieva, E. Razkazova-Velkova, V. Beschkov, L. Ljutzkanov, *J. Int. Scientific Publications, Ecology and Safety,* **10,** 256 (2016).
17. M. Martinov, E. Razkazova-Velkova, S. Stefanov, *J. International Scientific Publications: Ecology & Safety,* **11,** 55 (2016).
18. Sachkov M., BG Patent No110265/2013

СУЛФИДНА ГОРИВНА КЛЕТКА С ЕКОЛОГИЧНА НАСОЧЕНОСТ: ОПТИМИЗАЦИЯ НА ОКИСЛИТЕЛНИТЕ УСЛОВИЯ

С. Стефанов, М. Мартинов, Е. Разказова-Велкова

Институт по инженерна химия – Българска академия на науките, ул. „Акад. Георги Бончев", бл. 103, 1113, София, България

(Резюме)

Увеличаващото се световно население поставя все по-големи екологични изисквания върху всички индустрии, били те строителната, фармацевтичната или производството на електроенергия. Един от по-опасните и трудни за неутрализиране индустриални отпадъци са сулфитите (обикновено под формата на натриев и калциев сулфит), генерирани от пречистването на сяросъдържащите димни газове, получени при изгаряне на фосилни горива. Целта на нашия проект е неутрализирането на тези опасни съединения чрез окислението им в горивна клетка, разработена от екипа ни, като едновременно с това се генерира и електроенергия. Текущото изследване се фокусира върху намиране на подходящ катализатор за окислителния процес. Резултатите от експериментите показват, че графитна тъкан, покрита с никел, е подходяща за използване като аноден електрод в горивната клетка. Показани са и сравнения на електрохимичните показатели на избрана конфигурация на горивната клетка при използване на различни окислители (аерирана морска вода, водороден пероксид и амониев хлорид).

Ключови думи: горивна клетка, катализатор, сулфидни йони, окисление

Electrocatalysts with reduced noble metals aimed for hydrogen/oxygen evolution supported on Magneli phases. Part I: Physical characterization

P. Paunović[1*], O. Popovski[2], G. Načevski[1], E. Lefterova[3],A. Grozdanov[1] and A. T. Dimitrov[1]

[1] Faculty of Technology and Metallurgy, University "Sts. Cyril and Methodius"
Ruger Bošković Str., 16, 1000 Skopje, R. Macedonia
[2] Military Academy „Mihailo Apostolski", Mihajlo Apostolski Str., b.b., 1000 Skopje, R. Macedonia
[3]Institute of Electrochemistry and Energy Systems, Bulgarian Academy of Sciences, Acad. G. Bonchev Str., Bl.10, 1113 Sofia, Bulgaria

The subject of this study is preparation and physical characterization of nano-scaled electrocatalysts for water electrolysis, consisted of Magneli phases as a support and different metallic phases (Co, Pt, Ru, CoPt (Co:Pt = 1:1 wt.), CoRu (Co:Ru = 1:1 wt.) and CoPtRu (Co:Pt:Ru = 1:0,5:0,5 wt.)). Magneli phases were mechanically treated (top-down approach) to reduce their particles from micro to nano scale. Electrocatalytic materials were prepared by sol-gel procedure using organometallic precursors (Me-acetylacetonate) deposited on dispersed Magneli phases in wt. ratio 10% Me and 90% Magneli phases. Pure Magneli phases and the studied electrocatalysts were characterized by means of TEM, XRD and BET analysis. The obtained results have shown that the size of the micro-scaled Magneli phases after the applied mechanical treatment, were reduced to 180÷200 nm. Specific surface area of 4.2 m^2g^{-1} was determined by BET analysis. After grafting of the metallic phase over the Magneli phase, good dispersion of the catalytic centers over the support surface was achieved, that is appropriate for catalytic purpose. Metallic particles are nano-scaled in the range of 2 to 15 nm, thus the BET surface area of the electrocatalysts is higher (4.3 to 11 m^2g^{-1}) related to the BET surface area of pure Magneli phases.

Key words: Magneli phases,Co, Pt, Ru, hydrogen evolution, oxygen evolution.

INTRODUCTION

In the last decade, non-stoichiometric titanium oxides, so called Magneli phases (trade name Ebonex) have attracted great attention within the hydrogen economy, as potential support material for nano-scaled electrode materials for fuel cells and water electrolysis [1–3]. Generally, the support material should meet the following important characteristics, such as: i) highly developed surface area to provide better dispersion of the nano-scaled catalytic particles; ii) high electric conductivity to provide efficient electron transfer to ions involved in the electrochemical reactions, iii) mechanical and chemical stability and iv) to improve intrinsic catalytic activity of the active catalytic phase through the strong metal-support interaction (SMSI). In the electrocatalytic systems with metallic (catalytic phase), Magneli phases have bifunctional role: i) as a catalyst support and ii) contributes to the catalyst's overall synergetic effect by so called Strong Metal-Support Interaction (SMSI). The SMSI gives rise to both the electrocatalytic activity of the metal component as the main catalytic phase (by reinforcing it) and to the catalyst's stability (due to stronger adherence between catalyst's components) [4,5].

The main general formula of Magneli phase is Ti_nO_{2n-1} (4 < n < 10) [6]. It was observed that removing oxygen from the TiO_2 octahedra leads to shear planes in the crystal structure and forming of TiO octahedron. Depending of the ratio of TiO_2 vs. TiO octahedra within the crystal structure, different non-stoichiometric titanium oxides can appear [6,7]. Within this way formed crystal lattices, besides Ti^{4+} ions, also Ti^{3+} ions exist, which are responsible for increasing of electrical conductivity by three orders of magnitude, approaching the conductivity of graphite-like carbon nanomaterials [8,9]. Magneli phases show very similar physical properties to that of TiO_2, so they could be used for the same applications as that of TiO_2. The only difference in the properties of Magneli phases and TiO_2 is high electric conductivity, which make the Magneli phases applicable in more fields such as sensing [7], electrocatalysis [10,11] and energy storage [12–14]. The high electrical conductivity, chemical stability and possibility for interaction with the metallic catalytic phase, make them as an appropriate support material for electrocatalysts. The main disadvantage of Magneli phases as support material is the low specific surface area, compared with nano-scaled

---

carbon materials with specific surface area of more than 250 m^2g^{-1}. The maximal achievement of the "top-down" procedures for preparation of Magneli phases including mechanical reduction of the particle size (attrition and milling) was specific surface area to 1.6–3.0 m^2g^{-1} [11,15]. The "bottom up" approach employing high temperature reduction in atmosphere of hydrogen and inert gas (N_2 or Ar) has enabled specific surface area of 25.3 m^2g^{-1} [16] or 26.6 $m^2 \cdot g^{-1}$ [10] so far. Maximal achievement of "bottom up" approach was 45 m^2g^{-1} [17], but with lower electrical conductivity of 4.7 Scm^{-1}.

The aim of this work is to prepare and characterized a electrocatalysts with reduced amount of noble metals, deposited on Magneli phases as a support material.

EXPERIMENTAL

As a catalyst support commercial micro-sized Magneli phases were used (Ebonex®, Altraverda, UK). To reduce their particle size, top-down approach was applied, using mechanical treatment by Fritsch Planetary Mill (Pulverisisette 5) for 20 h with acceleration of balls of 200 rpm. The ball diameter was 1 cm, while the weight ratio of balls vs. treated material was 3:1.

The electrocatalytic materials were prepared using simplified sol-gel method proposed by the present authors [18]. Magneli phases were dispersed in organic solvent – anhydrous ethanol (Merck, p.a.), using magnetic stirrer with 600 to 900 rpm. Metallic phase as organometallic compound (Me-2,4-pentaedionate, Me = Co, Pt, Ru; Alfa Aesar, Johnson Matthey, GmbH) was added into the support's suspension. The mixture was evaporated at temperature bellow 60 oC, with continuous stirring. The obtained fine catalyst's powder was thermally treated for 1 h at 250 °C in inert (N_2) atmosphere in order to remove the residual organic groups from organometallics. The composition of the prepared electrocatalysts is shown in Table 1.

The catalyst support (mechanically treated Megneli phases) and the prepared electrocatalysts were observed by transmission electron microscope (TEM) FEI Tecnai G2 Spirit TWIN equipped with LaB6. XRD measurements were carried out by X-ray powder diffractometer Philips APD 15, with CuKa radiation. The diffraction data were collected at a constant rate of 0.02 deg over an angle range of 2θ from 20 deg to 80 deg. The average crystallite size was calculated from the broadening of the XRD peaks using the Scherrer's equation [19]. Specific BET surface area of the samples was determined using measurements of isothermal nitrogen adsorption by Quantachrome NovaWin, Quantachrome Instruments version 11.0. Zeta

potential measurements of Magneli phases were performed using Zeta Meter System 4.0 – electrochemical cell which works on the principle of electrophoresis, at room temperature (23 °C) and pH = 7. As a surface active agent (anionic surfactant), sodium dodecyl sulfate was used.

Table 1. Composition of the studied electrocatalysts

Sample	Metallic phase 10%, wt.	Support 90%, wt.
E-1	Co	Ebonex
E-2	Pt	Ebonex
E-3	Ru	Ebonex
E-4	CoPt, 1:1, wt.	Ebonex
E-5	CoRu, 1:1, wt.	Ebonex
E-6	CoPtRu, 1:0.5:0.5,wt.	Ebonex
E-6	CoPtRu, 1:0.5:0.5,wt.	Ebonex

RESULTS AND DISCUSSION
Characterization of the catalysts support – Magneli phases

According to TEM images shown in Fig. 1, it was determined that the size of mechanically treated Magneli phases (Ebonex) is in submicron-scaled region, near 180 to 200 nm. Our previous research [3] has shown that this value of particle size is maximum achievement of the mechanical treatment of Magneli phases. The difference of the particle size of Magneli phases treated for 16 and 20 h is only 10-15 nm. Therefore, further mechanical treatment would exceed the critical value of the surface energy and the treated material would tend to reach the thermodynamic steady state through agglomeration of the particles.
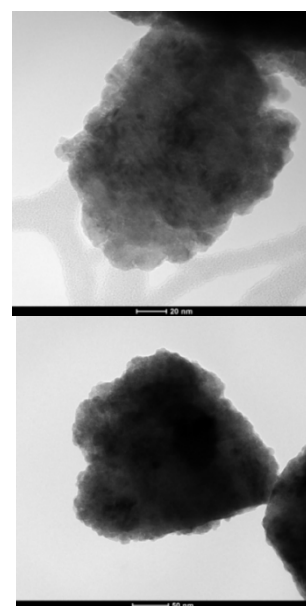
Fig. 1. TEM images of Magneli phases mechanically treated for 20 h
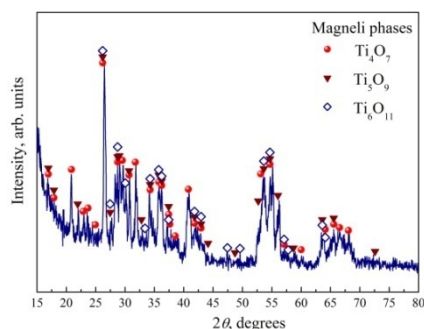
Fig. 2. XRD spectrum of Magneli phases mechanically treated for 20 h

Qualitative identification of Magneli phases was performed by means of XRD analysis. Characteristic peaks of the Magneli phase's constituents such as Ti_4O_7, Ti_5O_9 and Ti_6O_{11} are on different positions that correspond to peaks of the basic XRD peaks of rutile [20]. As the content of oxygen decreases within the rutile octahedra, TiO octahedron is forming. Due to the different ratio of TiO_2 and TiO in the different Magneli phases, different diffractions of X-rays occur than in rutile octahedral. As result, the XRD spectrum of Magneli phases contains larger number of less pronounced, widespread and less intensive peaks along whole range of 2θ [21] (Fig. 2). As result of presence of TiO, some of them are less shifted compared with the basic rutile peaks, but most of them are on quite different positions. The peaks of first three homologues Ti_4O_7, Ti_5O_9 and Ti_6O_{11} can be seen, while the rest homologues are in small quantity and their peaks are very less intensive and cannot be detected within the spectra.

Fig. 3. Nitrogen adsorption curves of Magneli phases: a) as-measured in plot $V^a \div p/p^0$ and b) linearized adsorbton curve in plot $1/[n^a \cdot (p^0/p - 1)] \div p/p^0$.

Specific surface area (m^2g^{-1}) of Magneli phases was determined by the nitrogen adsorption curve shown in Fig. 3a. After linearization of this curve (Fig. 3b), BET surface area of 4.2 m^2g^{-1} was calculated. This is good achievement of the applied mechanical treatment, compared with the corresponding results of other studies, ranging from 1.6 to 3 m^2g^{-1} [1,11].

Characterization of the electrocatalysts

The studied electrocatalysts were prepared by sol-gel route and contain only 10 %wt. metallic phase (see Table 1) deposited on mechanically treated Magneli phases as support material. Shown in Fig. 4 are their TEM images. Generally, one can say that metallic particles (active catalytic centers) are uniformly dispersed over the surface of catalyst support (Magneli phases), and there is no segregation on particular areas of the surface.

Uniform dispersion provides active participation of all catalytic centers (metallic particles) over the whole surface of the catalysts in adsorption/desorption processes with ionic/atomic participants in the electrochemical reactions. This intensifies the total electrochemical reaction, at constant intrinsic activity of the metallic phase. Good dispersion of the metallic particles was expected according to the Zeta potential value of the support material – Magneli phases. The measured value of –48.3 mV highlights on their good stability and dispersibility, while the negative sign points out that the particles of Magneli phases are surrounded by negatively charged ions within the suspension. This is suitable for better attracting the positive metallic ions over the whole surface of the support material. So, the result of Zeta potential measurements is in good agreement with TEM analysis.

a)

b)

c)

d)

e)

f)
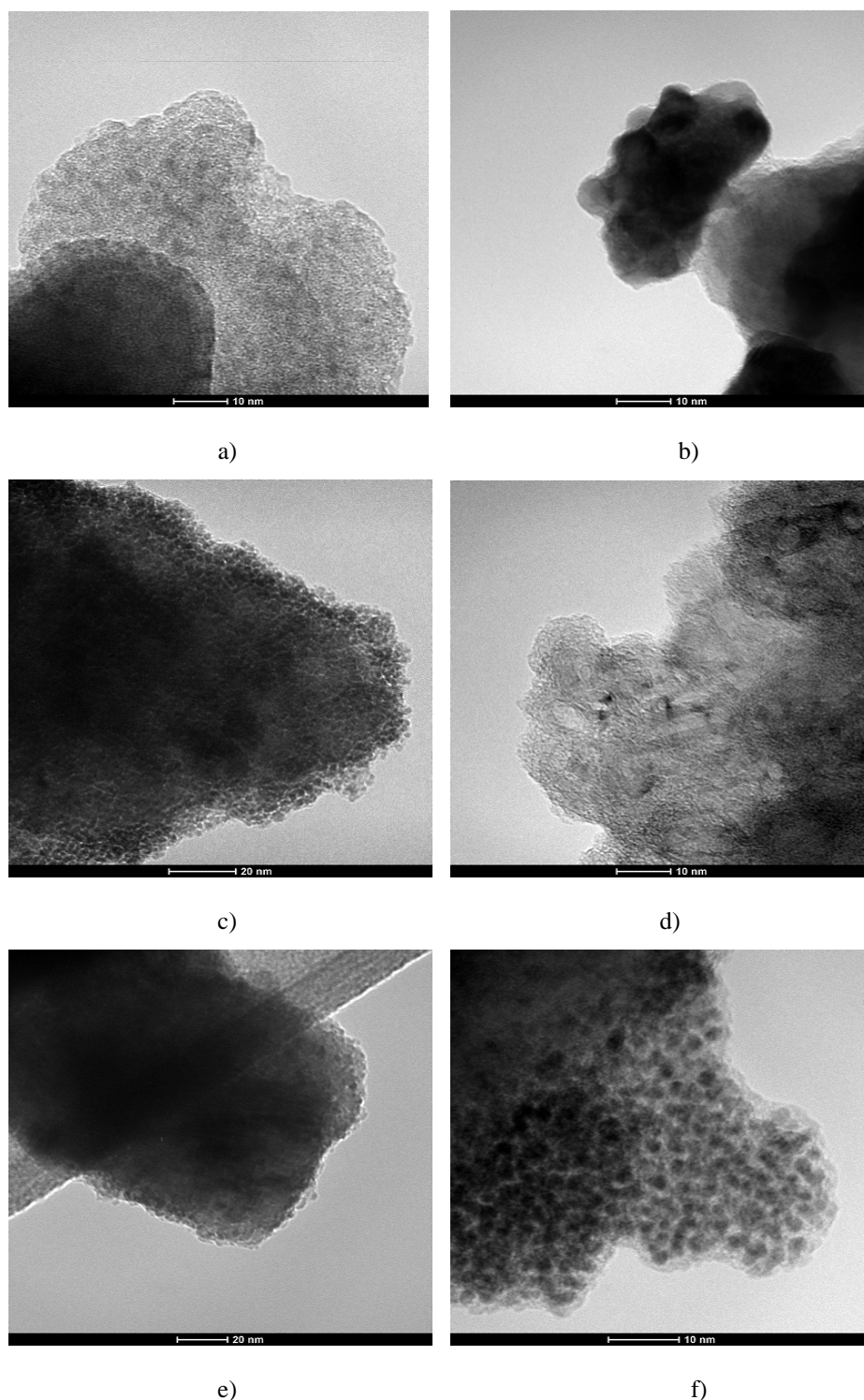
Fig. 4. TEM images of the studied electrocatalysts: a) E-1, b) E-2, c) E-3, d) E-4, e) E-5 and f) E-6

In sample E-1 (Fig. 4a) prevailing cobalt particles with an average size of 2 to 3 nm, and in the darker part of the image, particles with size of 10 to 15 nm can be seen. These larger particles are in very small amount. Sample E-2 (Fig. 4b) contains uniformly dispersed platinum particles with variation in size from 5 to 15 nm. Very fine dispersed particles of the metallic phase over the support surface, with size of 2 to 3 nm can be observed in the sample E-3 based

on Ru metallic phase (Fig. 4c). Also, the sample E-4 with mixed metallic phase, CoPt (Fig. 4d) has shown outstanding dispersion of the metallic particles with size of 2 to 3 nm, and less quantity with size of near 5 nm. The size of metallic particles in the sample E-5 containing CoRu (Fig. 4e) is 2 to 4 nm, while in the sample E-6 containing CoPtRu is 3 to 5 nm.

In order to detect the catalysts constituents, their crystalline state, possibility of formation the solid

solutions and/or intermetallic compounds in polymetallic phase, the presence of oxidized state, etc., XRD analysis was applied. The obtained XRD spectra of the studied electrocatalysts are shown in Fig. 5.
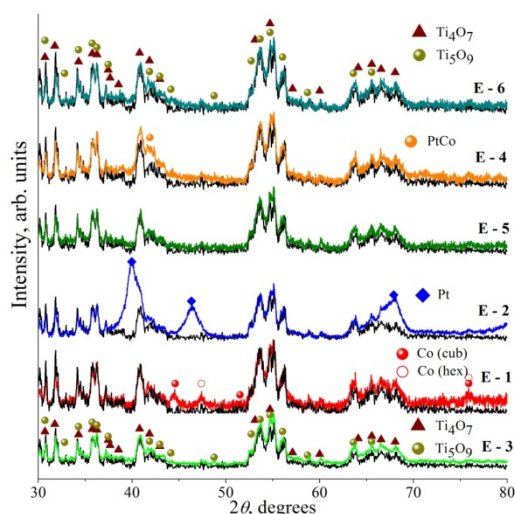
Fig. 5. XRD spectra of the studied electrocatalysts

In the electrocatalysts with pure Co and Pt (E-1 and E-2), crystalline metallic phase was detected. The crystallites size was determined using Scherrer equation [19] and fitting procedure was applied for determination of the FWHM (full width at half maximum). In the sample E-1 cubic and hexagonal crystalline metallic phase were detected with size of near 13 nm. The corresponding weak pronounced peaks, highlight on low amount of this phase within the electrocatalysts, while the size of the main part of the Co metallic phase is very small, near 2 nm, and in oxidized state. For the sample E-2, two strong, relatively broad platinum peaks were registered, corresponding to crystal orientation of 111 and 200. Average size of 111 crystallites is 8 nm, while that of 200 crystallites is 6 nm. In the spectrum of sample 4 with mixed metallic phase, CoPt, one can see weak and broad peak at position of $2\theta = 41.8°$, corresponding to the solid state solution type of CoPt alloy. The size of these particles is 2 nm. According to the previous researches [22,23], and here was confirmed that in the presence of cobalt, platinum has smaller particles, which means that cobalt is a promoter to reduce the platinum nanoparticles. Therefore, one can expect that the catalytic activity of this electrocatalyst (E-4) could be close or even better than that of electrocatalysts containing pure Pt as metallic phase (E-2), although it contains less than half quantity of Pt. XRD spectra of the electrocatalysts containing Ru (E-3) and mixed CoRu (E-5) metallic phase, coincide with the spectrum of pure Magneli phases, which means that no metallic phase was detected. Hence, the metallic

phase in these catalysts is in amorphous or most probably in oxidized state (oxides and/or hydroxides).

Shown in Table 2 are the values of BET surface area of the studied electrocatalysts, calculated as was explained in previous section. Addition of the nanoscaled metallic phase more or less increases the BET surface area of the electrocatalysts related to the pure Magneli phases. In the monometallic systems, this effect is most pronounced in the case of addition of Ru, while Pt has shown the lowest effect. In the sample E-2, platinum insignificantly increased the surface area related to the pure Magneli phases (4.3 vs. 4.2 m^2g^{-1}, respectively). The increased BET surface area of the sample E-4 (CoPt) is result of addition of Co. Comparing the Ru based electrocatalysts, one can see that addition of Co in the Ru metallic phase (E-5) decreases the BET surface area (9.4 m^2g^{-1}) related to the monometallic Ru based electrocatalysts (E-3), which has shown the highest BET surface area (11 m^2g^{-1}). Also, in the sample E-6 based on CoPtRu, platinum and cobalt have decreased the BET surface area to 6.4 m^2g^{-1}. Generally, higher BET surface area means higher catalytic activity as result of larger available area for adsorption/desorption processes. But also, one should consider the intrinsic catalytic activity of the metallic phase. However, the values of BET surface area can be used for explanation of electrocatalytic activity of the studied catalysts.

Table 2. BET surface area of the studied catalytic materials

	10% metallic phase + 90% Ebonex	BET s. a., $m^2 \cdot g^{-1}$
	Pure Magneli phases	4.2
E-1	Co	6.1
E-2	Pt	4.3
E-3	Ru	11.0
E-4	CoPt, 1:1, wt.	7.6
E-5	CoRu, 1:1, wt.	9.4
E-6	CoPtRu, 1:0.5:0.5, wt.	6.4

CONCLUSIONS

The study presented in this paper was motivated by the idea to use Magneli phase as support for electrocatalysts aimed for hydrogen/oxygen evolution, instead of nano-scaled carbon support materials, and to investigate the addition of non-noble metal Co in platinum or ruthenium metallic phase. According to the presented results the following conclusions can be drawn:

1.   The size of the micro-scaled Magneli phases by the applied mechanical treatment were reduced to 180 to 200 nm, with specific surface area of 4.22 m^2g^{-1} and high stability and dispersibility in liquid

media. This is a good achievement for this type of treatment.

2. Metallic phase was uniformly dispersed over the support surface providing active participation of all catalytic centers in adsorption/desorption processes with ionic/atomic participants in the electrochemical reactions.

3. The size of different metallic particles within the studied electrocatalysts is in range of 2 to 15 nm, which points out that the support material successfully prevent the agglomeration and segregation of metallic phase over the catalyst surface.

4. The obtained results point out that the studied electrocatalysts could be used as an effective electrode material for water electrolysis.

REFERENCES

1. M. Lj. M. Vračar, N. V. Krstajić, V. R. Radmilović, M. M. Jakšić, *J. Electroanal. Chem.*, **587**, 99 (2006).
2. E. Slavcheva, V. Nikolova, T. Petkova, E. Lefterova, I. Dragieva, T. Vitanov, E. Budevski, *Electrochim. Acta*, **50**, 5444 (2005).
3. P. Paunović, A. Petrovski, G. Načevski, A. Grozdanov, M. Marinkovski, B. Andonović, P. Makreski, O. Popovski, A. Dimitrov, in: Nanoscience Advances in CBRN Agents Detection, Information and Energy Security, P. Petkov, D. Tsiulyanu, W. Kulish, C. Popov (eds), Dordrecht: *Springer Science+Business Media*, 239, (2015).
4. S. G. Neophytides, S. H. Zaferiatos, M. M. Jakšić, *J. Electrochem. Soc.*, **150**, E-512 (2003).
5. M. M. Jakšić, *Int. J. Hydrogen Energy*, **12**, 727 (1987).
6. J. R. Smith, F. C. Walsh, R. L. Clarke, *J. Appl. Electrochem.*, **28**, 1021 (1998).
7. F. C. Walsh, R. G. A. Wills, *Electrochim. Acta*, **55**, 6342 (2010).
8. J. F. Houlihan, L. N. Mulay, *Phys. Status Solidi B*, **61**, 647 (1974).
9. R. L. Clarke, S. K. Harnsburger, *Am. Lab.*, **20**, 6 (1988).
10. S. Siracusano, V. Baglio, C. D'Urso, V. Antonucci, A. S. Aricò, *Electrochim. Acta*, **54**, 6292 (2009).
11. E. Antolini, E. R. Gonzales, *Solid State Ionics*, **180**, 746 (2009).
12. X. Li, A. L. Zhu, W. Qu, H. Wang, R. Hui, L. Zhang, J. Zhang, *Electrochim Acta*, **55**, 5891 (2010).
13. P. C. S. Hayfield (ed), Development of a new material - Monolithic Ti$_4$O$_7$Ebonex ceramic, Royal Society of Chemistry; Cambridge: Thomas Graham House, 2002.
14. S. Myung, M. Kikuchi, C. S. Yoon, H. Yashiro, S. Kim, Y. Sun, B. Scrosati, *Energy Environ. Sci.*, **6**, 2609 (2013).
15. Lj. M. Vračar, S. Lj. Gojković, N. R. Elezović, V. R. Radmilović, M. M. Jakšić, N. V. Krstajić, *J. New Mater. Electrochem. Syst.*, **9**, 99 (2006).
16. P. Krishnan, S. G. Advani, A. K. Prasad, *J. Solid State Electrochem.*, **16**, 2515 (2012).
17. S. T. Nguyen, J-M. Lee, Y. Yang, X. Wang, *Ind. Eng. Chem. Res.*, **51**, 9966 (2012).
18. P. Paunović, O. Popovski, A. Dimitrov, D. Slavkov, E. Lefterova, S. HadžiJordanov, *Electrochim. Acta*, **52**, 1810 (2006).
19. B. D. Cullity, Elements of X-Ray Diffraction, London: Addison-Wesley, 1978.
20. P. Paunović, A. Grozdanov, A. Češnovar, B. Ranguelov, P. Makreski, G. Gentile, E. Fidančevska, *J. Eng. Mater. Technol.*, **137**, 021003 (2015).
21. Y. Lu, Y. Matsuda, K. Sagara, L. Hao, T. Otomitsu, H. Yoshida, *Adv. Mater. Res.*, **415-417**, 1291 (2012).
22. P. Paunović, I. Radev, A. T. Dimitrov, O. Popovski, E. Lefterova, E. Slavcheva, S. HadžiJordanov, *Int. J. Hydrogen Energy*, **34**, 2866 (2009).
23. P.Paunović, D. StoevskaGogovska, O. Popovski, A. Stoyanova, E. Slavcheva, E. Lefterova, P. Iliev, A. T. Dimitrov, S. HadžiJordanov, *Int. J. Hydrogen Energy*, **36**, 9405 (2011).

ЕЛЕКТРОКАТАЛИЗАТОРИ С НАМАЛЕНО СЪДЪРЖАНИЕ НА БЛАГОРОДНИ МЕТАЛИ ЗА ОТДЕЛЯНЕ НА ВОДОРОД/КИСЛОРОД С МАГНЕЛИ ФАЗИ КАТО КАТАЛИТИЧЕН НОСИТЕЛ. ЧАСТ I: ФИЗИЧЕСКО ОХАРАКТЕРИЗИРАНЕ

П. Паунович[1*], О. Поповски[2], Г. Начевски[1], Е. Лефтерова[3], А. Грозданов[1], А.Т. Димитров[1]

[1]*Технологичен и металургичен факултет, Университет "Св. Кирил и Методий", ул. Руджер Бошкович 16, 1000 Скопие, Република Македония*

[2]*Военна академия "Михайло Апостолски", ул. Михайло Апостолски, 1000 Скопие, Република Македония*

[3]*Институт по електрохимия и енергийни системи "Акад. Е. Будевски", Българска академия на науките, ул. Акад. Г.Бончев, бл.10, 1113 София, България*

(Резюме)

Предмет на това изследване е синтез и физическо охарактеризиране на наноразмерни електрокатализатори за водна електролиза, състоящи се от Магнели фази като носител и различни метални фази (Co, Pt, Ru, CoPt (Co: Pt = 1:1 тегл.), CoRu (Co: Ru = 1:1 тегл.) и CoPtRu (Co:Pt:Ru = 1:0,5:0,5 тегл.)). Магнели фазите са механично обработени за да се намалят техните частици от микро до наноразмери. Електрокаталитичните материали са синтезирани по зол-гел метода, като са използвани органометални прекурсори (Ме-ацетилацетонат), нанесени върху диспергирани Магнели фази в тегловно съотношение 10% Ме и 90% Магнели фази. Чистите Магнели фази и изследваните електрокатализатори са охарактеризирани с помощта на ТЕМ, РД и БЕТ анализ. Получените резултати показват, че размерът на микроразмерните частици на Магнели фазите след приложеното механично третиране е намален до 180-200 nm. Специфичната повърхност, определена чрез БЕТ анализ е 4,2 m^2g^{-1}. След нанасяне на металната фаза върху Магнели фазите се постига добра дисперсия на каталитичните центрове върху носещата повърхност, което е благоприятно за каталитичния процес. Металните частици са наноразмерни в диапазона от 2 до 15 nm и следователно специфичната повърхност на електрокатализаторите е по-висока (4.3 до 11 m^2g^{-1}) спрямо тази на чистите Магнели фази.

Ключови думи: Магнели фази, Co, Pt, Ru, отделяне на водород, отделяне на кислород.

Electrocatalysts with reduced noble metals aimed for hydrogen/oxygen evolution supported on Magneli phases. Part II: Electrochemical characterization

P. Paunović[1*], O. Popovski[2], G. Načevski[1], A. Grozdanov[1] and A. T. Dimitrov[1]

[1] Faculty of Technology and Metallurgy, University "Sts. Cyril and Methodius"
RugerBošković Str., 16, 1000 Skopje, R. Macedonia
[2] Military Academy „Mihailo Apostolski", Mihajlo Apostolski Str., b.b., 1000 Skopje, R. Macedonia

This study is concerned with electrochemical testing of nano-scaled electrocatalysts consisted of Magneli phases as a support and different metallic phases (Co, Pt, Ru, CoPt (Co:Pt = 1:1 wt.), CoRu (Co:Ru = 1:1 wt.) and CoPtRu (Co:Pt:Ru = 1:0,5:0,5 wt.)). Electrocatalytic materials were prepared by sol-gel procedure using organometallic precursors (Me-acetylacetonate) deposited on dispersed Magneli phases in wt. ratio 10% Me and 90% Magneli phases. Electrochemical testing of the studied electrocatalysts was performed in aqueous alkaline electrolyte. The order of activity for hydrogen evolution was the following: CoPt > CoPtRu > CoRu, while for oxygen evolution: CoRu > CoPtRu > CoPt. Co has been shown as promoter for reducing Pt particles (the most active monometallic phase), so reduction of Pt quantity in the metallic phase was compensated with smaller particles. Also, mutual interaction between metallic phases (shifting the centre of d-band to values close to Fermi level) increases the intrinsic catalytic activity for both hydrogen and oxygen evolution. Due to large particle of Magneli phases, the catalytic activity is lower compared with corresponding electrocatalysts deposited on carbon nanomaterials. But, they are very good catalysts for oxygen evolution, because Magneli phases in this case, behave not only as support material, but also, as an active oxide electrode.

Key words: Magneli phases, Co, Pt, Ru, hydrogen evolution, oxygen evolution.

INTRODUCTION

One of the most challenging issues within the hydrogen economy as the most promising alternative energy system is finding out catalytically active electrode materials for water electrolysis/fuel cells with reduced amount or without platinum. The exploitation of platinum as a leading electrode material in the hydrogen economy is limited due to high price and low abundance [1]. There are two main approaches to enhance the catalytic activity of the metals: physical and chemical. The first approach is based on the reduction of the particles size, which implies increase of the real surface area (size-effect) [2]. So, this approach leads to nano-scaled electrocatalytic materials in hydrogen economy. The second one is based on alloying of the catalytic metal phase or interaction of metallic phase with the support material (intrinsic effect). According to Jakšić's hypo-hyper d-concept [3,4], the mixture of hyper d- electronic transition metals (having more electrons in the outer shell and good individual catalysts) with hypo d- electronic transition metals (having less electrons in the outer shell and poor catalysts as individual metals) exhibits pronounced synergetic effect of electrocatalytic activity. In this context, TiO₂ has shown unique hypo-hyper d-interaction with the metallic phase [5,6]. TiO₂ as an oxide material have high chemical stability, but it is non-conductive. Thus, it is used most commonly accompanied with carbon nanostructures as support material. Non-stoichiometric titanium oxides with high electrical conductivity could be potential substitution for carbon support within the electrode materials. Besides supportive role, Magneli phases behave as hypo d-phase, which interact with hyper d-metallic phase and contribute to the strong metal-support interaction (SMSI) [7,8]. As was mentioned in our previous work [9], the main disadvantage of Magneli phases as support material is the low specific surface area. The maximal achievement of the mechanical techniques for preparation of Magneli phases was the specific surface area in the range of $1.6–3.0 \text{ m}^2\text{g}^{-1}$ [10], instead of more than $250 \text{ m}^2\text{g}^{-1}$ in the case of carbon nanostructures [11].

The aim of this work is firstly, to examine a possibility of usage of Magneli phases as an electrocatalysts support material and secondly, to determine the effects of addition of non-noble metal – Co in the platinum or ruthenium metallic phase of electrocatalysts aimed for both hydrogen and oxygen evolution.

EXPERIMENTAL

As a catalyst support commercial The procedure for mechanical activation of Magneli phases, as well as the procedure for sol-gel

---

* To whom all correspondence should be sent.
E-mail: ppaunovik@gmail.com

preparation of the studied electrocatalysts is given in our previous work [9].

The composition of the prepared electrocatalysts is shown in Table 1.

Table 1. Composition of the studied electrocatalysts

	Metallic phase (hyper d-phase)	**Support (hypo-phase)**
	10%, wt.	**90%, wt.**
E-1	Co	Ebonex
E-2	Pt	Ebonex
E-3	Ru	Ebonex
E-4	CoPt, 1:1, wt.	Ebonex
E-5	CoRu, 1:1, wt.	Ebonex
E-6	CoPtRu, 1:0.5:0.5, wt.	Ebonex

Electrocatalytic activity of the studied electrocatalysts was tested by means of steady-state galvanostatic method. The measurements were performed using AMEL equipment (Function Generator AMEL 568, Potentiostate/Galvanostate 2053 and software package SOFTASSIST 2.0). As working electrodes three-phase gas-diffusion electrodes were used, prepared by hot pressing at 300 ºC and pressure of 300 kgcm^{-2} [12]. It consists of two layers: i) the electrolyte-side layer, covered by catalyst with low amount of PTFE, and ii) the gas-side layer consisted of carbon black bonded with PTFE.The counter electrode was of platinum wire, while Hg/HgO was used as a reference electrode. The electrolyte was an aqueous solution of 3.5 M KOH (p.a., Merck) at room temperature.

RESULTS AND DISCUSSION
Electrochemical characterization for HER

Electrocatalytic activity for both hydrogen and oxygen evolution was observed by steady-state galvanostatic measurements of overpotentials at different current densities. The results of $i \div \eta$ measurements for hydrogen evolution are summarized in Fig. 1. Also, Tafel slopes and corresponding exchange current densities (i_0) were determined in the region of low current densities. This is illustrated in Fig. 2, for sample E-1. Determined values of Tafel slopes and current densities are summarized in Table 2, where also, the corresponding overpotentials for hydrogen evolution at a reference current density of 80 mAcm^{-2} (η_{80}) are given.
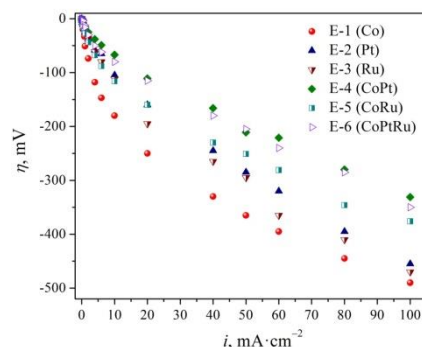
Fig. 1. Polarization curves of the studied electrocatalysts for HER in the plot $i \div \eta$.
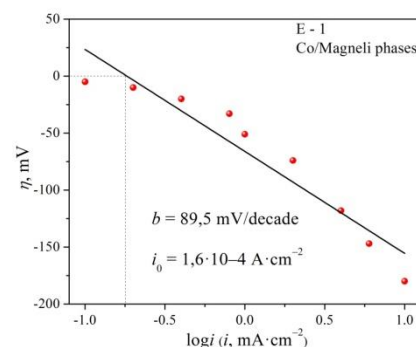
Fig. 2. Polarization curves of the studied electrocatalysts for HER in the plot $\log i \div \eta$, in region of low current densities

Generally, the monometallic electrocatalysts have shown lower activity for HER than the multimetallic ones, wherein the order of activity is as follows: E-2 (Pt) > E-3 (Ru) > E-1 (Co). This is the expected order according to the intrinsic activity of the studied metallic systems [13] as well as to the determined values of i_0 shown in Table 2. Considering that the sample E-2 (pure Pt as metallic phase) has the lowest specific surface area (almost 3 times than Ru, E-3 and 1.5 times than Co, E-1), one can notice that in monometallic systems, the intrinsic effect of electrocatalytic activity is more pronounced than the size effect.

Multimetallic electrocatalysts have shown considerably better activity for HER than monometallic ones. According to TEM and BET analysis (see ref. [9] in this issue), as well as to electrochemical results (Table 2), the improved activity in different electrocatalysts is result of size and/or intrinsic effect. The impact of size and intrinsic effect will be analyzed separately for each multimetallic system.

Table 2 Electrochemical indicators for electrocatalytic activity of the studied catalytic materials for HER and OER, BET surface area presented in [9]

Sample	10% metallic phase + 90% Ebonex	BET s. a., $m^2 \cdot g^{-1}$	b, $mV \cdot dec^{-1}$	i_0, $A \cdot cm^{-2}$	η_{80}, mV	η_{80}, mV
			HER			OER
E-1	Co	6.1	90	$1.60 \cdot 10^{-4}$	−445	475
E-2	Pt	4.3	46	$1.80 \cdot 10^{-4}$	−395	490
E-3	Ru	11.0	52	$1.68 \cdot 10^{-4}$	−410	450
E-4	CoPt, 1:1, wt.	7.6	31	$1.90 \cdot 10^{-4}$	−280	455
E-5	CoRu, 1:1, wt.	9.4	54	$1.79 \cdot 10^{-4}$	−345	400
E-6	CoPtRu, 1:0.5:0.5, wt.	6.4	40	$2.20 \cdot 10^{-4}$	−285	430

Firstly, to see how addition of non-noble metal – cobalt affects the electrocatalytic activity of platinum, comparing the results for sample E-4 (CoPt) and E-2 (Pt). The quantity of Pt in the bimetallic sample E-4 is twice lower than that of monometallic platinum based sample E-2, while the catalytic activity is considerably higher (–280 mV for E-4 vs. –395 mV for E-2, See Tab. 2). According to the values of particle size (TEM and XRD analysis [9]), BET surface area and exchange current densities, one can conclude that improvement of catalytic activity with addition of Co in Pt is result of both, size and intrinsic effect. The size effect is reflected in the considerably smaller (near 4 times) platinum particles in the bimetallic CoPt system E-4 (2 to 3 nm), compared with the pure Pt system E-2 (5 to 15 nm). It was already shown that Co behaves as promoter to reduce the size of platinum particles [14–16]. The smaller metallic particles affect on the increasing of the specific BET surface area of the catalyst as a whole (4.3 m^2g^{-1} for E-2 vs. 7.6 m^2g^{-1} for E-4) and consequently on better catalytic activity. Therefore, the size effect can be seen in the smaller metallic particles as an active catalytic centers over the catalyst's surface as well as in the higher BET surface area of the bimetallic catalyst as a whole. According to the values of exchange current densities (1.8.10^{-4} Acm^{-2} for E-2 vs. 1.9.10^{-4} Acm^{-2} for E-4), there is also an enhancement of intrinsic electrocatalytic activity. This means that there is a synergetic interaction between metallic phases in the bimetallic electrocatalysts E-4 (PtCo). This interaction comprises modification of electronic properties (electronic density and average electron configuration) of certain metallic phase in presence of the other one [17]. For better understanding of the synergetic interaction, so-called "d-band center theory" can be used, explained elsewhere [17–20]. The position of d-band has leading role in determining the affinity of d-metals to adsorption of variety of adsorbates, such as H, O, CO etc. The higher the d-band center lies regarding the Fermi level, the better is the interaction metal–adsorbate. The metals with larger atomic radius and electronegativity up-shift d-band center of Pt, thus improving its adsorptive ability and consequently, accelerate the overall electrode reaction. Theoretically, this does not occur in the case of addition of Co to Pt, because Co has smaller atomic radius than Pt. But, Nørskov and collaborators [18,19] have shown that as the Pt particles are smaller, the d-band center is approaching to Fermi level, achieving better adsorption of adsorbates. So, Co can not affect this synergism, but indirectly, through reduction of Pt nanoparticles causes the same synergetic effect.

Improvement of the catalytic activity of sample E-6 (CoRuPt) can be explained similarly. The catalytic activity is slightly lower (only 5 mV) than that of sample E-4 (CoPt), but in this case the quantity of platinum in the metallic phase is only 25 %.

Now to see how the addition of Co in the Ru improves electrocatalytic activity, comparing the results for samples E-5 (CoRu) and E-3 (Ru), where the overpotential for HER was decreased from –410 mV for monometallic catalyst (E-3) to –345 mV for bimetallic catalyst (E-5). Firstly, the size effect is considered. Specific BET surface area [9] of the sample E-5 (9.4 m^2g^{-1}) is lower than that of monometallic sample E-3 (11 m^2g^{-1}). Also, the average size of particle of bimetallic sample is slightly higher (2 to 4 nm for sample E-5 vs. 2 to 3 nm for sample E-3). These results highlight that there is not a size effect. On the other hand, the values of exchange current densities (1.68.10^{-4} Acm^{-2} for E-3 and 1.79.10^{-4} Acm^{-2} for E-5) point out that improvement of catalytic activity of bimetallic electrocatalysts E-5 is result only of intrinsic effect, i.e. of synergetic interaction between the present metals.

Generally, the activity of the studied electrocatalysts for HER is not so high compared with electrocatalysts deposited on nano-scaled carbon support material [15,21], mainly due to large

particles of the Magneli phases (180-200 nm) and consequently low specific surface area (4.2 vs. 250 m^2g^{-1} and more for nanoscaled carbon materials). Also, one should mention that the amount of metallic phase in the electrocatalysts is low, only 10 %.

Electrochemical characterization for OER

Polarization curves for oxygen evolution are shown in Fig. 3.
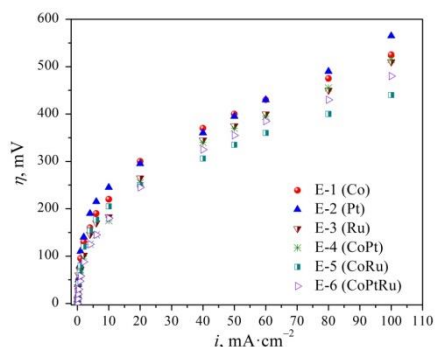
Fig. 3. Polarization curves of the studied electrocatalysts for OER

The order of activity of the monometallic samples is the follow: E-3 (Ru) > E-1 (Co) > E-2 (Pt). According XRD analysis [9], Ru surface structure was in oxidized state (oxides and/or hydroxides), and it is known that oxidized Ru is one of the most active electrodes for oxygen evolution [22]. The better activity of Co than that of Pt is result of higher specific surface area (6.1 vs. 4.3 m^2g^{-1}), but also, due to early transition of Co to Co(II) and then to Co(III) [21]. This oxidized surface is covered with hydroxyl groups, in so-called sandwich-structure Co/CoO/ Co(OH)$_2$ during Co(0) to Co(II) transformation [23] and sandwich-structure CoO/Co(OH)$_2$/Co$_3$O$_4$ during Co(II) to Co(III) transformation [24], which is an appropriate to accelerate oxygen evolution.

Similarly to HER, multimetallic electrocatalysts have shown better catalytic activity and for OER than the corresponding monometallic systems. Improvement of the catalytic activity for OER can be explained on the same way as was explained that for HER above. As the most active catalyst for OER sample E-5 based on CoRu has been shown. As was already shown, the improvement of catalytic activity in this system is result only of intrinsic effect, i.e. of synergetic interaction between Ru as the most active individual catalyst for OER and Co which has shown good individual catalytic activity for OER.

In contrast to the poor activity for hydrogen evolution, these catalytic systems have shown good activity for oxygen evolution, compared to other

electrocatalysts [14, 25-27]. Besides the electrode surface composition of the metallic phase (Co and Ru are in oxidized state at potentials close to oxygen evolution region), in this case, Magneli phases behave not only as support material, but also, as an active oxidized electrode. The surface structure in the electrolyte is a characteristic that distinguishes the oxide electrodes [28]. Their surface is characterized with high energy content and strong hydrophylicity, making it easier to interact with water molecules and to cover the top of oxide with layer of OH$^-$ ions. This layer mediates the action of the oxide's surface with the electrolyte species. The OH$^-$ groups are responsible for the exhibited electrocatalytic activity. The mechanism of surface charging of oxidized catalysts is quite different from that of bare metal surfaces, since it is governed by the pH-dependent acid–base dissociation of the surface OH$^-$ ions. Behaving as weak acids or basis, these groups exchange protons with the electrolyte. This is the basis of the mechanism by which the inner sites can be active in reactions involving water molecules [29].

CONCLUSIONS

This research was motivated by the idea to reduce the amount of noble metals in the electrocatalysts, studying the addition of non-noble metal Co in platinum or ruthenium metallic phase. According to the presented results the following conclusions can be drawn:

1. Addition of cobalt in platinum or in ruthenium considerably increases the catalytic activity of pure Pt or Ru for both hydrogen and oxygen evolution. In the Pt based systems this is due to both size and intrinsic effect, while in the case of Ru, this is result only of intrinsic effect. Co has shown as promoter for reducing of Pt particles (size effect), while smaller Pt particles cause the d-band center to approach to Fermi level, achieving better adsorption of adsorbates. As a total effect, considerably higher catalytic activity was achieved with double lower amount of platinum in the multimetallic systems than that of pure metallic catalysts.

2. The studied electrocatalytic systems have shown poor activity for hydrogen evolution due to large particles (180-200 nm) and low specific surface area (4.2 m^2g^{-1}) of the catalyst support – Magneli phases. One should be considered and the low amount of the metallic phase in the electrocatalysts of only 10 %. Contrary to the inferior activity for hydrogen evolution, the studied electrocatalysts have shown very satisfactory activity for oxygen evolution. In this case, Magneli

phases behave not only as support material, but also, as an active oxidized electrode.

Therefore, an appropriate "bottom-up" technique for preparation of Magneli phases should be applied to obtain support material in nanodimensions (20 to 50 nm) instead of the presented mechanical treatment. This would improve considerably the catalytic activity for hydrogen evolution, while extra-ordinary catalytic activity for oxygen evolution should be expected.

REFERENCES

1. K. Lee, J. Zhang, H. Wang, D. P. Wilkinson, *J. Appl. Electrochem.,* **36,** 507 (2006).
2. P. Paunović, O. Popovski, A. T. Dimitrov, in: Nanotechnological Basis for Advanced Sensors, J.P. Reithmaier, P.Paunović, W. Kulish, C. Popov, P. Petkov (eds), Springer Science+Business Media B.V., p. 545. (2011).
3. M. M. Jakšić, *Mater. Chem. Phys.,* **22,** 1 (1989).
4. M. M. Jakšić, *J. Mol. Catal.*, **38,** 161 (1986).
5. S. J. Tauster, S. C. Fung, R. L. Garten, *J. Am. Chem. Soc.,* 100, 170 (1978).
6. S. G. Neophytides, S. Zaferiatos, G. D. Papakonstantnou, J. M. Jakšić, F. E. Paloukis, M. M. Jakšić, *Int. J. Hydrogen Energy*, **30**, 131 (2005).
7. J. M. Jaksić, N. V. Krstajić, Lj. M. Vračar, S. G. Neophytides, D. Labou, P. Falaras, M. M. Jaksić, *Electrochim. Acta*, **53**, 349 (2007).
8. M. M. Jakšić, *J. New Mater. Electrochem. Syst.*, **3**, 153 (2000).
9. P. Paunović, O. Popovski, G. Načevski, E. Lefterova, A. Grozdanov, A. T. Dimitrov, *Bulg. Chem. Com.*, this issue.
10. E. Antolini, E. R. Gonzales, *Solid State Ionics,* **180**, 746 (2009).
11. P. Serp, M. Corrias, P. Kalck, *Appl. Catal.*, **A, 253**, 337 (2003).
12. BG patent appl. no 38581; 1978.
13. H. Kita, *J. Electrochem. Soc.*, **113**, 1095 (1966).
14. E. Slavcheva, V. Nikolova, T. Petkova, E. Lefterova, I. Dragieva, T. Vitanov, E. Budevski, *Electrochim. Acta*, **50**, 5444 (2005).
15. P. Paunović, I. Radev, A. T. Dimitrov, O. Popovski, E. Lefterova, E. Slavcheva, S. HadžiJordanov, *Int. J. Hydrogen Energy*, **34**, 2866 (2009).
16. A. E. Stoyanova, E. D. Lefterova, V. I. Nikolova, P. T. Iliev, I. D. Dragieva, E. P. Slavcheva, *Bulg. Chem. Com.*, **42**, 167 (2010).
17. S. Papadimitriou, A. Tegou, E. Pavlidou, S. Armyanov, E. Valova, G. Kokkinidis, S. Sotiropoulos, *Electrochim. Acta.*, **53**, 6559 (2008).
18. P. Norlander, J. K. Nørskov, F. Besenbacher, *J. Phys. F: Met. Phys.*, **16**, 1161 (1986).
19. J. K. Nørskov, T. Bligaard, A. Logadottir, S. Bahn, L. B. Hansen, M. Bollinger, H. Bengaard, B. Hammer, Z. Sljivancanin, M. Mavrikakis, Y. Xu, S. Dahl, C. Jacobsen, *J. Catal.*, **209**, 275 (2002).
20. R. Ojani, J. BakhshRaoof, E. Hasheminejad, *Int. J. Hydrogen Energy,* **38,** 92 (2013).
21. P. Paunović, D. StoevskaGogovska, O. Popovski, A. Stoyanova, E. Slavcheva, E. Lefterova, P. Iliev, A. T. Dimitrov, S. HadžiJordanov, *Int. J. Hydrogen Energy*, **36**, 9405 (2011).
22. S. Trasatti, *Electrochim. Acta*, **29**, 1503 (1984).
23. N. Sato, T. Ohtsuka, *J. Electrochem. Soc.*, **125**, 1735 (1978).
24. L. D. Burke, O. J. Murphy, *J. Electroanal. Chem.,* **109**, 373 (1980).
25. S. Siracusano, V. Baglio, C. D'Urso, V. Antonucci, A. S. Aricò, *Electrochim. Acta*, **54**, 6292 (2009).
26. M. García-Mota, A. Vojvodić, H. Metiu, I.C. Man, H-Y. Su, J. Rossmeisl, J. K. Nørskov, *Chem. Cat. Chem.,* **3**, 1607 (2011).
27. A. Stoyanova, G. Borisov, E. Lefterova, E. Slavcheva, *Int. J. Hydrogen Energy*, **37**, 16515 (2012).
28. S. HadžiJordanov, Bull. *Chem. Technol. Macedonia*, **16**, 75 (1997).
29. J. C. F. Boodts, S. Trsatti, *J. Appl. Electrochem.*, **19**, 255 (1989).

ЕЛЕКТРОКАТАЛИЗАТОРИ С НАМАЛЕНО СЪДЪРЖАНИЕ НА БЛАГОРОДНИ МЕТАЛИ ЗА ОТДЕЛЯНЕ НА ВОДОРОД/КИСЛОРОД С МАГНЕЛИ ФАЗИ КАТО КАТАЛИТИЧЕН НОСИТЕЛ. ЧАСТ II: ЕЛЕКТРОХИМИЧНО ОХАРАКТЕРИЗИРАНЕ

П. Паунович[1], О. Поповски[2], Г. Начевски[1], А. Грозданов[1] и А. Т. Димитров[1]

[1]*Технологичен и металургичен факултет, Университет "Св. Кирил и Методий", ул. Руджер Бошкович 16, 1000 Скопие, Република Македония*
[2]*Военна академия "Михайло Апостолски", ул. Михайло Апостолски, 1000 Скопие, Република. Македония*

(Резюме)

Предмет на това изследване е електрохимично тестване на наноразмерни електрокатализатори, състоящи се от Магнели фази като носител и различни метални фази (Co, Pt, Ru, CoPt (Co:Pt = 1:1 тегл.), CoRu (Co:Ru = 1:1 тегл.) и CoPtRu (Co: Pt: Ru = 1:0,5:0,5 тегл.)). Електрокаталитичните материали са синтезирани по зол-гел метода, като са използвани органометални прекурсори (Ме-ацетилацетонат), нанесени върху диспергирани Магнели фази в тегловно съотношение 10% Ме и 90% Магнели фази.

Електрохимичното тестване на изследваните електрокатализатори се извършва във воден алкален електролит. Редът на активността за отделяне на водорода е следният: CoPt > CoPtRu > CoRu, докато за отделянето на кислорода: CoRu > CoPtRu > CoPt. Co се проявява като промотор за намаляването на размера на Pt частиците (най-активната монометална фаза), така че намаляването на количеството Pt в металната фаза е компенсирано с по-малки частици. Също така взаимодействието между металните фази (преместването на центъра на d-нивото до стойности по-близки до нивото на Ферми) увеличава вътрешната каталитична активност, както за отделянето на водород, така и за кислорода. Поради големите частици на Магнели фазите, каталитичната активност е по-ниска в сравнение със съответните електрокатализатори, нанесени върху въглеродни наноматериали. Но те са много добри катализатори за отделянето на кислорода, тъй като Магнели фазите в този случай се държат не само като субстрат, но и като активен оксиден електрод.

Ключови думи: Магнели фази, Co, Pt, Ru, отделяне на водород, отделяне на кислород.

Characterisation of La$_{0.6}$Sr$_{0.4}$Co$_{0.2}$Fe$_{0.8}$O$_{3-\delta}$- Ba$_{0.5}$Sr$_{0.5}$Co$_{0.8}$Fe$_{0.2}$O$_{3-\delta}$ composite as cathode for solid oxide fuel cells

M. P. Carpanese[1,2], D. Clematis[1*], M.Viviani[2], S. Presto[2], M. Panizza[1], G. Cerisola[1], A. Barbucci[1,2]

[1]Department of Civil, Chemical and Environmental Engineering (DICCA), University of Genoa, P. le J. F. Kennedy 1, I-16129 Genova, Italy
[2]Institute of Condensed Matter Chemistry and Technology for Energy, National Research Council (CNR-ICMATE), Via De Marini 6, 16149 Genova, Italy

Mixture of La$_{0.6}$Sr$_{0.4}$Co$_{0.2}$Fe$_{0.8}$O$_{3-\delta}$ and Ba$_{0.5}$Sr$_{0.5}$Co$_{0.8}$Fe$_{0.2}$O$_{3-\delta}$, was investigated as promising cathode for intermediate temperature solid oxide fuel cells (IT-SOFCs). The two perovskites possess high catalytic activity for the oxygen reduction (ORR), although some problems related to their chemical and structural stability have still to be overcome in view of improving durability of the cell performance. The achievement of a stable and high-performing composite material is the aim of this study. In principle, chemical equilibrium at the LSCF-BSCF interface may be reached through ions interdiffusion during the sintering process, resulting in the chemical stabilization of the material. The composite-cathode deposited on Ce$_{0.8}$Sm$_{0.2}$O$_{2-\delta}$ electrolyte was then investigated by Electrochemical Impedance Spectroscopy (EIS) as a function of temperature, overpotential and time. The results exhibited an interesting electrochemical behavior of the electrode toward oxygen reduction reaction. XRD analysis was performed to detect structural modification during thermal or operation stages and it was found that after the sintering the two starting perovskites were no longer present; a new phase with a rhombohedral La$_{0.4}$Sr$_{0.6}$FeO$_3$-type structure (LSF) is formed. An improvement in composite cathode durability has been detected under the considered operating conditions (200 mAcm^{-2}, 700 °C) in comparison with the pure BSCF electrode. The results confirmed this new electrode as promising system for further investigation as IT-SOFC cathode.

Keywords: SOFC cathode, long-term stability, LSCF-BSCF.

INTRODUCTION

One of the main goals for solid oxide fuel cells is the reduction of operating temperature below 800 °C to improve long-term stability and reduce costs. On the other hand the lowering of operating temperature causes a reduction in performance, mainly due to the high activation energy required for oxygen reduction reaction at the cathode [1,2].

Different efforts have been made to investigate new kind of materials and microstructure with the aim to understand which phenomena are responsible of the cathode performance changes as a function of time, thermal cycling, operating conditions and others factors [1,3–5].

One class of materials widely investigated are perovskite, with a general formula ABO$_3$; the A-site is occupied by lanthanides or alkaline earth metals, B-site contains cations of transition metal as Fe and Co. In particular the attention has been focused on the materials that shown a large ionic and electronic conductivity with a good electrocatalytic reduction of oxygen [6].

Ba$_{0.5}$Sr$_{0.5}$Co$_{0.8}$Fe$_{0.2}$O$_{3-\delta}$ (BSCF) and La$_{0.6}$Sr$_{0.4}$Co$_{0.2}$Fe$_{0.8}$O$_{3-\delta}$ (LSCF) are two perovskites evaluated as promising cathode materials by several studies [7,8]. Excellent properties of BSCF were presented by Shao et al. [9] at the beginning of 2000.

This material showed a very high performance for temperature lower than 600 °C.

LSCF has been considered a possible electrode material thank to its electronic conductivity, over 300 S·cm^{-1} and oxygen conductivity near to 0.1 S·cm^{-1} at 800 °C, with consequent good results [10,11].

Nevertheless these two materials are affected by two main problems: stability and durability. LSCF suffers of La and Srinter diffusion pointed as the reason of degradation; in fact the cation interdiffusion to electrode/electrolyte interface leads to the formation of an insulating phases as La$_2$Zr$_2$O$_7$ (LZO) or SrZrO$_3$ (SZO) when yttrium stabilised zirconia (YSZ) is used as electrolyte [12,13]. The presence of these phases has a negative effect on ionic conductivity, reducing the global cell performance. A possible solution, to avoid the formation of the insulating layer, is the application of an interlayer made by Gd$_{0.2}$Ce$_{0.8}$O$_{3-\delta}$ (GDC) or Sm$_{0.2}$Ce$_{0.8}$O$_{3-\delta}$ (SDC) between cathode and electrolyte or as directly as electrode [13,14].

A further solution to block the Sr segregation is the modification of surface chemistry through the infiltration technique. In this case LSCF cathode backbone was infiltrated by a stable compound rich

* To whom all correspondence should be sent.
E-mail: davide.clematis@edu.unige.it

© 2018 Bulgarian Academy of Sciences, Union of Chemists in Bulgaria 95

in Sr[15], with the formation of a phase spread over all the surface. Other possible technique proposed by different authors are the preparation of composite materials [16–18] or the introduction of A-site deficiency.

About BSCF structural instability represents the main issue; the material for temperature below 900 °C suffers a phase transition and the cubic active phase evolves into an hexagonal structure that has a lower catalytic activity. The literature attributes this instability to a lattice distortion [22,23] caused by the changing valence of B-site cations, and also by doping quantity of A-site cations [25]. A second, but relevant problem, which affects BSCF is the formation of carbonates if exposed to CO_2 containing atmosphere, even for low concentration [28,29].

Known the problems introduced above, the aim of this study is exploit the excellent properties of these two materials, through a composite cathode made mixing the two powders. The base of the investigation is the assumption that the mixing could result in their mutual structural stabilisation, preserving a sufficient electrocatalytic activity. The composite electrode was investigated under structural, microstructural and electrochemical point of view. Influence of operating temperature and applied overpotential were investigated through equivalent circuit analysis and also a long-term stability behaviour was observed. Obtained results were compared with those obtained from LSCF and BSCF pure electrode.

EXPERIMENTAL

A set of samples of technically pure The LSCF-BSCF composite powder was prepared by mixing 50 vol. % LSCF (Fuel Cell Materials) and 50 vol. % BSCF (Treibacher) powders in ethanol, through a low energy ball milling for 20 hours at R.T.

The obtained paste was freeze-dried for 24 hours at -40 °C and 0.22 mbar (Labconco Free Zone 2.5), then, sieved for 30 minutes to separate powder from balls.

Electrolyte substrates were fabricated from $Ce_{0.8}Sm_{0.2}O_{2-\delta}$ powders (SDC20-HP, Fuel Cell Materials) by cold pressing at 60 MPa, followed by one-step sintering at 1450 °C for 5 hours in air. The resulting electrolyte disks had a diameter of 25 mm and a thickness of 1.2 mm.

The LSCF-BSCF composite powders were mixed in a mortar with alpha-therpineol (techn. 90%, Sigma Aldrich) to obtain a mixture suitable for deposition. The ink was deposited by slurry coating, using a shaped-mask and a blade to obtain symmetrical layers on both sides of the SDC pellets, thus obtaining working electrode, WE, and counter

96

electrode, CE. On one side of the cell a ring reference electrode, RE, used for three-electrode measurements and made by the same cathode slurry, was deposited around the WE. Its distance was equal to 3 times the electrolyte thickness, in order to avoid possible reference electrode polarization [30,31]. Sintering followed at 1100 °C for 2 hours. The thickness of the porous sintered electrodes was 30 µm while the geometric electrode area was about 0.28 cm². Composition mismatches and asymmetry of the electrodes were carefully considered to avoid appearance of artifacts in the impedance spectra [32].

Electrochemical impedance spectroscopy was used to investigate the electrocatalytic activity of the composite cathode in the three-electrode configuration. The sample was placed in a lab-constructed test station [33]. Pt meshes were placed as current collectors on the surface of the WE and CE and connected by Pt wires to a potentiostat coupled to a frequency response analyser (Autolab PSSTAT302N).

Impedance measurements were performed in the temperature range of 500-800 °C, at open circuit voltage (OCV) and at applied cathodic overpotentials (up to -0.2 V), by applying a perturbation of 10 mV in a 0.1 Hz - 100 kHz frequency range.

To analyse the cathode degradation a direct current (dc) load of 200 mA·cm⁻² was applied for 200 h, while the impedance measurements were collected at OCV after interruption of the load at different times.

To understand the kinetic of the reaction process, all the impedance data were analysed by ZView© software (Scribner Associates Inc.), using an equivalent circuit (EC) to model the cathode behaviour. The selected EC was formed from an electrolyte resistance (R_s) connected in series with two sub-circuits, each composed by a resistance (R) in parallel with a constant phase element (CPE).

In order to identify the crystalline phases and any second phase, the composite powder, the as sintered electrode and the tested electrode were analysed by X-ray diffraction (XRD), using a PAN analytical X'pert diffractometer with Cu-K_α incident radiation. The spectra were collected over the angular range $20° < 2\square < 90°$, in a constant scan mode with steps of 0.02° and a counting time of 40 s.

The microstructural investigation was performed through a Scanning Electron Microscopy (Hitachi SU3500) equipped with EDX detector. The porosity of the electrode was determined by an image analysis (Image J software).

RESULTS AND DISCUSSIONS

Fig. 1 reports the cross-section of the cathode/electrolyte interface, after the sintering of the mixed powders at 1100 ° for 2 h. The electrode structure is well-interconnected, though the porosity appears a little irregular. From the same image a good adhesion at the electrode/ electrolyte interface was detected.
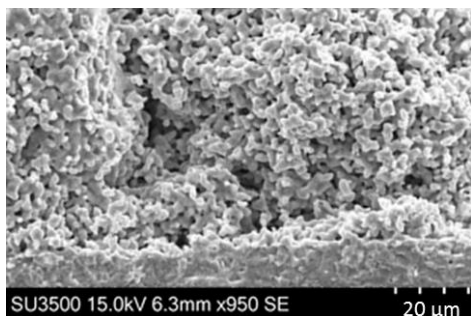
Fig. 1. Image of cross section of the cathode/electrolyte interface after the sintering treatment at 1100 °C x 2 h.

The XRD analysis of the LSCF – BSCF composite electrode, as sintered cathode and after electrochemical testing do not show any evident formation of new phases (Fig. 2a). The electrode structure is stable, however the original powders structure has remarkably changed during the sintering thermal treatment. In fact excluding the highest peaks attributed to the SDC substrate LSCF and BSCF phase (Fig 2b) were no longer detected after the sintering step. While, it is possible to identify a new phase with a rhombohedral La$_{0.4}$Sr$_{0.6}$FeO$_3$-type structure (LSF).

However, from these results it is not possible to exclude the presence of a La$_{0.5}$Ba$_{0.5}$CoO$_3$ Co-rich cubic phase (LBC), because all its peaks are completely overlapped with those of LSF.
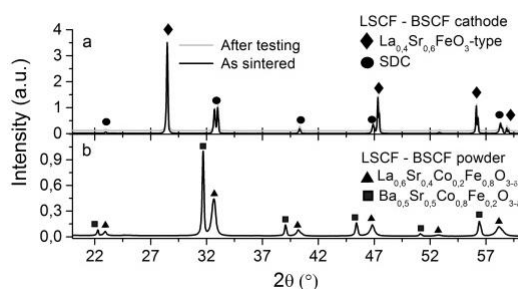
Fig. 2. (a) XRD spectra of the LSCF-BSCF composite cathode after sintering at 1100 °C x 2h (as-sintered, black pattern) and after testing (grey pattern). (b) XRD spectra of the LSCF – BSCF powder after mechanical mixing

It is evident that during the sintering stage a strong interdiffusion between the starting ceramic powders occurred, leading to a heavy structural

modification involved not only the interface between the two materials but the entire composite volume. Further investigation to better clarify the nature of the new electrode structure is object of future studies.

The Polarization resistance (R$_P$) of the composite cathode was obtained from electrochemical impedance spectroscopy analysis (EIS) on the composite half-cell in three electrode configuration. Fig. 3 summarizes the values obtained at different temperature. In this graph the composite cathode resistance was compared with those obtained for LSCF and BSCF pure electrode deposited on SDC substrate. Polarization resistance of the composite stays between those of BSCF and LSCF in the whole temperature range. Considering the Arrhenius behaviour the apparent activation energies (E$_{act}$) was calculated. The composite had the lowest valued 1 eV (96 kJ mol^{-1}), while BSCF and LSCF had E$_{act}$ of 1.18 eV (113 kJ mol^{-1}) and 1.52 eV (147 kJ mol^{-1}), respectively. The values extrapolated for the pure cathode were in accordance with literature (BSCF ~ 116 kJ mol^{-1}[9,40], LSCF ~ 140 kJ mol^{-1}[41]).

The low E$_{act}$ for the composite pointed out that this electrode is more active than BSCF at low temperature, while its higher value for R$_P$ could be attributed to small geometrical differences between the two porous structures.
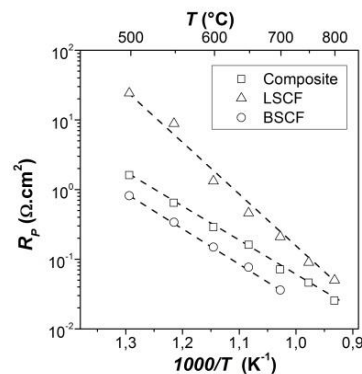
Fig. 3. Polarisation resistance (R$_p$) versus temperature for the composite and commercial LSCF and BSCF cathodes. Calculated activation energies values: BSCF, 1.18 eV (113 kJ mol^{-1}); composite, 1 eV (96 kJ mol^{-1}); LSCF, 1.52 eV (147 kJ mol^{-1}).

The impedance spectra were analysed. considering Jamnik interpretation [42], in agreement with different studies on mixed ionic electronic conductors [38,39,43,44]. In this analysis a well-known equivalent circuit was chosen as reported in the inset of Fig. 4.

The equivalent circuit was made by a resistance (R$_s$), ascribed to electrolyte resistance, in series with two identical sub-circuits. The first R$_{HF}$//CPE$_{HF}$ describes the high frequency part, and was associated to the charge transfer at the interface

between cathode and electrolyte; the second sub-circuit, R$_{LF}$//CPE$_{LF}$ (low frequency), was linked to the electrode mechanism. In particular was assumed that R$_{HF}$ described the surface oxygen exchange resistance, and CPE$_{HF}$ was related to the charge stored in the cathode volume due to its high values (1 ÷ 3 F cm^2) [45,46], and therefore was considered as a chemical capacitance. Fig. 4 shows experimental and fit curves, and confirms that this circuit is able to provide a good quality fitting at different temperature.
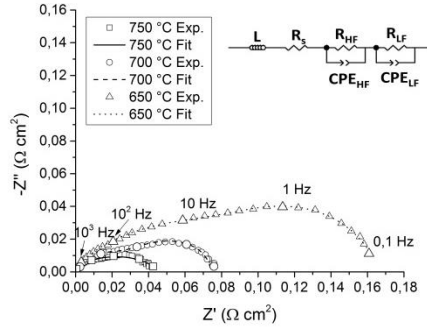
Fig. 4. Composite cathode impedance spectra obtained in the three-electrode configuration at 750 °C (□), 700 °C (○) and 650 °C (△) at OCV condition mol^{-1}); LSCF, 1.52 eV (147 kJ mol^{-1}).

To obtain equivalent capacitance C$_{LF}$ and C$_{HF}$ from constant phase (CPE) parameters the following equation was used:

$$C_{eq} = R^{\frac{1-n}{n}} \cdot Q^{\frac{1}{n}} \qquad (1),$$

where R is the resistance of the R//CPE element (R$_{LF}$ or R$_{HF}$), Q is the module of the capacitance value and n is the exponential parameter [47].

Table 1 summarizes resistance and capacitance values as a function of temperature for the two sub-circuits. R$_{LF}$ and R$_{HF}$ trend indicates that both the processes are thermally activated. The reduction of C$_{HF}$ as a function of temperature described a lower charge accumulation at the interface. Low frequency sub-circuit was connected with gas-electrode

interaction (R$_{LF}$) and electrode activity (C$_{LF}$). The very low R$_{LF}$ values calculated confirmed a high performance for the oxygen surface exchange for composite cathode, while the chemical capacitance directly related with the oxygen vacancy concentration reached a maximum between 600 and 650 °C and then decreased.

Table 1: EIS fitting parameters for composite cathode as a function of temperature

Temperature	R$_{HF}$	R$_{LF}$	C$_{HF}$	C$_{LF}$
500 °C	0.374	1.825	0.395	0.913
550 °C	0.092	0.774	0.341	0.955
600 °C	0.053	0.268	0.167	2.763
650 °C	0.052	0.115	0.093	3.193
700 °C	0.027	0.052	0.067	1.49
750 °C	0.011	0.031	0.075	0.932

The composite cathode was investigated by EIS also in real cathodic conditions, applying a dc overpotential (η). Total polarization resistance (R$_p$) for composite cathode increases up to an application of -80 mV and remain constant at higher η. BSCF and LSCF showed an opposite behaviour; the first increases its R$_P$ while the second reduces R$_P$ when an overpotential was applied.

Fig. 5 reports R$_{LF}$ (Fig. 5a) and C$_{LF}$ (Fig. 5b) trends as a function of η for all three tested cathodes. In literature is well reported that the application of η to LSCF cathode promotes the formation of new vacancies, enhancing the activity for ORR with a decreasing of R$_{LF}$[44,48,51,52]. The behaviour describes above is recognisable in the two figures 5 (a and b). Composite R$_{LF}$ slightly decreases, indicating that the net flux of currents, generated by the applied cathode overpotential, helps surface activity. This higher surface activity can be due to the formation of new vacancies, as reported by Fig. 5b.
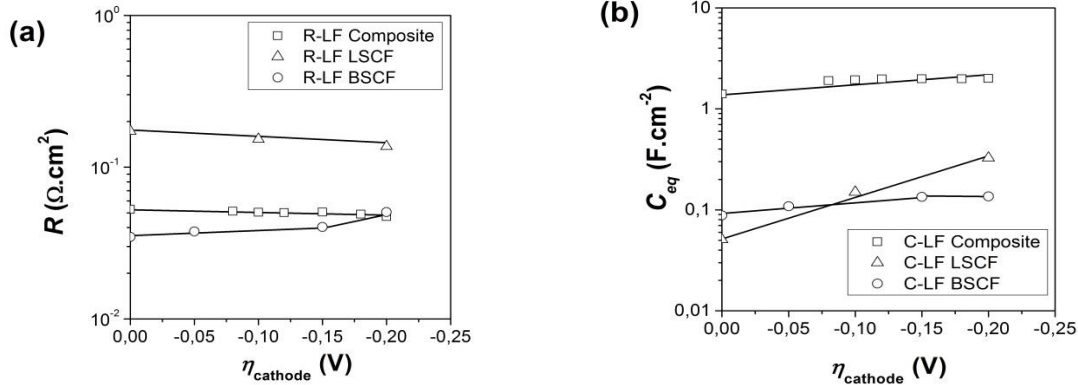
Fig. 5. (a) R$_{LF}$ and (b) C$_{LF}$, for composite (□), commercial LSCF (△) and commercial BSCF (○) cathodes

Furthermore, as regards C$_{LF}$ trend with η for the composite it shown an intermediate behaviour compared to the two starting materials. In fact, LSCF strongly increases its C$_{LF}$, while on BSCF a so strong effect was not detected. However the extremely high C$_{LF}$ value for composite, which means a higher ability to accommodate more oxygen vacancies, does not correspond to the lowest resistance and this behaviour remain an open issue. One key point for cathode materials is their long-term stability. A first ageing investigation on the composite cathode was performed and results compared with BSCF pure electrode, which is considered as reference electrode as regards performance but presents many problem of stability, as reported in the introduction. Ageing test was performed applying a current density of 200 mA·cm^{-2} at 700 °C, and every 12 hours impedance measurements at OCV was done to evaluate R$_P$.

Fig. 6 presents the R$_P$ trend for composite and BSCF cathode during an ageing test of 200 hours. The exposure time is in accordance with several literature works, that identified a period between 100-300 h as acceptable for a preliminary ageing test [53–56]. After 200 h composite cathode increased polarization resistance of about 5 %, which represents an important improvement if compared with the 38 % of degradation shown by BSCF under the same operation condition. Moreover another positive factor is the absence of carbonates after testing that indicates a good stability of composite material in CO$_2$-containing atmosphere.
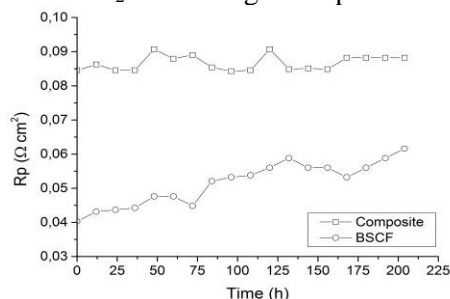
Fig. 6. Evolution of R$_p$ as a function of time for LSCF–BSCF cathode (□) and BSCF commercial cathode (○) during ageing with a current of 200 mA cm^{-2} at 700 °C.

A possible explanation of the composite performance loss could be due to some electrode morphological changes, as identified from SEM analysis (Fig. 7).

In fact, if the XRD analysis does not detected any structural modification after testing, from image analysis (Fig. 7a and 7b) a reduction of porosity (from 42 % to 35 %) was observed. The change of this parameter can affect polarization resistance, especially in the EIS low frequency arc, which describes oxygen surface exchange.

SEM images analysis highlighted also the formation on new nano-particles (~ 50 nm) on the

cathode surface. However, EDX analysis is not able to confirm chemical composition of these particles because of the substrate interference during the measurement. The presence of nanoparticles on the surface was observed also for BSCF electrodes [26,27,57]; in this case the interference with cathode performance seems to be limited and the presence of this segregate phase not affect the electrocatalytic activity.
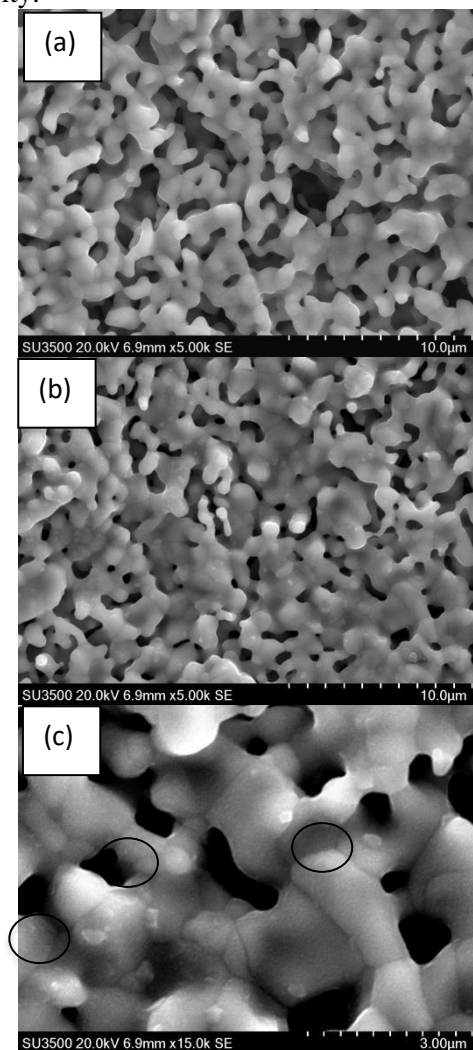
Fig. 7. SEM images of composite cathode surface before (a) and after (b, c) electrochemical test. In Figure (c) the circle identifies the formation of nanoparticles on the electrode surface

CONCLUSIONS

To our knowledge LSCF-BSCF composite electrodes are not yet studied in literature. The aim of this study was to obtain a mutual stabilisation between the two high-performing but unstable starting perovskites, without significantly losses on electrode performance. The electrode preparation is very easy by combining two commercial powders through a simple milling process.

99

The structural analysis performed on the powder and on the electrode, as sintered and after testing, showed that the two starting phases were no longer present after the sintering stage at 1100 °C. In other words, the starting composite was affected by a total structural transformation, which involved not only the interface but the whole cathode volume, resulting in a different electrode structure. The obtained new electrode globally demonstrated a high activity toward the ORR. In the range 500 – 800 °C an activation energy of 1 eV (96 kJ mol^{-1}) was calculated, quite low if compared to the values obtained for other MIEC materials. Moreover, the results of the ageing test performed under current load of 200 mA cm^{-2} gave evidence of an impedance degradation much lower that the degradation measured for BSCF under the same ageing conditions.

In conclusion, it is demonstrated that the composite LSCF-BSCF cathode is an interesting system, worth to be investigated for its possible application in IT-SOFCs.

REFERENCES

1. S.B. Adler, *Chem. Rev.***104,** 4791 (2004).
2. J.A. Kilner, M. Burriel, Annu. *Rev. Mater. Res.* **44,** 365 (2014).
3. M.R. Cesário, D.A. MacEdo, A.E. Martinelli, R.M. Nascimento, B.S. Barros, D.M.A. Melo, *Cryst. Res. Technol.,* **47**, 723 (2012).
4. M. Liu, M.E. Lynch, K. Blinn, F.M. Alamgir, Y. Choi, *Mater. Today.***14**, 534 (2011).
5. Q. Liu, X. Dong, G. Xiao, F. Zhao, F. Chen, *Adv. Mater.,* **22** , 5478 (2010).
6. T. Ishihara, *Solid Oxide Fuel Cells*, 1, 2009.
7. W. Araki, Y. Arai, J. Malzbender, *Mater. Lett.* **295**, 132 (2014).
8. E. Bucher, A. Egger, P.Ried, W. Sitte, P. Holtappels, *Solid State Ionics.,***179,** 1032 (2008).
9. Z. Shao, S.M. Haile, *Nature.***431,** 170 (2004).
10. A.Mineshige, J. Izutsu, M. Nakamura, K. Nigaki, J. Abe, M. Kobune, S. Fujii, T. Yazawa, *Solid State Ionics.,***176,** 1145 (2005) .
11. K. Lu, F. Shen, *Int. J. Hydrogen Energy.*, **39**, 7963 (2014).
12. R. Kiebach, W. Zhang, W. Zhang, M. Chen, K. Norrman, H. Wang, J.R. Bowen, R. Barfod, P. Vang, *J. Power Sources,* **283,** 151 (2015).
13. F. Wang, M. Nishi, M.E. Brito, H. Kishimoto, K. Yamaji, H. Yokokawa, T. Horita, *J. Power Sources,* **258,** 281 (2014).
14. M.Z. Khan, M.T. Mehran, R.H. Song, J.W. Lee, S.B. Lee, T.H. Lim, S.J. Park, *Ceram. Int.,* **42**, 6978 (2016).
15. M. Liu, M. Liu, D. Ding, K. Blinn, X. Li, L. Nie, *Int. J. Hydrogen Energy,* **37,** 8613 (2012).
16. Y. Leng, S.H. Chan, Q. Liu, *Int. J. Hydrogen Energy.* **33,** 3808 (2008).
17. H.J. Hwang, J.W. Moon, S. Lee, E.A. Lee, *J. Power Sources*, **145,** 243 (2005).
18. L. Agun, H. Abd. Rahman, S. Ahmad, A. Muchtar, *Adv. Mater. Res.,* **893,** 732 (2014).
19. S. Gangopadhayay, T. Inerbaev, A.E. Masunov, D. Altilio, N. Orlovskaya, ACS *Appl. Mater. Interfaces,* **1,** 1512 (2009).
20. D.N. Mueller, R. a De Souza, T.E. Weirich, D. Roehrens, J. Mayer, M. Martin, Phys. *Chem. Chem. Phys.,* **12,** 10320 (2010).
21. D.N. Mueller, R.A. De Souza, H.I. Yoo, M. Martin, *Chem. Mater.,***24**, 269 (2012).
22. S. Mcintosh, J.F. Vente, W.G. Haije, D.H.A. Blank, H.J. M. Bouwmeester, *Chem. Mater.,***18,** 2187 (2006) .
23. J.S. Kim, D.H. Yeon, D.W. Jung, C. Kwak, *J. Power Sources,***249,** 66 (2014).
24. M. Arnold, Q. Xu, F.D. Tichelaar, A. Feldhoff, *Chem. Mater,* **21,** 635 (2009).
25. S. Tanasescu, Z. Yáng, J. Martynczuk, V. Varazashvili, F. Maxim, F. Teodorescu, A. Botea, N. Totir, L.J. Gauckler, *J. Solid State Chem,* **200,** 354 (2013).
26. F. Deganello, L.F. Liotta, G. Marcì, E. Fabbri, E. Traversa, *Mater. Renew. Sustain. Energy,* **2,** 8 (2013) .
27. K. Efimov, Q. Xu, A. Feldhoff, *Chem. Mater,* **22,** 5866 (2010).
28. A. Yan, V. Maragou, A. Arico, M. Cheng, P. Tsiakaras, *Appl. Catal. B Environ,***76,** 320 (2007).
29. M. Arnold, H. Wang, A. Feldhoff, *J. Memb. Sci,* **293,** 44 (2007).
30. M. Cimenti, V.I. Birss, J.M. Hill, *Fuel Cells,***7,** 377 (2007).
31. J. Winkler, P.V. Hendriksen, N. Bonanos, M. Mogensen, *J. Electrochem. Soc.,* **145,** 1184 (1998).
32. M. P. Carpanese, A. Giuliano, M. Panizza, E. Mercadelli, A. Sanson, A. Gondolini, A. Bertei, A. Barbucci, *Bulg. Chem. Commun.,* **4,** 23 (2015) .
33. M.P. Carpanese, M. Panizza, M. Viviani, E. Mercadelli, A. Sanson, A. Barbucci, *J. Appl. Electrochem.* , **45,** 657(2015).
34. M. Koyama, C. Wen, K. Yamada, *J. Electrochem. Soc.,* **147,** 87 (2000).
35. M.C. Kim, S.J.A. Park, *J. Mater. Sci. Lett.,* **9,** 102 (1990).
36. M. V. Patrakeev, J.A. Bahteeva, E.B. Mitberg, I.A. Leonidov, V.L. Kozhevnikov, K.R. Poeppelmeier, *J. Solid State Chem.*, **172** , 219 (2003).
37. S. Pang, X. Jiang, X. Li, Q. Wang, Z. Su, *Int. J. Hydrogen Energy .***37,** 2157 (2012).
38. G.M. Rupp, A. Schmid, A. Nenning, J. Fleig, *J. Electrochem. Soc.*, **163,** F564 (2016).
39. R. Amin, K. Karan, *J. Electrochem. Soc.,* **157,** B285 (2010).
40. C. Duan, D. Hook, Y. Chen, J. Tong, R. O'Hayre, *Energy Environ. Sci.* **404,** 265 (2016).
41. J.M. Serra, J. Garcia-Fayos, S. Baumann, F. Schulze-Küppers, W.A. Meulenberg, *J. Memb. Sci.* **447,** 297 (2013).
42. J. Jamnik, J. Maier, *Phys. Chem. Chem.Phys.*, **3,** 1668 (2001).

43. J. Fleig, A. Schmid, G.M. Rupp, C. Slouka, E. Navickas, L. Andrejs, H. Hutter, L. Volgger, A. Nenning, *ActaChim. Slov.* **63**, 1 (2016).

A. Esquirol, N.P. Brandon, J.A. Kilner, M. Mogensen, *J. Electrochem. Soc.,* **151**, A1847 (2004).

44. S.B. Adler, J.A. Lane, B.C.H. Steele, *J. Electrochem. Soc.* **143**, 3554 (1996).

45. T. Kawada, J. Suzuki, M. Sase, A. Kaimai, K. Yashiro, Y. Nigara, J. Mizusaki, K. Kawamura, H. Yugami, *J. Electrochem. Soc.,* **149**, E252 (2002).

46. B. Hirschorn, M.E. Orazem, B. Tribollet, V. Vivier, I. Frateur, M. Musiani, *Electrochim. Acta.* **55**, 6218 (2010).

47. C.R. Kreller, T.J. McDonald, S.B. Adler, E.J. Crumlin, E. Mutoro, S.J. Ahn, G.J. la O', Y. Shao-Horn, M.D. Biegalski, H.M. Christen, R.R. Chater, J. A. Kilner, *J. Electrochem. Soc.*, **160**, F931 (2013).

48. J. Jamnik, J. Maier, S. Pejovnik, *Electrochim. Acta.*, **44**, 4139 (1999).

49. M. Søgaard, P. VangHendriksen, M. Mogensen, *J. Solid State Chem.,* **180**, 1489 (2007).

50. M. Kuhn, Y. Fukuda, S. Hashimoto, K. Sato, K. Yashiro, J. Mizusaki, *J. Electrochem. Soc.* **160**, 34 (2013).

51. D.N. Mueller, M.L. Machala, H. Bluhm, W.C. Chueh, *Nat. Commun.* **6**, 6097 (2015).

52. W.G. Wang, M. Mogensen, *Solid State Ionics.* **176**, 457 (2005).

53. K. Park, S. Yu, J. Bae, H. Kim, Y. Ko, *Int. J. Hydrogen Energy,* **35**, 8670 (2010).

54. C. Endler, A. Leonide, A. Weber, F. Tietz, E. Ivers-Tiffée, *ECS Trans.* **25**, 2381 (2009).

55. J. Kim, S. Choi, A. Jun, H.Y. Jeong, J. Shin, G. Kim, *ChemSusChem,* **7**, 1669 (2014).

56. S. Baumann, F. Schulze-Küppers, S. Roitsch, M. Betz, M. Zwick, E.M. Pfaff, W.A. Meulenberg, J. Mayer, D. Stöver, J. *Memb. Sci.*, **359**, 102 (2010).

ОХАРАКТЕРИЗИРАНЕ НА La$_{0.6}$Sr$_{0.4}$Co$_{0.2}$Fe$_{0.8}$O$_{3-\delta}$- Ba$_{0.5}$Sr$_{0.5}$Co$_{0.8}$Fe$_{0.2}$O$_{3-\delta}$ КОМПОЗИТ КАТО КАТОДЕН МАТЕРИАЛ ЗА SOFC

М.-П. Карпанезе[1,2], Д. Клематис[1*], М. Вивиани[2], С. Престо[2], М. Паница[1], Дж. Керисола[1], А. Барбучи[1,2]

[1]Катедра по гражданско, химическо и екологично инженерство (DICCA), Университет Генуа, P.le.F.Kennedy 1, I-16129 Генуа, Италия
[2]Институт по химия и технологии за енергия, Национален съвет за научни изследвания (CNR-ICMATE), Via De Marini 6, 16149 Генуа, Италия

(Резюме)

Смес от La$_{0.6}$Sr$_{0.4}$Co$_{0.2}$Fe$_{0.8}$O$_{3-\delta}$ and Ba$_{0.5}$Sr$_{0.5}$Co$_{0.8}$Fe$_{0.2}$O$_{3-\delta}$,е изследвана като перспективен катоден материал за горивни клетки с твърдооксидни форивни клетки, работещи при междинна температура(IT-SOFCs). Двата перовскита притежават висока каталитична активност за редукция на кислорода (ORR), въпреки че някои проблеми, свързани с тяхната химическа и структурна стабилност, все още трябва да бъдат преодолени с оглед подобряване на стабилността на характеристиките на клетката. Постигането на стабилен и високоефективен композитен материал е целта на това изследване. По принцип химическото равновесие при интерфейса LSCF-BSCF може да бъде постигнато чрез интердифузия на йони по време на процеса на синтероване, което води до химическа стабилизация на материала. Композитният катод, отложен върху Ce$_{0.8}$Sm$_{0.2}$O$_{2-\delta}$ електролит, след това беше изследван чрез електрохимична импедансна спектроскопия (EIS) като функция на температурата, свръхпотенциала и времето. Резултатите показаха интересно електрохимично поведение на електрода по отношение на кислородната редукция. XRD анализът е извършен за откриване на структурна модификация по време работа и е установено, че след синтероване двата изходни перовскити вече не присъстват; формира се нова фаза с ромбоедрична структура La$_{0.4}$Sr$_{0.6}$FeO$_3$ (LSF). Подобрената устойчивост на композитния катод е открита при разглежданите работни условия (200 mAcm^{-2}, 700°C) в сравнение с чистия BSCF електрод. Резултатите потвърдиха този нов електрод като перспективна система за по-нататъшно изследване като IT-SOFC катод.

Ключови думи: SOFC катод, дългосрочна стабилност, LSCF-BSCF

On the contamination of membrane-electrode assemblies of water electrolysers based on proton exchange membrane in the course of operation

S. A. Grigoriev[1*], D. G. Bessarabov[2], A. S. Grigoriev[3], N. V. Kuleshov[1], V. N. Fateev[3]

[1] National Research University "Moscow Power Engineering Institute", 14, Krasnokazarmennaya st., 111250 Moscow, Russia
[2] HySA Infrastructure Center of Competence, North-West University, Potchefstroom, 2520 South Africa
[3] National Research Centre "Kurchatov Institute", 1, Kurchatov sq., 123182 Moscow, Russia

The issues of contamination of membrane-electrode assemblies (MEAs) of water electrolysers based on proton exchange membrane (PEM) currently pose a subject for investigation. The analysis of structure and chemical composition of the MEA after its long-term testing shows, that the ions and/or the clusters of several contaminating elements (Ti, Pt, Ir, Fe, Ni, Cr, Si), originated from the constructional materials of MEA, electrolysis stack and external piping, are accumulated in the membrane and electrocatalytic layers. Quantitatively, the most predominant contaminating element is Ti (up to 12 wt. %). The cathode area (cathode active layer and membrane band adjacent to them) is extremely exposed to the contaminant's deposit.

INTRODUCTION

Pure aluminum and its low doped The aspects of stability of performances of PEM water electrolysers have been actively studied [1-8] over the last years. In particular, investigations have been performed to study the dissolution, migration and aggregation of the catalytic nanoparticles inside the active layer [4-6], the thermo-oxidative degradation of PEM [7-8] and other factors which negatively affected on the performances and operating life of the electrolyser.

This study covers issues of MEA contamination by various impurities (Ti, Pt, Ir, Fe, Ni, Cr, Si) originated from the constructional materials of MEA, electrolysis stack and external piping. The control MEA was exposed to stability tests, and after that, its structure and chemical composition was studied using an energy-dispersive X-ray spectroscopy (EDX), transmission and scanning electron microscopy (TEM and SEM) in order to define contaminating impurities.

EXPERIMENTAL

The MEA fabrication and testing

The MEA with 25 cm^2 active surface area was assembled using Nafion® 117 membrane (EI. DuPont de Nemours Co., USA) and current collectors/gas diffusion electrodes fabricated from porous sheets based on titanium alloy (TPP-7 grade, 0.95 mm thickness and 37% porosity).

Prior to the MEA assembling, the electrocatalytic layers were fabricated by spraying of the catalytic ink onto the current collectors. The Ir black (1.5 mg/cm2) was synthesized as described in [9] and applied on the anode; 40 wt. % of Pt on Vulcan XC-72 (1.0 mg/cm2 of total loading) was synthesized according to [10] and used on the cathode. 5 and 15 wt. % of D521 Nafion® polymer dispersion (EI. DuPont de Nemours Co., USA) were added to the anodic and cathodic electrocatalytic ink, respectively.

After preparation, the MEA was clamped in a lab-made thermally controlled electrolysis cell (figure 1). Both the cell holder and the flow-field plates were manufactured from titanium alloy (VT1-0 grade). External separators of hydrogen and oxygen were made of chemical glass; silicone tubes were used as a connecting piping. The anode was supplied with the bidistilled water additionally treated by the ion-exchange filter.

The control MEA underwent the stability test at 60°C and atmospheric pressure of gases. The electrolysis system operated in average for 6 hours every day. Then, prior to switching off for the night or weekend, the control measurement of current-voltage performances was implemented. The calculation of the operational time of MEA considered only its alive time (the idle time was not taken into account). Water changes were performed

---

several times during the stability tests in the cases when water resistance exceeded the value of 18 MOhm*cm.
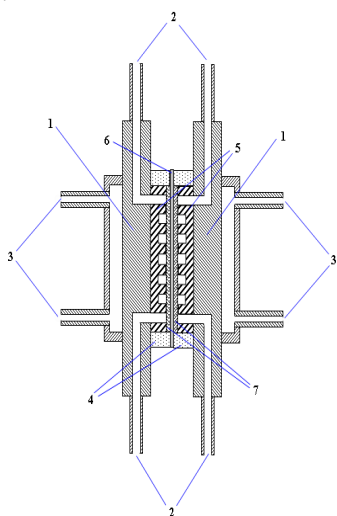
Fig. 1. Schematic diagram of the electrolysis cell. 1 – cell holder; 2 – fittings for reactant/products supply/removal; 3 – fittings for heating/cooling; 4 – sealants; 5 – flow-field plates; 6 – membrane; 7 – current collectors/gas diffusion electrodes with electrocatalytic layers

The electrolysis system operated under the above conditions within 4000 hours with daily measurements of current-voltage performances. Then, the system was shut down, the cell was disassembled, and the MEA structure and the chemical composition were examined.

Analysis of the MEA structure and chemical composition

The structure and chemical composition of the MEA after its long-term testing were investigated using the TEM, SEM and EDX. The MEA was locked using epoxy resin and cross-sliced using a ultramicrotom knife to produce thin (ca. 100-nm) strips.

The TEM and SEM micrographs of MEA cross-slices were obtained using the JEM 1200 EX TEMSCAN (JEOL) and Tescan Vega II LSU microscope (Oxford Instruments), respectively. The elemental analysis was performed using the Inca EDS micro-analysis system (Oxford Instruments).

RESULTS AND DISCUSSIONS

In the course of the stability test, the electrolysis cell voltage monotonously increased with an average rate *ca.* 35 µV/hour. After 4000 of running hours of electrolysis system, the experiment was stopped, and the control MEA underwent the above structural and chemical analysis.

The typical TEM micrographs of various areas of MEA cross-slices are shown in figure 2. Numeric symbols in micrographs correspond to positions of performing the EDX resulted in figure 3. The SEM micrographs of MEA cathodic area with the marked positions of execution of the element analysis is shown in figure 4 (lower part). The linear scanning EDX-spectrum of Ti concentration distribution across the MEA thickness in cathodic area is shown in figure 4 (upper part). The chemical composition of the near-cathode membrane area marked by circle in figure 4 is shown in Table 1.

| (a) | (b) | (c) |
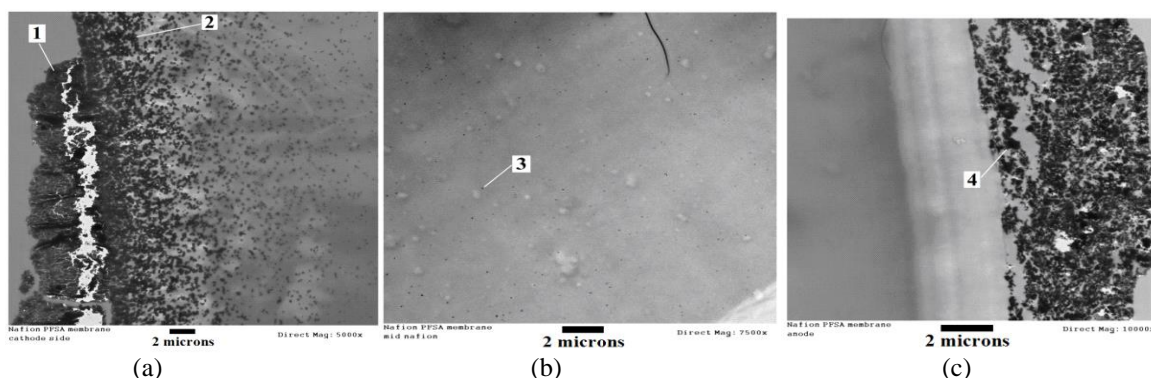
Fig. 2. TEM micrographs of MEA cross-section: (a) cathodic region of MEA, (b) membrane region equidistant from anode and cathode, (c) anodic region of MEA. Numbers in the micrographs correspond to positions of EDX measurements resulted in figure 3.
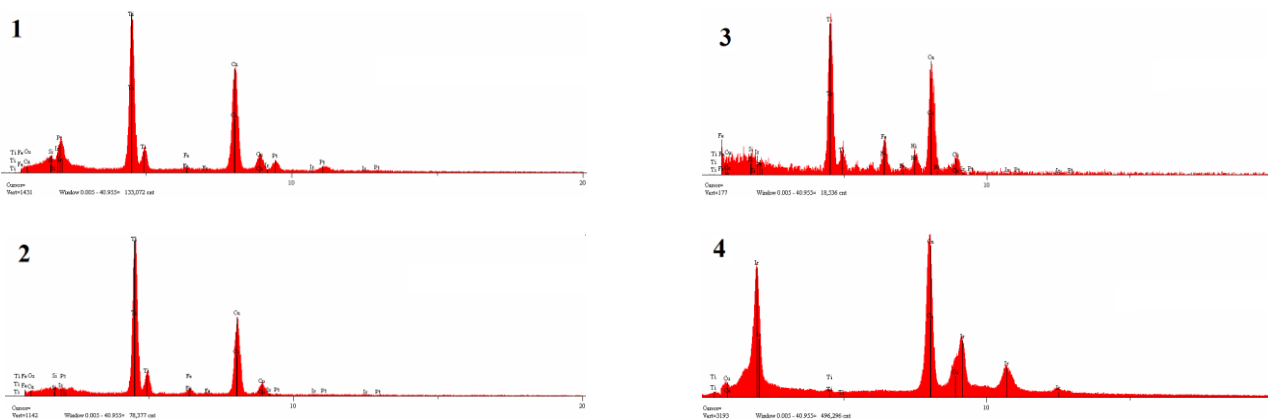
Fig. 3. Results of EDX analyses of electrocatalytic layers and membrane cross-sections. Numbers in spectra correspond to positions of EDX measurements specified in the micrographs provided on figure 2.

Figure 2 shows, that numerous agglomerates of contaminating particles are clearly seen in the near-cathode membrane area (figure 2(a)), whereas the individual impurity particles could only be seen in the membrane area located at the equal distance from the anode and the cathode (figure 2(b)), and no significant impurity inclusions are observed in the near-anode membrane zone (figure 2(c)). The size of the clusters formed by impurities and the density of their distribution decreases with increase of the distance from the cathode. Thus, the analysis of the micrographs concludes that the cathode is the nucleation zone for impurity clusters in a membrane.

The assumption is that, mainly, the impurity ions transfer in a membrane (and active layers) in the course of water electrolysis is caused by the water flow initiated by the flow of protons and directed from the anode to the cathode. At the same time, as the impurity ions approach to the cathode, their reduction expedites the deposition of particles. The reduction process is most likely caused by interaction of ions with hydrogen and with already partially reduced impurity ions.

Table 1. Results of the element analysis of near-cathode membrane region marked by circle in figure 4

Element	Content, wt. %	Source(s)
C	36.32	Membrane material
O	7.85	
F	22.34	
S	0.79	
Ti	11.96	Current collectors, flow-field plates, cell holder
Cr	3.42	
Fe	5.15	
Ni	3.02	
Si	0.96	Current collectors, flow-field plates, cell holder, glass tank-separator and silicon tubes
Pt	7.34	Cathodic active layer
Ir	0.85	Anodic active layer
Totals	100.00	

The analysis of EDX spectra (figure 3) allowed to determine the main elements of the membrane and catalytic layers contamination: Ti, Fe, Pt, Ni, Si, Cr, Ir. The Cu peak on figure 3 is explained by the fact that the copper grid has been used as a specimen support for the studied MEA samples. Apparently, the sources of Pt and Ir are cathodic and anodic electrocatalytic layers, respectively. Ti, Fe, Si, Cr and Ni are the components of titanium alloys (material of current collectors, flow-field plate and cell holder). In particular, according to the technical specifications, titanium alloy of TPP-7 grade (material of porous current collectors) contains up to 1.1 wt. % of Fe (Table 2).

Table 2. Chemical composition of titanium alloys used as construction elements of MEA and electrolysis cell according to GOST 19807-91, TS 14-1-1895-76 and TS 1715-449-05785388-99. Contents of elements are given in wt. %.

	Element	Ti	Fe	Si	H	O	N	Cl	C	Others (Ni, Cr, *etc*)
Grade of titanium alloy	**VT1-0**	97.00	0.25	0.10	0.01	0.20	0.04	-	0.07	0.30
	TPP-7	97.95	1.10	-	-	-	0.50	0.45	-	-

Technical titanium alloy of VT1-0 grade (material of flow-field plates and cell holder) according to the technical requirements contains Fe (0.25 wt. %), Si (0.10 wt. %) and others (Table 2). The EDX spectra show no traces of Ca, Mg, Na, K etc, which confirms that the purity of the water-reagent is high. The presence of Si can be explained by its outwashing with water from the glass tank-separator and the silicon tubes of the other piping elements (made of VT1-0 titanium alloy) of the electrolysis cell.

The results of the element analysis of a typical area of the near-cathode membrane region are shown in table 1. The first 4 elements (C, O, F and S) compose the membrane material and are not contaminants. However, the next elements are contaminating impurities. In particular, according to table 1, one of the main contaminants of the membrane and the cathode active layer is Ti and the other components of titanium alloys (Fe, Ni, Cr, Si). For instance, figure 4 shows, that the maximum Ti content in near-cathode contaminating band of membrane (2-3 μm from the boundary between the membrane and the cathodic active layer) is *ca.* 12 wt. %. Definitely, Ti, Fe, Ni, Cr and Si originate from the current collectors, flow-field plates and the cell holder. According to the diagram of potential − pH equilibrium (Pourbaix diagram) for titanium–water system [11], for the anode current collector and flow-field plate (working in 1.5-2.0 V potential range), the electrochemical corrosion of titanium with formation of hydroxides and TiO_2 oxide, and repassivation of titanium as a result of anode polarization, is thermo-dynamically possible. Therefore, the anode current collector and the flow-field plate may corrode during the electrolysis cell operation, and Ti^{2+} ions are passed into water and then oxidized to Ti^{3+}. Subsequently, the electroosmotic water flow with the dissolved titanium ions moves through a membrane from the anode to the cathode, and ions of titanium are reduced in a membrane with formation of clusters. A

similar mechanism could be considered for explanation of contamination by other components of titanium alloys. It is necessary to mention that the contaminating elements can form not only nanoparticles and clusters of metals (Ti, Fe, *etc*) in a membrane, but also their chemical compounds. In particular, it must not be excluded, that rather than the metallic iron, its oxides of the lowest valence and/or the mixed oxides are formed in the membrane matrix (being the acidic media).
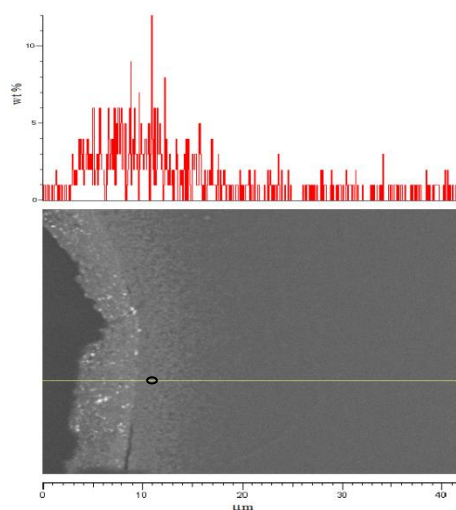
Fig. 4. Spectrum of Ti concentration profile across the MEA thickness in cathodic region, and the SEM

Contamination by Pt and Ir is associated with degradation processes in electrocatalytic layers [4, 5]. Metallic particles are exposed to oxidation in the course of electrolysis, are dissolved in water as cationic species, which then are transferred with circulating water flow. At some distance from the cathode, they start to react with dissolved hydrogen that cross-permeates from the cathode (or with already reduced species) and are chemically reduced into metallic particles.

Rearrangement of chemical elements, entering into the construction materials of components of MEA, electrolysis cell and auxiliary systems, results

in at least several negative effects. In particular, the loss of Pt and Ir in electrocatalytic layers leads to a decrease in their activity as well as to a decrease in their internal electronic and proton conductivity (due to the loss in coherence of particles). On the other hand, incorporation of nanoparticles of inorganic substances into the ion-exchange membrane leads to essential modifications of the system of pores and channels, as well as to deterioration of transport properties of membrane [4]. In particular, with increase in concentration of impurity metallic particles in a membrane its proton conductivity falls [11] and the probability of local overheating and a membrane burn-through (due to ohmic heating of percolating metal clusters) increases [2, 5]. According to [1], the cations can occupy the ion-exchange sites of the Nafion® polymer electrolyte in the catalyst layers and membrane, which results in the increase of the anode and cathode overpotentials. The assumption is that in the course of stability test the increase of electrolysis cell voltage was related to the combination of the abovementioned factors. The use of the ion-exchange filters and/or regular change of water in electrolysis system can be recommended in order to decrease the MEA contamination.

CONCLUSIONS

The results of microstructural and chemical analyses indicated that in the course of operation of PEM water electrolyser, the membrane and electrocatalytic layers are contaminated by the impurity elements originated from the MEA and cell components (electrocatalytic layers, current collectors, flow-field plates, cell holder) and external cell piping. As a result of corrosion of these components, the ions of titanium, iron, silicon, nickel, chrome, platinum and iridium are dissolved in water-reagent circulating through them and are reduced in membrane and active layers. These phenomena lead to a number of adverse effects (decrease of electrocatalytic layer activity and conductivity, deterioration of transport properties of membrane, etc), increasing the voltage of electrolysis cell. A use of ion-exchange filters and/or regular change of water in electrolysis system is recommended in order to reduce contamination of the membrane and electrocatalytic layers.

REFERENCES

1. M. Lamberti, F. Escher, Food Rev. 1. S. Sun, Z. Shao, H. Yu, G. Li, B. Yi, *J. Power Sources*, **267**, 515 (2014).
2. P. Millet, A. Ranjbari, F. de Guglielmo, S.A. Grigoriev, F. Aupretre, *Int J Hydrogen Energy*, **37**, 17478 (2012).
3. M. Langemann, D.L. Fritz, M. Müller, D. Stolten, *Int J Hydrogen Energy*, **40**, 11385 (2015).
4. S.A. Grigoriev, D.G. Bessarabov, V.N. Fateev, *Russian Journal of Electrochemistry*, **53,** 318 (2017).
5. S.A. Grigoriev, K.A. Dzhus, D.G. Bessarabov, P. Millet, *Int J Hydrogen Energy*, **39**, 20440 (2014).
6. C. Rakousky, U. Reimer, K. Wippermann, S. Kuhri, M. Carmo, W. Lueke, D. Stolten, *J Power Sources*, **342,** 38 (2017).
7. F. Fouda-Onana, M. Chandesris, V. Medeau, S. Chelghoum, D. Thoby, N. Guillet, *Int J Hydrogen Energy,* **41,** 16627 (2016).
8. C. Rakousky, U. Reimer, K. Wippermann, M. Carmo, W. Lueke, D. Stolten, *J Power Sources*, **326,** 120 (2016).
9. S.A. Grigoriev, A.A. Kalinnikov, *Int J Hydrogen Energy,* **42**, 1590 (2017).
10. A.A. Fedotov, S.A. Grigoriev, P. Millet, V.N. Fateev, *Int J Hydrogen Energy,* **38**, 8568 (2013).
11. Mousavi Ehteshami S. Mohsen, Amirhooshang Taheri, S.H. Chan, *J. Industrial and Engineering Chemistry*, **34**, 1 (2016).

ЗАМЪРСЯВАНЕ В ПРОЦЕСА НА РАБОТА НА МЕМБРАННО-ЕЛЕКТРОДНИТЕ ПАКЕТИ ВЪВ ВОДНИ ЕЛЕКТРОЛИЗЬОРИ, БАЗИРАНИ НА ПРОТОННО-ОБМЕННА МЕМБРАНА

С.А. Григориев[1*], Д.Г. Бесарабов[2], А.С. Григориев[3], Н.В. Кулешов[1], В.Н. Фатеев[3]

[1] *Национален изследователски университет Московски институт по енергетика, Красноармейская ул.,14, 111250 Москва, Русия*

[2] *HySA Инфраструктурен център за компетентност, Северозападен университет, Потсхефроом 2520, Южна Африка*

[3] *Национален изследователски център "Институт Курчатов", 1, пл. Курчатов., 123182 Москва, Русия*

(Резюме)

Проблемите на замърсяването на мембранно-електродните пакети (MEAs) на водни електролизьори, базирани на протонно-обменна мембрана (PEM), понастоящем представляват обект на изследване. Анализът на структурата и химичния състав на MEA след дългото му тестване показва, че йоните и / или клъстерите на няколко замърсяващи елементи (Ti, Pt, Ir, Fe, Ni, Cr, Si) произхождат от конструктивните материали на MEA, електролитния стек и външните тръби и се натрупват в мембраната и електрокаталитичните слоеве. Количествено, най-преобладаващият замърсител е Ti (до 12 тегл.%). Катодната зона (катодният активен слой и мембранната лента в непосредствена близост до тях) е изключително изложена на отлагане на замърсителя.

Ключови думи: водна електролиза, протонно-обменна мембрана, мембранно-електроден пакет, електрокаталитичен слой, замърсяване, примеси

Application of inkjet printing technology for SOFCs anode fabrication and modification

R.I. Tomov[1*], A. Fakeeh[1], T.B. Mitchell-Williams[1], M. Krauz[2], R.V. Kumar[1], B.A.Glowacki[1,3]

[1] *Department of Materials Science and Metallurgy, University of Cambridge, United Kingdom*
[2]*Institute of Power Engineering - Ceramic Department CEREL, Poland*
[3] *Institute of Power Engineering, Warsaw, Poland*

Feasibility of inkjet printing technology for fabrication and modification of SOFC electrodes and electrolytes was studied. Drop on demand inkjet printing offers fast, scalable and cost efficient processing path by reproducibly dispensing droplets in the range of *nL* to *pL* volumes at high rates (*kHz*) and high velocity (*1-10 m/s*). Electromagnetic print heads were utilized to dispense droplets of various inks (doped ceria, Ni oxide) on demand. Printing parameters including pressure, nozzle opening time were studied in order to optimize the inks jetting and delivery. Reduction of SOFC anode polarization losses was pursued via infiltration nano-engineering of the electrode's scaffolds. Two - step fabrication using inkjet printing was implemented. In the first step porous electrode scaffolds (Gd:CeO$_2$-NiO) were created by printing suspension inks. During the second step inkjet printing infiltration was utilized for controllable loading of Gd:CeO$_2$ nano-decorations on the scaffolds. Anode symmetrical cells were characterized by Electrochemical Impedance Spectroscopy in order to reveal the relation between the surface nano-structure and the electrochemical performance. Electrochemical impedance spectroscopy measurements confirmed a significant reduction and convergence of the area specific resistance (ASR) values for infiltrated anodes with different NiO/Gd:CeO$_2$ volume ratios. This work demonstrated the feasibility of achieving significant improvements in SOFC electrodes performances via simple industrially scalable procedure.

Keywords: inkjet printing, infiltration, nano decoration, doped ceria

INTRODUCTION

A combination of geopolitical, economic and environmental concerns regarding the depletion of fossil fuels reserves and global warming have been driving forces behind considerably renewed interest in fuel cell technologies. Fuel cells (FCs) offer direct electrochemical conversion of the energy into electricity and heat without efficiency limitations inherent to heat engines governed by the Carnot cycle. Demonstrated high electrical efficiencies can substantially exceed those typical for coal-fired power plants [1]. FCs can be scaled across a wide range of sizes - from systems with outputs as small as 1 W to facilities operating in MW range. Nickel is commonly used as anode material due to its high catalytic activity for fuel oxidation, high electrical conductivity and mechanical/ chemical compatibility with traditional ion conductive electrolytes [2]. The commercial anodes are based on cermet compositions like NiO–YSZ (yttrium stabilized zirconia) or NiO-Gd:CeO$_2$ (GDC) consisting of three different phases - metallic Ni, ion conductive ceramic and percolating pores acting as fuel and reactants diffusion pathways. The mixture of Ni and ion conductive phase in the cermet provides an extension of three-phase boundary (TPB) and alleviates the thermal stresses caused by

the difference of the thermal expansion coefficients (TECs) between NiO and electrolyte materials (TEC$_{8YSZ}$~10.4-11.0 ppmK^{-1}, TEC$_{GDC}$~12.7 ppmK^{-1}, TEC$_{NiO}$ ~14.2 ppmK^{-1}) which is beneficial for withstanding stresses caused by rapid thermal cycling. The cermet materials also offer chemical and thermal stability in oxidizing and reducing atmospheres as well as good oxygen ionic conductivity over a wide range of conditions [3, 4]. Depending on the design Solid Oxide Fuel cells (SOFCs) can operate at various temperatures within the region of 500-1000ºC [5,6]. Adversely, at elevated temperatures the Ni phases in the cermet have a tendency to coarsen and agglomerate, reducing the TBP due to poor adhesion of metal to the ceramic material. Such deterioration at high operational temperatures as well as the high overall cost of production effectively inhibit commercialization of SOFC technology. Commonly sought solution is to lower the operating temperature to intermediate temperature (IT) range of 600–800ºC. Such low operating temperatures can suppress the TPB deterioration and significantly expand the choice of materials e.g. enable the use of less expensive stainless steel as interconnects and manifolds. However, because of the lower

---

temperature the overall performance of a SOFC system would decrease due to exponential increase in electrode polarization losses. It has been shown that infiltration of the SOFC electrodes (both anode and cathode) with ionic conductive phase is an effective method to develop nano-engineered electrode materials with high performance and stability at IT [7].

This study reports on the application of Inkjet Printing (IJP) for the fabrication and infiltration of NiO/Gd-CeO$_2$ (GDC) anodes with different ratio of the constituent phases. The IJP technique is simple and cost-effective non-contact "wet" technique for fabrication of ceramic coatings onto variety of surfaces which allows utilization of very thin fragile porous support (ceramic or metal). It can reproducibly dispense droplets in the range of nL volumes at high rates (kHz). Drop-on-demand (*DOD*) ceramic inkjet printing offers excellent thickness and uniformity control and introduces the possibility of printing 2D and 3D patterns as well as continuous coatings. Inkjet systems offers wide scale of application - from experimentation platforms working with customized inks, up to mass manufacturing systems that can print rapidly and competitively on industrial scale. The technology is cost effective and environmentally friendly through waste minimization of the expensive precursors. The influence of the major printing parameters and required optimization steps were explored for both suspension and sol-gel inks. The production of anodes and electrolyte coatings with a modified Domino print head was reported previously by Tomov et al. [8] using suspension inks. Wang et al. [9,10] deposited GDC electrolytes on NiO-8YSZ cermet anodes using sol–gel-based precursor solutions. Sukeshini et al. [11] employed a DMP-2831 printer for the deposition of 8YSZ electrolyte layers, LSM-YSZ and LSM cathode layers on to NiO–8YSZ supports, reporting a maximum power density of 450 mW/cm^2 at 850°C in hydrogen.

EXPERIMENTAL
Inks preparation
Electrolyte and electrode depositions as well as ionic phase (GDC) infiltrations were performed by an electromagnetically (EM) driven print head with 100 μm ruby nozzle orifice and X-Y planar positioning system. EM technology was chosen because it offers simplicity and reliability of use, as well as wider range of ink/suspension compatibility. The preparation of stable suspension and sol-gel inks is of critical importance for achieving repeatable jetting without clogging the nozzles. For the suspension inks commercial NiO, and GDC powders were mixed with alpha-Terpineol and binders, and

ball milled with 3YSZ beads in 3YSZ bowls in a planetary mill. The mass load of the ceramic powders was limited by the rheological working window of the nozzles, which defined the regime of stable repeatable jetting. Hence, the viscosity of the suspension inks had to be adjusted by adding lower viscosity solvent – Methanol (MeOH). GDC precursor solution (1.5 M total metal concentration) was prepared by dissolving cerium (III) acetate hydrate (Sigma-Aldrich) and gadolinium (III) acetate hydrate (Sigma-Aldrich) in two steps in propionic acid (Sigma-Aldrich) under reflux for 4 hours at 120 °C. The solution was then cooled to room temperature and filtered through 0.3 μm polypropylene membrane syringe filter (Whatman) to eliminate possible contamination with dust particles. The precursor was further diluted to reduce the viscosity to a suitable level as determined by the print-head requirements. A number of different solvent/ precursor mixtures were tested to evaluate the stability of the ink, which was determined by observing precipitation levels after shelf storage for 24 hours. From the various solvents tested 1-propanol was selected as a diluting agent producing the most stable printable inks. The dilution at volume ratio 1:1 (precursor :solvent) was found suitable to produce stable jetting without observing any splashing effects. Jetting of all types of inks was optimized by drop visualization procedure with the aim to avoid formation of satellite drops at practical Weber and Reynolds numbers. The inks were filtered through 3 μm glass micro-fibre filters before being loaded into the nozzle compartments. The nozzles were observed to execute reproducible drop on demand tasks without clogging the internal fluidic pathways of the assembly.

Symmetrical cells fabrications
GDC powder, Hydroxypropyl cellulose and Ethanol were mixed and milled for 4 hours. Following evaporation of the solvent, the powder was uniaxially pressed into pellets with 12.5 mm diameter under 3 tonnes pressure. The pellets were sintered at a heating rate of 3°C min^{-1} to 900 °C and held for an hour. Anodes (NiO/GDC) with different constituents volume ratios (60:40 and 80:20 vol% ratio) suspension inks were printed on both sides of the GDC pellets and fired at 900 ºC in air forming porous NiO/GDC anode scaffolds. An infiltration of the GDC sol ink was carried out by inkjet printing of ~8 nL drops as determined by drop visualisation in a reciprocal pattern on each side of the cell. Each infiltration step (per side) contained 368 drops (~3.2 μL of ink). A horizontal drop spacing of 0.6 mm was used to achieve an overlap of 25% between the drops surface replicas. Each printed

layer was allowed to drain and the absolute position of the print head was offset by 0.3 mm in the X and Y directions to avoid drop stacking. An intermediate heat treatment was applied after every second deposition, increasing the temperature from ~20 ℃ to 300 ℃ within 10 minutes. Such treatment led to the removal of the solvent from within the scaffold aiding further infiltration steps. Various infiltration-loading levels of GDC nanoparticles into the anode scaffold were achieved by varying the number of printing steps. Finally, as treated pellets were sintered at 1400 ℃ for 4 hours in order to achieve fully dense electrolytes. As sintered symmetrical cell were ~0.5 mm thick and ~11 mm in diameter.

Characterization

Electrochemical impedance spectra (EIS) of the symmetrical cells were measured with the electrochemical interface and a frequency response analyser (Solartron 1260) under the open-circuit voltage (OCV) condition. Symmetrical cells were heated at 5 °C/min ramping rate to temperatures from 500 to 600 °C, and tested under Ar/4% H_2 in a frequency range of 1 MHz to 0.1Hz with AC amplitude of 10 mV. Silver mesh was painted to the electrodes in order to ensureconductivity along the surface of the electrodes.

RESULTS AND DISCUSSION
Drop visualisation

Drop visualisation was used to study the drop generation process for each combination of printing parameters (pressure and opening time) and, in conjunction with image analysis, to determine the corresponding drop velocity and drop volume. The greatest advantage of the drop visualisation system is that it allows rapid examination of whether the rheological condition of the ink is suitable for printing. Ideally, any ink should be tailored in such a way that each triggering event results in a single drop, without satellite drops, before reaching the substrate. Figure 1 shows jetting behaviour of GDC sol ink at optimized conditions where the initial drop breaks into a series of small drops after it detaches from nozzle, but the smaller drops then soon catch up with the main drop and form back to a single drop. Within the stable jetting regime, it was found that the drop volume was approximately 8 nL. The maximum velocity achieved in this case was ~ 2.2 m/s.

Infiltration effect

Multiple infiltrations were conducted by repeated inkjet-printing/low temperature calcinations. As seen in the high resolution SEM images shown in Figure 3, the NiO/GDC scaffolds

110
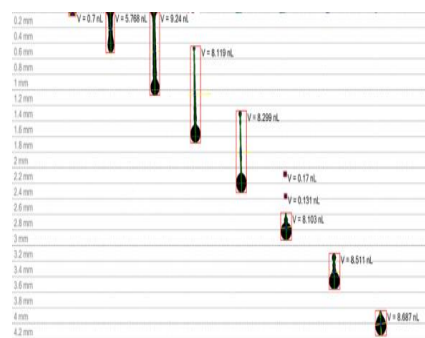
Fig.1. Montage of images from the drop visualisation showing optimized jetting of the GDC sol ink.

Anodes fabrication

Figure 2 presents tops surface SEM images of two blank (non-infiltrated) NiO/GDC anodes after high temperature sintering. The anode with 80:20 NiO/GDC ratio showed clear micro-cracking of the surface due to the difference in the TECs of the constituent phases. This was expected to lead to deterioration of both electronic and ionic conductive paths in the anode.
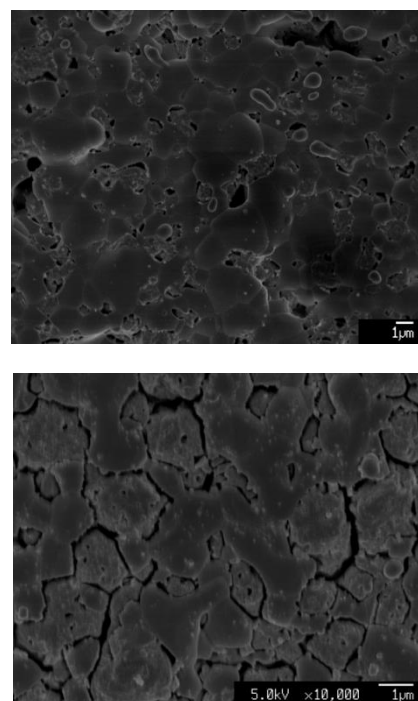
Fig. 2. SEM surface images of blank composite GDC:NiO anodes – (a) 60:40 NiO:GDC vol% ratio, and (b) 80:20 NiO:GDC vol% ratio

were composed of well-connected NiO and GDC grains with sizes ranging between 1 and 3 μm. After the infiltration, the scaffolds were uniformly decorated with GDC nanoparticles forming nano-scale sub-structures. All infiltrated samples showed

similar sub-structures with GDC nanoparticle size varying in the range of 50–200 nm. Remarkably, the infiltrated nano sub-structure was retained after the high temperature sintering at 1400 °C. Similar observation was reported by Lee et al. [12] for Ni-GDC infiltration. The exact nature of this effect is not clear as according to Rupp et al. [13] self-limited grain growth for nano GDC characterized by grain boundary diffusion was observed for temperatures below 1100ºC. One could speculate that the retention of the nano sub-structure could be related to the strong bonding between the GDC nano particles and the micro-strain defects in the anode scaffold.

A quantitative confirmation of the effect of infiltration on the electrochemical performance was investigated by EIS. Comparison of the Nyquist plots of the reference blank anodes and infiltrated anodes (8 infiltrations) at 550 °C is shown in Figure

4. The EIS spectra for all measured symmetrical cells were similar in shape, showing single arc associated with the activation polarization resistance (R_p) at the anode without clear separation between low and high frequency arcs.The total (R_t) and Ohmic (R_o) polarization resistances were estimated from the low and high frequency intercepts of the Nyquist plots with the real axis. R_p was calculated from the difference between these two values divided by two - $R_p = (R_t - R_o)/2$ in order to account for the symmetrical nature of the cells. The activation polarizations of samples with no infiltration corresponded to the ones derived from geometric model considerations published in the literature with 60:40 NiO/GDC scaffold showing significantly lower ASR than the 80:20 GDC scaffold (see Table 1). Despite the higher Ni content in the reduced anodes R_o of 80:20 anodes was found to be double the value of 60:40 anodes.

Table 1: .Impedance of samples with NiO:GDC of 60:40 and 80:20 with 0 and 8 infiltrations at 550˚C

Number of infiltrations	Rp, Ω cm^2		Ro, Ω	
	60:40	80:20	60:40	80:20
0	1.62	4.49	8.30	16.94
8	1.23	1.48	5.68	5.98
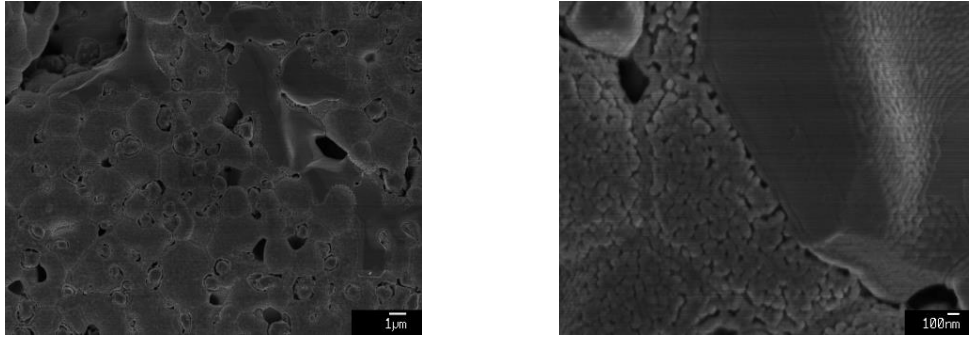
Fig. 3. NiO:GDC 60:40 scaffold nano-decorated with 8 infiltrations of GDC sol ink at increasing magnification

These deviations can be explained by the anode microstructure, which shows clear evidence of cracking for the 80:20 anode resulting from the TECs differences during high temperature sintering. Such cracking of the scaffold effectively resulted in local breakage of the ionic and electronic current paths and increase of R_o and R_p. Sharp decrease in R_p and R_o after the infiltration procedure was observed for both anode compositions converging in R_p values reaching 1.23 and 1.48 Ω cm^2 and R_o values reaching 5.68 and 5.98 Ω cm^2 at 550ºC. The promotion factors F_p and F_o were chosen as figures of merit defined as:

$$F_p = ASR_{ref} / ASR_{inf}$$
$$F_o = R_{o\text{-}ref} / R_{o\text{-}inf}$$

where ASR_{ref} was the area specific resistance of the reference anode (ASR=R_p x anode surface area) and the $R_{o\text{-}ref}$ was Ohmic resistance values of the reference (non-infiltrated) anode while ASR$_{inf}$ and R$_{o\text{-}inf}$ were the ASR and Ohmic resistance values of the infiltrated anodes. The inset in Figure 4 shows the frequency dependence of the impedance imaginary part for different NiO/GDC ratios. It was obvious that the infiltration procedure led to reduction of high frequency losses commonly associated with the charge transfer reaction. The observed effect can be related to the increase of TPB via infiltration of GDC. As seen in Figure 5 the activation polarization resistance promotion factor F_p was substantially higher for 80:20 scaffold

111

compositions reaching maximum of 4.95 at higher temperature (600ºC). Note that F_p for 60:40 scaffold reached lower value of 2.27. The promotion factor for the Ohmic resistance F_o was also shown to be systematically higher for the 80:20 anode ranging between 2.65 and 2.75 within the measured temperature range. Comparing the data in Table 1 we can conclude that the infiltration procedure led to near equalisation the R_o and R_p values of the two anode composition investigated.
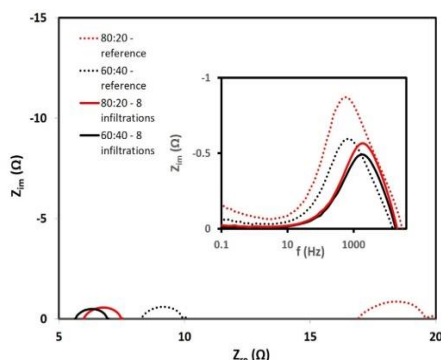
Fig. 4. EIS spectra of anodes with 0 infiltrations (reference) and 8 infiltrations at 550ºC

The insert shows the frequency dependence of the impedance imaginary part for different NiO/GDC ratios. This result indicated that both scaffolds reached similar lever of performance via infiltration and nano-decoration with ionic conductive GDC nanoparticles. The effect was due to the higher degree of TPB extension on Ni rich composition scaffold and cracks "healing" effect of the infiltrated GDC. The nano-decoration provided improved percolation more expressed at higher temperature where GDC was contributing to both ionic and electronic scaffold conductivity.
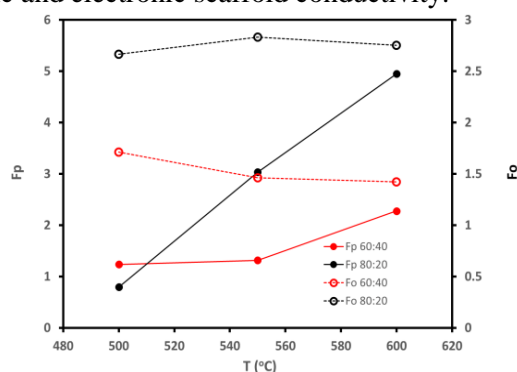
Fig. 5. Promotion factors F_p and F_o vs. testing temperature

CONCLUSION

It was demonstrated that the anode microstructure can be successfully nano-engineered by inkjet printing infiltration. The IJP infiltration enabled high precision permeation of the GDC sol ink allowing formation of GDC percolative nano-decoration on the anode scaffolds. As modified anode scaffolds showed significant enhancement of their electrochemical performance with the activation polarization improvement factor for 8 infiltration/heating cycles reaching $F_p = 4.95$ which led to equalization of the performances for both anode compositions.

REFERENCES

1. N.H. Menzler, F. Tietz, S. Uhlenbruck, H.P. Buczzhkremer, D. Stöver, *J. Mater. Sci.*, **45**, 3109 (2010).
2. S.P. Jiang, S.H. Chan, *J. Mater. Sci.*,**39**, 4405 (2004).
A. Weber, E.Ivers-Tiffee, *J. of Power Sources*, **127**, 273 (2004).
3. I.R. Gibson, G.P.Dransfield, and J.T. Irvine, *J. Eur. Ceram. Soc.*, **18**, 661 (1998).
4. S. Singhal S,, *Solid State Ionics*, **135**, 305 (2000).
5. S.P.S. Badwal, S.Giddey, C.Munnings, A. Kulkarni,*J. of the Australian Ceramics Soc.*, **50**, 23(2014).
6. S.P. Jiang, S.H. Chan, *J. Mater. Sci.*, **39**, 4405(2004).
7. R.I. Tomov, M.Krauz, J.Jewulski, S.C. Hopkins, J. R. Kluczowski, D. M. Glowacka, B. A. Glowacki, *J.of Power Sources*,**195**, 7160 (2010).
8. Ch.Wang, S. C. Hopkins, R. I. Tomov, R.V. Kumar, B. A. Glowacki, *J. of the European Ceramic Soc.*,**32**, 2317 (2012)
9. Wang, Ch., Tomov, R.I., Kumar, R.V., Glowacki, B.A., *J. of Materials Science*, **46**, 6889 (2011).
10. A.M. Sukeshini, R. Cummins, T.L. Reitz, R.M. Miller, *J. Am. Ceram. Soc.*, **92**, 2913 (2009).
11. K.T. Lee, H.S. Yoon, J. S. Ahn and E. D. Wachsman, *J. Mater.Chem.*, **22**, 17113(2012).
12. J.L.M. Rupp, A.Infortuna, L.J. Gauckler, *Acta Materialia*, **54**, 1721(2006)

ПРИЛОЖЕНИЕ НА МАСТИЛЕНО-СТРУЙНОТО ПРИНТИРАНЕ ПРИ ИЗГОТВЯНЕ И МОДИФИКАЦИЯ НА АНОДИ ЗА ТВЪРДОТЕЛНИ ГОРИВНИ КЛЕТКИ

Р.И. Томов[1*], А. Факее[1], ТТ.Б. Митчел-Уилямс[1], М. Крауз[2], Р.В. Кумар[1], В.А. Гловацки[1,3]

[1] Department of Materials Science and Metallurgy, University of Cambridge, United Kingdom
[2]Institute of Power Engineering - Ceramic Department CEREL, Poland
[3] Institute of Power Engineering, Warsaw, Poland

(Резюме)

Изследвана бе приложимостта на мастилено-струйното принтиране при изготвяне и модификация на твърдотелни горивни клетки. Мастилено-струйното принтиране във неговия вариант "Капка при поискване" предлага бърз, лесно мащабируем и икономически ефективен път за производство осигурявайки репродуктивно генериране на капки с обем между нано-литър до пико-литър с висока честота (*kHz*) и скорост (*1-10 m/s*). Елекромагнитни печатни глави бяха изполвани за генерация на капки от различни мастила (допиран цериев окис, никелов окис) при поискване. Принтиращи параметри като налягане и време за отваряне на дюзата бяха изследвани с цел оптимизация на генерацията и доставката на капки. Преследвано бе намаляването на поляризационните загуби в анода на твърдотелната клетка чрез нано инженерство на скелета на електрода. Беше приложен метод на принтиране в две стъпки. Първоначално бе създаден порист електроден скелет от $Gd:CeO_2$-NiO. Във следващия етап нано декорация на електродния скелет бе постигната с контролирано принтиране на $Gd:CeO_2$. Така изработените симетрични анодни клетки бяха изследвани с Електрохимична Импедансна Спектроскопия с цел разкриване на връзката между повърхностната нано структура и електрохимичната активност. Данните от измерванията с Електрохимичната Импедансна Спектроскопия потвърдиха значително намаляване и сближаване на стойностите на ареалното специфично съпротивление на инфилтрираните аноди характеризирани с различно обемно съотношение на $NiO/Gd:CeO_2$. Настоящото изследване демонстрира възможността за постигане на значително подобрение на активността на твърдотелните горивни клетки чрез използване на проста индустриално мащабируема процедура.

Ключови думи: мастилено-струйното принтиране, инфилтрация, нано декорация, допиран цериев окис

Nanosized Ag particles as catalyst in gas-diffusion electrodes for ORR

B. B. Mladenova[1,2], Y. D. Milusheva[1], M. I. Karsheva[2], I.D. Hinkov[2], T. E. Stankulov[1], G. R. Borisov[1], R. I. Boukoureshtlieva[1]

[1] *Institute of Electrochemistry and Energy Systems, Bulgarian Academy of Sciences, Acad. Georgi Bonchev Str., Block 10, 1113 Sofia, Bulgaria*
[2] *Department of Chemical Engineering, University of Chemical Technology and Metallurgy, 8 St. Kliment Ohridsky Blvd, 1756 Sofia, Bulgaria*

Silver nanosized particles were prepared via original process. The obtained silver particles size varied between 10 to 50 nm with a shape that was mainly spherical. The UV-visible spectroscopy investigation showed Plasmon resonance peak at between 440 and 470 nm for silver nanoparticles. Transmission electron microscopy study showed hexagonal and cubic crystal structures of silver particles.In order to verify the catalytic activity of the obtained silver nanoparticles they were incorporated in the active layer of the air gas-diffusion electrodes. The active layer of the gas diffusion electrode was prepared via four methods. The catalyst activity of these electrodes was studied in three-electrode half-cell with Ag/AgCl reference electrode using 4M NaCl solution as electrolyte. The results obtained showed stable operation of all electrodes up to 50 mA/cm^2, and for some – even up to 100 mA/cm^2.

Key words: Ag nanosized particles, Ag catalyst, air gas-diffusion electrodes

INTRODUCTION

During the recent years there is increased scientific interest toward the synthesis of nano materials and their applications. In the scientific literature there are many different applications of metal nanoparticles in areas such as electronics, optics and medicine. Recently, they are also used as catalysts [1], electrode materials for lithium ion batteries [2] as well as in the development of solar cells [3]. There are different methods for the production of silver nanoparticles [4], among them electrochemical methods [5], photocatalytic techniques [6] and chemical methods, particularly those using external energy fields, the most common being ultrasound [7] or microwaves [8].

Depending on the synthesis method and the working conditions, the resulting silver nanoparticles may have different sizes and shapes (spheres, cubes, tetrahedra, fibers, etc.).

Silver is known as one of the best catalysts for the electrochemical reduction of oxygen in an alkaline electrolyte [9-11]. Furthermore, silver appears to present a great catalytic activity for the heterogeneous decomposition of H_2O_2. H_2O_2 is generated during the operation of air electrode. Part of it decomposes to H_2O and $½ O_2$ in the pore volume of the electrode. This oxygen oxidizes chemically the carbon surface and it is the main reason for disruption of hydrophobic properties of carbon catalysts. This phenomenon leads to increased difficulties of the oxygen's transportation toward the electrochemically active centers of the catalyst and deterioration of the electrode properties in general. Therefore a highly active catalyst for the heterogeneous decomposition of H_2O_2 (silver for instance) is required in the air electrodes. Another part of H_2O_2 may migrate through the electrolyte and its presence there even in small quantities, increases the self-discharge of the metal electrode (Zn, Fe). All these processes are very important for the operation of the air electrode and even for some metal-air system as a whole. Therefore, silver is used in air gas- diffusion electrodes either purely or cast on different carbon materials [12, 13]. Different studies [9, 14-17] report about the use of silver catalysts cast on materials with a high specific surface area, most commonly activated carbon, in alkaline electrolyte-operating gas-diffusion electrodes.

The purpose of this work is to investigate the catalytic activity of ultrasonic silver nanoparticles in air electrodes operating in a neutral electrolyte. Various methods of depositing silver nanoparticles on active carbon during the preparation of the catalytic layer of air electrodes are used. The polarization characteristics of the air electrodes have been investigated for 20 days. In order to confirm the catalytic ability of the silver particles obtained by ultrasound, the results are compared with those of an air electrode with activated carbon catalyst.

EXPERIMENTAL
Silver nanoparticles synthesis methods

Silver nitrate (AgNO₃, Sigma-Aldrich), ethyl alcohol (96% C_2H_5OH, Valerus Co., Bulgaria) as a reducing agent and 25% aqueous ammonia solution (NH_4OH, Valerus Co., Bulgaria) were used to synthesize silver nanoparticles. A 6 mM silver nitrate solution was prepared using distilled water as solvent. The solution was mechanically stirred for about 10 minutes to complete dissolution of the silver nitrate by means of the magnetic stirrer with adjustable speed (Boeco MMS-3000). Without stopping the stirring, 0.8 ml of ethyl alcohol and 0.8 ml of ammonia solution were added one after the other to the solution. The total volume of the sample was 100 ml. The resulting mixture was placed in an ultrasonic bath model UST 2.8-100 (Siel Ltd., Gabrovo Bulgaria) with a power of 120 W for a period of about 5 minutes until a color change from colorless to deep yellow was detected. The temperature of the water in the ultrasonic bath was kept constant (50° C). The resulting samples were analyzed by a UV-Vis (T60 Uv-Visible spectrophotometer) and a transmission electron microscope (JEOL JEM 2100, 80-200 kV).

Gas-diffusion electrodes

The investigated gas-diffusion electrodes consist of a gas-supplying layer (100 mg/cm²) and a catalytic layer (20 mg/cm² and 30 mg/cm²). For the preparation of the gas-suplying layer, a hydrophobic material (carbon black P1042 and polytetrafluorethylene (PTFE)) was made using the procedure described in [18] and carbon paper. The used carbon paper is a commercial product known under the trade name (Freudenberg H2315) with carbon based microspores layer on one side. The thickness of the product was approximately 255μm, where the MPL (microspores layer) was only 50 to 55 μm. The through-plane ohmic resistance was 8 mΩ.cm⁻² (by data from the provider) which made it suitable for gas diffusion media in secondary batteries.

Catalytic layers of active carbon (Norit NK-600 m²/gspecific surface area) only are prepared as well as ones made using four different ways of applying silver nano particles on active carbon, namely:

- impregnation of active carbon with silver nanoparticle solution, 4% Ag;

- impregnation of active carbon with a solution of silver nanoparticles (4% Ag) and subsequent thermal treatment at 300 °C

- adsorption of silver nanoparticles on the active layer of the gas diffusion electrode, 5% Ag;

- adsorption of silver nanoparticles on one-sided hydrophobic carbon paper, 5% Ag.

Air electrodes of the same design and working area of 10 cm² were prepared from the samples. The electrochemical studies were performed by measurement of polarization curves under half-element conditions with an inert counter-electrode in 4 M NaCl at room temperature and working gas - air (for 20 days). Ag/AgCl was used as reference electrode.

RESULTS AND DISCUSSIONS
Characterization of Ag nanoparticles

On Fig. 1 a peak from UV-Vis spectrum is observed at a wavelength of about 420 nm, indicating the presence of spherical silver particles in the solution.

Further studies were carried out with a transmission electron microscope.
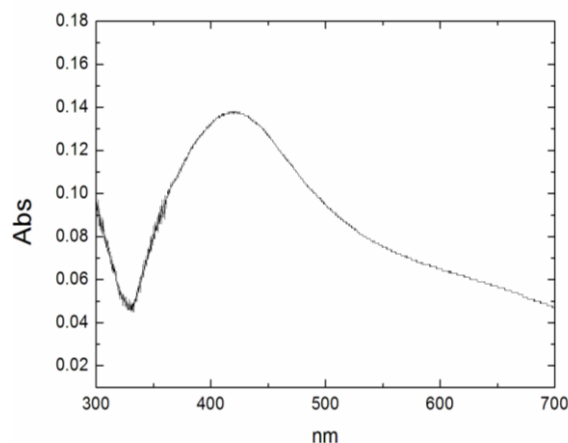
Fig. 1. UV-Vis spectrum of a colloidal solution containing silver nanoparticles

Fig. 2 (a) shows a general view of TEM sample at a magnification of 40, 000 times where separate evenly distributed particles are observed. There are also agglomerates. Increase 200,000 times (Fig. 2 (b)) the magnification of agglomerate it is seen that the dimensions of the individual particles are between 10 and 20 nm. The electron diffraction obtained via TEM is shown on Fig. 2. (c). The diffraction gives a description of the crystal structure of the silver nanoparticles. In this study it was found that it is hexagonal.
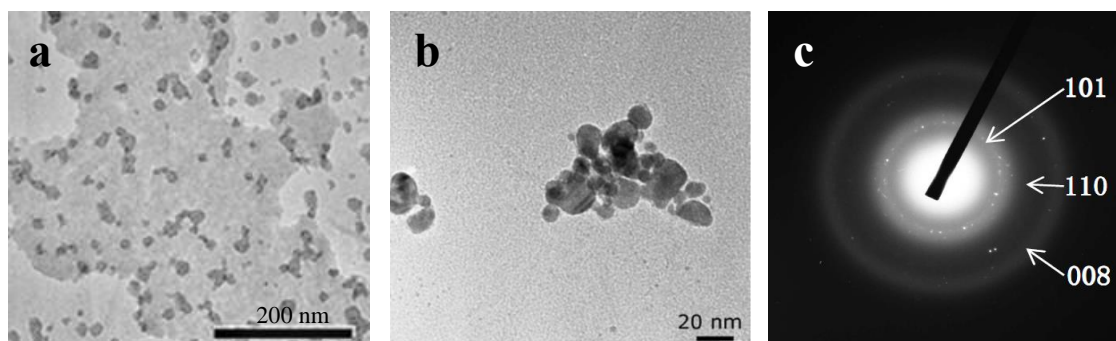
Fig. 2. TEM and diffraction images of silver nanoparticles synthesized using 6 mM aqueous solution of silver nitrate, ethanol and ammonia in an ultrasonic bath.

The XRD pattern of mixture of Norit NK – Ag nanoparticles is shown on Fig. 3. The broad peaks type "halo" at about 25.5 and 42.8 2θ are due to the amorphous carbon (Norit NK). The sharp peaks are related to the Ag particles. The low intensity of these peaks is due to the small amount (4%) of Ag nanoparticles. The comparison with PDF 04-0783 card proves the cubic structure of our nanoparticles. The particles with hexagonal structure are probably lower in compare with these with cubic structure, and by this reason, the XRD shows only these particles with cubic structure in the sample.
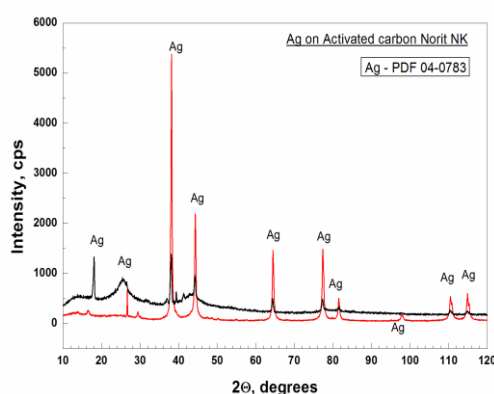
Fig. 3. XRD pattern of Norit NK – Ag nanoparticles mixture compared with cubic Ag standard

Application in gas-diffusion electrodes as catalyst

Fig. 4 shows the polarization characteristics of air electrodes with three types of catalysts: active carbon (Norit NK), the same active carbonactivated by silver nanoparticle solution and the last thermally treated after that at 300 °C.The electrodes have the same gas-supplying layers and equal active layer thickness made as a mixture of the respective catalyst and hydrophobic material at a ratio of 2:1. The amount of activating silver in the active layer of the electrodes is the same - 0.56 mg/cm². It is seen from the graphs that the introduction of a small amount of silver (4%) into the activated carbon improves the polarization characteristics of the

electrodes. The gas-diffusion electrode with catalyst obtained by impregnating the active carbon with silver nanoparticle solution and subsequently thermally treated has better electrochemical characteristics thanother two electrodes especially at high current densities of over 50 mA /cm².
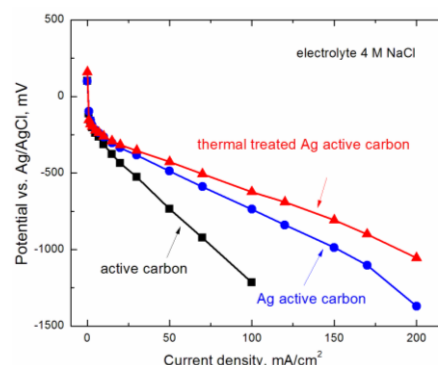
Fig. 4. Polarization curves of air electrodes with different catalysts, electrolyte 4 M NaCl

Ten polarization measurements were carried out on each of the electrodes under investigation during a period of 16 days. For this period the electrodes retain their working ability at a current density of 50 mA/cm², as shown on Fig. 5. This is more clearly seen in the electrode with a catalytic layer obtained by thermal treatment of the active carbon, impregnated with silver nanoparticle solution.

Fig. 6 shows polarization curves of air electrodes which have the same silver content (5%) in the catalytic layers. They differ in the gas-supplying layer and the way the silver nanoparticles have been applied. In one case, the silver nanoparticles are applied directly on the carbon paper, while in the other - on the active layer (Norit NK) of the gas-diffusion electrode.
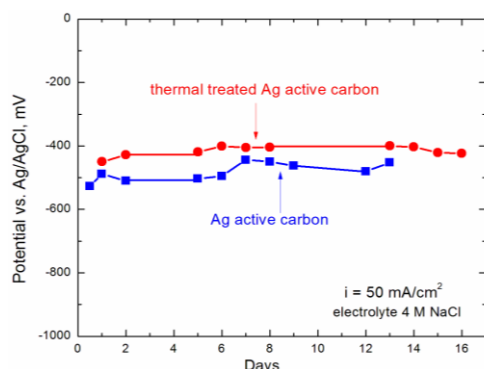
Fig. 5. Electrochemical behavior of the air electrodes at a current density of 50 mA/cm^2

The electrochemical reaction in the porous gas-diffusion layer is taking place on the active centers of the catalyst, located on the surface of the electrolyte-filled pores. The inclusion of silver nanoparticles by adsorption on active carbon results in a more uniform distribution of the catalyst over a large effective surface and an increase in its catalytic ability. It can be seen that when silver nanoparticles are deposited by adsorption on carbon paper, the polarization of the electrode is higher.
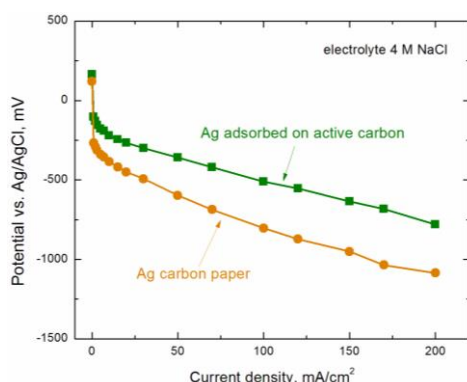
Fig. 6. Polarization characteristics of air electrodes with silver catalyst and various gas-supplying layers

One of the major transport processes in the air electrodes is the transfer of oxygen through the electrode's gas-supplying layer. Hindrances in this process are to a large degree determined by the properties of the porous structure of the gas-supplying layer. The difference in the polarizing dependencies of the two electrodes is due not only to the different ways of adsorption of silver nanoparticles, but also to the differences in the type of gas-supplying layers.

The transport hindrances of the oxygen through the various gas-supplying layers and the influence of the porous structure of a deposited catalyst are also reflected in the duration of the air gas-diffusion electrode operation. It is seen on Fig. 7 that during a period of 20 days, with 10 polarization characteristics carried out, the electrode with silver

nanoparticles applied on active carbon remains stable at a current density of 50 mA/cm^2.
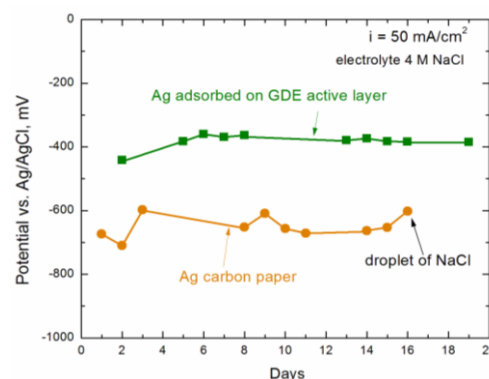
Fig. 7. Electrochemical behavior of air electrodes at 50 mA/cm^2

The electrode with adsorbed silver nanoparticles directly on carbon paper loses its hydrophobicity immediately after the tenth measurement. Disturbance of the hydrophobic properties leads to "electrolytic breakthrough" – passing of electrolyte through the electrode and leakage through its gas-supplying layer. This is most likely due to the large macro pores of the active layer, providing quick and easy electrolyte access to the carbon paper gas-diffusion layer.

CONCLUSION

The silver nanoparticles obtained by a new method are suitable for use as catalysts in gas-diffusion electrodes for Oxygen Reduction Reaction.

The good polarization characteristics of the electrodes, the small amount of activating silver used and the relatively easy preparation of the catalystsare a prerequisite for their future widespread application in different types of metal-air systems.

REFERENCES

1. S. Prabhu, E. K Poulose, *International Nano Letters,* **2:32** (2012).
2. K. M. Kim, K.-Y. Kang, S. Kim, Y.-G. Lee, *Current Applied Physics*, **12,** 1199 (2012).
3. S. S. Kanmani, K. Ramachandran, *Renewable Energy,* **43,** 149, (2012).
4. V. K.Sharma, R. A.Yngard, Y. Lin, *Advances in Colloid and Interface Science,* **145**, (1–2), 83 (2009).
5. C. Johans, J. Clohessy, S. Fantini, K. Kontturi, V.Cunnane, *Electrochem. Commun.*, **4**, 227 (2002).
6. Q. F. Zhou, Z.Xu, *Journal of Materials Science, 39*, 2487 (2004).
7. X.-K. Wang, L Shao, W.-L. Guo, J.-G. Wang, Y.-P. Zhu, C. Wang, *Ultrasonics Sonochemistry,* **16**, 747 (2009).
8. C.-T. Hsieh, D.-Y. Tzou, C. Pan, W.-Y. Chen, *Surface & Coatings Technology,* **207** 11 (2012).

9. H. K. Lee, J.-P. Shim, M.-J. Shim, S. –W.Kim, J.-S. Lee, Materials Chemistry and Physics, **45**, 238 (1996).

10. J. S. Spendelow, A. Wieckowski, *Physical Chemistry Chemical Physics*, **9** (21), 2654 (2007).

11. F. Bidault, D. Brett, P. Middleton, N. Brandon, *Journal of Power Sources*, **187**, 39 (2009).

12. S. Salomé. R. Rego. M. Cristina Oiveira, *Materials Chemistry and Physics*, **143**, 109 (2013).

13. Q. Hong, H. Lu, *Scientific Reports,* **7**, Article number:3378 (2017).

14. E. Gülzow, N. Wagner, M.Shulze, *Fuel Cell,* **3**, 67 (2003).

15. Z. C. Wang, L. Xin, X. S. Zhao, Y. Qiu, Z. Y. Zhang, O. A. Baturina, W. Z. Li, *Renew. Energy*, **62**, 556 (2014).

16. J. M. Linge, H. Erikson, A. Sarapuu, M. Merisalu, M. Rähn, L. Matisen, V. Sammelselg, K. Tammeveski, *Journal of Electroanalytical Chemistry*, **794**, 197 (2017).

17. A. Kaisheva, I.Iliev, S. Gamburtzev, *Journal of Power Sources*, **13**, 181 (1984)**.**

18. E. Budevski, I. Iliev, A. Kaisheva, S. Gamburtzev, E. Vakanova, US Patent 4031033 A (1977).

НАНОРАЗМЕРНИ Ag ЧАСТИЦИ КАТО КАТАЛИЗАТОР В ГАЗОДИФУЗИОННИ ЕЛЕКТРОДИ ЗАРЕДУКЦИЯ НА КИСЛОРОД

Б. Б. Младенова[1,2], Й. Д. Милушева[1], М. И. Кършева[2], И. Д. Хинков[2], Т. Е. Станкулов[1], Г. Р. Борисов[1], Р. И. Букурещлиева[1]

[1]Институт по електрохимия и енергийни системи, Българска академия на науките, ул. Акад. Г. Бончев., бл.10, 1113 София, България

[2] Катедра „Инженерна химия", Химикотехнологичен и теталургичен университет, бул. Климент Охридски № 8, 1756 София , България

(Резюме)

Използван е оригинален метод за получаване на сребърни наноразмерни частици. Частиците са главно със сферична форма, като размерите им варират между 10 и 50 nm. Направената UV-Vis спектроскопия показва плазмен резонансен пик между 440 и 470 nm, което е индикация за наличие на сребърни наночастици. Изследването чрез трансмисионен електронен микроскоп показва, че имат хексагонална и кубична кристална структура.За да се потвърди каталитичната активност на получените сребърни наночастици, те са включени в активния слой на газодифузионни електроди. Активният слой на газодифузионните електроди е приготвен по четири начина. Каталитичната активност на тези електроди е изследвана в условията на полуелемент в електролит 4M NaCl и сравнителен електрод Ag/AgCl. Получените резултати показаха стабилна работа на всички електроди до 50 mA cm^{-2}, а на някой от тях до 100 mA cm^{-2}.

Ключови думи: Ag наноразмерни частици, Ag катализатор, въздушен газодифузионен електрод

Ni incorporation in pSOFC anode ceramic matrix: Part II. Wet chemical reduction in an anhydrous medium

M. V. Gabrovska[1]*, D. A. Nikolova[1], E. A. Mladenova[2], D. E. Vladikova[2], S. K. Rakovsky[1], Z. B. Stoynov[2†]

[1]*Institute of Catalysis, Bulgarian Academy of Sciences, Acad. G. Bonchev Str., Bldg. 11, 1113 Sofia, Bulgaria*

[2]*Acad. Evgeni Budevski Institute of Electrochemistry and Energy Systems, Bulgarian Academy of Sciences, Acad. G. Bonchev Str. Bldg. 10, 1113 Sofia, Bulgaria*

The well-known proton conductive electrolyte yttrium-doped barium cerate $BaCe_{0.85}Y_{0.15}O_{2.925}$ (BCY15) was used as an anode ceramic matrix for synthesis of Ni-based cermet anode with application in proton conducting solid oxide fuel cell (pSOFC). A cost-effective and energy-efficient wet-chemical reduction approach was presented by using of nickel chloride hexahydrate as precursor, ethylene glycol as anhydrous medium, hydrazine hydrate as reducing agent and alkaline solution as pH regulator. The characterization of the Ni-cermet was performed by Powder X-ray diffraction, N_2-physisorption and SEM techniques. The electrochemical properties of anode cermet were determined by impedance spectroscopy after high-temperature sintering followed by reduction in hydrogen atmosphere. It was found that the preparation of BCY15/Ni cermet in ethylene glycol medium leads to (i) Structure preservation of the proton conducing ceramic matrix in the anode composite;(ii) Increase the specific surface area as result of metal Ni phase formation, a precondition for existence of numerous active sites for fuel electrochemical oxidation; (iii) Obtaining of homogeneous, nano-scaled, uniform distributed and non-agglomerated metal nickel particles. The cermet elaborated by ethylene glycol assisted route possesses a capacity to be promising anode in BCY-based pSOFC devices because of the anode ceramic matrixstructure preservation and demonstrated electrochemical performance.

Keywords: BCY15/Ni anode cermet; Ethylene glycol; Hydrazine; PXRD; SEM; Electrochemical impedance spectroscopy.

INTRODUCTION

The anodes for protonic solid oxide fuel cells (pSOFC) are often applied as composites (mixtures) of the electron conducting electrode material and the proton conducting electrolyte. One of the most commonly used anode for hydrogen oxidation is a porous cermet structure consisting of two interpenetrating and interconnecting networks of Ni-metal and electrolyte particles. Yttrium-doped barium cerate $BaCe_{1-x}Y_xO_{3-\delta}$ (BCY) with ABO_3perovskite-type structure is known as a widely applicable solid proton conductive electrolyte [1-5].

Generally, the anode cermet is fabricated by incorporation of NiOin theBCY electrolyte, applying standard ceramic technology, namely mixing, cold pressing and sintering, followed by reduction of the anode before operation of the cell. The low kinetics and high temperature, typical for this approach results in obtaining of solids with low homogeneity, presence of undesired secondary phases and uncontrolled (and typically large) particle size of low surface area [6]. Another

complication is the eventual formation of parasitic phases at the electrode/electrolyte interfaces that can limit the ionic migration, thereby increasing the electrode polarization [7].

It was reported that the formation of small-sized Ni particles in the Ni/YSZ cermet promotes the development of fine continuous Ni network and results in improvements in electrical conductivity and porosity [8]. The existence of small Ni^0 particles will provide for generation of numerous catalytic sites for the hydrogen adsorption provoking the enhancement of the anode activity. Thereby, the usage of synthesis modes for preparation of nano-sized metal nickel particles is one of the solutions for better efficiency of the anode cermet [9].

The preparation of fine nickel powders has been investigated intensively by the reduction of nickel salts in aqueous solution due to the good solubility of nickel salts in water, the low reaction temperature and the simple procedure [10]. A successful synthesis route represents the wet-

---

reduction mode, using hydrazine (N_2H_4) where the morphology of nickel powders, such as the shape and the size of particles, the size distribution and the degree of agglomeration, can be easily controlled by the reaction parameter, the solvent composition, the nucleation agent, the surfactant, etc. [11-14]. Hydrazine is attractive reducing agent for the preparation of fine nickel powder due to its strong reduction properties in low temperature range and high pH values. The temperature and pH dependence of hydrazine reducing ability makes the synthesis easily controllable [15, 16].

Hydrazine has a standard reduction potential of −1.16V in an alkaline solution, represented by the oxidation reaction ($N_2H_4 + 4OH^- = N_2 + 4H_2O + 4e^-$) [15, 17]. Nickel, which has a standard reduction potential of −0.25V, is consequently able to be reduced by N_2H_4 ($2Ni^{2+} + 4e^- = 2Ni$) [15]. Therefore, a chemical reduction of the Ni^{2+} ion with N_2H_4 in basic environment at high pH (favorable to form pure Ni nanoparticles) [14, 15]can be simply shown in the following equation: $2Ni^{2+} + N_2H_4 + 4OH^- \rightarrow 2Ni + N_2 + 4H_2O$. The reduction is accompanied by gaseous nitrogen evolution, followed by growth of Ni^0 particles. The degree of reduction can be determined from the nitrogen volume according to the above mentioned reaction. Solution pH influences the synthesis of the nickel nanoparticles. The discharge of the nickel nano-powders is enhanced when the redox potential increases because of the increasing pH of the solution, by adding a strong base at a certain temperature and constant nickel ion concentration. In addition, it has been shown that black nickel powder, cannot be produced if the pH is less than 9.5 [14, 15].

In our previous paper [18] the metal Ni was incorporated in the anode ceramic matrix of yttrium-doped barium cerate, $BaCe_{0.85}Y_{0.15}O_{2.925}$(BCY15) by wet-chemical approach as an alternative to the traditional ceramic method for pSOFC Ni-based cermet anode preparation. The possibility of metal Ni incorporation in BCY15 by wet-chemical reduction with hydrazine route in an aqueous medium was examined. It was found that Ni-anode cermet demonstrated electrochemical performance similar to that of commercial NiO-based anode cermets in respect to the electronic conductivity of the Ni net. It was established that the preparation of Ni-cermet anode precursor in an aqueous medium results in partial reorganization of the initial BCY15 structure due to the hydrophilic properties of the used ceramic matrix.

Another approach for synthesis of nickel nano-particles is the reduction with hydrazine in an anhydrous environment [19]. In this regard, in the so-called polyol process (polyol is an alcohol containing functional OH groups), the ethylene glycol (EG) as monomeric polyol serves as both reducer and solvent.EG with a relatively high boiling point (198°C) is a good dispersive medium for starting reactants and as a good capping agent with two OH groups, it can hold free metal ions tightly in the solution [20, 21]. No metal Ni particles can be formed in EG medium without adding sufficient amount of hydrazine indicating that Ni^{2+}ions are reduced by hydrazine instead of EG.

It can be expected that if the incorporation of Ni in pSOFC anode ceramic matrix is performed in EG medium a preservation of the anode ceramic matrix in the BCY15/Ni cermet may be achieved.

EXPERIMENTAL
Sample preparation
BCY15/Ni-EG sample with a composition of NiO/BCY15 = 44.4/55.6 (volume ratio) was synthesized in non-aqueous surroundings by means of Ethylene glycol anhydrous, 99.8% acquired by SIGMA-ALDRICH.More detailed description of the preparation procedure was presented in Ref. 18. Briefly, this technique consists in obtaining of BCY15/Ni cermet precursor powder by chemical reduction of $NiCl_2$ with hydrazine. The role of EG is to prevent a high affinity of BCY15 to water.

To get reference sample for the characterization of BCY15/Ni-EG, unsupported nickel denoted as Ni-EG, was also prepared in the same manner, however in the absence of the anode ceramic matrix.

Sample characterization
Powder X-ray diffraction (PXRD) data were collected on an APD 15 Philips 2134 diffractometer employing CuKα radiation (λ = 0.15418 nm), operated at U = 40 kV and I = 30 mA. The crystalline phases were identified using Joint Committee on Powder Diffraction Standards (JCPDS) files.

The morphological studies were performed using Electron microscope JEOL 6390 equipped with INCA Oxford an energy dispersive X-ray spectroscopy (EDS).

The texture characteristics were determined by low-temperature (77.4K) nitrogen adsorption in a Quantachrome Instruments NOVA 1200e (USA) apparatus. The nitrogen adsorption–desorption isotherms were analyzed to evaluate the specific surface area, determined on the basis of the BET

equation. The samples were outgassed for 16 h in vacuum at 80ºC before the measurements.

For *in situ* analysis of the Ni network performance an impedance approach for direct measurements of the Ni cermet electronic conductivity in the classical Ni-YSZ was applied [22]. The electrochemical impedance measurements were performed on IVIUM - CompactStat e10030 in the temperature interval 100–750°C and frequency range 1 MHz–0.01Hz with a density of 5 points/decade and amplitude of the AC signal 1 mA in reduction atmosphere. The testing is performed on single "bare" anodes sandwiched between two Ni contact nets. The direct analysis starts in the beginning of the reduction stage at 750°C. In this way, the electronic conductivity is directly measured giving accurate information regarding the nickel network formation in the bulk anode structure.

RESULTS AND DISCUSSIONS

The PXRD patterns of BCY15 (Fig. 1a) show the presence of a single phase that can be attributed to orthorhombic pervoskite, isostructural with $BaCeO_3$ (JCPDS file 00-022-0074) and yttrium doped analogue, $BaCe_{0.9}Y_{0.1}O_{2.95}$(JCPDS file 01-081-1386). The recoded well-formed reflections $BaCeO_3$ are in agreement with the calculated mean crystallite size of 150 Å. No diffraction peaks due to Y_2O_3 phase are registered indicating that yttrium ions are incorporated into the perovskite lattice [18].

As it can be seen from the diffractogram of BCY15/Ni-EG (Fig. 1b), the typical reflections of the metal Ni with cubic lattice symmetry (fcc) according to standard of metal Ni (JCPDS file 00-004-0085) and reference patterns of sample Ni-EG (Fig. 1c) are observed. Furthermore, the respective 2θangles of the characteristic peaks of BCY15 in the BCY15/Ni-EG sample have no changes compared to the original BCY15 perovskite, indicating that no excrescent reactions taken place during the BCY15/Ni-EGpreparation and good chemical compatibility between the BCY15 and metal Ni.

The calculated metal Ni lattice parameter (*a*) and the metal Ni cell volume (V_{cell}) of BCY15/Ni-EG are presented in Table 1, displaying values similar to those of standard metal Ni (JCPDS file 00-004-0850). A difference in the intensity of the metal Ni reflections going from BCY15/Ni-EG to unsupported reference Ni-EG sample is detected, showing a different degree of crystallinity.
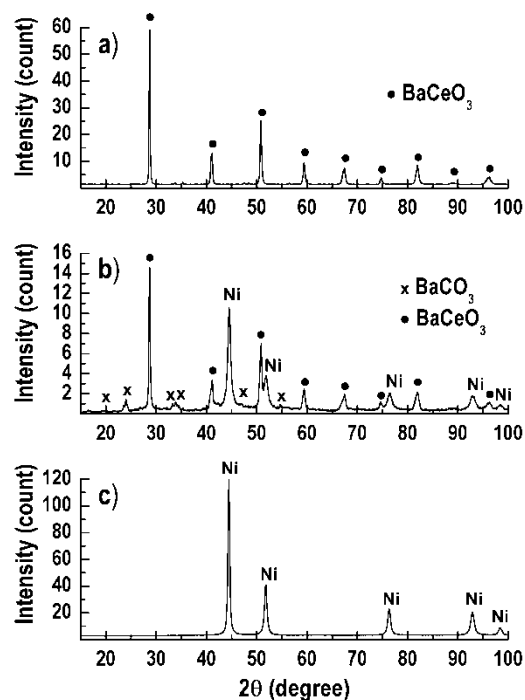
Fig. 1. PXRD patterns of BCY15 (a), BCY15/Ni-EG (b) and Ni-EG (c) solids

The positive role of the BCY15 presence in the anode composite on the metal nickel dispersion is clearly demonstrated by the values of the bulk mean Ni^0 crystallite sizes (L) estimated from the full-width at half-maximum value of the most intensive peak of the Ni^0 phase (111) situated at 2θ ≈ 44.5°. The data collected in Table 1 discloses the smaller size of metal Ni crystallites in BCY15/Ni-EG (130 Å) in comparison with those of unsupported reference sample Ni-EG (220 Å). On another hand, the smaller mean Ni^0 crystallite size of BCY15/Ni-EG than that one in analogue sample, prepared in water (157 Å) [18] illustrates the dispersive role of EG medium.

Well-organized reflections of orthorhombic $BaCeO_3$ phase are also recorded with the as-prepared BCY15/Ni-EG(Fig. 1b) as opposed to the sample prepared in water [18]. PXRD analysis unveils only a few low in intensity reflections of$BaCO_3$ phase with orthorhombic lattice symmetry (JCPDS file 00-045-1471). The observed phenomenon evidences for the preservation of the ceramic matrix BCY15 structure during synthesis of the Ni-based anode sample in EG environmen.

Table 1. Lattice parameters of metal Ni and NiO obtained after treatment of BCY15/Ni-EG in different atmospheres

| Parameter | BCY15/Ni-EG | | | Reference | JCPDS files |
	as-prepared[a]	sintered[b]	post-impedance[a]	[a]Ni[0] (00-004-0850)	[b]NiO (00-047-1049)
a (Å)	3.5056(15)	4.1788(17)	3.5269(9)	3.5238	4.1771
V_{cell} (Å^3)	43.083(56)	72.97(11)	43.87(34)	43.76	72.88
L (Å)	130.0(92)	153.0(27)	248.1(19)	-	-

N_2-physisorption analysis reveals that BCY15 anode matrix is a typical macroporous material such is confirmed from type of its isotherm (Fig. 2a), II Type characteristic of aggregated powders as clays, cements, etc. [23].
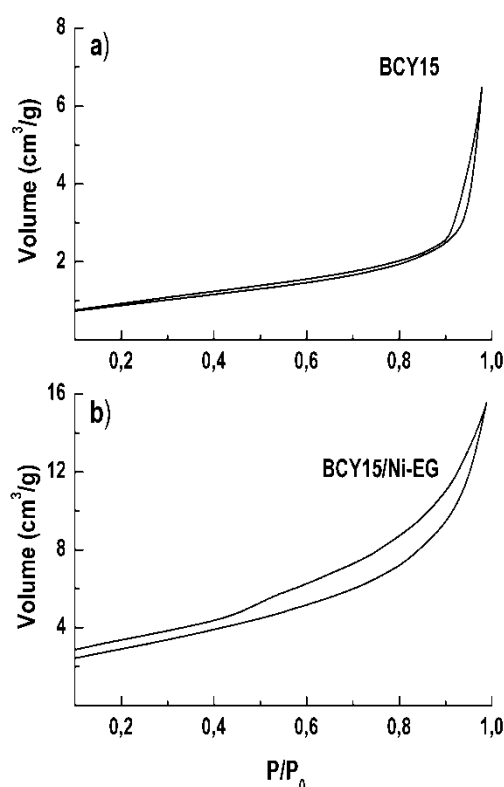
Fig. 2. Adsorption–desorption isotherms of BCY15 (a) and BCY15/Ni-EG (b) solids

The observed very narrow hysteresis loop displays presence of some mesopores on the surface which are termed as Type IIb exhibiting Type H3 hysteresis. Type H3 hysteresis loop is a distinctive of aggregates of platy particles or adsorbents containing slit-shapes pores [23].

The character of the isotherm type is preserved after incorporation of Ni^{2+} ions subsequent by reduction to the metal Ni state (Fig. 2b). The clearly detected hysteresis (H3 type) for BCY15/Ni-EG confirms generation of new mesopore system from metal nickel phase on BCY15. This finding corresponds to increase in the BET surface area from 3 m^2/g for BCY15 to 11 m^2/g. The three and a half times increase in BET surface area is a

precondition for existence of numerous surface active sites where the electrochemical fuel oxidation is carried out.

The microstructure observations by SEM indicate that anode matrix BCY15 possesses relatively homogeneous porous structure. The powder surfaces consist of randomly distributed particles similar in kind and shape (Fig. 3a).The deposition of metal nickel on BCY15 surface does not altered the morphology of the ceramic matrix (Fig. 3b).
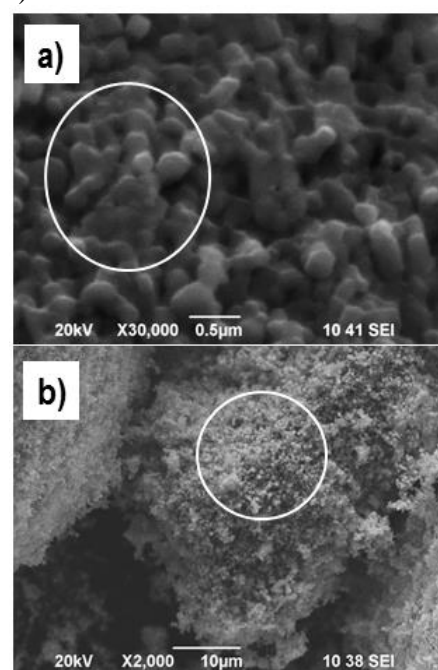
Fig. 3. SEM micrographs of BCY15 (a) and BCY15/Ni-EG (b) solids

The image of BCY15/Ni-EG show easily recognizablemono-dispersed spherical Ni^0 particles (Fig. 3b). The surface is composed of identical in shape fine-grained particles signifying that the synthesis in EG medium induces obtaining of precursor with smaller particle size than in water. It may be remarked also that single independentfragments of BCY15 anode matrix are not recorded on the surface of BCY15/Ni-EG as in the case of the analogue sample prepared in water [18]. This result prompts higher sample homogeneity and uniform distribution of the metal

nickel particles on the perovskite phase in BCY15/Ni-EG.

The surface elemental analysis performed by Energy Dispersive Spectroscopy (EDS) is presented in Table 2. The marked areas in both images documented the presences of all the elements from the sample composition. The Ba/Ce ratio evidences the preservation of BCY15 structure.

Table 2. The surface elemental analysis of the studied solids

Element (wt. %)	O	Ni	Ba	Ce	Y	Ba/Ce
BCY15	16.54	-	42.34	36.95	4.17	1.145
BCY15/Ni-EG	10.99	62.44	13.38	11.84	1.35	1.130

The characterization data suggest that the preparation of supported on BCY15 Ni-based cermet anode by EG assisted synthesis approach leads to the preservation of the proton conducing ceramic matrix in the anode composite. The metal Ni phase provides the required catalytic activity and electronic conductivity for the oxidation of hydrogen fuel. It is of significant importance the existence of BCY15 phase in the cermet because it plays an essential electrocatalytic role in the creation of additional reaction sites where the anode reactions may occur, providing a conductivity network for H^+ ions and extends the triple-phase boundary (TPB) length, thereby resulting in improved electrode performance in addition to the inhibiting of the coarsening and grain growth of the metal Ni particles [1, 7, 24].

For analysis of the Ni network quality in the structure of a real anode, the standard ceramic technology was used for the preparation of pressed tablets from BCY15/Ni-EG (cold pressing. 3t/5 min), followed by their sintering in air at 1200°C for 5 h. The volumetric shrinkage of the tablet didn't exceed 6%. Because the NiO phase is reduced to the metal Ni in a separate step, the sintering of cermet at lower temperatures than 1200°C can induce poor performance due to poor connectivity in the electrolyte.

PXRD patterns of sintered BCY15/Ni-EG (Fig. 4a) exhibits thin and intensive reflections of well-crystallized NiO phase with lattice parameters (*a* and V_{cell}) close to the standard NiO (JCPDS file 00-047-1049) (Table 1). Well-defined diffraction lines of $BaCeO_3$ phase are also detected, signifying presence/preservation of the perovskite structure. Furthermore, an appearance of very low in intensity diffraction lines characteristics fororthorhombic Y_2BaNiO_5 oxide phase is documented (JCPDS file 00-047-0090). Likewise, a poorly crystallized $BaNiO_{2.36}$ phase with hexagonal crystal symmetry (JCPDS file 00-047-0089) was identified in sintered sample, prepared in water [18]. Similar results was reported for sintered BZY20/NiO proton conducting ceramic which contains second-impurity phases as $BaNiO_x$ (2<x<3) and Y_2BaNiO_5, that host unincorporated Ni^{2+} ions into BZY [25].

A comparison of the NiO mean particle size shows larger values in BCY15/Ni-EG (153 Å) than that one in analogue sample, prepared in water (124 Å) [18] which corresponds with the better crystallization of NiO phase in BCY15/Ni-EG. Nevertheless, it may be noted that the sintering prompts formation of nano-metric NiO particles (Table 1) dispersed over the BCY15 matrix.

The next stage for BCY15/Ni-EG cermet formation represents a step-wise standard reduction procedure, performed at 750°C with a H_2/N_2 gaseous mixture. The first reduction step was accomplished with gaseous mixture of N_2 (flow rate of 35 nml/min·cm^{-2}) and gradually increasing portions of H_2 (flow rate of 10 nml/min·cm^{-2}). This treatment results in reduction of NiO surface until to formation of the Ni net. The second reduction step concerns treatment only with H_2 gas (flow rate of 35 nml/min·cm^{-2}) for 60 min.
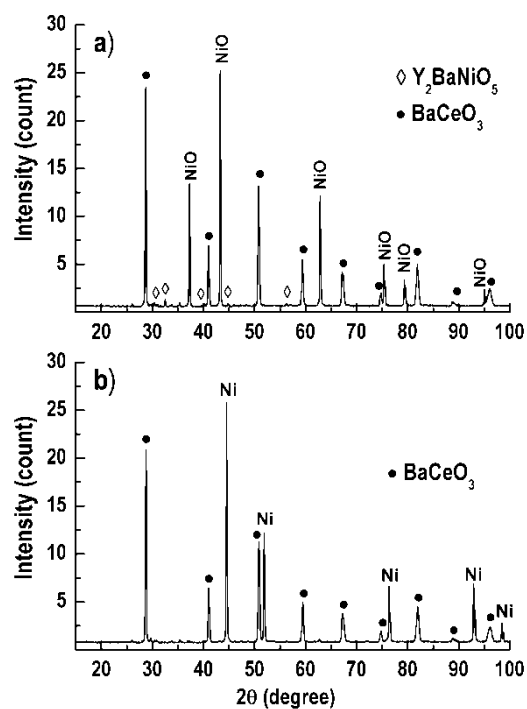
Fig. 4. PXRD patterns of BCY15/Ni-EG after sintering (a) and after impedance measurements (b)

The impedance measurements shows thatprior to the reduction (0 min) the resistance of

BCY15/Ni-EG is changed in large interval from 180 to 215 Ω(Fig. 5a) in comparison with the cermet prepared in water that demonstrates a fairly low resistance of 31.5 Ω [18].

The reduction of BCY15/Ni-EG (Fig. 5b) starts at 11 min after the beginning of the process and displays similar resistivity to the cermet, synthesized in water medium, which reduction starts at 8 minute [18]. Thereduction progression of BCY15/Ni-EG proceeds slowly and after 37 minutes from the beginning of the reduction, the resistance of Ni net drops down to 52 mΩ. The resistivity value remains unchanged until the end of the reduction cycle of 137 minutes. Inversely, the reduction of cermet prepared in water advances more rapidly thus the resistance of Ni net decreases down to 70 mΩ for about 20 minutes and remains unchanged until the end of the reduction cycle of 123 minutes [18].
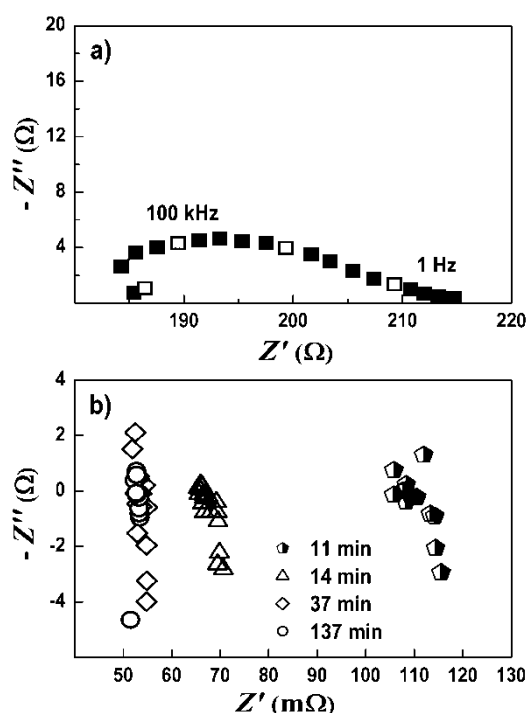
Fig. 5. Impedance diagrams measured during the reduction of BCY15/Ni-EG cermet before the beginning of the reduction (a) and after 11, 14, 37 and 137 minutes of reduction (b)

A comparative analysis allows to be noted that BCY15/Ni-EG exhibits improved electrochemical performance than the analogue cermet synthesized in water because at the end of reduction cycle, the resistivity of BCY15/Ni-EG reaches lower value than the prepared in water cermet.

A possible explanation of the demonstrated electrochemical behavior may be found in the results obtained from PXRD experiments of the sintered and post-impedance (reduced) cermets.

Sintering of the cermet prepared in water leads to the obtaining of rather complex material consisting of NiO and BCY15 perovskite as prevailing phases, and $BaNiO_{2.36}$ and $Y_{0.10}Ce_{0.90}O_{1.95}$ as impurity phases [18]. After reduction/impedance, reflections of metal Ni along with these corresponding to $BaCeO_3$, $BaNiO_{2.36}$ and $Y_{0.10}Ce_{0.90}O_{1.95}$ phases were registered. The existence of hexagonal $BaNiO_{2.36}$ phase indicates that the incorporated Ni ions into $BaNiO_{2.36}$ cannot be reduced to the metal state at temperature of 750°C. This explains a shorter time of about 20 minutes needed for reduction only of the Ni^{2+} ions included in the NiO phase.

The relatively slow reduction of sintered BCY15/Ni-EG (37 minutes) may be ascribed to the reduction of Ni^{2+} ions from dominant NiO phase assisted by the reduction of Ni^{2+} ones that exist within the Y_2BaNiO_5 second-phase (Fig. 4a).

PXRD patterns of post-impedance BCY15/Ni-EG cermet (Fig. 4b) displays only reflections of well-organized cubic metal Ni along with BCY15 perovskite structure.Apparently, the Ni^{2+} ions incorporated in Y_2BaNiO_5 second-phase are completely reduced to the metal Ni suggesting high purity and absence of parasitic phases which may affect the cermet conductivity.The results obtained demonstrate the advantage of the EG assisted synthesis method.

The calculated metal Ni lattice parameter values of post-impedance BCY15/Ni-EG cermet are comparable to these of the standard metal Ni (Table 1). The estimation of the mean metal Ni crystallite sizes (L) from the full-width at half-maximum values of the (111) diffraction lines at $2\theta \approx 44.5°$ reveals that the reduction/impedance causes growth of the initial metal Ni crystallites being also in nano-metric scale.

The slightly longer reduction time for BCY15/Ni-EG cermet induces formation of relatively larger metal Ni particles (248 Å) in comparison with these one of the cermet prepared in water (231 Å) [18].

CONCLUSIONS

The synthesis of Ni cermet in non-aqueous medium preserves the proton conducing ceramic structure in the anode composite thus suppresses the thermally induced coarsening of metal Ni particles thereby ensures their dispersion; increases the specific surface area as a result of the metal Ni phase creation enhancing the number of active sites, which is a precondition for improved electrochemical performance of the anode cermet.

The wet-chemical reduction mode using hydrazine is a cost-effective and energy-efficient

promising route for metal Ni incorporation in the BCY15 anode ceramic matrix providing homogeneity and uniform distribution of the nano-scaled metal Ni particles.

It may be concluded from this study that the cermet elaborated by ethylene glycol assisted approach possesses a capacity suitable to be used as anode in BCY-based pSOFC devices because of the anode ceramic matrixstructure preservation and improved electrochemical performancein comparison with Ni-cermet prepared in water medium.

REFERENCES

1. N. Mahato, A. Banerjee, A. Gupta, S. Omar, K. Balani, *Prog. Mater.Sci*., **72**, 141 (2015).
2. P. Frontera, V. Modafferi, F. Frusteri, G. Bonura, M. Bottari, S. Siracusano, P. Antonucci, *Int. J. Hydrogen Energy*, **35**, 11661 (2010).
3. H. Iwahara, T. Esaka, H. Uchida, N. Maeda, *Solid State Ionics,* **34**, 359 (1981).
4. H. Iwahara, H. Uchida, K. Ono, K. Ogaki, *J. Electrochem. Soc.,* **135**, 529 (1988).
5. H. Iwahara, *Solid State Ionics*, **52**, 99 (1992).
6. R. Bell, G. Millar, J. Drennan, *Solid State Ionics*, **131**, 211 (2000).
7. E. Fabbri, D. Pergolesi, E. Traversa*, Sci. Technol. Adv. Mater.*, **11** (2010) article 044301.
8. Z.-C. Chen, Y. Sakane, T. Tsurumaki, Y. Ayame, F. Fujita, Proceedings of 16th International Conference on Composite Materials, Kyoto, Japan, 2007, WeKM1-08_chenzc229918p.pdf.
9. B. Zhu, R. Raza, G. Abbas, M. Singh, *Adv. Funct. Mater.*, **21**, 2465 (2011).
10. Y. Li, C. Li, H. Wang, L. Li, Y. Qian, *Mater. Chem. Phys.,* **59**, 88 (1999).
11. Y. Moon, H. Park, D. Kim, C. Kim*, J. Am. Ceram. Soc.*, **78**, 2690 (1995).
12. H. Park, Y. Moon, D. Kim, C. Kim*, J. Am. Ceram. Soc*., **79**, 2727 (1996).
13. J. Zhang, S. Yang, Q. Xue, *J. Mater. Res*., **15**, 541 (2000).
14. D. P. Wang, D.-B. Sun, H.-Y.Yu, and H.-M. Meng, *J. Crys. Growth*, **310**, 1195 (2008).
15. J. Park, E. Chae, S. Kim, J. Lee, J. Kim, S. Yoon, J-Y. Choi, *Mater. Chem. Phys*., **97**, 371 (2006).
16. G-Y. Huang, S-M. Xu, G. Xu, L-Y.Li, L-F. Zhang, *Trans. Nonferrous Met. Soc. China*, **19**, 389 (2009).
17. D. V.Goia, *J. Mater. Chem*., **14**, 451 (2004).
18. M. Gabrovska, D. Nikolova, E. Mladenova, D. Vladikova, S. Rakovsky, Z. Stoynov, *Bulg. Chem. Commun*., **49**, Special Issue C, 171 (2017).
19. S.-H. Wu and D.-H. Chen, *J. Colloid Interface Sci.*, **259**, 282 (2003).
20. L. Kurihara, G. Chow, P. Schoen, *Nanostruct. Mater.*, **5**, 607 (2008).
21. H. Hu, M. Mo, B. Yang, X. Zhang, Q. Li,W. Yu, Y. Qian, *J. Cryst. Growth*, **258**, 106 (2003).
22. D. E. Vladikova, Z. B. Stoynov, Z. Wuillemin, D. Montinaro, P. Piccardo, I. Genov, M. Rolland, *ECS Transactions*, **68**, 1161 (2015).
23. F. Rouquerol, J. Rouquerol, K. Sing, In Adsorption by Powders and Porous Solids, Principle, *Methodology and Applications*, Academic Press, New York, 1999.
24. M. Mogensen and S. Skaarup, *Solid State Ionic*, **86–88**, 1151 (1996).
25. J. Tong, D. Clark, L. Bernau, M. Sanders, R. O'Hayre, *J. Mater. Chem.*, **20**, 6333 (2010).

ВЪВЕЖДАНЕ НА Ni В АНОДНАТА КЕРАМИЧНА МАТРИЦА НА ПРОТОН ПРОВОДЯЩИ ТВЪРДООКСИДНИ ГОРИВНИ КЛЕТКИ: ЧАСТ II. МОКРА ХИМИЧНА РЕДУКЦИЯ В БЕЗВОДНА СРЕДА

М. В. Габровска[1]*, Д. А. Николова[1], Е. А. Младенова[2], Д. Е. Владикова[2],
С. К. Раковски[1], З. Б. Стойнов[2]

[1]*Институт по катализ, Българска академия на науките, ул. Акад. Г. Бончев, бл. 11, 1113 София, България*
[2]*Акад. Евгени Будевски Институт по електрохимия и енергийни системи, Българска академия на науките, ул. Акад. Г. Бончев, бл. 10, 1113 София, България*

(Резюме)

Добре известният протон проводящ електролит итрий-дотиран бариев церат, $BaCe_{0.85}Y_{0.15}O_{2.925}$ (BCY15) е използван като анодна керамична матрица за синтез на Ni керамичен анод с приложение в протон проводящи твърдооксидни горивни клетки. Представен е рентабилен и енергийно-ефективен метод на мокра химична редукция при използване на никелов хлорид хексахидрат като прекурсор, етилен гликол като безводна среда, хидразин хидрат като редуциращ агент и алкален разтвор като регулатор на pH. Охарактеризирането на Ni кермет е извършено чрез прахова дифракция на рентгенови лъчи, нискотемпературна сорбция на азот и сканираща електронна микроскопия. Електрохимичните свойства са изследвани чрез импедансна спектроскопия след високотемпературно синтероване и редукция с водород. Установено е, че получаването на BCY15/Ni кермет в присъствие на етилен гликол води до (i) Запазване структурата на протон проводящата керамичната матрица от анодната композиция;(ii) Увеличаване на специфичната повърхност в резултат от образуване на металната никелова фаза, което е предпоставка за наличие на голям брой активни центрове за електрохимичното окисление на горивото; (iii) Получаване на хомогенни, нано-размерни, равномерно разпределени и не агломерирани метални никелови частици.Керметът, получен в среда на етилен гликол притежава качества, които го правят подходящ като анод в BCY15 протон проводящи твърдооксидни горивни клетки поради съхраняване структурата на анодната керамична матрица и неговото електрохимично поведение.

Ключови думи: BCY15/Ni аноден кермет, етилен гликол, хидразин, PXRD, СЕМ, Електрохимична импедансна спектроскопия

One step solid-state synthesis of lanthanum cobalt oxide perovskites as catalysts for oxygen evolution in alkaline media

S. Enache[1*], M. Dragan[1**], A. Soare[1], D. Ion-Ebrasu[1], A. Zaulet[1], M. Varlam[1], K. Petrov[2]

[1] National Institute for Cyogenics and Isotopic Technologies ICSI-Rm. Valcea, Uzinei Street No. 4, 240050, Romania
[2] Acad. Evgeni Budevski Institute of Electrochemistry and Energy Systems, Bulgarian Academy of Sciences, Acad. G. Bonchev Str., Bl.10, 1113 Sofia, Bulgaria

Lanthanum cobalt oxide perovskites exhibit good catalytic activity and stability towards oxygen evolution reaction in alkaline media. This makes them especially attractive as electrodes for water electrolysis since they may substitute the more expensive ones used so far, such as iridium and ruthenium oxides. Although various preparation methods are well documented in literature, the fabrication of lanthanum cobalt oxides is often laborious, involving intermediate grinding and annealing steps. Different from that, we show that lanthanum cobalt oxide perovskites can be readily and thoroughly obtained by solid-state synthesis from lanthanum and cobalt oxide precursors, without making use of intermediate processing steps. The resulted powders are essentially within a polycrystalline single phase with well-defined structural and morphological properties. In order to assess the activity towards the oxygen evolution reaction, electrodes obtained from the resulted powders are investigated in a three electrode electrochemical cell in 1N KOH.

Keywords: water electrolysis, perovskite, solid-state synthesis

INTRODUCTION

Although the initial discovery of water electrolysis has been demonstrated in acidic aqueous solutions, nowadays trend towards mass production of hydrogen involves alkaline media, such as potassium hydroxide [1]. When compared to acidic media, the advantage of water electrolysis in alkaline solutions is the increased hydrogen production efficiency and corrosion resilience, together with a prolonged life time performance since the alkaline water electrolysis may be operated at much lower over-potentials and current densities [2]. Apart from that, the possibility to substitute platinum-based catalysts for less expensive materials (e.g., nickel and cobalt oxide) with enhanced catalytic activity and stability towards hydrogen and oxygen evolution reactions makes it especially attractive from an applicative point of view, since the manufacturing of large scale operating hydrogen production stations often demands laborious and expensive processing routes for the catalytic material [3,4].

Among various platinum-free catalysts, the most promising ones are the oxides of the *3d*-band transition metals, with an activity trend towards oxygen evolution reaction varying such as: Ni > Co > Fe > Mn [2-5]. Although mixtures and alloys of these transition metals and their oxides exhibit valuable potency towards oxygen evolution reaction, it is the perovskite-like crystalline structure of these elementals with lanthanum in the form of $LaTMO_3$

(i.e., TM - Ni, Co, Fe and Mn) that has attracted a lot of interest lately, mainly due to their enhanced ionic conductivity and stability in alkaline media [6]. In literature, these systems documented as ABO_3 perovskite structures, in which A ions can be rare earth, alkaline earth and alkali that fit into dodecahedral sites of the crystalline lattice, whereas the B ions can be 3-, 4- and 5d-transition metal ions which occupy octahedral sites [3]. The perovskite lattice can accommodate multiple substitutions on both A and B sites, making it possible to fine tune the overall physical properties, such as ionic conductivity and dielectric constant, as well as chemical stability and activity towards oxygen evolution reaction. One special case is $LaCoO_3$, whose microstructure, catalytic activity, electronic and ionic conductivity depend strongly on the synthesis route. To that, oxygen deficiency plays an important role [3,7].

As a direct synthesis route, $LaCoO_3$ perovskites can be prepared by solid-state reaction of pure lanthanum and cobalt oxides, carbonates and oxalates at temperatures as high as 1200°C [8]. The procedure often involves intermediate processing steps such as calcination to remove residual solvents and organic contaminants and intermittent grinding to homogenize the mixtures. The resulted powders are inhomogeneous and coarse, with non-uniform particle size distribution. In order to overcome that, wet chemical methods such as sol-gel [9], co-

precipitation [10] and hydrothermal methods [11] have been employed to synthesise $LaCoO_3$ powders with desired stoichiometry, particle size and even shape. However, several disadvantages have been noted with these techniques such as the evaporation of solvents resulting in phase segregation and the alteration of stoichiometry due to incomplete precipitation, expensive chemicals and time-consuming processes. Alternatively, the combustion of a precursor solution containing metal ions, oxidant and a fuel leads to fine crystalline powders, with homogeneous particle size distribution (i.e., around 10 - 15nm) [12]. Although the combustion method is suitable to obtain catalytic $LaCoO_3$ powders with high specific area (i.e., as high as $80m^2/g$), it turns out that it demands an elaborate preparation procedure, involving corrections for the oxidant-to-fuel ratio and for the pH of solution. Moreover, the inherent contamination with carbon upon the auto-ignition process requires a post-processing annealing step at 1250^0C, which leads to grain coarsening and sintering, eventually [9, 12].

In this work, we show that $LaCoO_3$ powders can be directly and thoroughly obtained by one step solid state synthesis in air from lanthanum and cobalt oxides upon heat treatment at most 8 hours and temperatures not higher than 1000^0C, without making use of intermediate processing steps. The resulted powders are essentially within a single crystalline phase (i.e., with hexagonal *R-3c* crystal symmetry) that consists of micro-meter sized grains which may also exhibit a slight difference in oxygen deficiency [12]. This is important since oxygen deficiency is often associated with an increased ionic and electrical conductivity, as well as an enhanced catalytic activity towards oxygen evolution reaction. In order to assess the activity towards the oxygen evolution reaction, electrodes obtained from the resulted powders are investigated in a three electrode electrochemical cell in 1N KOH.

EXPERIMENTAL

$LaCoO_3$ powders are obtained by conventional solid-state reaction. For that, equimolar quantities of La_2O_3 and Co_3O_4 (i.e., from Aldrich, with >99.8% purity) were mixed and ground thoroughly in agate mortar using alcohol as lubricant (i.e., isopropanol, with >96% purity from Chimopar SA). The powder was then let to dry out and placed in alumina (i.e., Al_2O_3) crucibles, moved to furnace and fired in air at different temperatures between 600°C and 1000°C for 8 h, with a heating / cooling rate of 2°C/min.

Differential scanning calorimetry (DSC) and thermo-gravimetric (TG) measurements are carried out on precursors and their equimolar mixture. For that, we make use of a modular Thermogravimetric

Analyzer STA 449 F5 Jupiter® from NETZSCH-Gerätebau GmbH that allows to measure the heat flow and the mass loss simultaneously, upon heat treatment and under specific conditions (i.e. in air). The instrument is equipped with Proteus® software to carry out the measurement and for data evaluation. The DSC/TG curves are recorded up to 1000°C, with a temperature heating rate of 10°C/min. From that, the precursor stability and perovskite formation temperature are determined upon heating, respectively.

Crystalline structure of thermally treated powders is evaluated by X-ray diffraction using a MiniFlex 600 Rigaku with fixed Ni filtered Cu anode and rotating silicon strip detector. 2θ scans are performed between $2\theta = 5°$ and $90°$, with a speed of 1°/min and resolution of 0.01°/step. The XRD peaks are indexed by using the Inorganic Crystal Structure Database (ICSD). Lattice constants and quantitative values for the identified phases are obtained from fit to the corresponding XRD spectra by using the PDXL powder diffraction analysis package from Rigaku.

Morphology of as-prepared powders is studied by using a Zeiss Evo 50 XVP scanning electron microscope (SEM) with LaB6 cathode enabling 2 nm resolution. For that, the powder is dispersed in distilled water by using an ultrasonic bath and drop-cast on a conducting double faced carbon tape. Additionally, x-ray dispersive electron spectroscopy (EDS) is used to determine stoichiometry.

The electrochemical assessment of perovskite $LaCoO_3$ catalysts is carried out in a three electrode configuration in 1N KOH aqueous solution at room temperature, with Pt wire as counter electrode and 3M Ag/AgCl electrode as reference (i.e., +0.196 V vs. REH). The working electrode is made out of compacted mixtures of $LaCoO_3$ powders with Teflon on Ni foam used as support. To measure the I-V curve, currents up to 100 mA are applied between the working and counter electrodes, whereas the corresponding potential drop between the working and the reference one is measured by using a multi-meter.

RESULTS AND DISCUSSIONS
Precursor analysis

The thermal analysis results indicate that Co_3O_4 is stable up to 1000°C. The La_2O_3 precursor exhibits mass loss upon heating; i.e., up to 1.38 wt.% at temperatures as high as 350°C. This is associated to the decomposition process of $La(OH)_3$ to LaOOH as an intermediate phase. From that, La_2O_3 forms readily at about 720°C. These features are in agreement with previous studies [13]. At temperature as high as 750°C, the equimolar mixture

of precursors exhibits the onset of perovskite phase formation.

In order to have a clear view on solid-state synthesis process of perovskite $LaCoO_3$ from lanthanum and cobalt oxide, the structural and morphological properties of precursors are investigated by x-ray diffraction (XRD) and scanning electron microscopy (SEM). The results are shown in Fig. 1, together with the corresponding XRD spectrum measured on powder mixture.
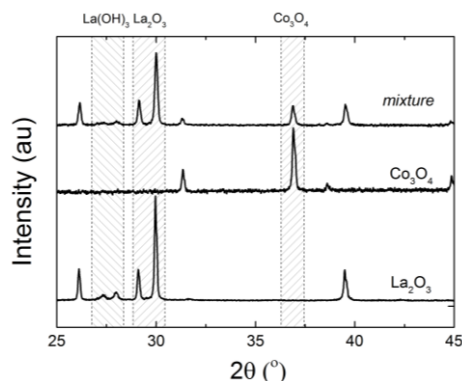
Fig. 1. X-ray diffraction characterization of the lanthanum and cobalt oxide precursors and their equimolar mixture. The main Bragg reflections of the $La(OH)_3$, La_2O_3 and Co_3O_4 phases are indicated.

In Fig. 1, the XRD data measured on Co_3O_4 powders indicate that the precursor is single-phase, with cubic crystal symmetry (space group *Fd-3m*) [14]. The lattice constant value obtained from fit to data is $a = 0.8083$ nm. Different from that, the lanthanum oxide precursor exhibits the features of a mixed phase, which consists of hexagonal $La(OH)_3$ (space group *P63/m*) [15] and tetragonal La_2O_3 (space group *P-3m1*) [16]. The corresponding lattice constant values are $a = b = 0.6529$ nm and $c = 0.3859$ nm for $La(OH)_3$ and $a = b = 0.3937$ nm and $c = 0.6132$ nm for La_2O_3.

The co-existence of $La(OH)_3$ and La_2O_3 phases within the lanthanum oxide precursor is in essence related to a high affinity of the hexagonal La_2O_3 phase to partially decompose and form $La(OH)_3$ at the grain boundary interface, upon exposure to air. From TGA data, the residual hydroxide phase is found to be ~1.38 wt.%. However, in order to restore stoichiometry, lanthanum oxide powders are often subjected to a calcination step at temperatures above 600ºC. This also assures that water and organic contaminants are removed so as mixed powders of lanthanum and cobalt oxides with desired stoichiometry can be prepared. In our case, we do not make use of that, since the stoichiometry deficiency may always be compensated by adding the molar equivalent of 1.38 wt% Co_3O_4.
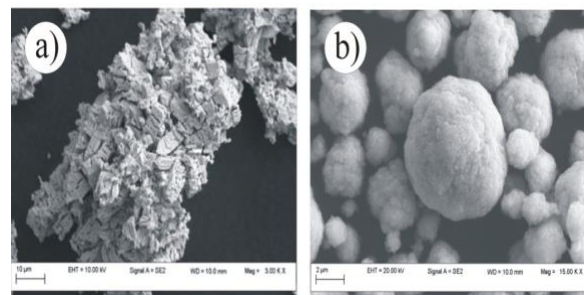
Fig. 2. SEM micrographs of lanthanum oxide in a) and cobalt oxide in b) powders used in this work.

In Fig. 2, we show the SEM micrographs of the lanthanum and cobalt oxide powders used in this work. They exhibit different degrees of clustering, owing to their intrinsic morphology. For instance, lanthanum oxide has chalky aspect, which is most probably due to lanthanum hydroxide presence at the grain boundary interface. Different from that, cobalt oxide powders consist of nano-meter sized grains which are self-organized in bulky conglomerates due to their high surface energy.

Solid-state synthesis of perovskite LaCoO$_3$

For the solid-state synthesis, the alumina crucibles containing the equimolar mixture of precursors are heat-treated at temperatures between 600ºC and 1000ºC for 8 h, with a heating rate of 2 ºC/min. After each treatment step, the structural properties are investigated by x-ray diffraction in order to monitor formation and evolution of the perovskite $LaCoO_3$ phase at the expense of precursor consumption. The XRD data indicate that the lanthanum hydroxide phase is vanished upon heat-treatment at 600ºC. This feature indicates that the perovskite $LaCoO_3$ phase forms readily from La_2O_3 and Co_3O_4.

In Fig. 3, we show the XRD spectra measured on powders thermally treated at the selected temperatures. Together with that, the diffraction peaks corresponding to La_2O_3, Co_3O_4 and $LaCoO_3$ are indicated. The XRD data show that the perovskite $LaCoO_3$ phase forms upon heat treatment at 750ºC and grows gradually with increasing temperature, up to 1000ºC. This is accompanied by a gradual decrease of the peak intensities of the precursor phases (i.e., La_2O_3 and Co_3O_4). Upon heat treatment at 1000ºC, the resulted powder is essentially within a single phase, which corresponds to perovskite $LaCoO_3$ with trigonal crystal symmetry space group *R-c3* [17]. The lattice constant values obtained from fit to data are $a = b = 5.444$ nm and $c = 13.102$ nm.

As a general rule, XRD spectra measured on mixed powders present *all* Bragg reflections of the constitutive phases. The relative intensity values of

their main peaks mediated by their corresponding areas is a quantitative measure of the degree of mixture in these powders. One can use that to de-convolute the XRD spectra in order to obtain valuable information on the amount of each phase present in powder mixtures. For instance, we use that to analyze the XRD spectra in Fig. 3 to determine the amount of $LaCoO_3$ formed upon solid-state synthesis at the given temperatures. The results are shown in Fig. 4. Note that solid-state synthesis of $LaCoO_3$ is a thermally activated process whose kinetics depends strongly on the synthesis temperature. This is essential since the grain coarsening during the synthesis process may be controlled by dwelling at lower temperatures in order to obtain powders with smaller particle size.
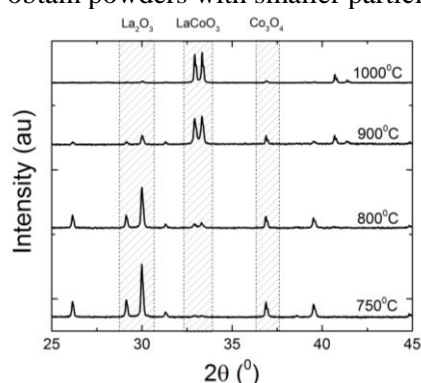
Fig. 3. Temperature dependent x-ray diffraction spectra measured on equimolar mixtures calcined at the indicated temperatures. The peaks corresponding to precursors (i.e., La_2O_3 and Co_3O_4) and reaction product (i.e., $LaCoO_3$) are indicated.
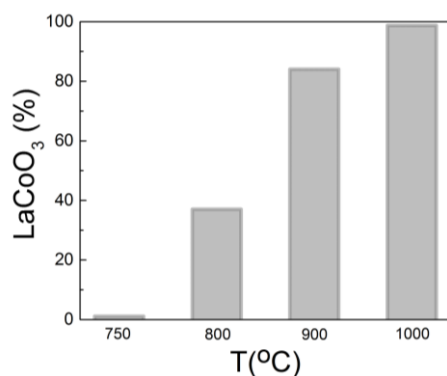
Fig. 4. Temperature dependent phase evolution (i.e., in wt.%) of the perovskite $LaCoO_3$ phase upon solid state synthesis, determined from fit to the XRD data in Fig. 3.

In Fig. 5, the perovskite $LaCoO_3$ powders obtained by solid-state synthesis at 1000°C consist of pre-sintered conglomerates of grains with well defined shape and size. From an application point of view, it is, however, essential to obtain well-dispersed powders with high specific surface area and narrow grain size distribution.
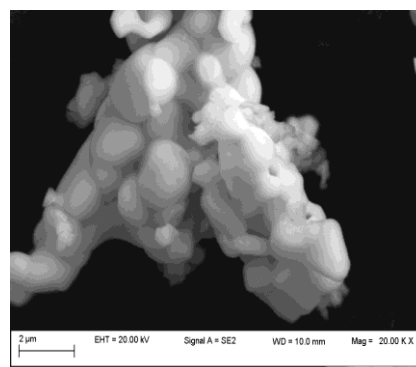
Fig. 5. SEM micrograph of $LaCoO_3$ powders obtained by solid-state synthesis at 1000°C

An estimate for the specific surface area (i.e., in m²/g) of spherical particles is *6 / (d·ρ)*, with *d* the particle size (i.e., in μm) and *ρ* the density (i.e., 7.27 g/cm³, for perovskite $LaCoO_3$). This leads to a relatively low specific surface area, whose average value is as high as 0.82 m²/g for 1 μm sized $LaCoO_3$ grains. One should note that, however, the specific surface area may be increased by up to one order of magnitude by optimizing both the solid-state synthesis temperature and the dwell time, in a way that the grain coarsening is hampered by slow reaction kinetics at lower temperatures.

I-V characterization

In order to assess the electrochemical activity of perovskite $LaCoO_3$ powders towards oxygen evolution reaction, hot pressed electrodes are made by using Teflon as binder on nickel foam supports. The compacted electrode is then moved to an electrochemical cell containing 1N KOH aqueous solution. The I-V characteristic is determined by applying constant currents up to 100 mA, whereas the potential is measured with respect to a reference electrode (i.e., Ag/AgCl , +0.196 mV *vs.* RHE). The results are shown in Fig. 6, together with those obtained for Co_3O_4 electrodes prepared in a similar way.

In Fig. 6, the I-V curves exhibit very similar features, in the sense that they fall on top of each other, although the potential values for the $LaCoO_3$ electrode are lower than those for the Co_3O_4 one, at *all* applied currents. The onset potential values for the oxygen evolution reaction at 1 mA applied current are 1.348V vs. RHE for $LaCoO_3$ and 1.355V vs. RHE for Co_3O_4.

These features indicate that $LaCoO_3$ has a higher catalytic activity towards oxygen evolution reaction in alkaline media. At currents above 20 mA, the potential dependence on the applied current is linear, corresponding to the ohmic regime.
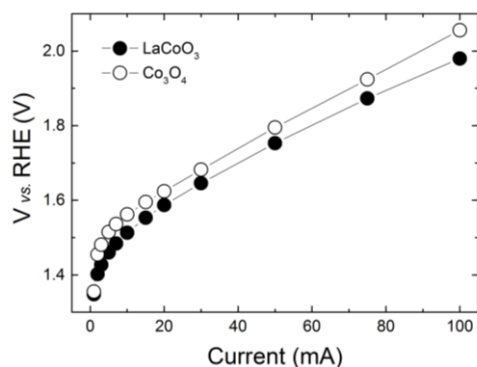
Fig. 6. I-V characteristic of $LaCoO_3$ electrodes in 1N KOH aqueous solution. For comparison, the I-V characteristic measured on Co_3O_4 in similar conditions is shown.

For Co_3O_4, the equivalent resistance value is 5.3Ω, whereas the corresponding value for $LaCoO_3$ is 4.7Ω. These high resistance values are due to the relatively poor intrinsic conductivity of the oxides, mediated by high inter-grain resistances due to presence of insulating Teflon, which acts as binder. In order to minimize that, one may either reduce the binder amount without compromising electrode integrity or add metallic species, to provide a low resistive path for electron conduction and exchange at the catalytic material grain boundary.

CONCLUSIONS

In this work, we show that perovskite $LaCoO_3$ powders can be readily obtained from lanthanum and cobalt oxide precursors by solid-state synthesis in air, without making use of intermediate steps. In the synthesis process, the $LaCoO_3$ phase nucleates at 750°C and grows gradually with increasing temperature, at the expense of reactants consumption. At 1000°C, the reaction is essentially complete. Although the resulted powders are within a single crystalline phase, the constitutive grains have wide particle-size distribution whose average value corresponds to a specific surface area of 0.82 m^2/g. In order to prevent grain coarsening, powders with smaller and narrower particle size distribution may be obtained at dwelling at lower synthesis temperatures.

Teflonized $LaCoO_3$ electrodes exhibit catalytic activity towards the oxygen evolution reaction in alkaline media. The onset of oxygen evolution is as high as 1.348V vs. RHE in 1N KON aqueous solution, when a constant current of 1mA is applied. At higher currents (i.e., above 20 mA), the I-V characteristic is linear and corresponds to a ohmic

regime, whose equivalent resistance value of 4.5 Ω is high. This is related to a poor intrinsic conductivity of the perovskite, mediated by a high inter-grain resistance due to Teflon presence, which acts as binder. One may, however, enhance that either by reducing binder load or by adding metallic species in order to provide high conductivity paths for electron transfer at the grain boundary of the catalytic material.

REFERENCES

1. V. Maruthapandian, M. Mathankumar, V. Saraswathy, B. Subramanian, S. Muralidharan, *ACS Appl. Mater. Interfaces*, **9**,13132 (2017):.
2. McCrory C.C.L., Jung S., Peters J.C., Jaramillo T.F., *Journal of the American Chemical Society*, **135**, 16977 (2013).
3. E. Fabbri, A. Habereder, K. Waltar, R. Kötz, T.J. Schmidt, *Catal. Sci. Technol.,* **4**, 3800 (2014).
4. D. E. Hall, *J. Electrochem. Soc.*, **128**,740 (1981).
5. A.C.C. Tseung, S. Jasem, *Electrochim. Acta*, **22,** 31, (1977) .
6. X. Wang, H. Luo, H. Yang, P.J. Sebastian, S.A. Gamboa, *Int. J. Hydrogen Energy*, **29** 967 (2004) .
7. T. Ishihara, editor. Perovskite oxide for solid oxide fuel cells (fuel cells and hydrogen energy). New York: Springer Science and Business Media, 2009.
8. P. Ravindranathan, S. Komarneni, R. Roy, *J. Mater. Sci. Lett.*, **12**, 369 (1993).
9. C. Vazquez-Vazquez, P. Kogerler, M.A. Lopez-Quintela, R.D. Sanchez, *J. Mater. Res.*, **13**, 451 (1988).
10. G. Shabbir, A.H. Qureshi, K. Saeed, *Mater. Lett.*, **60,** 3706 (2006).
11. W. J. Zheng, R.H. Liu, D.K. Peng, G.Y. *Meng, Mater. Lett.*, **43,** 19 (2000).
12. S. V. Bangale, D.R. Patil, S. R. Bamane, *Arch. Appl. Sci. Res.*, **3**, 506 (2011).
13. D. Walter, *Z. Anorg. Allg. Chem.*, **632**, 2165 (2006).
14. W.L. Roth, *J. Phys. Chem. Solids* **25**, 1 (1964).
15. I. Djerdj, G. Garnweitner, Su Dangsheng, M.J. Niederberger, *Solid State Chem.* **180**, 2154 (2007).
16. P. Aldebert, J.P. Traverse, *Mater. Res. Bull.*, **14**, 303 (1979).
17. O. Haas, R.P.W.J. Struis, J.M. J. McBreen, *Solid State Chem.*, **177,** 1000 (2004).

ЕДНОСТЪПКОВ СИНТЕЗ НА ПЕРОВСКИТ- LaCoO₃ В ТВЪРДО СЪСТОЯНИЕ КАТО КАТАЛИЗАТОР ЗА ОТДЕЛЯНЕ НА КИСЛОРОД В АЛКАЛНА СРЕДА

С. Енаке[1*], М. Драган[1**], А. Соаре[1], Д. Йон-Ебрасу[1], А. Заулет[1], М. Варлам[1], К. Петров[2]

[1] *Национален институт за криогенни и изотопни технологии, ICSI-Римнику Вълча, 240050, Румъния*
[2] *Институт по електрохимия и енергийни системи „Акад. Евгени Будевски", Българска академия на науките, ул. Акад. Г. Бончев, бл.10, 1113 София, България*

(Резюме)

Перовскитите от лантанов кобалтов оксид имат добра каталитична активност и стабилност при реакция на отделяне на кислород в алкална среда. Това ги прави особено атрактивни като електроди за електролиза на вода, тъй като могат да заменят по-скъпите електроди, използвани досега, като иридий и оксиди на рутений. Въпреки, че различните методи за синтез са добре описани в литературата, производството на лантано-кобалтови оксиди често е трудно, включващо междинни етапи на смилане и отгряване. За разлика от този способ, ние показваме, че первоскити от лантанов кобалтов оксид могат лесно да се получат чрез синтез в твърдо състояние от прекурсори на лантанов и кобалтов оксид, без междинни етапи на обработка. По същество, получените прахове са в единична поликристална фаза с добре дефинирани структурни и морфологични свойства. За да се оцени активността по отношение на реакцията на отделяне на кислород, електродите синтезирани от получените прахове, се изследват в три електродна електрохимична клетка в 1 N KOH.

Ключови думи: водна електролиза, перовскит, синтез в твърдо състояние

Electrochemical characterization of metal oxides as catalysts for oxygen evolution in alkaline media

Daniela Ion-Ebrasu[1]*, Adnana Zaulet[1], Stanica Enache[1], Mirela Dragan[1], Dorin Schitea[1], Elena Carcadea[1], Mihai Varlam[1] and Konstantin Petrov[1,2]

[1]National Institute for Cryogenics and Isotopic Technologies ICSI-Rm. Valcea
[2]Acad. Evgeni Budevski Institute of Electrochemistry and Energy Systems, Bulgarian Academy of Sciences

An investigation of $LaCoO_3$ catalysts for Oxygen Evolution Reaction (OER) in alkaline media is presented. The material has been obtained by an original one step method. The effect of various parameters such as the catalyst and PTFE loading, catalyst layer thickness and fabrication technique on the electrode performance are described. The catalytic activity of the OER in 0.1 M KOH was determined from Tafel plots, obtained from galvanostatic current-voltage measurements as well as by the Rotating Disk Electrode (RDE) method. Long term tests have been conducted showing a good stability of the catalysts for the OER in 0.1 M KOH

INTRODUCTION

In Polymer Electrolyte Conduction (PEM.OH⁻) OH⁻ Cation electrolysis significant overpotential is found to occur at the anode where the oxygen evolution reaction (OER) takes place. For this reason, the oxygen evolution reaction (OER) has been intensively studied for many decades in order to elucidate the reaction mechanism and minimize the energy loss during water electrolysis. Improving the OER kinetics would indeed favor a widespread market penetration of (PEM.OH⁻) electrolysers. There are several chemical aspects of the steps of the reaction mechanisms that have been used to rationalize and explain the trends in catalytic activity of OER catalysts in an alkaline electrolyte (alkaline and PEM), such as acid–base properties [1], redox potentials of the catalyst [2], binding energies of the metal component to hydroxyl ions [3], binding energies of the metal component of the catalyst to oxygen [4], to the number of d-electrons [5] and the geometrical factors [6]. The catalyst that generally shows the best trade-off between catalytic activity and stability, both in acidic and alkaline media, is IrO_2. However, since iridium is quite expensive and limited as a typical secondary metal resource, research efforts have been directed towards the development of OER catalysts with a reduced amount of Ir or based on other transition metal oxides. This is particularly the case for (PEM.OH⁻) electrolysers since base metals such as cobalt, nickel and perovskite oxides were proven to be quite stable and active in alkaline media.

Perovskite oxides (ABO_3) with alkaline or rare-earth cations in the A-site and first-row transition-metal cations in the B-site have shown the potential of being efficient oxygen electrodes in alkaline solutions[7-9]. Bockris and coworkers [5, 10, 11] correlated the activity of perovskite oxygen-evolving electrodes in alkaline solutions with the enthalpy of formation for the corresponding metal hydroxides and the bond strength of M–OH estimated by a modified version of one of the Ruetschi and Delahay's methods [3]. Note that the type of A-ion in the perovskite ABO3 compounds had little effect on the oxygen evolution activity of their catalysts, the correlation was based on the B-ion of the catalyst [10]. However, lanthanum-based perovskites containing different transition metal active sites ($LaBO_3$, B = Ni, Ni, Fe, Co, Mn) are synthesized by a general colloidal method, yielding phase pure catalysts of homogeneous morphology and surface area ($8-14$ m^2/g)[12-14].

The present study represents a continuing effort in the search for more active OER in alkaline media electrode materials. We report herein a study on the electrochemical properties of $LaCoO_3$ as a catalyst synthesized using the solid state reaction route and used as an electrode in the form of a coating on a nickel foam support. The effect of various parameters such as the catalyst and PTFE loading, catalyst layer thickness and fabrication technique on the electrode performance are studied, in comparison with a commercial IrO_2 catalyst. The catalytic activity towards the OER of catalysts was

---

* To whom all correspondence should be sent.
E-mail daniela.ebrasu@icsi.ro

determined from Tafel plots obtained from galvanostatic current-voltage measurements. The electrocatalytic activity toward the ORR in 0.1 M KOH was studied by the Rotating Disk Electrode (RDE) method at room temperature.

EXPERIMENTAL
Material synthesis

The LaCoO$_3$ (LCO) perovskite powder was synthesized using the solid state reaction route from stoichiometric amounts of La$_2$O$_3$ and Co$_3$O$_4$ powder as precursors. Following dry mixing of the precursors, thermal treatment in air was applied in order to obtain the targeted single phase material. This synthesis method is presented in detail in the work of S. Enache, M. Dragan, A. Soare, D. Ion-Ebrasu, A. Zaulet, M. Varlam, K. Petrov, "One step solid-state synthesis of lanthanum cobalt oxide perovskites as catalysts for oxygen evolution in alkaline media".

The electrodes were prepared on rounded shapes of Ni foam with 93% porosity acquired from Goodfellow, having different catalyst and PTFE loading (Table 1). Moreover, in order to improve the electrode conductivity, silver was added in different ratios. The electrodes were prepared by an in house method: the catalyst was mixed with PTFE and silver and added on to the Ni foam support that was then placed in a matrix. The electrode surface is 1 cm^2. The catalyst/Ni foam was pressed at 300 kgf, for 1 minute at 300° C.

Table 1. LCO catalyst, PTFE and silver loading

Catalyst (mg)	Silver (mg)	PTFE (mg)	Support	Sample name
150mg IrO$_2$	-	20	Ni foam	150IrO$_2$/20PTFE/Nifoam
150 LaCoO$_3$	-	20	Ni foam	150LCO/20PTFE/Nifoam
100 LaCoO$_3$	-	16,6	Ni foam	100LCO/16.6PTFE/Nifoam
75 LaCoO$_3$	-	10	Ni foam	75LCO/10PTFE/Nifoam
65 LaCoO$_3$	10	10	Ni foam	65LCO/10Ag/10PTFE/Nifoam
60 LaCoO$_3$	15	10	Ni foam	60LCO/15Ag/10PTFE/Nifoam
50 LaCoO$_3$	25	15	Ni foam	50LCO/25Ag/10PTFE/Nifoam

Electrochemical measurements

Electrochemical tests include both stationary and non-stationary methods.The galvanostatic experiments were conducted using a three conventional three-kept for electrode Pyrex glass cell using a programable power source HMP4040 with four channels. The measurements were carried out at room temperature, using Hydrofelx Hydrogen Reference Electrode (RHE) as reference electrode, 1 M KOH and a Pt plate as the counter electrode. A potassium hydroxide 1M solution was prepared using Milli-Q ultrapure water. The samples were then mounted in a glass tube sealed with an encapsulant paste from Dupont.

In order to measure catalyst stability, the 150LCO/20PTFE/Nifoam sample was kept at 5 mA for 888 hours and at 50 mA for 720 hours respectively. After each long term measurement, the current-voltage curves were recorded.

Electrocatalytic activities with respect to the ORR were studied by the Rotating Disk Electrode (RDE) method. An OrigaFlex 5 A potentiostat/galvanostat controlled by commercial software was used in the experiments. Electrochemical measurements were carried out in a conventional three-electrode Pyrex glass cell. The working electrode was an OrigaTrod glassy carbon rotating disk electrode (RDE) with a geometric area of 0.196 cm^2 embedded in polytetrafluoroethylene (PTFE). A catalyst ink including 5 mg of catalyst, 20 µl of a Fumion® FAA-3-Solut-10 solution and 240 µl of isopropanol was sonicated and mixed overnight. An aliquot of 10 µl was deposited on the glassy-carbon disk. Prior to deposition, the RDE was polished to a mirror finish with 1.0 μm alumina and 0.05 μm diamond paste (PK-3 Electrode Polishing Kit) in sequence. After each polishing step, the RDE electrodes were ultrasonically cleaned in Milli-Q water. Finally, the glassy carbon (GC) electrode was ultrasonically cleaned in Milli-Q water in sequence and dried under argon flow. A Hydrofelx Hydrogen Reference Electrode (RHE) was used as a reference and a platinum plate as the counter-electrode. The experiments are carried out at room temperature in a 0.1 M KOH electrolyte which was purged with high purity O$_2$ for 30 minutes. All potentials in this paper are reported vs. a RHE reference electrode

RESULTS AND DISCUSSIONS
Galvanostatic measurements

To determine the effect of catalyst loading and the impact of silver inclusion, the electrode voltage dependence was plotted at 50 mA. Figure 1 (a) shows the increase in the electrode voltage as a function of the decrease in catalyst load. From Figure 1 (b) we can deduce a different trend of the electrode voltage when silver is added to the LCO powder. The voltage decreases with the increase in silver quantity, but this value (1.70 V) is higher than the one corresponding to the sample containing 75 mg of LCO (1.68 V), without a precious metal. This behavior can be explained by the incomplete coverage of the electrode when the catalysts loading is lower than 75 mg, followed by the enhanced contribution of the Ni foam to the overall performance of the electrode.

Presented in Figure 2 are the galvanostatic current-voltage curves recorded for different LCO/PTFE loading in comparison with the IrO_2 commercial catalyst, in the range 0÷100 mA.

Figure 3 shows the Tafel plots (log j) versus V and the slopes calculated from the curves presented in Figure 2. The slopes for the LCO samples are in the domain of 93 mV/decade (75 mg LCO) to 133 mV/decade (150 mg LCO). This is because the overpotential will rise slower if the current density is increasing when using this material as a catalyst in the OER. Since the overpotential is the energy loss during the OER, the smaller slope indicates a better catalysis performance. The value of the slope for a *75LCO/10PTFE/Ni foam* sample is close to the one corresponding to the commercial IrO_2 catalyst (87 mV/decade), which indicates that this probe can be considered to have the best electrode structure and composition for a OER in alkaline media related to the perovskite catalyst presented in this work. These considerations confirm that the OER proceeds along four paths since this reaction involves four electrons and is in accordance with the results presented in the next paragraph [15-18].
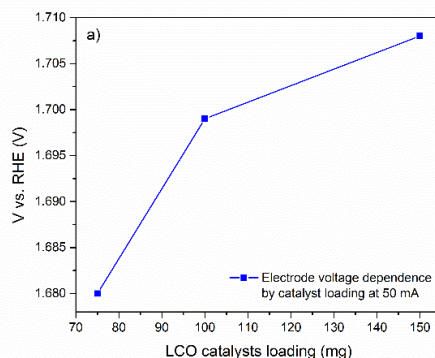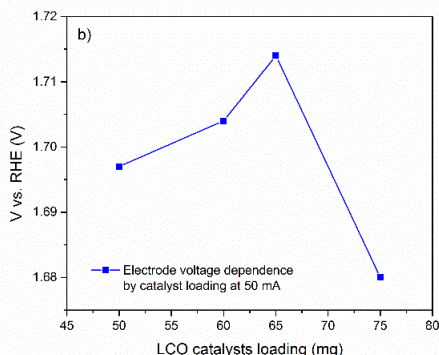
Fig. 1 Electrode voltage dependence versus LCO catalysts loading calculated at 50 mA (without silver); (b) with silver mixed with LCO powder.
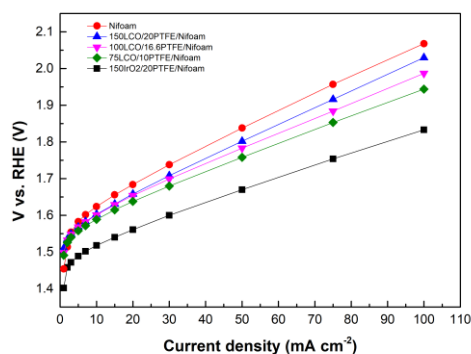
Fig. 2. Galvanostatic current-voltage curves recorded for different LCO/PTFE loading in comparison with an IrO_2 commercial catalyst, in the range 0÷100 mA.
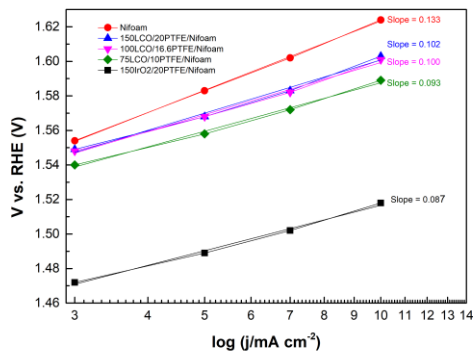
Fig. 3. Tafel plots recorded for different LCO/PTFE loading in comparison with an IrO_2 commercial catalyst, in the range 3÷10 mA.

In order to increase the $LaCoO_3$ oxide based electrode, different quantities of silver were added by substituting part of the LCO catalyst. Figure 4 (galvanostatic current-voltage curves recorded for different LCO/PTFE/Ag loadings on Ni foam) and Figure 5 (Tafel plots) respectively, indicate that there is no noticeable improvement in electrode conduction after silver introduction. Therefore, we conclude that doing this does not make sense, since it will increase the cost of electrode production.

However, further experiments may be carried out by keeping constant the 75 mg of LCO and adding controlled quantities of silver.
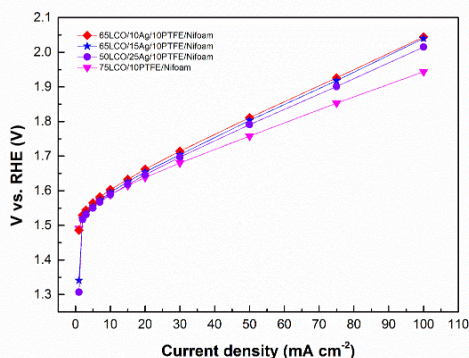
Fig. 4. Galvanostatic current-voltage curves recorded for different LCO/PTFE/Ag loadings on Ni foam
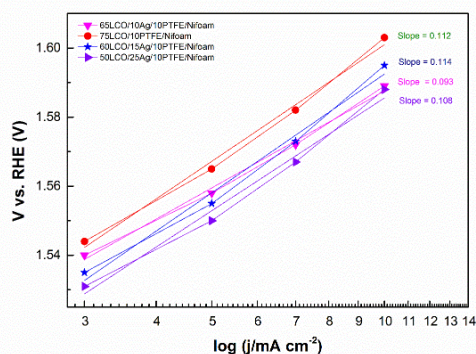
Fig. 5. Tafel plots recorded for different LCO/PTFE/Ag loadings on Ni foam

RDE Measurements

The catalytic performance of LCO with respect to the oxygen reduction reaction(ORR) was evaluated in a 0.1 M KOH solution using the RDE cycling voltammetry method. All the RDE voltammetric experiments were carried out under bench top conditions at an ambient temperature (24 ± 1 °C) in an oxygen saturated atmosphere.

The effect of sweep rate variation from 5 to 500 mV/s is shown in Figure 6. Voltammograms were plotted from 0.5V to -0.55 V, 0.5 to -0.5 V *vs.* RHE and the solution was purged with oxygen for 15 minutes after each voltammogram. The results show that the anodic and cathodic peaks increase with the increasing sweep rate and the ORR peak becomes sharper. This behavior proves that the LCO catalyst has a good stability with respect to the ORR.
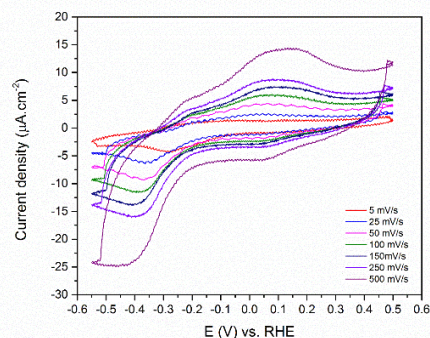
Fig. 6. Cycling voltammograms showing the effect of sweep rate for the LCO catalyst.

Stability measurements of the samples were carried out using one step pulse chronoamperometry in 0.1 M KOH exposed to atmospheric oxygen at -0.15 V over a test period of two hours and a 200 rpm rotation speed. In Figure 7 we observe a relatively stable performance of the catalysts with respect to the oxygen reduction reaction (ORR)/
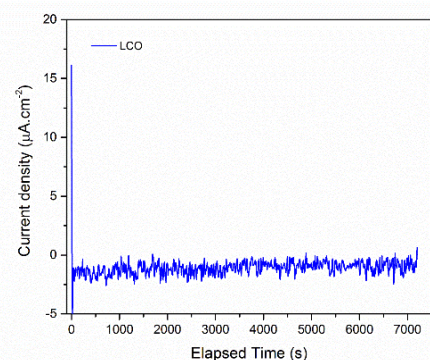
Fig. 7. Chronoamperometric stability measurements for the ORR recorded at -0.15V vs. RHE and rotation at 500 rpm in 0.1 M KOH saturated with oxygen

The kinetics of the catalytic oxygen-reduction reaction of LCO was studied by linear sweep voltammetry (LSV) measurements using the RDE electrode. We carried out LSV measurements at different rotation speeds from 400 to 1400 rpm on RDE in 0.1 M KOH saturated with O_2. As shown in Figure 8, it can be seen that the onset potential moves to more negative values, the current is increasing and all the current-potential curves are smooth with the increase in rotation rate.
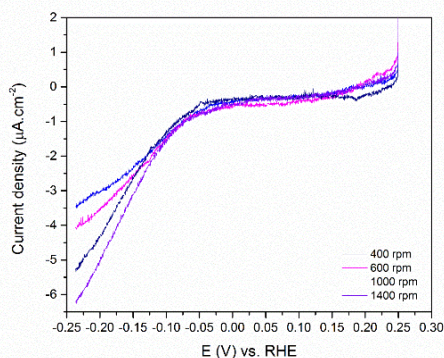
Fig. 8. LSV curves for LCO at different rotation speeds between 400 to 1400 rpm on RDE in 0.1 M KOH saturated with O_2.

Figure 9 shows the fitted Koutecky–Levich plots (Current density^{-1} (mA^{-1}/cm$^2_{geo}$) vs. w$^{-1/2}$)(rad/s$^{-1/2}$)) of the LCO catalyst calculated from LSV currents under variable rotation rates in the potential range -0.15 to -0.24 V. The plots show a good linearity for all potentials and a slope of between 1.4 and 1.8. Moreover, the calculated *n* number of moles of electrons transferred in the half reaction is close to 4 corresponding to a ORR in alkaline media proceeding by direct four-electron reduction (ec. 1) [14]:

$$O_2 + 2H_2O + 4e \rightarrow 4OH^- \qquad (1)$$
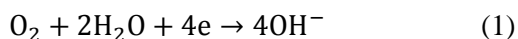
The stability of the LCO catalyst was measured for the 150LCO/20PTFE/Ni foam sample. From Figures 10 and 11 it can be seen that the electrode is stable over more than 700 hours, both at a low current (5 mA) as well as at a higher current (50 mA).
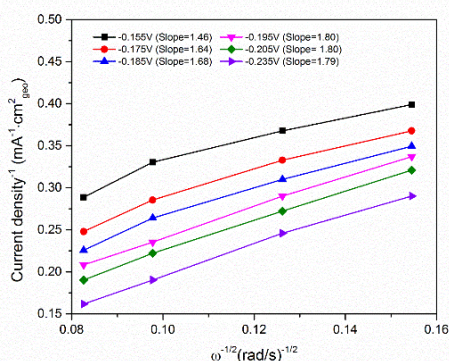
Fig. 9. Fitted Koutecky–Levich plots of the LCO catalyst calculated from LSV currents under different rates of rotation in the potential range -0.15 to -0.24 V.

The results presented above confirm the catalytic activity and stability of LCO for the OER and the fact that the best sample is the one with 75 mg of LCO and 10 mg of PTFE.
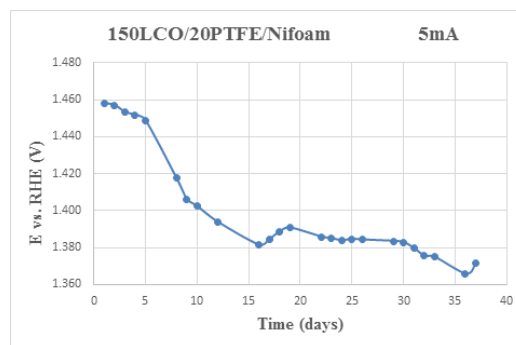
Fig. 10. Long term measurements of 150LCO/20PTFE/Nifoam at 5 mA for 888 hours.
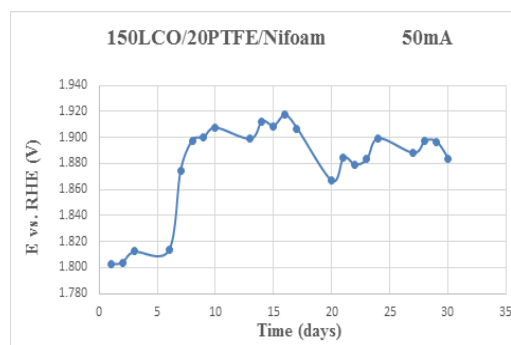
Fig. 11. Long term measurements of 150LCO/20PTFE/Nifoam at 50 mA for 720 hours.

CONCLUSIONS

We have shown in this paper that the catalyst LaCoO$_3$ perovskite synthesized using the solid state reaction route manifests good catalytic activity and stability for the OER. Silver added to the LCO powder together with PTFE doesn't noticeably improve the electrode conductivity therefore we can conclude that the addition of silver does not make sense, since this will increase the cost of electrode production. However, further experiments may be carried out by keeping constant the 75 mg of LCO and adding controlled quantities of silver.

The RDE cycling voltammetry measurements prove that the LCO catalyst has a good stability with respect to the ORR. Chronoamperometry shows the performance of the LCO perovskite catalyst to be relatively stable with respect to the oxygen reduction reaction (ORR).

However, the number of electrons transferred in the half reaction is close to 4 corresponding to the ORR in alkaline media that proceeds by direct four-electron reduction and hence the mechanism of the ORR is complementary to the LaCoO$_3$ catalysts presented in this paper and corresponds to a direct reduction of O$_2$ to OH$^-$.

REFERENCES

1. S. Trasatti, Surface chemistry of oxides and electrocatalysis. *Croatica Chemica Acta*, **6**, 313 (1990).
2. P. Rasiyah, A. C. C. Tseung et al., *J. Electrochem. Soc.*, **129**, 1724 (1982).
3. P. Ruetschi P, P. Delahay, *J. Chem. Phys.*, **23**, 565, (1955).
4. S. Trasatti, *J. Electroanal. Chem.,* **111**, 125 (1980).
5. J.O.M. Bockris, T. Otagawa, V. Young, *J. Electroanal. Chemistry*, **150**, 633 (1983).
6. K. Kinoshita K, Electrochemical Oxygen Technology. John Wiley & Sons, New York (1992).
7. E. Fabbri, A. Habereder, K. Waltar, R. Kotz, T. J. Schmidt, *Catal. Sci. Technol.*, **4**, 3800 (2014).
8. S. Gupta, W. Kellogg, H. Xu, X Liu, J. Cho, G. Wu, *Chem. Asian J.,* **11,** 10 (2015).
9. J. Suntivich, K. J. May, H. A. Gasteiger, J. B. Goodenough, Y. Shao-Horn, *Science,* **334**, 1383 (2011).
10. J. O. M. Bockris, T. Otagawa, *J. Phys. Chem.,* **87**, 2960 (1983).
11. J. O. M. Bockris, T. Otagawa, *J. Electrochem. Soc.*, **131,** 290 (1984).
12. R. A. Silva, C. O. Soares, M. D. Carvalho, C. M. Rangel, M. I. da Silva Pereira, *J Solid State Electrochem.,* **18,** 821 (2014).
13. F. Mitlitsky, B. Myers, A. H. Weisberg, *Energy Fuels,* **12**, 56 (1998).
14. W. G. Hardin, J. T. Mefford, D. A. Slanac, B. B. Patel, X. Wang, S. Dai, X. Zhao, R. S. Ruoff, K. P. Johnston, K. J. Stevenson, *Chem. Mater,*. **26**, 3368 (2014).
I. C. Man, *Chem. Cat. Chem.* **3**, 1159, (2011).
15. J. K. Nørskov, T. Bligaard, J. Rossmeisl, C. H., *Nat. Chem.* **1**, 37 (2009).
16. J. Rossmeisl, Z. Qu, H. Zhu, G. Kroes, J. Norskov, *J. Electroanal. Chem.* **607**, 83 (2007).
17. J. K. Nørskov, J. Rossmeisl, A. Logadottir, L. Lindqvist, J. R. Kitchin, T. Bligaard, H. Jonsson, J. *Phys. Chem. B*, **108**, 17886 (2004) .

ЕЛЕКТРОХИМИЧНО ОХАРАКТЕРИЗИРАНЕ НА МЕТАЛНИ ОКСИДИ КАТО КАТАЛИЗАТОРИ ЗА ОТДЕЛЯНЕ НА КИСЛОРОД В АЛКАЛНИ СРЕДИ

Д. Йон-Ебрасу[1]*, А. Заулет[1], С. Енаке[1], М. Драган[1], Д. Скитя[1], Е. Каркадя[1], М. Варлам[1], К. Петров[1,2]

[1]*Национален институт за криогенни и изотопни технологии, ICSI-Римнику Вълча, Румъния*

[2] *Институт по електрохимия и енергийни системи „Акад. Евгени Будевски", Българска академия на науките, ул. Г. Бончев, бл. 10, 1113 София*

(Резюме)

Изследвани са катализатори на база $LaCoO_3$ за реакции на отделяне на кислород в алкална среда. Материалът е получен по оригинален метод (едностъпков). Изследвано е въздействието на различни параметри като тефлонизиране на катализатора, дебелината на каталитичния слой и техниката на изработка на електрода. Каталитичната активност при реакцията на отделяне на кислород в 0.1 M KOH се определя от Тафеловите наклони, получени от поляризационните криви на галваностатичните измервания, както и от измерванията с ротиращ дисков електрод. Проведени са дългосрочни тестове за дълготрайна стабилност на катализаторите за отделяне на кислород в 0.1 M KOH.

Ключови думи: перовскит- $LaCoO_3$, метални оксиди, отделяне на кислород

Electrochemical testing of an innovative dual membrane fuel cell design in reversible mode

Z. Stoynov[1†], D. Vladikova[1*], B. Burdin[1], A. Thorel[2], A. Chesnaud[2], P. Piccardo[3], M. Slavova[1], R. Spotorno[3]

[1]Institute of Electrochemistry and Energy Systems, Bulgarian Academy of Science, 10 Acad. G. Bonchev St., Sofia 1113, Bulgaria
[2]Centre des Matériaux, MINES-ParisTech, PSL, UMR CNRS 7633 BP 87, France
[3]University of Genoa, Department of Chemistry and Industrial Chemistry, I-16146 Genoa, Italy

Solid oxide fuel Cells (SOFC) are intrinsically reversible which makes them attractive for the development of reversible devices (rSOC). The main hurdles that have to be overcome are the higher degradation in electrolyzer (EL) mode and the slow and difficult switching form mode to mode. This work aims at the development and experimental validation of a concept for rSOC based on a new dual membrane fuel cell (dmFC) design which can overcome the existing problems of the classical SOFC. The kernel of the system is additional chamber - central membrane (CM) for water formation/evacuation in FC mode and injection in El mode. Its optimization in respect of microstructure and geometry in laboratory conditions is carried out on button cells. The electrochemical performance is evaluated based on volt-ampere characteristics (VACs) combined with impedance measurements in different working points. The influence of a catalyst in the water chamber is also examined. The VACs which give integral picture of the cell performance are in excellent agreement with the impedance studies which ensure deeper and quantitative information about the processes, including information about the rate limiting step. The results from the optimization of the water chamber show that the combination of design and material brings to important principle advantages in respect to the classical rSOC – better performance in electrolyzer mode combined with instantaneous switching.

Key words: Reversible solid oxide cells, dual membrane fuel cell, BCY15, impedance measurements

INTRODUCTION

The ambitious European targets for CO_2 emission reduction require accelerated transition to clean and efficient energy system, since two thirds of the greenhouse emissions result from energy production and use. The problem solving approach is to increase the energy efficiency and integration of renewables in the energy mix, based on new technological solutions. Hydrogen is determined as the energy vector of the future, since it is a universal clean energy carrier which can be produced by water electrolysis with renewable energy, and then transformed by fuel cells into electricity and heat for transport and stationary applications. Solid Oxide Cells (SOC) are intrinsically reversible. They can be operated in electrolysis mode (EL) to produce hydrogen from steam, or in fuel cell (FC) mode to produce electricity. Using two separate devices - an electrolyser and a fuel cell means both will be used part time, which increases the investment costs. However, they can achieve higher efficiency and flexibility using the same device. The present State of the Art shows that in electrolyzer mode the degradation is much higher - about 2-5% after 1000h

of operation for the H_2O electrolysis reaction, which is behind the commercialization threshold [1]. In this respect special measures are taken for improvement of the electrodes performance and stability. This will reflect also in the reversible operation of solid oxide cell (rSOC) devices. Although the construction of SOELs and SOFCs looks similar, there is no optimized application of reversible high temperature electrochemical device due to their asymmetry which causes big differences in the operating conditions. For instance the high current density associated with a large amount of water in the fuel electrode for SOELs compared to SOFCs strongly increases the polarization resistance, the constraints on interconnects and the overall degradation rate [1]. Durability, performance and efficiency of rSOC are also affected by accelerated degradation and delamination at the electrodes due to the presence of water, slow and difficult switching form mode to mode, high humidity of the produced H_2, and difficulties in cell pressurization [2-6]. Studies point out the negative effect of water vapor on interconnect durability both in a reducing and oxidizing environment (related to Cr diffusion/evaporation), which renders the presence

* To whom all correspondence should be sent.
E-mail: d.vladikova@bas.bg

of a coating to protect interconnects mandatory [7, 8]. Thus the ability of rSOC to perform real dynamic cycling between power storage and power generation modes (SOEL to SOFC and back) while keeping an acceptable degradation combined with fast switching between the two modes and lower costs, is still an important target.

Recently a new design of SOFC with a separate chamber for the water production and evacuation named "dual membrane fuel cell" (dmFC) was introduced [9]. It was proved in the FP 7 FET project IDEAL Cell [10-12]. The new architecture eliminates the problems coming from the water formation and evacuation from the electrodes [11, 12]. The assembly combines the cathode compartment (cathode/electrolyte) of a SOFC and the anode compartment (anode/electrolyte) of pSOFC sandwiching a porous central membrane (CM) layer with mixed proton and oxide ion conductivity, where the water is produced and evacuated. This leads to numerous advantages (no dilution of fuel or oxidant, lower electrodes overpotential, easy pressurization). Since water is the major source of SOFC and SOEL failure, the long term viability of this concept should be significantly enhanced.

The separation of the water in a special compartment which eliminates its damaging presence at the electrodes in both modes, combined with the reduced operating temperature from 800-950°C to 600-800°C, are strong logical arguments in favor of the idea for development of advanced reversible electrochemical device based on the dmFC design. Additionally a mixed ionic conductivity in the proton conducting electrolyte (BCY15) was registered and preliminary experiments were performed on the so called "monolithic design" which strongly simplifies the technology since only one type of electrolyte with mixed ionic conductivity is used [13-15]. It was also supposed that the registered new phenomenon – formation of highly polarizable nanometer film of "organized" water at the surface of the BCY15 pores should facilitate the water formation/splitting [16].

The central membrane is the new component which ensures the advantages of the dmFC. On the one hand it should have high mixed ionic conductivity, which is favored by a dense microstructure. On the other hand it plays a role of a chemical reactor where water is formed and evacuated or injected, which requires porous microstructure. For the optimization of the CM a new design of an experimental symmetrical half-cell with CM support and Pt electrodes was investigated applying a combination of several experimental

techniques: (i) impedance spectroscopy for collection of information about the mixed conductivity by measurements of samples with different porosity in different atmospheres and temperatures; (ii) SEM for microstructural characterization; (iii) gases permeability measurements applying especially developed simple and fast procedure and equipment [16, 17].

The systematic studies of the central membrane of monolithic dual membrane fuel cell showed that 25-35% porosity could ensure an optimal microstructure in respect to conductivity, gas permeability and mechanical stability [17].

The next optimization parameter is the thickness of the CM. It has to guarantee smaller resistance combined with sufficient periphery for evacuation/injection of water. Since the CM works as chemical reactor, the density of the reaction triple phase boundaries in its volume should be sufficient.

This work aims at optimization of the CM in respect to its thickness by electrochemical testing of the electrolytes-central membrane assembly (ECMA) in full cell configuration. Since the reaction in the CM involves the most active particles – protons and oxide ions, the question which arises is about the need of a catalyst. Its answer is also in the scope of the study.

EXPERIMENTAL

The electrolytes-central membrane assembly $BCY15_{dense}/BCY15_{porous}/ BCY15_{dense}$ was prepared by the standard ceramic technology following a procedure of three- step cold pressing: the three layers were pressed one after the other with pressure 1.72 kN/cm^2 for several seconds, followed by a final pressing at 5.16 kN/cm^2 for 5 minutes. The second layer which forms the Central Membrane has graphite pore former which ensures the optimal porosity [18]. In half of the cells a catalyst - Pt particles (Aldrich) with grains size $0.14 – 0.45$ μm in quantity 1 wt. % in respect to the CM weight was also added. The samples were sintered at 1300°C for 5 hours. The final dimensions of ECMA were: diameter 21 mm and thickness 1, 2 mm. For the fabrication of cells with different thickness of the CM the total quantity of the raw material was kept constant, while the BCY15 weight ratio for the two dense electrolytes and that for the CM was varied. Samples with CM between 200 and 500 μm were fabricated. The exact thickness was determined by SEM (Fig. 1). Since the kernel of the monolithic dmFC design is the ECMA, Pt electrodes (with active surface 0.28 cm^2) were used which eliminates eventual influence of the electrodes composition and deposition technology on the electrolytes behavior [18].
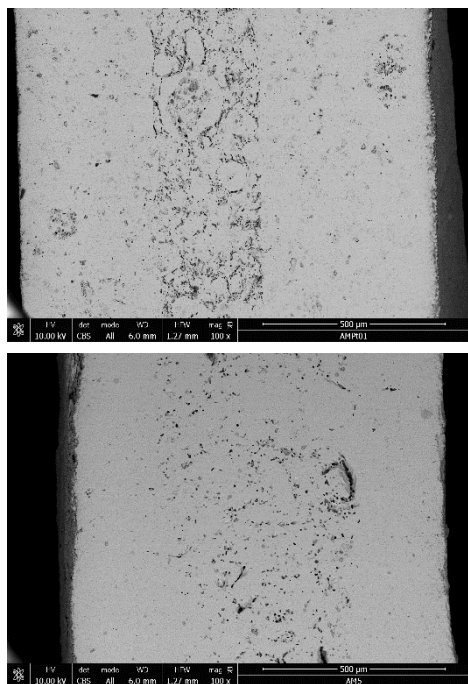
Fig. 1. SEM images of ECMA with different thickness of the Central Membrane: about 250 μm (upper position); about 500 μm (lower position)

The electrochemical testing included measurements of the volt-ampere characteristics (VACs) combined with impedance in different working points, performed on IVIUM - CompactStat e10030 in frequency range 1 MHz – 0,01 Hz with density 5 points/ decade in the temperature interval 600ºC - 850ºC. The working gas atmospheres were: air (61,85 ml.min^{-1}) or oxygen (133 ml.min-1) and hydrogen (54,32 ml.min^{-1}).

A comparative analysis was performed on samples with different thickness of the CM and presence or absence of Pt catalyst. More details about the measured samples are given in Table 1.

RESULTS AND DISCUSSIONS

The linear shape of the volt-ampere curves for all samples measured at different temperatures in both FC and EL mode can be attributed to domination of the transport losses (Fig. 2). Since non-optimized cells with similar thickness show influence of the activation losses [19], the bigger cell thickness cannot be the only reason for the observed linear dependence. This result suggests for good catalytic activity of the water formation/splitting reaction, which is confirmed by the impedance

measurements (Fig. 2c) that show small charge transfer resistance.

Table 1. Samples tested in FC/EL mode

Sample	**CM [μм]**	**Pt**
Sample 1	250	Yes
Sample 2	250	No
Sample 3	500	Yes
Sample 4	500	No

It is well known that proton conductivity is higher than the oxide ion one and above 700ºC it exhibits significant decrease [20, 21]. The measured VACs show performance improvement in both FC and EL mode with the increase of the temperature (Fig. 2). As it has been experimentally confirmed [15, 17] at operating temperatures (about 700ºC) BCY15 has similar proton and oxide ion conductivity which is one of its advantages. Since in the dmFC both types of conductivity are used, the decrease in proton conductivity is compensated by the increase of the oxide ion one, which enhances the range of working temperatures. For operation in reverse mode the upper temperature limit is also important.

The comparison of the volt-ampere curves for cells with CM thickness 250 and 500 μm in the presence of Pt catalyst registers better electrochemical performance of the cell with the thinner CM in both FC and EL mode (Fig. 3). For the samples without catalyst the influence of the thickness is not so essential (Fig. 4). As it was already marked the thicker membrane ensures better evacuation/injection of the water, while the thinner one improves ECMA conductivity.

Obviously in samples without Pt the transport losses of water cannot be compensated by the decrease of the resistance in the thinner membrane. It is possible that the presence of catalyst outside the reaction zone of the CM facilitates the transport. This hypothesis is confirmed by the impedance measurements which register the water transport in the low frequency range [11, 15]. As it can be seen in Fig. 4c, regardless the differences in the impedance behavior in the high frequency range, the samples with different thickness of the CM have similar total resistance. Those observations bring to a new direction of optimization concerning the cell architecture. One approach is the "Zebra" design [22].
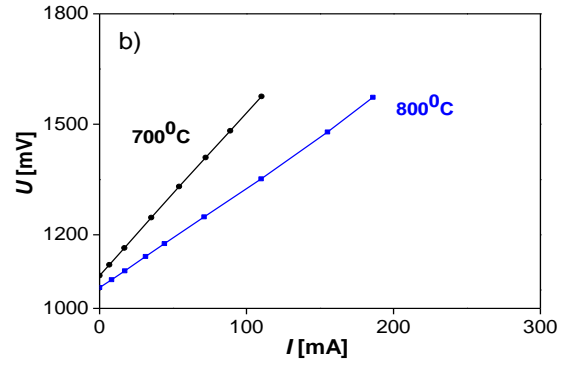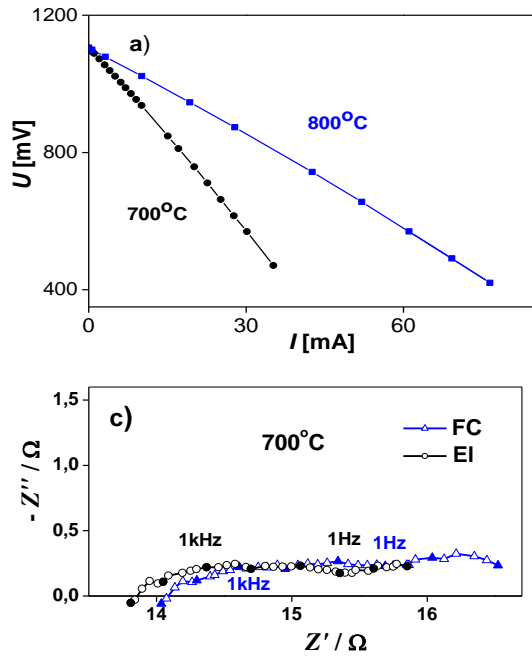
Fig. 2. Electrochemical testing of Sample 1 at different temperatures: a) Volt-ampere characteristics in fuel cell mode; b) Volt-ampere characteristics in electrolyzer mode; c) impedance diagrams in FC and EL mode at OCV
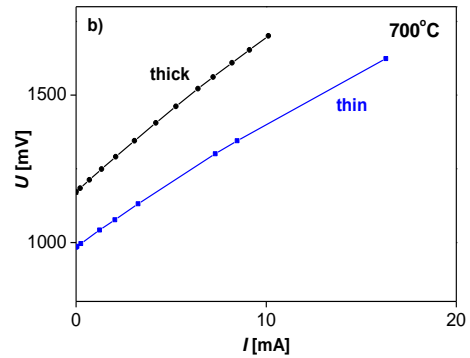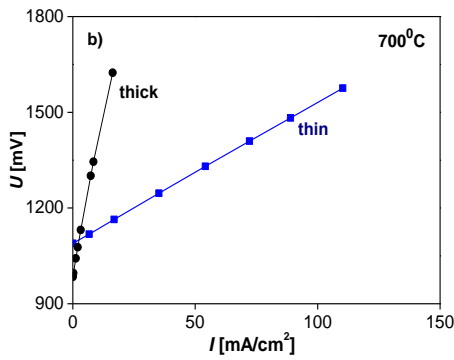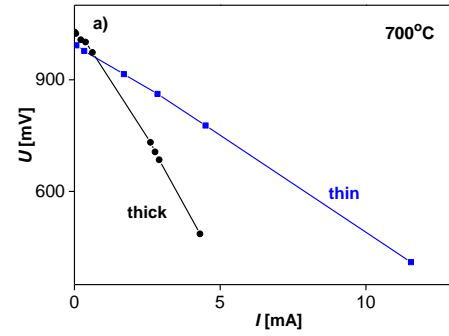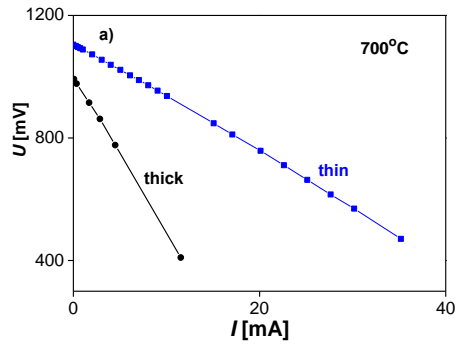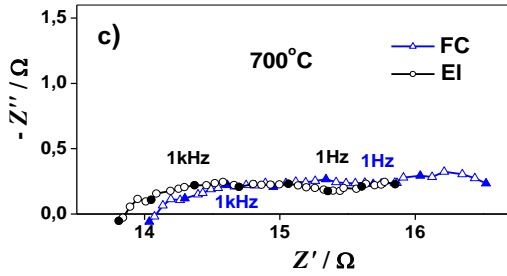
Fig. 3 Electrochemical testing of Samples 1 and 3 (with Pt in the CM): a) Volt-ampere characteristics in FC mode; b) Volt-ampere characteristics in EL mode.
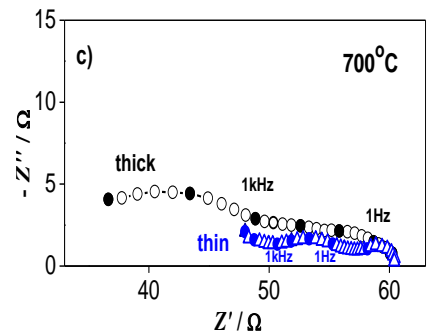
Fig. 4. Electrochemical testing of Samples 2 and 4 (with Pt in the CM): a) Volt-ampere characteristics in FC mode; b) Volt-ampere characteristics in EL mode; c) impedance diagrams in FC mode at OCV.

142

For optimization of the dmFC reversible monolithic design it is important to study the effect of the catalyst. As already mentioned, in FC mode the central membrane serves as a chemical reactor where the most active particles - protons and oxide ions meet. In EL mode the application of BCY15 which has the natural property to split water also facilitates the process. The first experiments showed good performance without catalyst. For experimental proof of the preliminary hypothesis

that the catalyst might not strongly influence the operation of the reverse cell, a comparison between the electrochemical behavior of ECMA with and without catalyst was done. Both VACs and impedance analysis confirmed the positive influence of the catalyst in FC and EL mode (Fig. 5). The effect is more pronounced for the cells with thin CM probably due to activation outside the reaction zone of the CM.
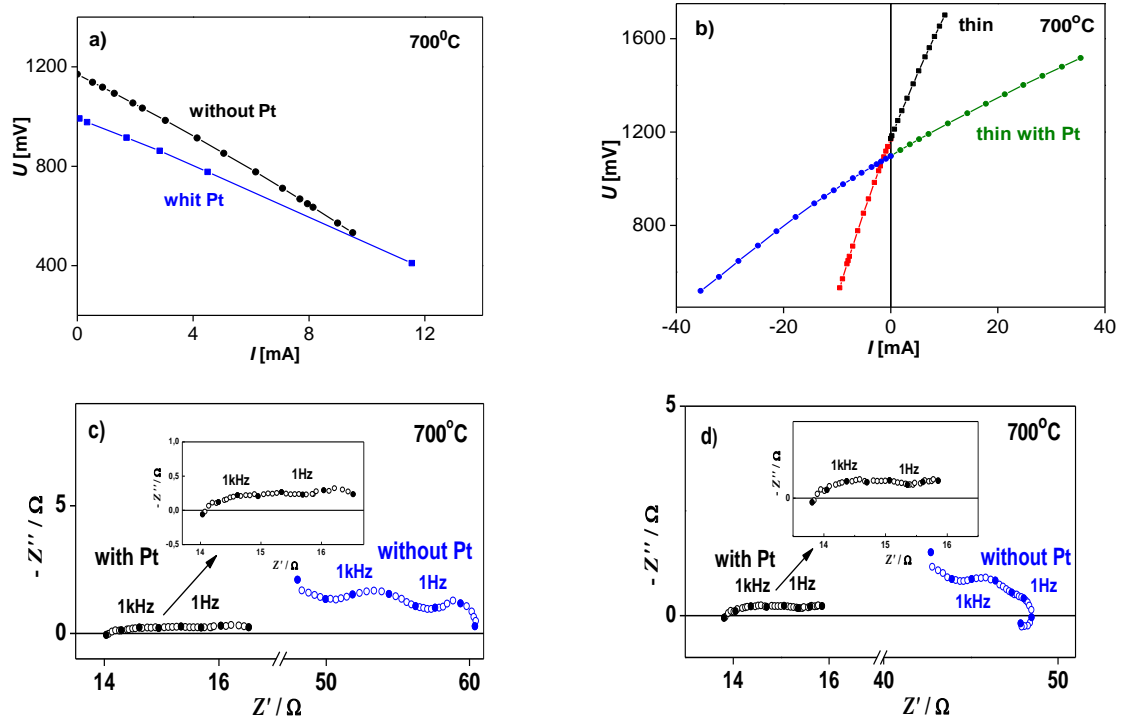
Fig. 5. Electrochemical testing of samples with and without Pt in the CM: a) Volt-ampere characteristics of Samples 3 and 4 (thick CM) in FC mode; b) Volt-ampere characteristics of Samples 1 and 2 (thin CM) in both FC and EL mode; c) Impedance diagrams of Samples 1 and 2 (thin CM) in FC mode at OCV; d) Impedance diagrams of Samples 1 and 2 (thin CM) in EL mode at OCV.
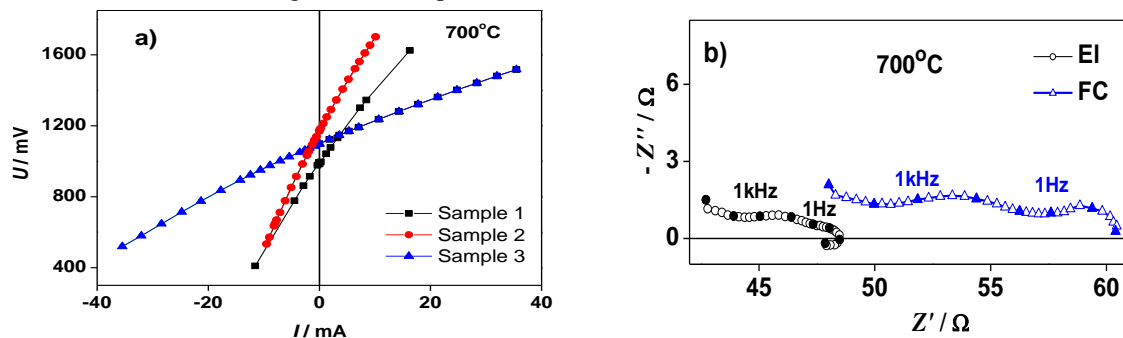
Fig. 6. Electrochemical testing of Samples 1 - 4 in reverse mode: a) Volt-ampere characteristics of Samples 1, 2 and 3 in FC and El mode; b) Impedance diagrams of Sample 4

The main goal of this study is to analyze the operation of the monolithic dmFC in reverse mode, for which a comparison of the electrochemical behavior of Samples 1-4 was performed in both FC

and EL mode. The Volt-ampere characteristics confirm better performance for all cells in electrolyzer mode (Fig. 6). This result is interesting and important, since the main disadvantage of the

143

classical rSOC is the worst performance in EL mode. In addition the selection of BCY15 which splits water also influences positively the operation in EL mode. This result illustrates the big potential of the dmFC concept in rSOC which is one of the directions for increased efficiency of RES introduction in the energy mix.

An important parameter for reversibility is the switching time. In the dmFC the reversibility was found to be in practice instantaneous due to the presence of water in the common "water chamber", adsorbed on the defect surface of the CM pores [16]. Thus the combination of design and material makes the dmFC concept very promising for reversibility.
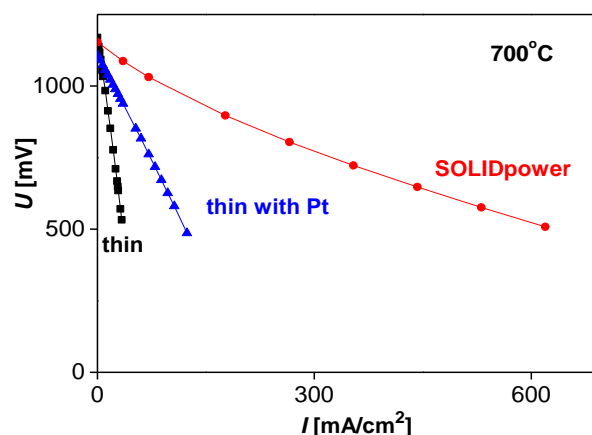
Fir. 7. Comparison of VACs in FC mode

Table 2. Maximum power of the Samples in Fuel Cell

Sample	P_{max} [mW/cm^2]/Air				P_{max} [mW/cm^2]/O$_2$		
	600°C	700°C	800°C	850°C	700°C	800°C	850°C
1	35.3	60.2		123	80	132.4	159.4
2	5.5	18	28.5			32.3	
3	8.32	16.7					
4	5.6	18.3					
SOLID power	113	315	584				

CONCLUSIONS

The electrochemical studies of reversibility applying the innovative concept of the "monolithic" dual membrane fuel cell which has a separate "water chamber" show that the combination of design and material brings to important principle advantages in respect to the classical rSOC – better performance in electrolyzer mode combined with instantaneous switching. The VACs which give integral picture of the cell performance are in excellent agreement with the impedance studies which ensure deeper and quantitative information about the processes, including information about the rate limiting step. This work can be accepted as giving "green light" for further development of the dmFC concept combining fundamental and technological improvements.

REFERENCES

1. http://www.fch.europa.eu/page/call-2018 (p. 69).
2. H. Uchida, P. Puengjinda, K. Miyano, K. Shimura, H. Nishino, K. Kakinuma, M. E. Brito, M. Watanabe, *ECS Transactions,* **68**, 3307 (2015).
3. O.A.Marina, L. R. Pederson, M. C. Williams, G. W. Coffey, K. D. Meinhardt, C. D. Nguyen, E. C. Thomsen, *J. Electrochem. Soc.*, **154**, B452 (2007).
4. N. Q. Minh, M. C. Williams, *ECS Transactions*, **68**, 3301 (2015).
5. T. Ishihara, A. Inoishi, H. Kim, S. Ida, *ECS Transactions*, **68**, 3279 (2015).
6. S. Presto, A. Barbucci, M.P. Carpanese, M. Viviani, R. Marazza, *J. Appl. Electrochem.,* **39**, 2257 (2009).
7. Y. Zhang, K. Chen, C. Xia, S. P. Jiang, M. Ni, *Int. J. Hydrogen Energy*, **37**, 13914 (2012).
8. V. N. Nguyen, Q. Fang, U. Packbier, L. Blum, *Int. J. of Hydrogen Energy*, **38**, 4281 (2013).
9. A.Thorel, Patent N°0550696000 (2005).
10. www.ideal-cell.eu.
11. D. Vladikova, Z. Stoynov, G. Raikova, A. Thorel, A. Chesnaud, J. Abreu, M. Viviani, A. Barbucci, S. Presto, P. Carpanese, *Electrochimica Acta*, **56**, 7955 (2011).
12. A.Thorel, J. Abreu, S. Ansar, A. Barbucci, T. Brylewski, A. Chesnaud, Z. Ilhan, P. Piccardo, J. Prazuch, S. Presto, K. Przybylski, D. Soysal, Z. Stoynov, M. Viviani, D. Vladikova, *J. Electrochem. Soc*., **160**, F360 (2013).
13. A.Thorel, Z. Stoynov, D. Vladikova, A. Chesnaud, M. Viviani, S. Presto, Fuel Cell With Monolithic Electrolytes Membrane Assembly, US Patent № 20120156573, 21.06.2012.
14. M. Viviani, S. Presto, A. Barbucci, M. P. Carpanese, R. Amendola, A. S. Thorel, A. Chesnaud, J. Abreu, R. Costa, Z. Ilhan, S-A. Ansar, D. E. Vladikova, Z. B. Stoynov, *MRS Proceedings,* 1330 (2011).
15. D. Vladikova, Z. Stoynov, A. Chesnaud, A. Thorel, M. Vivianu, A. Barbucci, G. Raikova, P. Carpanese, M. Krapchanska, E. Mladenova, *Int. J. Hydrogen Energy*, **39**, 21561 (2014).
16. Z. Stoynov, D. Vladikova, E. Mladenova, *J. Solid State Electrochem*., **17**, 555 (2013).

17. D. Vladikova, Z. Stoynov, B. Burdin, G. Raikova, M. Krapchanska, A. Thorel, A. Chesnaud, *Machines, Technologies, Materials*, **4**, 190 (2017).

18. M. Viviani, G. Canu, M. Carpanese, A. Barbucci, A. Sanson, E. Mercadelli, C. Nicolella, D. Vladikova, Z. Stoynov, A. Chesnaud, A. Thorel, Z. Ilhan, S. Ansar, *Fuel Cells 2012 Science & Technology – A Grove Fuel Cell Event*, Energy Procedia, **28**, 182 (2012).

19. D. Vladikova, Z. Stoynov, G. Raikova, A. Thorel, A. Chesnaud, J. Abreu, M. Viviani, A. Barbucci, Z. Ilhan, P. Carpanese, S. Presto, *Proc. 15th European Fuel Cell Forum Lucerne: Switzerland*; Ch. 18/B1205, 29 (2011).

20. S. C. Singhal, K. Kendall, Solid Oxide Fuel Cells: Fundamentals, Design and Applications, Elsevier (2003).

21. K. C. Liang, A. S. Nowick in: T.A. Ramanarayanan (Ed.), Ionic and Mixed Conducting Ceramica III, The Electrochemical Society Proceedings Series, Pennington, NJ **28**, 97 (1997).

22. Z. Stoynov, D. Vladikova, A. Thorel, A. Chesnau, M. Viviani, A. Barbucci, Patent N ES2554456T3 (2011).

ЕЛЕКТРОХИМИЧНО ТЕСТВАНЕ НА ИНОВАТИВЕН ДИЗАЙН НА ДВОЙНОМЕМБРАННА ГОРИВНА КЛЕТКА В ОБРАТИМ РЕЖИМ

З. Стойнов[1†], Д. Владикова[1*], Б. Бурдин[1], А. Торел[2], А. Чено[2], П. Пикардо[3], М. Славова[1], Р. Споторно[3]

[1]*Институт по електрохимия и енергийни системи, Българска академия на науките, ул. Акад. Г. Бончев, бл. 10, София 1113, България*
[2]*Център по материали, MINES-ПаржТех, PSL, UMR CNRS 7633 BP 87, Франция*
[3]*Университет Геноа, Катедра „Химия и индустриална химия", I-16146 Геноа, Италия*

(Резюме)

Твърдооксидните горивни клетки (SOFC) са вътрешно обратими, което ги прави привлекателни за разработването на обратими твърдооксидни клетки (rSOC). Основните препятствия които трябва да бъдат преодолени, са повишената деградация в режим на електролизьор (EL) и забавеното и затруднено превключване между двата режима. Настоящата работа има за цел разработване и експериментално потвърждение на концепцията за rSOC въз основа на новия дизайн на двойно мембранна горивна клетка (dmFC), който преодолява проблемите на класическите SOFC. В центъра на разработката е въвеждането на допълнителна камера, т.н. централна мембрана (CM), в която в режим на FC се формира и евакуира вода, а в режим на El тя се впръсква отвън. Оптимизацията на CM в лабораторни условия по отношение на микроструктурата и геометрията е проведена на клетки тип „копче". Електрохимичното им поведение е оценено въз основа на волт-амперни характеристики (VAC), в комбинация с измервания на импеданса в различни работни точки. Изследвано е и влиянието на катализатора във водната камера . Волт-амперните характеристики, които дават цялостна картина на поведението на клетките, са в съответствие с импедансните изследвания, което осигурява по-задълбочена количествена информация за процесите, в т.ч. и за скорост-определящия стадий. Резултатите от оптимизацията на CM показват, че комбинацията от дизайн и материал осигурява важни основни предимства спрямо класическия rSOC - по-добро поведение в режим на електролиза, комбинирано с много бързо превключване на режимите.

Ключови думи: обратима твърдооксидна горивна клетка, двойно мембранна горивна клетка, BCY15, импедансни измервания

Effect of the concentration of MnO_2 in the composite electrode and the electrolyte on the electrochemical properties of a hybrid supercapacitor

G. D. Ivanova[1*], A. E. Stoyanova[1], M. A. Mladenov[1], R. G. Raicheff[1], D. G. Kovacheva[2]

[1]Institute of Electrochemistry and Energy Systems – Bulgarian Academy of Sciences, 10, G. Bonchev Str., 1113 Sofia, Bulgaria
[2]Institute of General and Inorganic Chemistry- Bulgarian Academy of Sciences, 11, G. Bonchev Str., 1113 Sofia, Bulgaria

A novel hybrid supercapacitor based on a composite of acetylene black and MnO_2 as positive electrode and activated carbon as negative electrode has been developed. The effect of the electrolyte (K_2SO_4, KOH and KOH+LiOH) and the concentration of MnO_2 in the composite electrode is investigated. A supercapacitor using 50 wt.% MnO_2/XC composite electrode and mixed KOH electrolyte demonstrates highest and most stable discharge capacitance (about 1400 cycles), as well as a highest effectiveness of the charge-discharge process. This result can be related one hand with the better electroconductivity of KOH solution in comparison to K_2SO_4electrolyte and on the other - with the presence of Li^+ ions, which favors the faradaic charge-transfer reaction.

Key words: hybrid supercapacitors, manganese dioxide, composite electrode material, alkaline electrolytes

INTRODUCTION

The supercapacitors (SCs) have emerged as one of the most attractive electrochemical energy storage systems featuring high power delivery and long-term cycling stability [1]. The application area of SCs is constantly growing as the new power sources arise from consumersin electronics to industrial and transportation [2].

Carbon-based active materials (AC) are the most widely used electrode materials in these systems due to their physical and chemical properties[3]. The integration of supercapacitors and batteries in energy storage and delivery systems gives a possibility to combine the high transient performance of the supercapacitors with high steady-state characteristics of the batteries. In order to improve the energy density while keeping long cycle life of the supercapacitors, hybrid electrochemical systems involving hybridization of a faradaically rechargeable battery-type electrode with an electrochemical double-layer capacitor-type electrode (e.g. asymmetric supercapacitors), are introduced. A prominent advantage of the hybrid cell is the enlarged operating potential window, which noticeably enhances the energy and power performance. In aqueous systems, this is of particular interest as it may allow the capacitor to be operated at a potential window wider than the water decomposition voltage of 1-2 V, if electrode materials with high overpotentials for hydrogen or oxygen evolutions are carefully selected [3,4]. One

particular issue with hybrid supercapacitors is non-linear charge–discharge, nevertheless promising results from various research groups indicated that this can be avoided by an appropriate cell fabrication [5].

Various hybrid capacitor configurations, consisting of activated carbon as a positive electrode and a negative electrode based on metal oxides (nickel, lead or manganese oxides) [6–8], conducting polymers [9] are suggested.The engineering of MnO_x with suitable materials of complementary properties to form a composite, or into specifically effective nanostructures to assist charge transport, represents an important direction of development. Appropriate cell configuration has been proven to be the necessity for the optimisation of the capacitive performance of MnO_x based supercapacitors. Based on these literature findings, the authors believe that manganese oxides represent a promising and very competitive electrode material for applications in supercapacitors [10] because of such superior characteristics as large specific capacitance, environmental benignity nature, natural abundance and low cost [11]. It was found that the textural characteristics, crystal forms and ion conductivity of MnO_2strongly influence its electrochemical performances [12,13].

There are a lot of reports on MnO_2 preparation technologies, such as a co-preparation method, a thermal decomposition method, a sol-gel method

---

and other methods [14-16]. Hybrid supercapacitors with MnOx as the cathode and carbon materials such as activated carbon [17-20] as the anode have been fabricated. These hybrid systems exhibited superior capacitive behaviour in comparison with thesymmetrical carbon based systems. A better cycling stability can be achieved,since the reduction of Mn^{4z} to soluble Mn^{2z} species, and hydrogen and/or oxygen evolution occurred when the hybrid cell was cycled over an operating potential window of 2,2 V [20].

However, MnO_2 suffers from low electronic conductivity and poor cation diffusivity,which results in poor utilization and limited rate performance of traditional MnO_2 powder electrodes,obtained by pressing a mixed paste of MnO_2 powder, conductive additive and polymer binder ontometallic current collectors [10].

The choice of electrolyte also has significant impacts on the performance of the MnOx electrodes. The pH condition is an important determinant of the operating potential window; and different existing ions determine the rate of intercalation and the situation of corrosion. Thus, desirable electrode performance can be obtained only by choosing the composition of the electrolyte carefully [10].

It was reported that electrolyte with equal transference numbers for both cation and anion can promote capacitive behaviour and anions with smaller hydration sphere and smaller size leads to faster diffusion and higher chemisorption rates [21]. Experiments comparing the electrochemical performance of the MnO_2 material in several neutral aqueous electrolytes including NaCl, KCl and LiCl with the same concentration of 2 $moldm^{-3}$ have been conducted [21,22]. It was claimed that although Li^+ is smaller than Na^+ and K^+, it has a larger hydration sphere, which makes it disadvantageous. And this theory was supported by the results from several other research groups [23,24]. However, a more recent study on the electrochemical behaviour of the MnO_2 electrode in 1 mol dm^{-3} KOH and 1 mol dm^{-3}LiOH [18, 25] declared that the reaction mechanism of MnO_2 electrode in LiOH appears to be Li^+ ion insertion/extraction in the MnO_2 solid, followed the battery reaction of $MnO_2^++Li^++xe^-=Li_xMnO_2$.This finding may elicit further thoughts upon the mechanism of the charge storage within MnOx.

In our previous work it has been shown that Li^+ ions and H_2O from the LiOH-KOH electrolyte are intercalated into α-$Ni(OH)_2$ and as a result, the α-$Ni(OH)_2$/AC displays an improved performance in the mixed LiOH-KOH electrolyte than that in the individual KOH electrolyte[26].

In this study we demonstrate the electrochemical properties a novel type hybrid supercapacitor cell composed by two different electrode – commercial MnO_2 (Fluka) (selected on the basis of our previous research [27]) with teflonized acetylene black (XC-35).The content of MnO_2 in the composite electrode is optimized in the range from 0 to 100%. Three types aqueous electrolytes were used (0,1M K_2SO_4, 7M KOH and mixed electrolyte 7M KOH + 1.45 M LiOH) in order to study the effect of the electrolyte on the capacitive properties of MnO_2/XC-35 composite electrode. The structure and morphology changes of the composite electrode are monitored by X-ray Diffraction (XRD), Scanning and Transmission Electron Microscopy (TEM, SEM). The supercapacitor performance of the composite electrodes is tested by means of galvanostatic charge/discharge experiments.

EXPERIMENTAL
Physicochemical characterization of the electrode materials

The used materials are previously structurally characterized by X-ray Diffraction (XRD), Scanning and Transmission Electron Microscopy (TEM, SEM) [27, 28]. Powder X-ray diffraction patterns were collected within the range from 5.3 to 80∘ 2θ with aconstant step 0.02∘ 2θ on Bruker D8 Advance diffractometer with Cu Kα radiation andLynxEyedetector. The microstructure of the electrode materialsis is studied by means JEOL JSM-5510 and JEOLSuperprobe 733 scanning electron microscope(SEM) and JEOL 2100 Transmission electron microscope (TEM).
The specific surface area is investigated by BET method using Area Meter, Strolen-Germany. The measurement is recordedby nitrogen gas adsorption at −197 °C. The samples are completely degassed by drying (100^0C), thermostating (120^0C), and blowing with nitrogen.

Preparation of supercapacitor cells and electrochemical testing

The hybrid supercapacitor cell is composed by a positive electrode – a composite of teflonized acetylene black (XC-35) and commercial MnO_2 in concentration range from 0 to 100 wt.%, and a negative electrode of activated carbon (Cabot CGP Super) with addition of PTFE and carbon black (Cabot SC2). The formed sheet electrodes (surface area 1,75 cm^2) were dried at 140°C for 12 hours and pressed under pressure of 20 Mpa, soaked in the electrolyte under vacuum and then mounted in a coin-type cell with Viledon 700/18F separator and filled with electrolyte. Three types of alkaline

147

solutions were used as electrolytes:0, 1 M K_2SO_4 solution, 7 M KOH solution and 7 M KOH solutions with additives of 35 gl^{-1} LiOH (i.e. 1,45M LiOH). The capacitor cells were subjected to galvanostatic charge-discharge cycling using an Arbin Instrument System BU-2000. The test program was carried out at constant current mode at different current load (from 30 to 360 mAg^{-1}) and room temperature [28]. Some cells are subjected to continuous cycling charge/discharge at current rate of 60 mAg^{-1} up to 1400 cycles.

RESULTS AND DISCUSSIONS
Physicochemical characterization

The powder diffraction pattern of the active materials used (Cabot CGP Superand MnO_2) are presented in Fig. 1. It is seen that Cabot CGP Super and MnO_2 differ in their phase composition and size of the crystallites.
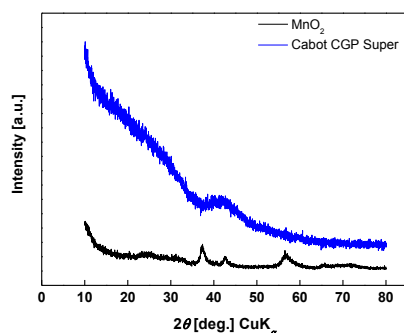
Fig.1. XRD pattern of the Cabot CGP Super and MnO_2 [26, 27]

On the powder pattern of the activated carbon typical amorphous hums are observed in the range 20-25 degrees, which corresponds to (001) reflections of the graphite and 38-48 degrees corresponding to (101) diffraction of the graphite. The pattern of MnO_2-sample shows a single phase MnO_2 – akhtenskite type structure with crystallites sizes about 5–6 nm.

The TEM images of the activated carbon and manganese dioxide illustrate their structural and morphological characteristics (Fig. 2).

The high specific surface area and high distribution of the Cabot CGP Super material and all textural parameters suggest that it is an appropriate electrode material for carbon electrodes in supercapacitor systems (Fig. 2a), consisting mainly of small particles clusters. The micrographs of MnO_2 (Fig. 2b) demonstrate crystalline structures with homogeneous definition of crystalline grains and nanosized particles.
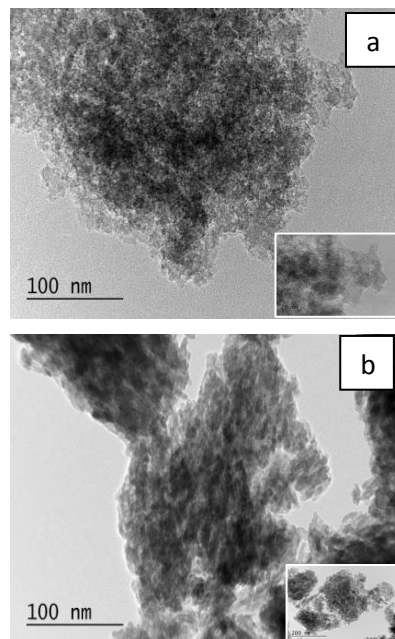
Fig. 2. TEM images of Cabot CGP Super(a) and MnO_2 (b)

The pore textures of the activated carbons are studied by takingthe nitrogen adsorption/desorption isothermsof the samples. The results show that the Cabot CGP Super possesses a very high surface area (1825 m^2g^{-1}) and large micropore volume independently from the smaller total pore volume [28]. The specific surface area on MnO_2 is 58.80 m^2g^{-1}.

Electrochemical performance of the supercapacitor cells

The electrochemical performance of the supercapacitor cells developed are studied by charge/ discharge cycling test under identical experimental conditions, at different (increasing in values) constant current loads with minimum 25 cycles at each current rate.

Figure 3 gives the dependences of the specific dischargecapacityon the current load for the supercapacitor cells free of manganese dioxide with different electrolytes (0,1M K_2SO_4, 7M KOH with and without addition of LiOH).The analysis of the cycling behaviors shows that the asymmetric supercapacitor cells using mixed electrolyte (KOH+LiOH) demonstrate highest discharge capacity compared to the other two cells (about 15-17% higher than the cell without LiOH and about 50% than the supercapacitators with K_2SO_4).
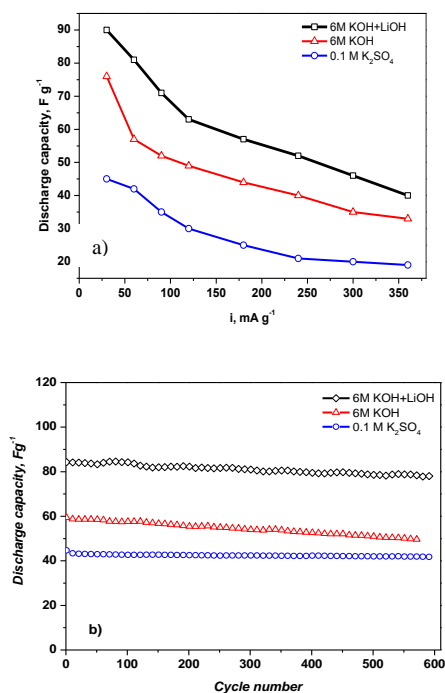
Fig. 3. Dependence of the discharge capacity on the current load (a) and on the cycle number at current load 60 mAg^{-1} (b) for the supercapacitor cells free of manganese dioxide

Fig. 4. Discharge capacitance for supercapacitors with MnO_2 in various content as a function on the current load (a) and on the MnO_2 content at different current loads (b)

The relation in figure 3a shows that the discharge capacity for the supercapacitor free of manganese dioxide with mixed electrolyte is very stable at prolong cycling and after 600 cycles it drops only by about 7 - 10%. The discharge capacity for the supercapacitors cell using 0,1M K_2SO_4 is very stable too, but its values are the lowest, while in pure KOH it is less stable and with lower values than in the presence of a small amount of LiOH. Obviously Li$^+$ ions from the electrolyte display a positive effect on the discharge capacitance and the cycling stability of the supercapacitor performance.

Figure 4a gives the dependences of the discharge capacitance as a function of discharge current density and cycle number for supercapacitors with composite electrodes containing 0 – 100 wt.% MnO_2 while the dependence of the discharge capacitance on the MnO_2 content, determined at low and high current loads, is illustrated on Figure 4b.

Irrespective of the current loads, the discharge capacitance curve passes through a maximum between 40 and 60% wt.% MnO_2, as the highest capacitance value being observed at 50 wt.% MnO_2.

The hybrid supercapacitors demonstrate a higher and a stable discharge capacitance, as well as a higher effectiveness of charge-discharge process, in the whole range of current loads. Above 80 wt.% and below 30 wt.% of MnO_2 the discharge capacitance of the hybrid capacitors becomes lower than that of the supercapacitor free of manganese dioxide. This non-monotonous dependence can be related with formation of composite electrodes, where double layer capacitance and Faradaic pseudocapacitance are expected to be active. Below 30 wt.% of MnO_2, it appears that homogeneous composites XC/MnO_2 with improved electrical conductivity are formed due to the high porosity of XC (58,13% [29]). Above 35 wt.% of MnO_2, the reduction of AC content leads to a decrease of the electrical conductivity of the electrode, as a result of which the discharge capacitance decreases [30].

The effect of the alkaline electrolyte on the hybrid supercapacitor performance is investigated using XC/MnO_2 as composite electrode. Figure5 shows the dependence of the discharge capacity of the hybrid supercapacitors a function on the current load in different alkaline electrolytes. The dependence here is the same as for the supercapacitor free of manganese dioxide (Fig. 3a) and the discharge capacitance values are higher. The increasing here is about 40% at 60 mAg^{-1} and at higher current load (240 mAg^{-1}) the effect of Li$^+$

149

decreases (24%), but the discharge capacitance in K_2SO_4 solution increases significantly to about $20 Fg^{-1}$ (the value of the discharge capacitance in KOH+LiOH electrolyte here is 100 Fg^{-1}).
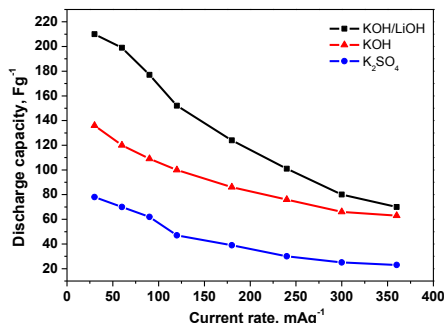
Fig. 5. Dependence of the discharge capacity of hybrid supercapacitors on the current load at different electrolytes

Figure 6 shows charge/discharge curves of the 50 wt.% MnO_2/XC composite electrode working in different electrolytes. All three devices exhibit galvanostatic charge– discharge curves which resemble those of electrochemical double layer capacitor. However, a closer look indicates that the slopes of the three systems slightly differ from linearity as a result of the pseudo-Faradaic processes for the oxide electrodes [8]. This trend is more pronounced for the device using K_2SO_4 as electrolyte. This supercapacitor has the lowest capacitance, despite its enhanced cell potential compared to cells using KOH as an electrolyte. The reason for the lower capacity in sulfate solution is probably due to its lower conductivity compared to that of 7M KOH.

As can also be seen from Fig. 6, the iR-drop of the suprecapacitor in the mixed LiOH-KOH electrolyte is slightly lower than that in the two others electrolytes: 0.20 V (LiOH-KOH) versus 0.24 V (KOH) and 0.29 V (K_2SO_4) respectively. This results in a high discharge capacitance of the supercapacitor working with mixed LiOH-KOH electrolyte.
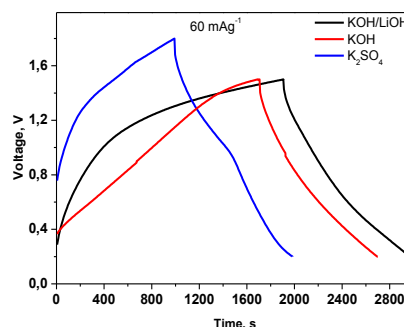
Fig. 6. Galvanostatic charge and discharge curves of hybrid supercapacitor with 50 wt.% MnO_2 in the composite electrode

The improved capacitance can be related with a change in the conductivity of the mixed LiOH-KOH electrolyte. Furthermore, the higher discharge capacitance in the mixed LiOH-KOH electrolyte can be related also with the reaction mechanism for energy storage. The appearance of Li+ ions in the alkaline electrolyte favors, in addition to the capacitive reactions, the reactions that take place by a faradaic charge-transfer mechanism [28]. The redox reaction in the MnO_2 electrode can be viewed as the reversible insertion/extraction of Li^+ in MnO_2 solid, which is different from the case of using pure KOH electrolyte, and this can explain the significantly higher capacity increase in hybrid supercapacitors in mixed electrolyte [25].

As it is seen, the hybrid supercapacitor based on anode material with 50% manganese oxide in the composite electrode exhibits the highest discharge capacity in mixed solutions and because of this in Fig. 7 are shown its electrochemical characteristics. The proposed supercapacitor exhibits high discharge capacitance (above 200 Fg^{-1}) and high efficiency (97- 98%) and stable cycle life (above 1400 cycle).
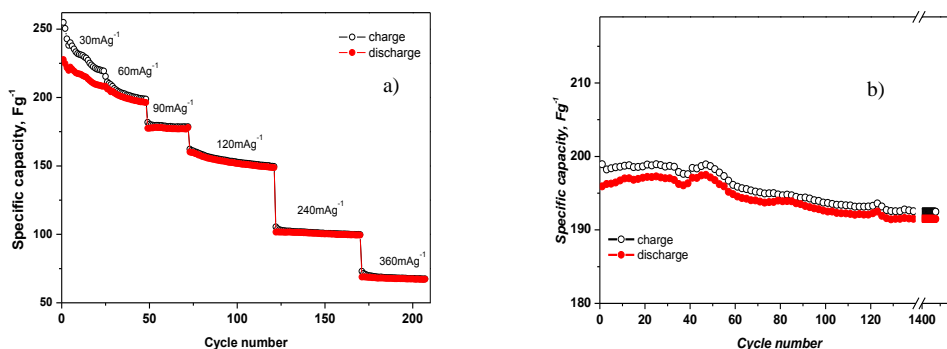
Fig. 7. Discharge capacitance as a function of the current load (a) and the cycle number at current load 60 mAg^{-1} (b) of hybrid supercapacitors with composite electrode containing 50 wt% MnO$_2$/XC and mixed electrolyte of 7 M KOH with addition of LiOH

CONCLUSIONS

A novel hybrid supercapacitor based on a composites of acetylene black (XC-35) and commercial MnO$_2$ as positive electrode and activated carbon as negative electrode using three different electrolytes (0,1M K$_2$SO$_4$, 7M KOH and mixed electrolyte 7M KOH + 1.45 M LiOH) has been developed. The ratio between MnO$_2$ and acetylene black is varied in a whole concentration range from 0 to 1,0. The supercapacitors with 50 wt. % MnO$_2$ and mixed electrolyte KOH + LiOH demonstrate highest and most stable discharge capacitance, as wellas a highest effectiveness of charge-discharge process. The better performance of the composite electrode in the mixed electrolyte is related with the better electroconductivity of KOH solution in comparison of K$_2$SO$_4$ and the presence of Li$^+$ ions, which favors the faradaic charge-transfer reaction.

REFERENCES

1. L. Zhang, K. Tsay, C. Bock, J. Zhang, *J. Power Sources*, **324**, 615 (2016).
2. V. Khomenko, E. Raymundo-Piñero and F. Béguin, *J. Power Sources*, **77**, 643 (2008).
3. W. Pell and B. Conway B., *J. Power Sources*, **136**, 334 (2004).
4. K. C. Ng, S. Zhang and G. Z. Chen, *ECS. Trans,* **16**, 153 (2008).
5. A. Burke, *J. Power Sources*, **91**, 37 (2000).
6. A. Di Fabio, A. Giorgi, M. Mastragostino, F. Soavi., *J. Electrochem. Soc.*, **148**, A845 (2001).
7. D. Cericola, R. Kötz, *Electrochim. Acta*, **72**, 1 (2012).
8. T. Cottineau, M. Toupin, T. Delahaye, T. Brousse, D. Bélanger, *Appl. Phys. A*, **82**, 599 (2006).
9. W. Wei, X. Cui, W. Chen, D. G. Ivey, *Chem. Soc. Rev.*, **40**, 1697 (2011).
10. S. W. Zhang and G. Z. Chen, *Energy Materials,* **3**, 186 (2008).
11. R. Kötz and M. Carlen, *Electrochim. Acta,* **45**, 2483 (2000).
12. O. Ghodbane, J.L. Pascal, F. Favier, *ACS Appl. Mater. Interfaces*, **1**, 1130 (2009).
13. W. Pell, B. Conway B., *J. Power Sources,* **136**, 334 (2004).
14. Y.U. Jeong, A. Mantiram, *J. Electrochem. Soc.*, **149**, 1419 (2002).
15. X. Y. Chen, X. Li, Y. Jank, *Solid State Commun.*, **136**, 94 (2005) .
16. J. Li,X.Y. Wang, Q. H. Huang, W. G. Huang, P. J. Sebastian, S. Gamboa, et.al., *J. Power Sources,* **158**, 784 (2006).
17. M.S. Hong, S.H. Lee, S.W. Kim: *Electrochem. Solid-State Lett.*, **5**, A227 (2002).
18. A.Yuan and Q. Zhang, *Electrochem. Commun.*, **8**, 1173 (2006).
19. V. Khomenko, E. Raymundo-Pinero, F. Beguin: *J. Power Sources*, **153**, 183 (2006).
20. T. Brousse, M. Toupin, D. Belanger, *J. Electrochem. Soc.*,**151**, A614 (2004).
21. Y.U. Jeong, A. Manthiram, *J. Electrochem. Soc.*, **149**, A1419 (2002).
22. H.Y. Lee, J. B. Goodenough,*J. Solid State Chem.*, 144, 220 (1999).
23. M. Wu, G.A. Snook, G.Z. Chen, D.J. Fray, *Electrochem. Commun.*, **6**, 499 (2004).
24. R.N. Reddy, R.G. Reddy, *J. Power Sources,* **124**, 330 (2003).
25. A. Yuan, Q. Zhang, *Electrochem. Comm.*, **8**, 1173 (2006).
26. L. Soserov, T. Boyadzhieva, V. Koleva, Ch. Girginov, A. Stoyanova, R. Stoyanova, *Chem Select, Chemistry Select* **, 2,** 6693 (2017).

27. G. D. Ivanova, A. E. Stoyanova, L. S. Soserov, D. G. Kovacheva, D. B. Karashanova, *Bulg. Chem. Comm.* **49**, 71 (2017).

28. Ch. Girginov, L. Stoyanov, S. Kozhukharov, A. Stoyanova, M. Mladenov, R. Raicheff, *Proc. Scientific Papers at the University of Ruse "Angel Kanchev"*, **54**, 10.1, 89 (2015).

29. Илиан Попов, Автореферат (2017).

30. L. Soserov, T. Boyadzhieva, V. Koleva, A. Stoyanova, R. Stoyanova, *ECS-trans*, **74**, 213 (2016)

ВЛИЯНИЕ НА КОНЦЕНТРАЦИЯТА НА MnO$_2$ В КОМПОЗИТНИЯ ЕЛЕКТРОД И НА ЕЛЕКТРОЛИТА ВЪРХУ ЕЛЕКТРОХИМИЧНИТЕ СВОЙСТВА НА ХИБРИДНИ СУПЕРКОНДЕНЗАТОРИ

Г. Д. Иванова[1*], А. Е. Стоянова[1], М. А. Младенов[1], Р. Г. Райчев[1], Д. Г. Ковачева

[1]Институт по електрохимя и енергийни системи – Българска академия на науките, ул. Акад. Г. Бончев 10, 1113 София
[2]Институт по обща и неорганична химия– Българска академия на наукит, ул. Акад. Г. Бончев 11, 1113 София

(Резюме)

Разработен е нов хибриден суперкондензатор на базата на ацетиленови сажди и MnO$_2$ като положителен електрод и активен въглен, като отрицателен електрод. Изследван е ефектът на електролита (K$_2$SO$_4$, KOH и KOH+LiOH) и концентрацията на MnO$_2$ в композитния електрод. Суперкондензаторите с композитен електрод, съдържащ 50 тегл.% MnO$_2$ и смесен електролит на KOH+LiOH показват най-висок и най-стабилен разряден капацитет (до 1400 цикъла), както и най-висока ефективност при зарядно-разрядния процес. Този резултат се дължи от една страна на по-добрата електропроводимост на KOH в сравнение с K$_2$SO$_4$, а от друга страна - на наличието на Li$^+$ йони, които благоприятстват Фарадеевата реакция.

Ключови думи: хибридни суперкондензатори, манганов диоксид, композитен електроден материал, алкален електролит

Electrochemical impedance study of HTSC ceramics YBCO and BSCCO in presence of electrolyte

P.A. Lilov[1], A.Y. Vasev[1], A.E. Stoyanova[2], Y.G. Marinov[1], A.K. Stoyanova-Ivanova[1*]

[1] *Georgi Nadjakov Institute of Solid State Physics, Bulgarian Academy of Sciences, 72 Tzarigradsko Chaussee Blvd., 1784 Sofia, Bulgaria*
[2] *Institute of Electrochemistry and Energy Systems "Academician Evgeni Budevski", Bulgarian Academy of Sciences, Acad. Georgi Bonchev Str, Block 10, 1113 Sofia, Bulgaria.*

Electrochemical studies of high temperature superconductuctors (HTSC) began immediately after their discovery and numerous studies of ionic transport in HTSC solid electrolytes were conducted. The search for approaches to the problems in HTSCs was largely based on analogies with electrochemical studies of semiconductors, since the majority of HTSC materials exhibit semiconducting properties at ambient temperatures. The analogy thus stimulated the electrochemical studies on the degradation of HTSC in water and acid solutions and their relative stability in strong alkaline solutions. HTSC cuprate ceramics find applications also as an additive in the zinc electrode in nickel-zinc batteries. Such cells are a potentially cheaper and easier to recycle, replacement for toxic nickel-cadmium batteries. Electrochemical tests showed that the Ni-Zn battery cells with YBCO and BSCCO superconducting ceramic additives in the zinc electrode exhibited good cyclic operation ability and capacity stability, as well as a higher specific capacity than the cells with a zinc electrode with a "classic" carbon conducting additive. The study presented here is focused on the electrochemical characterization of nanocomposite conductive cuprate ceramics - $Bi_2Sr_2CaCu_2O_x$ (BSCCO -2212), $Bi_2Sr_2CuO_y$ (BSCO - 2201) and $YBa_2Cu_3O_x$ (YBCO - 123) in the following electrolytes: 7M KOH, the electrolyte used in Ni-Zn cells, an alkaline phosphate (AF) - electrolyte containing KOH and $Na_3PO_4.12H_2O$, and a proprietary PSPAA electrolyte. The electrical conductivity of ceramic/electrolyte system was investigated by Electrochemical Impedance Spectroscopy measurements performed by a Bio-logic SP-200 potentiostat. The impedance responses for all ceramics are compared and discussed in terms of equivalent circuits.

Keywords: electrochemical impedance, HTSC ceramics, BSCCO, YBCO.

INTRODUCTION

The expression "high-temperature superconductivity" HTSC has been used for several decades [l], but it changed from an abstract term to a real one only in 1986 after the famous publication of Bednorz and Muller [2]. All the more revolutionary, both in the fundamental and in the applied aspects, became the subsequent discovery of the oxide HTSC of the YBCO system with a T_c, higher than liquid nitrogen temperature, followed by the discovery of other cuprate systems with even higher characteristic values, such as BSCCO. Most HTSC oxides have the structure of perovskite (though some of them have a spinel-type structure), which pertains to more than 35 structural classes [3], and includes more than a hundred typical unit cells [4]. For fundamental studies of superconductivity in oxides, both the absolute T_c, values and the variety of properties and structures are essential.

Electrochemical studies of HTSC began immediately after their discovery and the numerous studies of ionic transport in HTSC solid electrolytes were conducted. Hence, the electrochemistry of HTSC can be considered as a direction in electro-chemical science and technology [1].

The search for approaches to the problems in HTSCs was largely based on analogies with electrochemical studies of semiconductors [5-9], since the majority of HTSC materials exhibit semiconducting properties at ambient temperatures. Moreover, technological problems arising in the practical application of materials of these classes (such as in the electronics field) are similar. The analogy thus stimulated the electrochemical studies on the degradation of HTSC in water and acid solutions [10, 11] and their relative stability in strong alkaline solutions [1].

HTSC cuprate ceramics, exhibiting superconductivity at low temperatures (80-100K) find other applications as well, such as an additive in the zinc electrode in nickel-zinc batteries [11, 12], which might replace toxic nickel-cadmium batteries. The positive effect on capacity and cycling stability of cuprate ceramic additives has been previously demonstrated [12, 13]. Studies have revealed that YBCO samples are remarkably stable, thus leaving

---

the superconducting properties of the 123-type phase unchanged after the alkaline treatment. The possibility of using the superconducting YBCO ceramics as a conducting additive to the zinc electrode mass of nickel-zinc alkaline rechargeable batteries was also studied. The electrochemical tests showed that the battery cells with a YBCO superconducting ceramic additive in the zinc electrode exhibited a better cyclic operation ability and capacity retention after prolonged cycling, as well as a higher (by about 30%) specific capacity than the cells with a zinc electrode with a "classic" carbon conducting additive to the zinc electrode mass and thus may contribute to extending the battery life [12].

Powder superconductive cuprate ceramic BSCCO 2212 system is produced by solid-state synthesis and physicochemically characterized. The chemical stability of BSCCO ceramics in alkaline medium of the Ni-Zn battery is confirmed by structural and morphological analysis (XRD, SEM and EDX) and the superconducting properties of samples are evaluated before and after prolonged exposure to 7M KOH. The electrochemical tests are carried out by Stoyanov et. al. [12] with conventional sintered type nickel electrodes and pasted zinc electrode with active electrode mass based on ZnO with addition of BSCCO powder or carbon (acetylene black) as conductive additives show that the zinc electrode with BSCCO ceramic additive exhibits very good cyclability, remarkable capacity stability and much higher discharge capacity at prolonged charge/discharge cycling in comparison to the zinc electrode with the "classic" carbon conductive additive. It is suggested that the addition of BSCCO ceramics improves not only conductivity and electrochemical homogeneity of the electrode mass and reduces the gas evolution but also stabilizes its porosity structure. The results obtained prove the possibility of application of superconducting BSCCO ceramics as a multifunctional additive to the active mass of the zinc electrodes for alkaline nickel-zinc battery systems [12].

In this work we examine the conductivity of YBCO and BSCCO HTSC ceramics through impedance spectroscopy to obtain initial qualitative data about their electrical characteristics and behavior exposed to different electrolyte solutions.

EXPERIMENTAL

Through solid state reaction ceramic tablets of nominal composition: $Bi_2Sr_2CaCu_2O_y$ (BSCCO 2212) and $Bi_2Sr_2CuO_y$ (BSCO 2201) were obtained. Powder samples of $Bi_2Sr_2CaCu_2O_y$ are produced by two-stage conventional solid-state synthesis from high-purity (99,99 %) reagents - Bi_2O_3, CuO, $SrCO_3$ and $CaCO_3$. After thorough mixing and grinding and initial heat treatment at 780°C for 24 hours in air the powder obtained is ground and pressed into pellets (5-6 MPa). BSCO 2201 was sintered at 830°C for 24 hours, BSCCO 2212 at 830°C for 48 hours in air atmosphere.

Another sample of nominal composition: $YBa_2Cu_3O_x$ (YBCO) was obtained. Powder samples are produced by solid-state synthesis from high-purity (99,99 %) oxides - Y_2O_3, CuO and $BaCO_3$. After thorough mixing and grinding the first stage is a heat treatment at 900°C for 21 hours. After grinding, the powder was sintered for a second time at 940°C under the same conditions, followed by a slow cooling and an additional annealing at 450°C for 2 hours. The pellets were then pressed at 5-6 Mpa and sintered for a third time at 950°C for 23 hours, and subsequently annealed at 450°C for 23 hours.

The electrochemical system SP-200: potentiostat/galvanostat was used to perform potentiostatic electrochemical impedance spectroscopy (PEIS) measurements applying the EC-Lab software. The impedance of the conductive ceramic tablets (YBCO and BSCCO) was measured using a two probe method. The samples are prepared with a rectangular shape and their surface area was calculated. Silver conductive paste was applied on two parallel and opposite faces, with known surface area and distance between them. The specific electrical resistance ρ was calculated taking the resistance value measured at the low frequency point of the impedance curve intersection with the real axis. PEIS measurements were also taken using BSCCO and YBCO as the working electrode (WE) a three electrode electrochemical cell. The working surface area of the electrodes was 0.4679 cm^2, 0.88 cm^2 and 0.257 cm^2 for BSCO 2201, BSCCO 2212 and YBCO, respectively. The counter-electrode (CE) was a platinum plate. The potential was measured relative to a saturated calomel electrode (RE). The applied potential is referenced to the open circuit potential of the working electrode. The applied sine-wave potential amplitude is 10 mV, in some cases a higher potential of 20 or 30 mV was required in order to noise free data. In all experiments the frequency was swept form 1 MHz down to 0.1 Hz. Three supporting electrolytes were used: 7M KOH, the electrolyte used in Ni-Zn cells, an alkaline phosphate (AF) electrolyte containing KOH and $Na_3PO_4.12H_2O$ [14], and a proprietary PSPAA electrolyte containing anti-corrosion agents. Impedance spectra were taken at room temperature in order to examine electrical and electrochemical behavior near the working conditions of Ni-Zn cells.

RESULTS AND DISCUSSIONS

The impedance of the BSCCO conductive ceramic tablets was measured using a two probe method. Fig. 1 shows the Nyquist plot of impedance of bulk BSCCO ceramics. From the real part of the impedance at the lowest frequency specific electrical resistance ρ was calculated to be 0.124 Ω.cm for BSCO 2201 and 5052.3 Ω.cm for BSCCO 2212. PEIS measurements were taken using BSCCO and YBCO as the working electrode (WE) in a three electrode electrochemical cell. The impedance spectra of BSCO 2201 and 2212 in the three different electrolytes are presented in Fig. 2, 3 and 4 for KOH, AF and PSPAA respectively.
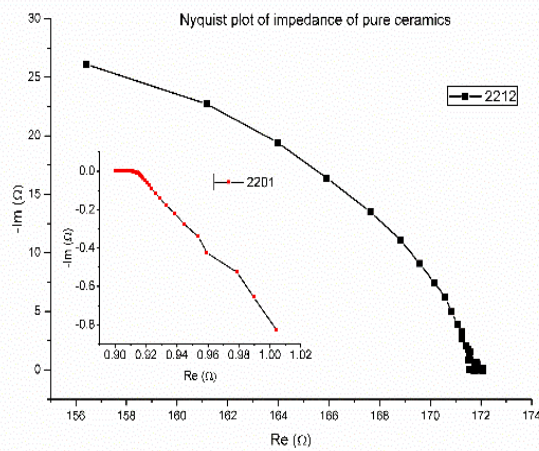
Fig. 1. Nyquist plot of the impedance for the pure ceramics.
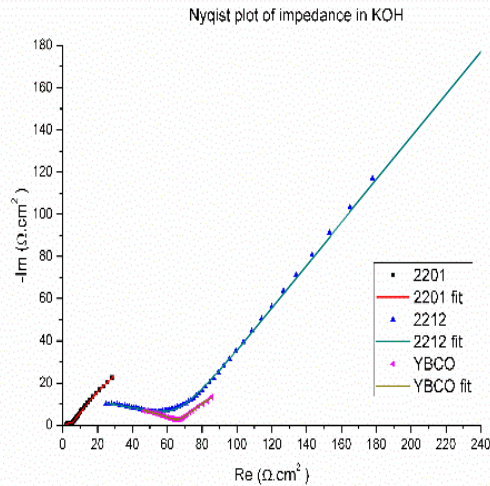
Fig. 2. Nyquist plot of the impedance for the ceramics in KOH electrolyte.
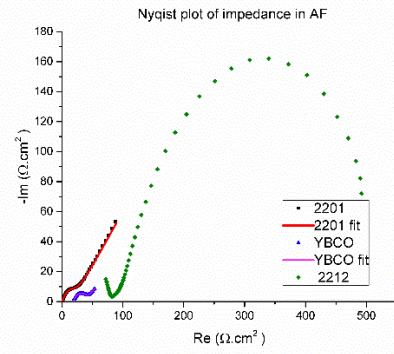
Fig. 3. Nyquist plot of the impedance for the ceramics in AF electrolyte
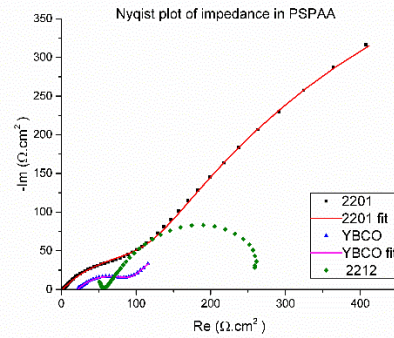
Fig. 4. Nyquist plot of the impedance for the ceramics in PSPAA electrolyte.

The raw data was normalized per unit surface area. Using the EC-Lab software we fitted the obtained curves to an equivalent circuit electrode model presented in Fig. 5a for BSCCO 2212 and YBCO and Fig 5b for BSCO 2201. Figures 2, 3 and 4 show the curves of the fits related to the obtained measurement data. The reasoning behind these models is supposition of surface modification observed in BSCCO ceramics on exposure to electrolyte [12].
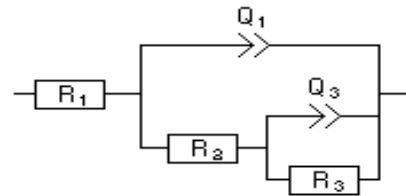
Fig. 5a. Proposed equivalent circuit model for BSCCO 2212 and YBCO ceramics.
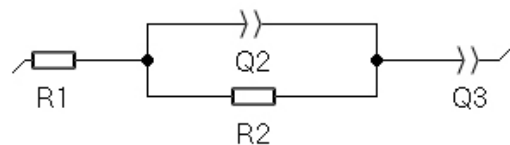
Fig. 5b. Proposed equivalent circuit model for BSCO 2201 in AF.

Table 1. Area-normalized parameter values obtained by curve-fitting

Model Param.	BSCO 2201			BSCCO 2212	YBCO			(Units)
	Electrolytes							
	KOH	AF	PSPAA	KOH	KOH	AF	PSPAA	
R1	1.70031	0.66838	1.75573	-171.952	8.468	18.200	21.739	$\Omega.cm^2$
Q1	6.73E-04	-	5.54E-04	1.03E-04	1.87E-4	1.53E-03	1.32E-03	$F.s^{(a-1)}cm^{-2}$
a1	0.5728	-	0.5125	0.1523	0.3162	0.5031	0.4772	-
R2	3.80597	16.9092	178.345	251.944	58.8016	25.664	82.856	$\Omega.cm^2$
Q2	-	4.34E-04	-	-	-	-	-	$F.s^{(a-1)}cm^{-2}$
a2	-	0.7165	-	-	-	-	-	-
Q3	1.47E-02	1.34E-02	1.31E-03	2.86E-03	3.00E-03	5.03E-03	2.03E-03	$F.s^{(a-1)}cm^{-2}$
a3	0.5784	0.41	0.7162	0.5235	0.4467	0.4553	0.698	-
R3	180.928	-	1505.85	22242.88	135.284	85.915	209.789	$\Omega.cm^2$

Degradation products may be less conductive and it is likely that they create a porous layer blocking the electrode surface. Here R1 represents the electrolyte resistance between RE and WE, R2 is the polarization resistance, R3 is the resistance of the electrolyte confined in the pores. Q1 and Q3 are the outer surface and pore double layer capacitances. Capacitances are substituted with constant phase elements (CPE) due to surface inhomogeneity, roughness and varying degrees of surface modification. Equivalent circuit parameter values are presented in Table 1. In the case of BSCO 2201 in the alkaline phosphate electrolyte another circuit model was used, presented in Fig. 5b, where R1 and R2 have the same meaning, while Q2 is equivalent to Q1. However, the behavior of BSCCO 2212 in the PSPAA and alkaline phosphate electrolytes could not be modeled by these equivalent circuits. The real part of the impedance at the lowest frequency is presented further below.

The parameter "a" describes the variation of the constant phase elements' impedance from purely capacitive (a=1) to purely resistive (a=0).

It must be noted that for BSCCO 2212 in KOH R1 is extrapolated by the software to a negative value due to lack of information about higher frequency behavior. At the highest frequency of 1 MHz the real part of the complex impedance is measured to be 24.64 $\Omega.cm^2$. The real part of the impedance of BSCCO 2212 at the lowest frequency is 492.03 $\Omega.cm^2$ for the AF electrolyte and 258.89 $\Omega.cm^2$ for PSPAA (fig.3, fig. 4).

BSCO 2201 exhibits the lowest values for R2 in both KOH and AF, with R2 being lowest in KOH. In the case of YBCO the opposite is true – R2 is smaller in AF than in KOH. In PSPAA R2 is substantially higher for both BSCCO 2201 and YBCO. While both BSCCO ceramics impedance varies substantially depending on the electrolyte solution content, YBCO displays less variation. The PSPAA electrolyte has an effect of increasing the polarization resistance for BSCO 2201 and YBCO and decreasing it in BSCCO 2212.

CONCLUSIONS

In this work we examined the conductivity of BSCCO and YBCO conductive ceramics through impedance spectroscopy to obtain initial qualitative data about their electrochemical characteristics and behavior exposed to various electrolyte solutions as a basis for their potential application as a conductive additive in Ni-Zn batteries. An equivalent circuit model was proposed and cell parameters were obtained through curve fitting. BSCO 2201 and YBCO exhibit lower overall resistance, BSCO 2201 and BSCCO 2212's behavior strongly depends on electrolyte composition. Results suggest that among the three examined ceramics BSCO 2201 is the best candidate for a conductive additive for the zinc anode in Ni-Zn batteries.

REFERENCES

1. Oleg A. Petri and Galina A. Tsirlina, *Advances in Electrochemical Science and Engineering*, **5**, 63 (1987).
2. J. G. Bednorz, K. A. Muller, *Z. Phys B,* **64**, (1986) 189.
3. R. J. Cava, *Nature* (London) **362**, 204 (1993).
4. J. Hauck, K. Mika, *Physica C* **175**, 386 (1991).
5. M. W. Breiter, W. J. Lorenz, G. Saemann-Ischenko, *Surface Sci.*, **230**, 213 (1990).
6. A.K. Vijh, Electrochemistry of Metals and Semiconductors, Marcel Dekker, New York, 1973
7. W. Kern, G. L. Schnable in: The Chemistry of the Semiconductor Industry, S. J. Moss, A. Ledwith (eds.), Chapman and Hall, New York (1987), 225.
8. A.Hamnett, in: Comprehensive Chemical Kinetics, *Elsevier,* Amsterdam 27, 61 (1987).
9. Yu. V. Pleskov, Yu. Ya.Gurevich, Semiconductor Photoelectrochemistry, Consultants Bureau, New York (1986).
10. M. F. Yan, R. L. Barns, H. M. O'Bryan, P. K. Gallagher, R. C. Sherwood, S. Jin, *Appl. Phys. Lett.* **51**, 532 (1987).
11. P. G. Egdell, W. R. Flavell, P. C. Hollanby, *J. Solid State Chem.*, **79**, 238 (1989) .
12. L. Stoyanov, S. Terzieva, A. Stoyanova, A. Stoyanova-Ivanova, M. Mladenov, D. Kovacheva, R. Raicheff, *Journal of Progressive Research in Chemistry*, **2**, 83 (2015) .
A. K. Stoyanova-Ivanova, S. D. Terzieva, G. D. Ivanova, M. A. Mladenov, D. G. Kovacheva, R. G. Raicheff, S. I. Georgieva, B. S. Blagoev, A. J. Zaleski, V. Mikli, *Bulg. Chem. Commun*., **47**, 41 (2015).
13. R. Raicheff, M. Mladenov, L.Stoyanov, N. Boshkov, V. Bachvarov, *Bulg. Chem. Commun*., **48**, 61 (2016).

ЕЛЕКРОХИМИЧНИ ИМПЕДНАСНИ ИЗСЛЕДВАНИЯ НА ВИСОКО ТЕМПЕРАТУРНИ СВРЪХПРОВОДИМИ КЕРАМИКИ ОТ ВИДА YBCO И BSCCO В ПРИСЪСТВИЕ НА ЕЛЕКТРОЛИТИ

П. А. Лилов[1], А. Ю. Васев[1], Л. З. Стоянов[2], Й. Г. Маринов[1], А. К. Стоянова-Иванова[1*]

[1] *Институт по физика на твърдото тяло, Българска академия на науките, бул. "Цариградско шосе" 72, София 1784, България*

[2] *Институт по електрохимия и енергийни системи "Академик Евгени Будевски", Българска академия на науките, ул. "Акад. Георги Бончев", бл. 10, София 1113, България.*

(Резюме)

Електрохимичните изследвания на високотемпературни свръхпроводници (ВТСП) започват непосредствено след тяхното откриване, като от тогава са проведени многобройни изследвания върху йонния транспорт в тях, с цел приложението им за електроди. Подходите за изследване на ВТСП се базират основно на аналогии с електрохимичните изследвания на полупроводниците поради това, че повечето от тях проявяват полупроводникови свойства при стайна температура. Тази аналогия е стимулирала проучвания на тяхната деградация в кисели и неутрални водни среди и сравнителната им стабилност в силно алкални разтвори. В последно време ВТСП намират приложение и като добавка в състава на цинковия електрод в никел-цинкови батерии. Тези батерии са пересперктивен кандидат за замяна на токсичните никел-кадмиеви батерии. Електрохимични тестове показват, че Ni-Zn клетки с добавки от YBCO и BSCCO свръхпроводящи керамики в масата на цинковия електрод, показват повишен специфичен капацитет и по-голяма стабилност на капацитета, при голям брой цикли на зареждане и разреждане Настоящото изследване се фокусира върху електрохимичното характеризиране на нанокомпозитни проводящи купратни керамики от вида $Bi_2Sr_2CaCu_2O_x$ (BSCCO - 2212), $Bi_2Sr_2CuO_y$ (BSCO - 2201) и $YBa_2Cu_3O_x$ (YBCO - 123) в следните електролитни разтвори: 7M KOH - електролит използван в Ni-Zn батериите, алкален фосфатен (AF) електролит - съдържащ KOH и $Na_3PO_4.12H_2O$ и специализиран PSPAA електролит. Проводимостта на системата керамика/електролит е изследвана чрез използване на електрохимична импедансна спектроскопия, проведени с потенциостатична система Bio-logic SP-200. Импеднасните характеристики на керамиките в различните електролити са сравнени и обсъдени посредством предложени еквиваленти електрохимични схеми. Предложен е модел, описващ елементите на електричната верига и са получени стойностите на параметрите, посредством апроксимиране на спектралните криви. Измерените електрически съпротивления на купратните свръхпроводими керамики от вида BSCO 2201 и YBCO показват относително ниски стойности. Поведението на BSCO 2201 и BSCCO 2212 силно зависи от състава на електролита. Резултатите показват, че от трите изследвани керамики, BSCO 2201 е с най ниско съпротивление и е най-подходяща за проводима добавка към цинковия анод в никел-цинковите батерии.

Ключови думи: електрохимичен импеданс, HTSC керамики, BSCCO, YBCO

Key parameters determining the performance of lithium sulfur batteries

P. Półrolniczak*, M. Przybylczak, K. Wasiński, M. Walkowiak

Institute of Non-Ferrous Metals, Division in Poznań, Central Laboratory of Batteries and Cells, Forteczna 12, 61-362 Poznań, Poland

Lithium sulfur battery is a promising electrochemical system offers high energy density of 2500 Wh kg^{-1}, which is almost five folds higher than those of state-of-art Li-ion batteries. However, commercialization of Li/S batteries still cannot be realized due to many problematic issues, such as poor electronic conductivity of sulfur, solubility of lithium polysulfides in organic electrolytes and the use of highly reactive metal lithium as anode. In this paper we discuss key parameters, in particular carbon/sulfur ratio, carbon porosity, sulfur loading and electrolyte volume, which impact the battery performance. We found that increasing the carbon content in the sulfur cathode from 20 to 40% resulted in 30% capacity improving of the Li/S battery. The optimized sulfur loading was found to be 2.2 mg S per cm^{-2} and electrolyte volume should not be lower than 75 µl per mg of sulfur.

INTRODUCTION

Lithium-ion batteries since their first commercialization of more than 20 years ago have dominated the market of chemical power sources for portable electronic devices [1-3]. However, the limited energy density and the theoretical capacity of the Li-ion battery and the growing demand and requirements of the market forces searching for other solutions.

Metallic lithium with the lowest density and the highest theoretical capacity (3861 mAh g^{-1}) is considered the best anode material. The elemental sulfur with a theoretical capacity of 1673 mAh g^{-1} appears to be preferred opposite electrode for lithium. Lithium-sulfur battery can potentially reach energy density of 2 500 Wh kg^{-1}, which is up to five times higher compared to lithium-ion batteries [4-6]. Low cost, non-toxicity and the natural abundance of sulfur in the environment is also conducive to the growing interest of the scientists. Nevertheless, there are still several major issues facing rechargeable Li-S batteries that impede their practical application, which include: low charging efficiency, poor cyclic stability and high self-discharge rate [7]. Disadvantages of Li-S batteries result from a number of reasons. Sulfur has a poor electrical conductivity, and therefore composing the cathode a large amount of conductive additive has to be added, which reduces the amount of sulfur itself and reduces the energy density of the cell. The second major problem is the solubility of lithium polysulfides formed during the electrode reaction in organic electrolytes

and their migration towards the anode, wherein further reaction of lithium leads to the formation of insoluble and non-conducting Li$_2$S and Li$_2$S$_2$. These polysulfides are accumulated at the anode causing the corrosion and polarization, and thus reduce the amount of the cathode active material [8-10].

In our study the influence of key parameters on the performance of Li-S batteries has been investigated. The impact of active material content, coating thickness and type of carbon additive on the specific capacity and cycle stability of the Li-S batteries have been studied. Different electrolyte composition has been proposed and tested towards polysulfides dissolution and Li-S batteries performance.

EXPERIMENTAL

The sulfur/carbon cathode composites were prepared by manually mixing elemental sulfur and carbon in different weight ratios in an agate mortar. The S/C mixture was dispersed in sodium carboxymethyl cellulose aqueous (Sigma Aldrich) solution to form a slurry which was subsequently casted onto Al foil as a current collector. The resulting cathodes were dried at 60°C under vacuum for 24 h. The cathodes were assembled in an argon-filled glove box (MBraunLABstar) in Swagelok-type cells with metallic lithium as the anode and Celgard 2400 as the separator. The electrolyte was a solution of lithium trifluoromethanesulfonate (0.5 M, Sigma Aldrich) and of LiNO$_3$ (0.5 M, Fluka) in a 1:1 mixture of 1,2-dimethoxyethane (DME, Sigma Aldrich) and 1,3-dioxolane (DOL, Sigma Aldrich).

---

* To whom all correspondence should be sent.
E-mail: paulina.polrolniczak@claio.poznan.pl

The cells were galvanostatically charged/discharged at a current density of 0.005, 0.05, 0.1, 0.5 and 1 C between 1.7 and 2.7 V vs. Li/Li$^+$. Cyclic voltammetry experiments were carried out at the scan rate of 0.05 mV s^{-1} also between 1.7 and 2.7 V. All electrochemical measurements were carried out using multi-channel VMP3 potentiostat/galvanostat (Bio-Logic).

RESULTS AND DISCUSSIONS

Sulfur has poor electronic conductivity thus it needs to be blended with a conducting agent, e.g. carbon black. High sulfur content in the cathode favors high energy density, however, too low carbon amount in the cathode will lead to the formation of electrically isolated islands in the electrode [11]. It is crucial to have a balanced carbon to sulfur ratio in the cathode. The performance of Li-S batteries using S/C cathode with different S/C ratio is shown in Fig. 1. The Li-S battery with cathode composed of 70% of elemental sulfur and 20% of carbon black delivered 450 mAh g^{-1} in the first cycle at 0.05 C and the capacity decreases in the next 10 charge/discharge cycles. As the carbon content was increased to 40%, the capacity in the first cycle at 0.05 C increases to 580 mAh g^{-1}. The cyclic stability was also improved. Higher carbon content (above 50%) leads to obtain electrodes mechanically unstable.

High capacity and good cycling life of Li-S batteries depends also on the structure, surface area and pore size diameter of the carbon added to the sulfur cathode. Following the first sulfur-carbon composite proposed by Wang et al.[12], and further work of Nazar's group [13], the approach was adopted by various groups, and new research avenues were opened, based on the concept of sulfur confinement inside a porous carbon structure. This strategy was the most studied one during last four years, since it was believed to solve both issues simultaneously, drastically improved high rate cyclability due to enhanced electronic conductivity and inhibited polysulfides migration due to confinement of sulfur and adsorption properties of carbon [14-16].
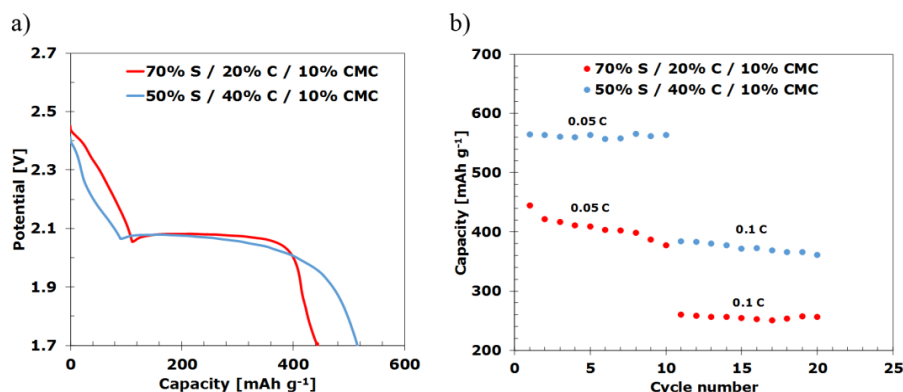
Fig. 1. a) Galvanostatic charge/discharge profiles of first cycle in the voltage window of 1.7-2.7 V at 0.05 C of S/C cathode with different S/C ratio, b) rate capability of S/C cathode with different S/C ratio

Three different carbons, depending on their porosity, were utilized as sulfur cathode component: carbon black, CMK-3 ordered mesoporous carbon and humic acid-derived mesoporous carbon (HAMC). CMK-3 and HAMC carbons have been synthesized according to procedures published elsewhere [17]. The carbon content in the cathode was 40% wt. The initial discharge profiles and cycling performance of S/C cathode with abovementioned carbons are shown in Fig. 2. The sulfur cathode with carbon black which is non-porous material with low surface area delivers capacity of about 550mAh g^{-1} in the first discharge and the capacity significantly decreases with the next charge/discharge cycles. Surprisingly, sulfur cathode with CMK-3 carbon, which is ordered mesoporous carbon with high specific area similar to HAMC carbon (see Table1), exhibits lower capacity of about 600 mAh g^{-1} in comparison to 880 mAh g^{-1} obtained for cathode with HAMC carbon. Such difference of electrochemical performance among S/CMK-3 and S/HAMC cathodes can be ascribed to the difference of pore size diameter and mesoporous structure perfection. Apparently, short range order with a significant amount of structural imperfections may favor faster mass transfer kinetics. Also relatively large pore diameter observed for HAMC (7.6 nm, in contrast with 3.8 nm for CMK-3) can facilitate sulfur species accommodation and release.
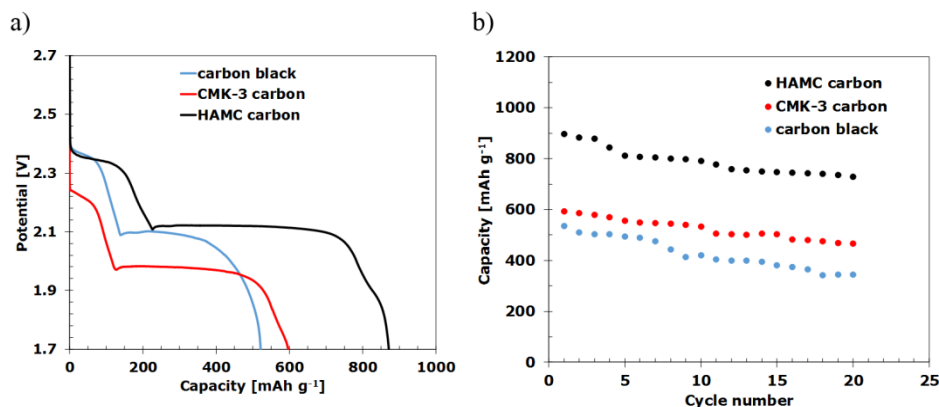
Fig. 2. a) Galvanostatic charge/discharge profiles of first cycle in the voltage window of 1.7-2.7 V at 0.05 C of S/C cathode with different carbon, b) cycling stability of S/C cathode with different carbon.

Table 1. Porosity data of different carbon materials used in sulfur cathode.

Carbon	Surface area [m²/g]	Pore diameter [nm]
HAMC	670	7.6
Carbon black	45	Non-porous
CMK-3	740	3.8

The active material loading in electrode significantly impacts the energy density of an electrode. To improve energy density, the loading of sulfur and/or thickness of electrode can be increased. Sulfur/carbon black composites electrodes with different sulfur loadings were prepared using doctor-blade coating by changing blade thickness. Such obtained electrodes had increasing coating thicknesses (8, 16, 24, 28 μm), linearly proportional to the sulfur loadings (0.9, 1.7, 2.2, 2.7 mg S cm^{-2}). The initial discharge profiles for S/C cathode with different sulfur loadings are displayed in Fig. 3 a). When the sulfur loading was increased from 0.9 to 2.2 mg cm^{-2}, the capacity per unit mass of sulfur was improved, from 541 mAh g^{-1} to 752 mAh g^{-1}. But further increase of sulfur loading, to 2.7 mg cm^{-2} resulted in a sharp capacity fade (394 mAh g^{-1}). The corresponding areal capacities at varied sulfur loading are calculated to be 0.49 mAh cm^{-2} (0.9 mg cm^{-2}), 1.02 mAh cm^{-2} (1.7 mg cm^{-2}), 1.65 mAh cm^{-2} (2.2 mg cm^{-2}) and 1.06 mAh cm^{-2} (2.7 mg cm^{-2}), respectively (Fig. 3 b). The cyclic stability of S/C cathodes with different sulfur loadings is presented on Fig. 3 c. The main problem with high loaded electrodes is the mechanical stability of the electrode. Thicker films from composite of sulfur and carbon are

brittle and tend to peel off from Al current collector. The second explanation of capacity fade in high loaded cathodes is the lithium polysulfides diffusion issue [18]. High loaded cathodes are thick and the polysulfides anions formed during discharge are unable to effectively diffuse out of the electrode. As a result, polysulfides anions stay on the carbon surface and isolate the remaining sulfur from the contact with carbon.
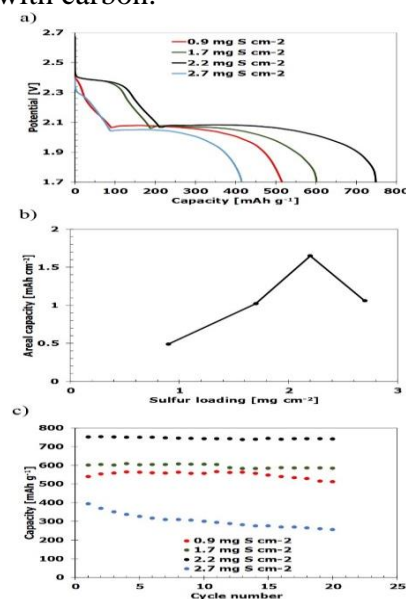
Fig. 3. a) Initial discharge voltage profile, b) areal capacity vs. sulfur loading curve, c) cycling performance of S/C cathode with different sulfur loading.

Electrolyte volume is another important parameter determining energy density and capacity of lithium-sulfur battery. Larger volume of the electrolyte better wet the electrode and dissolves more lithium polysulfides, but the brought-in drawback is the decrease of the energy density. The effect of the electrolyte volume on the capacity and cyclic stability is presented on Fig. 4. It can be seen that as the electrolyte volume was increased from 25

to 75 µl/mg S, the capacity increases from 115 to 500 mAh g^{-1}. As the electrolyte volume was further increased to 125 µl/mg S, the increase in capacity slowed down.
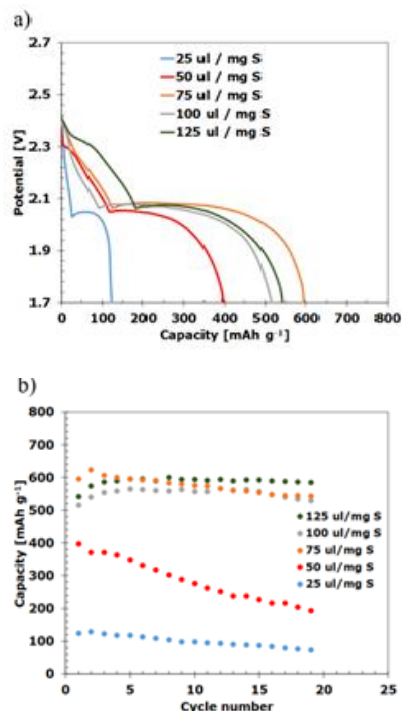
Fig. 4. a) Galvanostatic charge/discharge profiles of first cycle in the voltage window of 1.7-2.7 V at 0.05 C of S/C cathode with different electrolyte volume, b) cycling stability of S/C cathode with different electrolyte volume.

CONCLUSIONS

The performance of a Li-S battery is affected by multiple parameters such as electrolyte volume, carbon/sulfur ratio and sulfur loading, as well as the choice of carbon source. The development of a fully functional Li-S battery is a complex challenge to research and technology, and requires simultaneous optimization of a number of important parameters. At present, many problems remain unresolved, despite intense efforts and the work carried out around the world.

REFERENCES

1. V. Etacheri, R. Marom, R. Elazari, G. Salitra, D. Aurbach, *Energy Environ. Sci.*, **4**, 3243 (2011).
2. J.B. Goodenough, Y. Kim, *Chem. Mater.*, **22**, 587 (2010).
3. B. Scrosati, J. Garche, *J. Power Sources*, **195,** 2419(2010).
A. Manthiram, Y. Fu, S.-H.Chung, Ch. Zu, Y.S. Su, *Chem. Rev.*, **114**, 11751 (2014).
4. L. Chen, L.L. Shaw, *J. Power Sources*, **267**, 770 (2014).
5. R.M. Dell, *Solid State Ionics*,**134**,139 (2000).
6. W. Kang, N. Deng, N., J. Ju, Q. Li, D. Wu, X. Ma, L. Li, M. Naebe, B. Cheng, *Nanoscale*, **8**, 16541 (2016).
7. N. Ding, S.W. Chien, T.S.A. Hor, Z. Liu, Y. Zong, *J. Power Sources*, **269**, 111 (2014).
8. C. Barchasz, J.-C.Leprêtre, F. Alloin, S. Patoux, *J. Power Sources*,**199**, 322 (2012).
9. J. Scheers, S. Fantini, P. Johansson, *J. Power Sources*, **255**, 204 (2014).
10. Y. V. Mikhaylik, J. R. Akridge, *J. Electrochem. Soc.*,**151**, A1969 (2004).
11. J. Wang,L. Liu, Z. Ling, J. Yang, C. Wan, C. Jiang, *Electrochim. Acta*,**48**, 1861 (2003).
12. X. Ji, K.T. Lee, L.F. Nazar, *Nat. Mater.*,**8**, 500 (2009).
13. M. Rao, W. Li, E.J. Cairns, *Electrochem. Commun.*,**17**, 1 (2012).
14. T. Zeng, X. Hu, P. Ji, G. Zhou, *Solid State Ionics*, **291**, 47 (2016).
15. J.-S. Parl, G.-B.Cho, H.-S.Ryu, J.-H.Ahn, H.-J.Ahn, K.-W. Kim, *Mater. Tech.*, **28**, 270 (2013).
16. P. Półrolniczak, K. Wasiński, M. Walkowiak, *Int. J. Electrochem. Sci.*,**10**, 9370, (2015).
17. S.S. Zhang, *Energies*, **5**, 5190 (2012).

ОСНОВНИ ПАРАМЕТРИ, ОПРЕДЕЛЯЩИ ЕФЕКТИВНОСТТА НА ЛИТИЕВО-СЕРНИ БАТЕРИИ

П. Пулролничак, М. Пшибилчак, К. Васиньски, М. Валковиак

Институт за цветни метали, отдел в Познан, Централна лаборатория за батерии и клетки, 61-362 Познан, Полша

(Резюме)

Литиево - сярната батерия е обещаваща електрохимична система, която предлага висока енергийна плътност от 2500 Wh kg^{-1}, което е почти пет пъти по-висока от тази на най-съвременните литиево-йонни батерии. Въпреки това, комерсиализацията на Li/S батерии все още не може да се осъществи поради съществуващи проблеми, като лошата електропроводимост на сярата, разтворимостта на литиевите полисулфиди в органичните електролити и използването на високо реактивен метален литий като анод. В тази статия са дискутирани основните параметри, по-специално съотношението въглерод/сяра, въглеродната порьозност, съдържанието на сяра и обема на електролита, които оказват влияние върху ефективността на батерията. Установено е, че увеличаването на количеството въглерод в серния катод от 20 до 40% води до подобряване на капацитета на Li/S батерия с 30%. Оптимизираното съдържание на сяра е 2,2 mg на S cm^{-2}, като обемът на електролита не трябва да бъде по-малък от 75 μl на mg сяра.

Ключови думи: литиево - сярна батерия, серен катод, активен въглен, електрохимични характеристики.

Lithium ion batteries: active electrode materials based on manganese dioxide

K. Banov[1,2], D. Ivanova[2], L. Fachikov[2], V. Kotev[4], T. Stankulov[1], B. Banov[*1,3]

[1] *Institute of Electrochemistry and Energy Systems, IEES, 1, Acad. G. Bonchev str., bl. 10, 1113 Sofia*
[2] *University of Chemical Technology and Metallurgy – UCTM, bul. "Kl. Ohridski" 8, 1756 Sofia*
[3] *European Polytechnical University – EPU, 23, "St. St. Cyril and Methodius" str., 2300 Pernik*
[4] *Institute of Mechanics, IM, 1, Acad. G. Bonchev str., bl. 4, 1113 Sofia*

Lithium cobaltate used in commercial rechargeable lithium ion batteries possesses good cyclability, high discharge potential and acceptable energy density. Its synthesis is easy and can be realized on a large industrial scale. However, the price of cobalt is very high and determines the end user price of the lithium battery. Cobalt and its oxides are very toxic. Lithium manganese dioxide spinel combines high specific energy density – volumetric and gravimetric, high coulomb efficiency - close to the theoretical one, long cycle life. It is non-toxic, environmentally friendly and with low cost but possesses some disadvantages as low starting capacity and low stability at elevated temperatures. Optimising the synthesis methods and elucidating the factors influencing the electrochemical stability, we have obtained manganese dioxide spinel, which is very attractive and prospective cathode material for large scale application. Cathode materials based on manganese dioxide spinel with high coulomb efficiency close to 90%, discharge rates of 4C and cycle life up to 1000 cycles are presented.

Keywords: Lithium ion batteries, Manganese dioxide spinel, Elevated temperatures stability

INTRODUCTION

Commercially available rechargeable lithium batteries refer to the Li-Ion battery, which uses carbon powder as negative active electrode material and lithiated metallic oxides as cobaltate and nickelate for positive active electrode material. For the moment only $LiCoO_2$ (lithium cobaltate) is present at the market as positive electrode material. However, the cost of this material is so high that it would take up too much of the battery cost and besides, its specific energy density is not the highest, therefore, it may be replaced by the concurrent $LiNiO_2$. The price of $LiNiO_2$ (lithium nikelate) is less because of the highest specific gravimetric capacity but it is difficult for synthesis and treatment. Both materials are not environmentally friendly.

Thus the nearest future is devoted to the development of positive electrode materials with the following features:

- High specific energy density – volumetric and gravimetric;
- Improved coulomb efficiency close to the theoretical one;
- Cycle life, meeting the requirements;
- Easy for synthesis and treatment;
- Non-toxic and environmentally friendly;
- Low cost.

There is only one group of candidates that can meet these requirements - cathode materials based on manganese dioxide working in the 3 and 4 volts range.

The success of lithium batteries in the last 20 years is due to their big advantages over classical electrochemical systems as high specific energy density, stable and flat discharge profile, long storage life and wide operating temperature range.

Electrode components – general assumptions

The electrochemical parameters of lithium battery electrodes depend on the active mass (AM) and applied technology. Twenty years ago our lab (IEES former CLEPS) successfully developed a dry technique for electrode preparation [1, 2]. The electrode typically consists of active electrode materials (AM) mixed with electronic conductor and some amount of polymer playing the role of binder. The ratio between all above-mentioned compounds in general is as follows: 80% active electrode material (AM), 10% electronic conductor – graphite for example and 10% PTFE as a binder. We use preliminary prepared mixture of acetylene black and PTFE transformed in the so-called Teflonized Acetylene Black (TAB-2). The abbreviation TAB-2 denotes the content of PTFE in the dry mixture (typically 5%). In this way the test electrodes consist of 85% AM and 15% CB. Reduction in the content of PTFE is very important especially from a practical point of view.

The main factor for the electrochemical behavior of AEM in use is the stoichiometry and the purity of the used compounds: cobaltate, nickelate and manganese dioxide spinel. The particles size together with porosity and micro and macro pore distribution plays a decisive role for the electrochemical features [3, 4, 5]. A summary of the chemical and physicochemical properties for an improved active electrode material is given below.

Chemical characteristics

• Chemical formula - $LiCoO_2$, $LiNiO_2$, $LiMn_2O_4$ - strict stoichiometry;
• Purity of active electrode material (avoiding impurities generated during the synthesis process, which deteriorate the electrochemical performance);
• Correctly selected starting chemical compounds (including purity grade);
• Appropriate thermal treatment & gas atmosphere;
• Modification of the basic structure with the aim to improve some characteristics: thermal stability, enhanced lithium diffusion coefficient, cycleability.

Physico-chemical properties

• Specific Surface Area SSA (the higher the SSA, the lower the polarization), higher delivered capacity, improved reversibility and longer cycle life;
• Particles size - nanoparticles - balance of size depending on the specific application (the smaller the particles size the higher the discharge rate but delivered capacity is lower);
• Porosity of the particles and pore distribution - suitable micro- and macro pore ratio;
• Conductive binder ensuring an appropriate porosity and suitable electronic conductivity.

MANGANESE DIOXIDE SPINEL

During the last 10 years a high-energy demand has existed at the lithium battery market. Lithium cobaltate and lithium nickelate have successfully found a niche in this growing market. Some non-toxic, environmentally friendly, low cost candidates with specific energy density close to 450 Wh g^{-1} are under intensive investigation for replacement of the cathode materials based on Ni and Co. Lithium manganese spinel $LiMn_2O_4$ is very attractive and prospective cathode material, combining the advantages to be non-toxic, environmentally friendly, with low cost and theoretical specific energy density of 475 Wh g^{-1} [3, 6-8]. It has been under investigation since the beginning of the new century, but displays the big disadvantage of premature capacity loss especially at elevated

temperature – over room temperature (RT) [9-11, 13, 15-17].

The same problem exists also in regard to cathode materials based on lithiated nickel and cobalt oxides, however, less pronounced.. Various authors have proposed two different solutions to the problem, which can be summarized in three directions:

• *Increased lithium content in the initial structure, the so-called overlithiated manganese dioxide spinel;*
• *Modification of the manganese dioxides spinel with foreign ions*

The main instability of $LiMn_2O_4$ is due to the so-called Mn^{3+} disproportion described by the equation:

$$2Mn^{3+} = Mn^{4+} + Mn^{2+}_{(sol)}$$
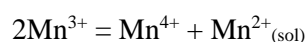
The increased lithium content in the overlithiated manganese dioxide spinel of $Li_{1+x}Mn_{2-x}O_4$ type stabilizes the crystal structure and suppresses the dissolution of Mn^{3+}. This reflects in increased stability during cycling at elevated temperatures. However, the gain in cycleability is accompanied by diminishing of the delivered reversible capacity of the material.

The next option is to substitute small amount of Mn^{3+} ions by another ion. Some authors [9-16] propose stabilization of the structure by partially replacing Mn^{3+} ions by Ni or Co ones. We have also piled up experience in this regard. The obtained stability of Co doped spinel with chemical formula $LiCo_{0.1}Mn_{1.9}O_4$ is excellent during long term cycling at room temperature [7, 18-21] but is not satisfactory at elevated temperatures. This substitution can also be performed using Mg. The result is improved cycleability but reduced initial reversible capacity.

OVERLITHIATED MANGANESE DIOXIDE SPINELS

Manganese dioxide spinels of the type $Li_{1+x}Mn_{2-x}O_4$ $(0.01 < x < 0.15)$ with increased Li content.

Expected results:
• Starting capacity 100 mAh g^{-1} (65% Q_{th}) - 135mAh g^{-1}(90% Q_{th});
• Cycleability of 300 cycles at RT (up to 50% from the initial capacity);
• Improved cycleability at elevated temperatures (55°C).

The overlithiation of manganese dioxide spinel is the simplest way to increase the stability of the active electrode material at elevated temperatures. We have prepared a series of overlithiated

manganese dioxide and subjected it to high temperature tests (Table 1). As it was already mentioned, this approach offers reduced reversible capacity in the beginning but the cycle life is improved significantly. The capacity fade at room temperature (RT) decreased from 0.4% to 0.032% per cycle – more than ten times. On the other hand the starting delivered capacity was reduced from 135 mAh g^{-1}, to 101 mAh g^{-1}. The capacity fade at elevated temperatures (55ºC) starts form 1.3% (three times higher than at RT) per cycle and drops to 0.067%, which is very close to the value displayed at RT for the spinel with chemical formula $Li_{1.11}Mn_{1.89}O_4$. The graphical presentation of the capacity changes at long term cycling for the investigated overlithiated samples is given in Fig. 1.

Taking into account the so-called "accumulated capacity" the best choice would be the sample "IEES", because the accumulated capacity, graphically represented by the area limited by the cycling curve is the biggest one.
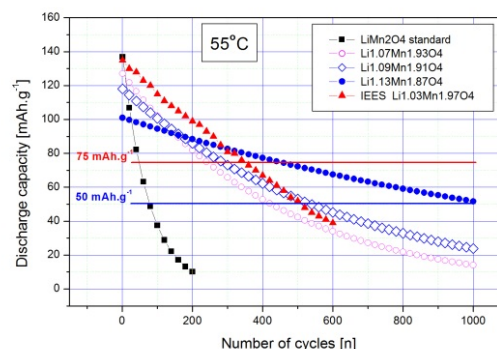
Fig. 1. Discharge capacity at long term cycling of overlithiated $Li_{1+x}Mn_{2-x}O_4$ samples at 55ºC

If the cycle life is set to 1000 cycles, the leader would be the sample with chemical formula $Li_{1.13}Mn_{1.87}O_4$. For middle cycle life (for example 400 cycles), there is no best choice, because all tested samples offer nearly the same accumulated capacity, excluding the spinel with maximum lithium content - $Li_{1.13}Mn_{1.87}O_4$.

Table 1. Theoretical and observed capacity dependence on extra lithium content in manganese dioxide spinel

Spinel Formula $Li_{1+x}Mn_{2-x}O_4$	RT Initial Capacity, [mAh g^{-1}]	Fade %/cycle at 50th cycle	55º C Initial Capacity, [mAh g^{-1}]	Fade %/cycle at 50th cycle	(a) [Å]
Standard $LiMn_2O_4$	135	0.4	135	1.300	8.248
$Li_{1.02}Mn_{1.98}O_4$	123	0.11	134	0.770	8.243
$Li_{1.05}Mn1_{.95}O_4$	121	0.11	133	0.450	8.235
$Li_{1.07}Mn_{1.93}O_4$	121	0.11	120	0.290	8.228
$Li_{1.09}Mn_{1.91}O_4$	118	0.06	118	0.170	8.222
$Li_{1.11}Mn_{1.89}O_4$	101	0.05	101	0.080	8.218
$Li_{1.13}Mn_{1.87}O_4$	101	0.032	101	0.067	8.207

CONCLUSIONS

• A series of overlithiated manganese dioxide spinel $Li_{1+x}Mn_{2-x}O_4$ are successfully synthesised and tested as cathode material for prospective LIB;

• Overlithiated manganese dioxide spinel $Li_{1+x}Mn_{2-x}O_4$ with different overlithiation ratios are suitable for different applications;

• There are no universal overlithiated active electrode materials solving all customer requirements without any compromise;

• Different approach for each specific application is needed;

Overlithated samples tested present very good and promising cycleability at elevated temperature.

SUBSTITUTED MANGANESE DIOXIDE SPINEL

Manganese dioxide spinels of the type $LiMe_xMn_{2x}O_4$ (0.01<x<0.20) modified with Mg ions.

Expected results

• Starting capacity 100 mAh g^{-1} (65% Q_{th}) – 120 mAh g^{-1} (80% Q_{th});

• Improved thermal stability & electrochemical characteristics;

• Improved cycleability up to 700 cycles;

• Target: batteries for EV&HEV.

The advantages of doping with foreign ions are investigated on manganese dioxide spinel $LiMg_{0.05}Mn_{1.95}O_4$, i.e. the selected doping ion is Mg. Based on our previous investigations, lithium acetate and manganese carbonate have been chosen as lithium and manganese source, and magnesium nitrate - as Mg doping agent ($CH_3COOLi.2H_2O$, $MnCO_3$, $Mg(NO_3)_26H_2O$). These initial compounds are not widely used in lithium manganese spinel preparation. The optimal conditions to obtain a high quality active cathode material for lithium batteries

operating in the 4 volts region are published in [1, 3, 19-21].

Experimental

The newly proposed method of synthesis is based on two different techniques: impregnation and decomposition inside the particle. $MnCO_3$ with mean particle size about 20 μmis chosen as starting compound and manganese source [2, 3, 6, 7,]. Magnesium nitrate is introduced in the reaction composition as an aqueous solution. The manganese carbonate is well soaked with the magnesium nitrate. After drying and good mixing, lithium acetate is introduced and the mixture is again dried at temperature of 120ºC. The real synthesis starts with a thermal pretreatment at 250ºC for 24h. The temperature is selected according to the decomposition temperatures of $Mg(NO_3)_26H_2O$ and $CH_3COOLi.2H_2O$. During the initial thermal pretreatment at relatively low temperature (about 120ºC) the composite mixture is subjected to impregnation by the lithium acetate and magnesium nitrate. The final thermal decomposition of manganese carbonate/lithium acetate/ magnesium nitrate takes place at high temperatures (750ºC). Doped llithium manganese spinel with high purity and perfect crystal structure has been obtained as a result of this synthesis. The XRD of thus prepared samples is presented on Fig. 2a. It can be seen no difference in the XRD patterns of pure ($LiMn_2O_4$) spinel and substituted one ($LiMg_{0.05}Mn_{1.95}O_4$). This is due to the occupation of 16(d) places by the Mg ions. For comparison apure manganese spinel is synthesized by standard solid-state procedure. Chemical manganese dioxide (CMD) with high purity and high specific surface area (SSA) about 100 m^2 g^{-1} and lithium acetate $CH_3COOLi.2H_2O$ are mixed in an appropriate molar ratio 2:1 [4, 5, 8]. The medium particle size of the used MnO_2 is about 100 μm. Lithium acetate is chosen due to its low decomposition temperature, which is around 70ºC. Thermal pre-treatment for 24 hours at 750ºC is done. The syntheses are performed in a tube furnace with 0.5 dm^3 total volume under a constant air flow of 25 dm^3 h^{-1}. The gas flow is very important because of the generated carbon dioxide. The synthesis reaction of $LiMn_2O_4$ requires oxygen for the end product synthesis. The sample is cooled at 10ºC min^{-1} cooling rate. In both cases - with and without doping, an active cathode material with SSA (measured by the B.E.T. method) about 10 m^2 $g^{-1}$is obtained [2-4, 19-21]. The phase composition of the samples is determined by X-ray diffraction analysis using Philips APD 15 powder diffractometer with ***Cu-Kα*** radiation. The electrochemical characteristics are tested in a three-electrode glass cell with lithium reference electrode in excess of electrolyte and with a floating test electrode, described in [4, 5]. The electrolyte consists of 1M $LiClO_4$ solution in a mixture of EC:PC:DMC in 1:1:2 volume ratio. The composite test electrode material is a mixture of the investigated compounds with *Teflonized Acetylene Black*(TAB-2) [1, 3-5] at a 1:1 ratio by weight, pressed on expanded nickel grid with 15 mm diameter. The test electrodes weight is typically 50 mg without the nickel grid. To carry out the electrochemical tests a standard charge/discharge current of C/3 is applied.

Results and discussions

The XRD pattern of the manganese spinel doped with 5 atomic percent Mg is equal to those of the pure $LiMn_2O_4$, i.e. the phase of the doped spinel is also *Fd3m*. The doping agent cannot be detected on the XRD patterns sown on Fig. 1b of $LiMg_{0.05}Mn_{1.95}O_4$ spinel.
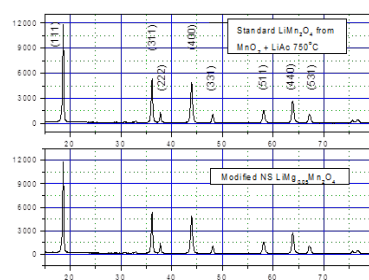
Fig. 2. XRD diagram of pure $LiMn_2O_4$ and Mg doped spinel $LiMg_{0.05}Mn_{1.95}O_4$

That confirms that Mg occupies 16(d) places. The morphology of the obtained powdered active electrode material is presented on Fig. 3.
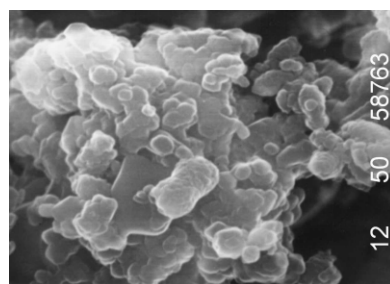
Fig. 3. SEM micrograph of $LiMg_{0.05}Mn_{1.95}O_4$ powder

The micrograph shows that the lithium spinel preserves in maximum the shape of the initial manganese source - $MnCO_3$ [8, 20-22]. The obtained doped and non-doped spinels possess specific SSA of ~ 10 m^2 g^{-1}. The combined impregnation - decomposition process leads to the formation of particles with high porosity and spherical shape. XRD and SEM micrographs show that the

preparation technique is very suitable. The charge/discharge profiles of pure $LiMn_2O_4$ active electrode material are presented in Fig. 4.
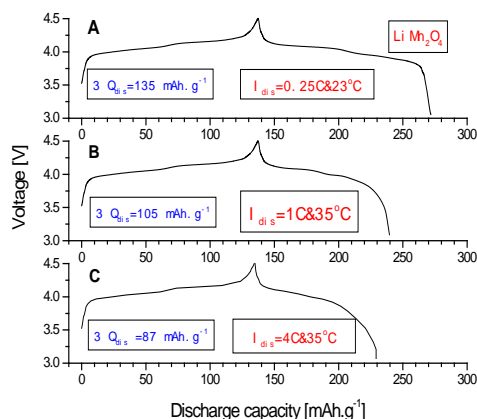
Fig. 4

Charge/discharge profiles of pure lithium manganese spinel $LiMn_2O_4$ at different temperatures and discharge rates: $0.25C/23^{o}C$; $1C/35^{o}C$ and $4C/35^{o}C$

The electrochemical tests are performed at different discharge rates and temperatures - room temperature (RT) $23^{o}C$ and elevated one $35^{o}C$, respectively. The first curve (Fig. 4A) shows the pure spinel behavior applying 4h charge/discharge $(0.25C)$rate at $23^{o}C$ (RT). Due to the high SSA of the sample (10 m^2 g^{-1}), the charge/discharge profile is very flat. The delivered capacity is 135 mAh g^{-1}. When a charge/discharge rate of 1C is applied and the temperature is increased to $35^{o}C$, the obtained capacity is 105 mAh g^{-1}. The discharge profile at high current density (4C) and $35^{o}C$ is presented inFig. 4C. In this case the exhibited discharge capacity is only 87 mAh g^{-1}. The reduction is 35% in regard to RT and about 18% against $1C/35^{o}C$. The displayed results are interesting and promising. Fig. 5 shows the charge/discharge profiles of newly prepared $LiMg_{0.05}Mn_{1.95}O_4$ active electrode material.

Three discharge/charge profiles: at 0.25C/RT, $1C/35^{o}C$ and $4C/35^{o}C$ are presented again for comparison with the pure spinel. At 0.25C rate and room temperature there is no difference in the discharge capacity due to the low discharge current and the high SSA of the sample [1-5, 19-21]. The sample exhibits capacity close to that of the pure material, which means that the very small amount of doping agent does not affect the discharge capacity. At elevated temperature $35^{o}C$ and discharge rate of 1C the delivered capacity is 122 mAh g^{-1}. The displayed reversible capacity decreases to 105 mAh g^{-1} when a high current drain and temperature are applied ($4C/35^{o}C$). Compared to the tested pure spinel, the value increases about 16% and 20%,

respectively. In all of the tests the charge current rate is kept constant (0.25C) to ensure optimal conditions for low polarization charging. The obtained results confirm our assumption that combining different techniques and starting compounds it is possible to prepare a highly efficient cathode material.
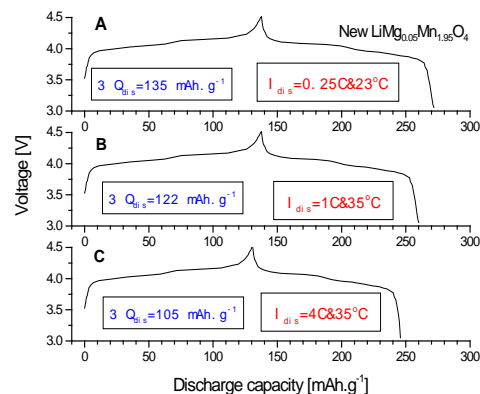
Fig. 5. Charge discharge profiles of lithium manganese spinel doped with Mg ($LiMg_{0.05}Mn_{1.95}O_4$) at different temperatures and discharge rates: $0.25C/23^{o}C$, $1C/35^{o}C$ and $4C/35^{o}C$

Conclusions

• $LiMg_{0.05}Mn_{1.95}O_4$ is successfully synthesised as cathode material with improved stability at elevated temperatures;

• A very high rate (4C) active electrode material ($LiMg_{0.05}Mn_{1.95}O_4$) for lithium batteries is obtained by our cathode preparation technique;

• The overall efficiency of $LiMg_{0.05}Mn_{1.95}O_4$ is enhanced by 20% at high rate (4C) and elevated temperature ($35^{o}C$);

• Combining different techniques of preparation and modification, it is possible to prepare highly efficient, environmentally friendly cathode material with high charge and discharge rates at elevated temperatures.

ELECTROCHEMICAL BEHAVIOUR OF $LIMN_2O_4$ ACTIVE ELECTRODE MATERIAL IN THE 3 VOLTS REGION

The lithium manganese spinel $LiMn_2O_4$ possesses twodischarge plateaux, at 4 volts and at 3 volts one. So far the efforts of R&D has been oriented to improve the discharge capacity and the cycleability of the high potential region – the 4 volts one. We have already demonstrated that it is possible to obtain $LiMn_2O_4$ with 90% (Fig. 1) of the theoretical capacity in the 4 volts region during long term cycling at high charge/discharge rate of C/3 [1, 3, 8]. The techniques of preparation, sol-gel or solid-state syntheses, the influence of the starting compounds on the obtained precursor and final product, and the physicochemical properties and

electrochemical behavior of the active electrode materials have been discussed 1-3, 13-16, 18-21]. The challenge is to improve the electrochemical characteristics of lithium manganese spinel $LiMn_2O_4$ working in the low potential region of 3 volts, modifying the physicochemical parameters and applying an appropriate synthesis method.

Experimental

Based on our previous investigations, lithium spinel is prepared by a new synthesis approach. The standard solid-state reaction is applied for comparison. Lithium acetate is used in both methods to avoid the influence of the starting compounds. The new synthesisis based on a two-step technique: impregnation and decomposition. The particles of manganese carbonate with average particle size of 20 μm are impregnated by lithium acetate at about 150°C. The final thermal decomposition of the manganese carbonate takes place at temperature about 550°C. Thus lithium manganese spinel is obtained at relatively low temperature [18-21]. Lithium spinel prepared at low temperature possesses low discharge capacity at 4 volt range.

Results and discussion

XRD patterns of materials prepared at 550°C and 750°C are the same, *Fd3m* space group, i.e. a spinel was successfully obtained at relatively low temperature (550°C). The pattern of the new synthesis shows only a little lower intensity of the peaks. The morphology of the obtained active electrode material powders is presented on Fig. 6. It can be seen that the lithium spinel preserves in maximum the spherical shape of the starting manganese source, the CMD Faradizer M. The SEM picture (Fig. 6 a, b) shows that the particles are built from fine nanosized needles, at 750°C Fig. 6 a and at 550°C Fig. 6 b. A small difference appears in the particles dimensions Fig.6 a, b resulting in different SSA of thus prepared samples.
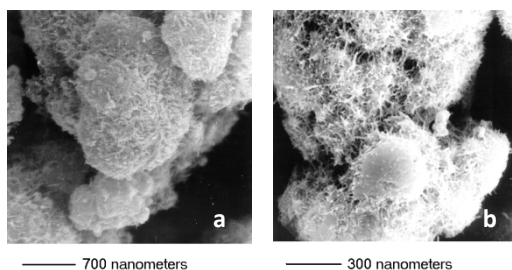
Fig. 6. SEM pictures of pure $LiMn_2O_4$ powders obtained by: (a) solid-state reaction; (b) new complex synthesis (impregnation) method

The measured SSA ($10m^2$ g^{-1}) is three times higher than that of the reference material (standard lithium spinel prepared at 550°C). The discharge profile in the 3 volts region of active electrode material prepared by the standard synthesis way (750°C) is presented in Fig.7.
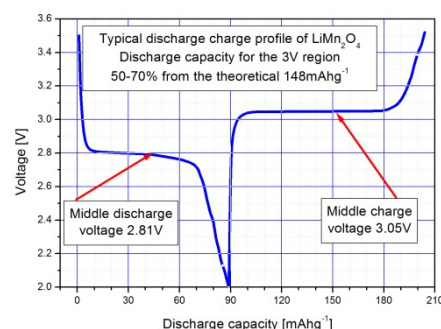
Fig. 7. Discharge/charge profile of standard lithium manganese spinel in the 3 volts region

It has capacity of 90 mAh g^{-1} with discharge plateau at 2.81 V. From theoretical point of view the plateau must be situated at 2.95 V. The observed difference is due to the discharge polarization. The charge plateau is at 3.05 V and the charge capacity is 115 mAh g^{-1}. The efficiency of the total electrochemical reaction discharge/charge is 78% and the calculated specific energy density - 253 Wh g^{-1}. In the 4 volts region the same active electrode material displays a reversible capacity of 135 mAh g^{-1} at the 3rd cycle. The cycleability in the same region is pretty good, 115 mAh g^{-1} at the 100th cycle. The discharge/charge profile of the active electrode material prepared by the new synthesis procedure is presented in Fig. 8.
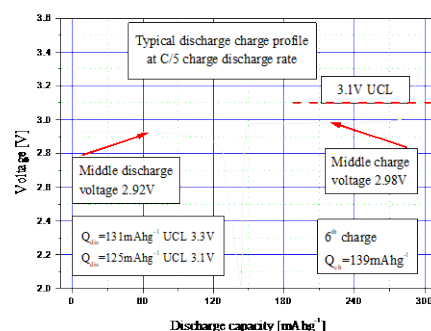
Fig. 8. Discharge/charge profile of electrode material prepared by the new complex synthesis (impregnation) method

The first difference between both syntheses is observed in the discharge plateau. It is situated at 2.92 V, a value very close to the theoretical one - 2.95 volts. The second difference is in the displayed discharge capacity-131mAh g^{-1}. Normally the capacity in the 3 V region is close to 60 % from the theoretical one, i.e. around 90 mAh g^{-1}. In our case the obtained value is 1.4 times higher. A specific

energy density of 375 Wh.g⁻¹ is achieved. The charge plateau shows reduced polarization – the middle charge voltage is 2.98 volts. The charge capacity of the new material is 139 mAh g⁻¹ with an efficiency of about 94%, a very high and attractive value. As described above (Fig. 8), its microstructure is characterized with very fine particles, which cause increase in the SSA and porosity, thus allowing more electrolyte to be in contact with the active electrode material, not only on the surface but in the whole volume. According to similar investigations [13,14], the higher SSA and porosity bring to higher discharge capacity and to lower polarization, which is in agreement with our results. They are summarized in Table 2.

Table 2. Comparison of specific capacity and coulomb efficiency of LiMn₂O₄ synthesized by different methods and LiCoO₂ as reference

Cathode material	Type material [V]	Cycling limits [V]	Theoretical capacity [mAh g⁻¹]	Practical Specific Capacity [mAh g⁻¹]			*CE* [%]
				5ᵗʰ	25ᵗʰ	50ᵗʰ	
Li₀.₃MnO₂	3	3.5-2.0	200	180	165	155	90-75
Standard LiMn₂O₄	3	3.5-2.0	148	90	75	60	60-40
New synthesis LiMn₂O₄	3	3.5-2.0	148	131	95	80	85-55
LiMn₂O₄	4	4.5-3.0	148	135	120	115	85-75
LiCoO₂	4	4.5-3.0	275	160	155	150	60-52

CE coulomb efficiency

For comparison, the electrochemical performance of other types of active electrode materials working in the 3 and the 4-volt regions are given. The obtained results show that the lithium spinel in the 3 volts region is very attractive cathode material for practical use in lithium batteries.

CONCLUSIONS

- Applying an appropriate synthesis method, the 3 volts region of LiMn₂O₄ spinel becomes very attractive for practical use, with specific energy density more than 375 Wh g⁻¹;
- The synthesis techniques and the starting precursors play preponderant role for the electrochemical behaviour of the active electrode materials;
- The charge discharge profile of the active electrode material is improved with the increasing of the SSA;
- The overall efficiency of manganese dioxide spinel working in the 3 volts region is increased up to 94% from the theoretical one.

REFERENCES
1. A. Momchilov, A. Trifonova, B. Banov, B. Puresheva, A. Kozawa, *ITE Battery Letters*, **1**, 155 (1999) .
2. B.Banov, A. Momchilov, M. Massot, C. Julien, *B-solid state materials for advanced technology*, **100**, 87 (2003).
3. V. Manev, B. Banov, A. Momchilov, A. Nassalevska, *J. Power Sources*, **57**, 99 (1995) .
4. N. Ilchev, B. Banov, *Progress in Batt. &Batt. Materials, JEC Press* **10**, 232 (1991).
5. N. Ilchev, B. Banov, *J. Power Sources*, **35,** 175 (1991).
6. S. Uzunova, B. Banov, A. Momchilov in: C. Julien, J.P. Rereira-Ramos, A. Momchilov, (Eds), *New trends in intercalation compounds for energy storage, NATO Science Series* vol. **61**, 545, Kluwar Press, 2002.
7. B. Banov, S. Uzunova, A. Momchilov, I. Uzunov in: C. Julien, J.P. Rereira-Ramos, A. Momchilov, (Eds*), New trends in intercalation compounds for energy storage, NATO Science Series* vol. **61**, 591 Kluwar Press, 2002.
8. V. Manev, B. Banov, A. Momchilov, A. Nassalevska, Proc. 9th IBA Battery Materials Symposium, Cape Town, South Africa, 20-22 March 1995, Ext. Abstr., p. 20.
9. Y.K. Sun, K.J.Hong, J. Prakash, *J. Electrochem. Soc.*, **150**, A970 (2003).
10. Y. K. Sun, Y.S.Lee, M. Yoshio, K. Amine, *Electrochem. and Solid-State Letters*, **5**, A99 (2002).
11. Y.S. Lee, Y.K. Sun, S. Ota, T. Miyashita, M. Yoshio, *Electrochem. Comm.*, **4**, 989 (2002).
12. M. S. Whittingham, P. Zavalij, *Solid State Ionics*, **131**,109 (2000).
13. H. Kurimoto, K. Suzuoka, T. Murakami, Y. Xia, H. Nakamura, M. Yoshio, *J. Electrochem. Soc.*, **142**, 2156 (1995).
14. M. Yoshio, H. Noguchi, T. Miyashita, H. Nakamura, A. Kozawa, *J. Power Sources*, **4**, 483 (1995).
15. J. Chao, Y.J. Kim, B. Park, *J. Electrochem. Soc.*, **149**, A127 (2002).
16. J. Chao, T-J. Kim, B. Park*, J. Electrochem. Soc.*, **149**, A288 (2002).
17. H. Huang, P. Bruce*, J. Electrochem. Soc.,* **141**, L76 (1994).

18. B. Banov, A. Momchilov, A. Trifonova, B. Puresheva in: C. Julien, Z. Stoynov, (Eds.), *Materials for lithium-ion batteries. Design and optimization, NATO Science Series*, Vol. **85**, 555 Kluwar Press, 2000.
19. B. Banov, Y. Todorov, A. Momchilov, V. Manev, Proc. 8th IMLB, July 1996, Nagoya, Japan, Ext. Abstr., p.452
20. B. Banov, Y. Todorov, A. Trifonova, A. Momchilov, V. Manev, *J. Power Sources*, **68**, 578 (1997).

21. Y.Todorov, C. Wang, B. Banov, M. Yoshio, ISE Annual Meeting Sept., 1997, Paris, France, Ext. Abstr. 97-18, p. 176.
A. Szatvanyi, L. Predoana, M. Zaharescu, H. Vassilchina, N. Velinova, B. Banov, A. Momchilov in: Z. Stoynov, D. Vladikova, (Eds), Proc. Ist Workshop Advanced techniques for Energy storage and Investigation, Sept., 2004, Sofia, p. P4-1.

ЛИТИЕВО ЙОННИ БАТЕРИИ - АКТИВНИ МАТЕРИАЛИ НА БАЗАТА НА МАНГАНОВИ ДИОКСИДИ

Кр. Банов [1,2], Д. Иванова [2], Л. Фачиков [2] , В. Котев [4], Т. Станкулов [1],
Бр. Банов[*] [1,3]

[1).] *Институт по Електрохимия и Енергийни Системи, ИЕЕС, ул. "Акад. Г. Бончев" Бл. 10. 1113 София*
[2)] *Химико Технологичен и Металургичен Университет, бул. "Кл. Охридски" 8, 1756 София*
[3)] *Европейски Политехнически Университет, ЕПУ, ул. "Св. Св. Кирил и Методи" N:23, 2300 Перник*
[4)] *Институт по Механика, ул. "Акад. Г. Бончев" N:1, Бл. 4. 1113 София*

(Резюме)

Литиевият кобалтат използван в болшинството комерсиални литиево йонни акумулаторни батерии притежава добра циклируемост, висок разряден потенциал и приемлива плътностна енергията. Лесно се синтезира и може да бъде изготвян в големи индустриални количества. За съжаление цената на кобалта расте с непредвидими темпове, а тя е определяща в основната си част за цената на крайния продукт – литиево йонната батерия. Кобалтът, както и неговите оксиди са изключително токсични. Литиево мангановодиоксидния шпинел притежава, висока специфична енергийна плътност, тегловна и обемна, както и висока Кулонова ефективност, близка до теоретичната и дълг цикличен живот. Той не е токсичен, екологично приемлив, с ниска цена, но притежава и някои недостатъци, като нисък начален разряден капацитет и понижена стабилност при повишена температура. Оптимизирайки методите на синтез и вниквайки в дълбочина на факторите, влияещи върху електрохимическата стабилност, успешно е изготвен литиран маганово диоксиден шпинел, който е много привлекателен и перспективен катокатоден материал за широко индустриално използване. В това изследване е представен успешно синтезиран и изследван катоден материал на основата на манганово диоксиден шпинел с висока Кулонова ефективност близо до 90% спрямо теоретичната, работещ в режим от 4С и показващ стабилна циклируемост от повече от 1000 цикъла.

Ключови думи: литиево йонни батерии, манганово диоксиден шпинел, стабилност при повишена температура.

High voltage cathode materials based on lithium cobaltate with nickel and manganese doping

K. Banov[1,2], T. Petkov[2], R. Boukoureshtlieva[1], D. Ivanova[2], L. Fachikov[2], V. Kotev[4,] B. Banov[*][1,3]

[1]*Institute of Electrochemistry and Energy Systems, IEES, Acad. G. Bonchev str., bl. 10, 1113 Sofia*
[2]*University of Chemical Technology and Metallurgy – UCTM, bul. "Kl. Ohridski" N:8, 1756 Sofia*
[3]*European Polytechnical University – EPU, 23, "St. St. Cyril and Methodius" str., 2300 Pernik*
[4]*Institute of Mechanics, IM, 1,Acad. G. Bonchev str., bl. 4, 1113 Sofia*

Doped lithium cobaltates $LiCo_{1-y}M_yO_2$ (M = Mn, Ni, y = 0.1, 0.3, 0.5) have been prepared by low temperature solid-state reaction. The structure of the samples was characterized by X-ray diffraction (XRD). The specific surface area (SSA) of the materials was examined by B.E.T. method. The synthesized powders were found to have rhombohedral structure, except for $LiCo_{0.5}Mn_{0.5}O_2$, which crystallises with cubic spinel-like structure (space group Fd3m). The electrochemical performances of the compounds were studied by galvanostatic cell cycling in the high-voltage range between 3.0 and 4.8 V vs. Li/Li⁺ electrode. It was shown that the type and the amount of the doping element greatly affect the structure, electrochemistry and cycle life characteristics of the investigated materials. $LiCo_{0.9}Mn_{0.1}O_2$ has shown better cycling results compared to all other compounds.

Keywords: High voltage cathodes; cobaltate and nickelate doped with manganese, NMC cathodes.

INTRODUCTION

Lithium cobalt oxide ($LiCoO_2$) is the most commonly used positive electrode material in commercial lithium-ion batteries due to its high energy density, high working voltage and good thermal and structural stability during cycling [1,2]. The theoretical capacity of $LiCoO_2$ is 274 mAh g⁻¹ however its practical capacity attainable is only about 140 mAhg⁻¹ when cycled in the voltage range of 3.0 - 4.3 V. By increasing the cut off voltage, the energy density of the cell can be increased by ~ 15%. However, the cyclability of $Li_{1-x}CoO_2$ rapidly deteriorates for x > 0.5 (i.e. above 4.3 V) due to crystallographic phase transitions and the associated unit cell volume changes [3]. Moreover, the formed Co^{4+} ions with their strong oxidative character lead to dissolution of the electrolyte on the particle surface, resulting in considerable gas release, which is responsible for the capacity fade and mechanical failure of the cells. [4, 5].

Doping with metal ions is an effective approach, which has been applied to stabilize the layered structure of the cathode material allowing good reversibility at high voltages and increasing the capacity of the system $LiCo_{1-y}M_yO_2$ (M = metal) [6, 7]. Theoretical studies indicate that transition metal doping of $LiCoO_2$ leads to an increased capacity, while non-transition metal doping can increase the voltage at the expense of the capacity. Different metal substituents like Fe, Mn, Ni, Al, Mg [8-12] at the Co – site in $LiCoO_2$ have been studied with respect to possible improvement in the electrochemical performance of the material.

In the present study, we report on the synthesis of doped lithium cobaltates $LiCo_{1-y}M_yO_2$ (M = Mn, Ni). The compounds have been obtained by solid-state method at relatively low temperatures with respect to the classic solid-state reactions using also alternative precursors and optimising the synthesis conditions. The materials were subjected to structural and electrochemical characterization in order to study their potential use as high-voltage cathode materials in lithium-ion batteries.

EXPERIMENTAL

The phases $LiCo_{1-y}M_yO_2$ (M = Mn, Ni, y = 0.1, 0.3, 0.5) were synthesized by solid-state method using nitrate precursors: $LiNO_3$, $Co(NO_3)_2.6H_2O$, $Mn(NO_3)_2$ and $Ni(NO_3)_2.6H_2O$ (Merck). The stoichiometric amounts of the precursors were mechanically homogenized in a ball mill for 1 h. Ten percent excess of $LiNO_3$ was added to the mixtures in order to avoid the loss of Li as Li_2O. The obtained powders were initially heat treated in an oven at 450⁰C for 24 h following by additional grounding for 2 h in a ball mill. Further the samples were annealed in air at 650⁰C for 12 h. The mixture was cooled, mixed thoroughly and subjected to physical and electrochemical characterizations. Powder X-ray diffraction (XRD) patterns of the phases were

---

* To whom all correspondence should be sent.
E-mail: bbanov@iees.bas.bg

obtained using a Philips APD-15 diffractometer with CuKα radiation, internal Si standard and computer data management. The lattice parameters were calculated using the dependence between the Miller indices (hkl) and d-spacing, with the program UNIT CELL - TJB Holland & SAT Redfern method (1995) applying the least-squares method. The Specific Surface Area (SSA) of the samples was determined by B.E.T. (Brunauer-Emmet-Teller) method by means of BET areameter Stroehlein (Germany). The electrochemical characterizations were carried out using a three-electrode metal cell fully modelling a coin cell 2032 with the advantage of lithium reference electrode. The electrolyte consisted of a solution of 1M $LiPF_6$ + 0.2M $LiClO_4$ in EC (ethylene carbonate) : DMC (dimethyl carbonate) : DEC (diethyl carbonate) in 1:1:1 volume ratio. The composite test electrode materials were a mixture of the compounds studied with Teflonized Acetylene Black (TAB-2) at 8:2 ratio by weight. The prepared mix was coated onto an aluminium foil that served as a current collector by applying 10 t cm^{-2} pressures using a hydraulic press. The cells were assembled in an argon-filled glove box and were subjected to galvanostatic charge-discharge cycling tests. The electrochemical tests were performed on a computer controlled multi-channel battery-cycling device at a current rate of 0.2C in the voltage range of 3.0-4.8 V at room temperature.

RESULTS AND DISCUSSIONS
Structural characterization
$LiCo_{1-y}Mn_yO_2$ cathode materials

Fig. 1. shows the X-ray diffraction patterns of $LiCo_{1-y}Mn_yO_2$ (y = 0.1, 0.3, 0.5) samples synthesized by solid-state method and calcined at 650^0C. It can be seen that all compositions do not form a single phase. The existence of secondary phases, which can be indexed to Co_3O_4 and MnO_2 is observed. The intensity of the peak at $2\theta = 36.8^0$ corresponding to Co_3O_4 phase increases considerably with increasing the Mn content to y = 0.3 (Fig. 1b). In the XRD patterns of $LiCo_{0.9}Mn_{0.1}O_2$ and $LiCo_{0.7}Mn_{0.3}O_2$ (Fig. 1a, b) it can be observed that the fingerprint peaks, (003), 101, 006, 102, 104, 108 and 110 are clearly identifiable thereby suggesting the existence of hexagonal lattice structure of the α-$NaFeO_2$ type (R-3m space group). With increasing the Mn amount to y = 0.5 the crystal structure is changed and the X-ray patterns of $LiCo_{0.5}Mn_{0.5}O_2$ can be indexed to a cubic unit cell (fcc) of the spinel-type structure (space group Fd3m). These results confirm the reports available in the literature about Mn doped lithium cobaltates [10, 13].
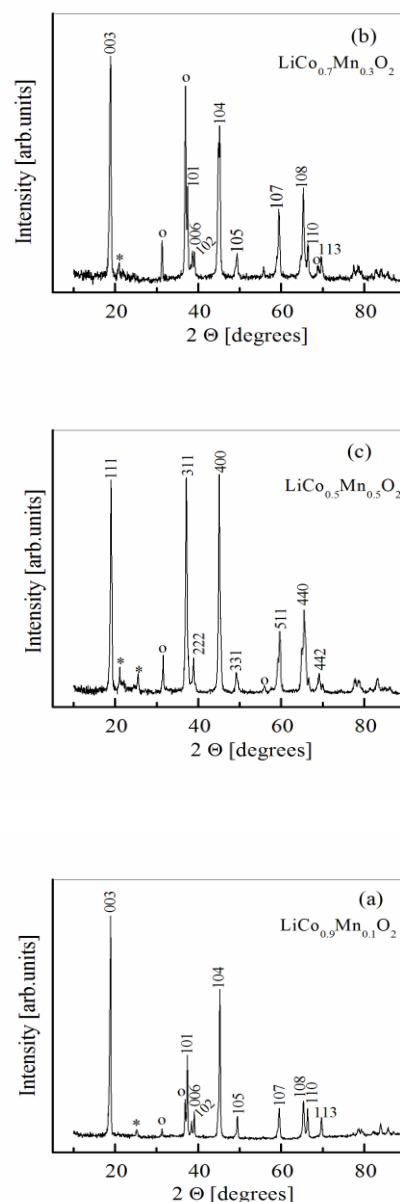
Fig.1. XRD patterns of a) $LiCo_{0.9}Mn_{0.1}O_2$, b) $LiCo_{0.7}Mn_{0.3}O_2$ and c)$LiCo_{0.5}Mn_{0.5}O_2$ powders prepared by low temperature solid-state method at 650^0C. Secondary phases in the powders are indexed to Co_3O_4 (○) and MnO_2 (*).

The unit cell parameters of all $LiCo_{1-y}Mn_yO_2$ compositions calculated from the XRD patterns are listed in Table 1. The results indicate that the hexagonal-close packed lattice is maintained only for y = 0.1 and y = 0.3. The values of the lattice parameters for these samples are slightly larger than those reported for pure $LiCoO_2$ [14-18]. With increasing content of the Mn-dopant, both the metal-metal intrasheet distance (*a*) and the metal-metal interlayer distance (*c*) increase. The substitution of Mn for Co leads to expansion of the unit cell parameters and overall cell volume, which is in tune

172

with the ionic radii of the elements ($Co^{3+} = 0.545$ Å, $Mn^{3+} = 0.67$ Å) [19]. As can be seen in Table 1, the c/a ratio of 4.99 indicates a well-defined layered structure and an ordered distribution of lithium and transition-metal ions in the lattice. The ratio of

intensities of the XRD lines $I_{(003)}/I_{(104)}$ is considered as an indicator of the ordering of the lithium and transition metal ions [20]: the larger the ratio, the better expressed layered structure.

Table 1. Structural data of the compounds $LiCo_{1-y}Mn_yO_2$ (y = 0.1, 0.3, 05)

Material	Structural data						
	Space group	(a) [Å]	(c) [Å]	c/a	U. cell vol. [Å^3]	$I_{(003)}/I_{(104)}$	Crystal Size [nm]
$LiCo_{0.9}Mn_{0.1}O_2$	R3m	2.8131	14.0480	4.99	96.2753	1.49	30
$LiCo_{0.7}Mn_{0.3}O_2$	R3m	2.8190	14.0685	4.99	96.8188	1.44	21
$LiCo_{0.5}Mn_{0.5}O_2$	Fd3m	8.0826			528.0240		20

The $I_{(003)}/I_{(104)}$ values are more than unity for y = 0.1 and y = 0.3 (Table 1) suggesting the formation of ordered layered structure. The well defined doublets (006)/(102) and (108)/(110) observed in XRD patterns of $LiCo_{0.9}Mn_{0.1}O_2$ support this conclusion. On the other hand, the (108) peak of the (108)/(110) doublet is higher in the pattern of $LiCo_{0.7}Mn_{0.3}O_2$ (Fig. 1b), which could be discerned as an indication of possible inhomogeneous distribution of Mn and Co ions in the structure. Based on the structural data it can be expected that $LiCo_{0.9}Mn_{0.1}O_2$ will exhibit better electrochemical behaviour. The average crystallite size *L* of the doped materials was calculated from X-ray data applying Debye-Scherer equation [21]. As can be seen from Table 1 the mean crystallite size of the $LiCo_{1-y}Mn_yO_2$ materials decreased with increasing the amount of the manganese component. The same tendency was

observed for the Specific Surface Area (SSA) of the compounds. The largest SSA was obtained for the sample $LiCo_{0.9}Mn_{0.1}O_2$ (3.48 m^2 g^{-1}), while the materials with y = 0.3 and y = 0.5 showed SSA of 1.90 m^2 g^{-1} and 1.78 m^2 g^{-1}, respectively.

$LiCo_{1-y}Ni_yO_2$ cathode materials

The XRD patterns of the synthesized $LiCo_{1-y}Ni_yO_2$ (y = 0.1, 0.3, 0.5) materials are shown in Fig. 2. All diffraction peaks could be indexed based on a hexagonal α-$NaFeO_2$ structure with a space group of R-3m. The patterns appear to be similar to those reported for pure layered $LiCoO_2$ [22]. There is a clear splitting of the (006)/(102) and (108)/(110) doublet peaks, which indicate uniform ordering of lithium and transition-metal ions in the structure [13].

Table 2. Structural data of the compounds $LiCo_{1-y}Ni_yO_2$ (y = 0.1, 0.3, 05)

Material	Structural data					
	(a) [Å]	(c) [Å]	c/a	U. cell vol. [Å^3]	$I_{(003)}/I_{(104)}$	Crystal Size [nm]
$LiCo_{0.9}Ni_{0.1}O_2$	2.8128	14.0296	4.99	96.1280	1.35	27
$LiCo_{0.7}Ni_{0.3}O_2$	2.8133	14.0404	4.99	96.2338	1.12	30
$LiCo_{0.5}Ni_{0.5}O_2$	2.8139	14.0487	4.99	96.2765	1.11	31

All peaks are sharp and well defined suggesting that materials are well crystallized. In all spectra the presence of some extra peaks due to impurities of NiO are observed. The hexagonal cell parameters of the doped compounds, calculated from the XRD spectra, are given in Table 2.

The results show that the hexagonal-close-packed lattice is preserved for all samples. With increasing the amount of the doping element a slight increase of the lattice parameters (*a*) and (*c*) can be seen, since the ionic radius of Ni^{3+} (0.69 Å) is larger than that of Co^{3+} (0.545 Å). The intensity ratio $I_{(003)}/I_{(104)}$ exceeds unity, which is a further evidence of the cation ordering in the obtained structures.

This is confirmed also by the values of the (*c/a*) ratio, which is higher than 4.90, corroborating the layered structure of the materials. As seen in Table 2, the $I_{(003)}/I_{(104)}$ ratio decreases with increasing the Ni content in $LiCo_{1-y}Ni_yO_2$ samples, which indicates that higher Ni concentrations could result in probable cation mixing in the structure. In contrast with the Mn doped compounds the mean crystallite size of $LiCo_{1-y}Ni_yO_2$ powders increases with increasing the Ni content. Subsequently a slight increase of the measured SSA can be observed in the order $LiCo_{0.9}Ni_{0.1}O_2$ (1.72 m^2 g^{-1}) $<LiCo_{0.7}Ni_{0.3}O_2$ (1.81 m^2 g^{-1}) $<LiCo_{0.5}Ni_{0.5}O_2$ (1.88 m^2 g^{-1}).

Electrochemical characterization

The electrochemical performance of the prepared cells was evaluated galvanostatically by cycling the cells from 3.0 to 4.8 V. The cells exhibited an open circuit voltage of around 3.0 V (vs. Li metal). In Fig.3 the discharge curves of $Li//LiCo_{1-y}Mn_yO_2$ and $Li//LiCo_{1-y}Ni_yO_2$ cells recorded at C/5 rate are presented *(5 hours discharge rate according to the theoretical capacity value of used cathode material)*. As the manganese doping content increased from x = 0.1 to 0.5 significant decrease of the discharge voltage is observed (Fig.3a), which is in accordance with the theoretic calculations of Ceder et al. and Venkatraman et al. [4, 7, 23], concerning the effect of Co substitution (partly or completely) with 3d metal in $Li_{1-x}(Co_{1-y}M_y)O_2$ at given *x*.
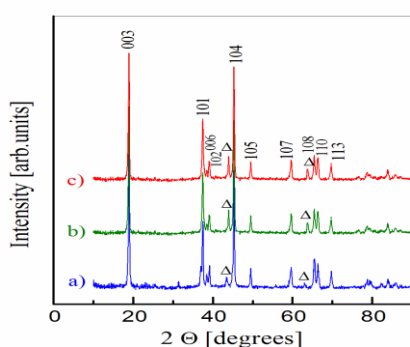
Fig. 2. XRD patterns of a) $LiCo_{0.9}Ni_{0.1}O_2$, b) $LiCo_{0.7}Ni_{0.3}O_2$ and c)$LiCo_{0.5}Ni_{0.5}O_2$ powders prepared by low temperature solid-state method at 650^0C. The impurity peaks are indicated as NiO (Δ).

All doped materials exhibit a potential slightly lower than for the pure $LiCoO_2$ phase, which could be attributed to the different morphology and structure changes during cycling. For the Ni doped compounds, the increase of the Ni mol part does not change the discharge plateau (Fig. 3b), which is due to the fact that Co and Ni can be substituted mutually without changing the $LiCoO_2$ structure.

Besides the discharge plateau at 3.8 V a second discharge plateau at about 4.4 V in both doped materials, $LiCo_{1-y}Mn_yO_2$ and $LiCo_{1-y}Ni_yO_2$, can be observed, which is attributed to second lithiation process. The dependence of the specific capacity on the number of the cycles is presented on Fig. 4.

It can be seen that $LiCo_{0.9}Mn_{0.1}O_2$ shows comparatively high initial capacity of 140 mAh g^{-1} and very good cycling stability (Fig. 4a), which means that doping with 10 mol % Mn stabilizes the structure of the lithium cobaltate.
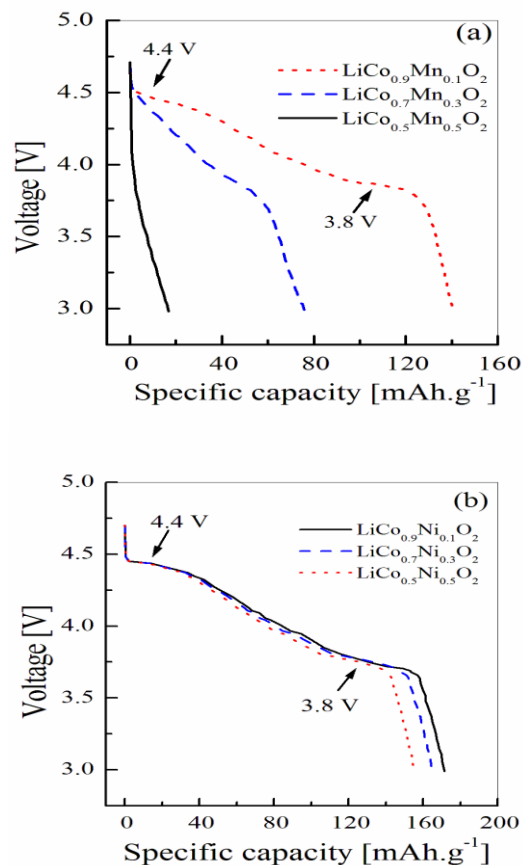
Fig.3. Discharge curves of the compounds (a) $LiCo_{1-y}Mn_yO_2$ (y = 0.1, 0.3, 0.5) and (b) $LiCo_{1-y}Ni_yO_2$ (y = 0.1, 0.3, 0.5) in the voltage window 3.0 – 4.8 V

However the discharge capacities of the $LiCo_{1-y}Mn_yO_2$ (y = 0.1, 0.3, 0.5) materials decreased with increasing the Mn content. The results of the electrochemical testing of the compound consisted of equal amounts of transition elements ($LiCo_{0.5}Mn_{0.5}O_2$) show that it possesses low electrochemical activity, which may be due to the structural change of the material. In contrast to the Mn doped compounds, in case of $LiCo_{1-y}Ni_yO_2$ the increase of the Ni content leads to a considerable increase of the initial capacity of the material, reaching 170 mAh g^{-1} for $LiCo_{0.5}Ni_{0.5}O_2$ (Fig. 4b). Similar increase of the starting capacity when doping with Ni is reported also by Li et al. [24]. However, at the same time the stability during cycling deteriorates, which could be due to a kinetic problem – it is known that some of the $LiCo_{1-y}Ni_yO_2$ phases are low electron conductors.

Another possible explanation could be the occupation of Li sites in the structure by Ni ions, which hinders the lithiation-delithiation process.
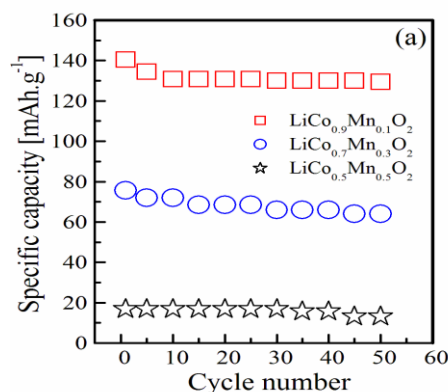
Fig.4. Plots of specific capacity versus cycle number for the compounds (a) $LiCo_{1-y}Mn_yO_2$ and (b) $LiCo_{1-y}Ni_yO_2$ in the voltage window 3.0 – 4.8 V

The presence of cation mixing can be confirmed also by the X-ray patterns. The increased Ni content leads to a decrease of the intensity ratio of the diffraction lines (003) and (104), reflecting an increased Ni content at the Li sites, which correspondingly results in deteriorated cycling stability of all Ni doped compounds. From all materials under investigation $LiCo_{0.9}Mn_{0.1}O_2$ shows the best electrochemical behaviour due to its structural and morphological properties. Its intensity ratio $I_{(003)}/I_{(104)}$ of the material is 1.49, i.e the highest value in comparison to the other doped materials. $I_{(003)}/I_{(104)}$ ishigher than unity suggesting the formation of well ordered layered structure. $LiCo_{0.9}Mn_{0.1}O_2$ is characterized also with the largest SSA, which considerably influenced its electrochemical performance.

CONCLUSIONS

Doped lithium cobaltates $LiCo_{1-y}M_yO_2$ (M = Mn, Ni; y = 0.1, 0.3, 0.5) were synthesized by solid-state method from nitrate precursors. The effect of Mn and Ni doping on the structural and electrochemical properties of the materials was investigated. XRD analysis shows that the layered structure of lithium cobaltate is preserved up to doping with 50 mol % Ni and about 30 mol % of Mn. We demonstrated that $LiCo_{0.9}Mn_{0.1}O_2$ synthesized in this way is a promising cathode material for use in lithium-ion batteries, delivering capacities of 130 mAh g^{-1} at a 0.2C rate when cycled in the high voltage range (4.8V). Moreover, it possesses very good cycling stability in the extended galvanostatic cycling studies (50 cycles). Doping with 10, 30 and 50 mol % Ni results in an increased initial capacity (by 20 %), but also leads to deterioration with cycling.

REFERENCES

1. K. Mizushima, P.C. Jones, P.J. Wiseman, J.B. Goodenough, *Solid State Ionics*, **3-4**, 171 (1981).
2. J. M. Tarascon, M. Armand, *Nature*, **414**, 359 (2001).
3. S. Levasseur, M. Menetrier, E. Suard, C. Delmas, *Solid State Ionics*, **128**, 11 (2000).
4. G. Ceder, Y.-M. Chiang, D.R. Sadoway, M.K. Aydinol, Y.-I. Jang, B. Huang, *Nature,* **392**, 694 (1998).
5. G. G. Amatucci, J.M. Tarascon, L.C. Klein, *Solid State Ionics*, **83**, 167 (1996).
6. Ceder, G.; Chiang, Y. M.; Sadoway, D. R.; Ayginol, M. K.; Jang, Y. I.; Huang, B. *Nature,* **392**, 894(1998).
7. S. Venkatraman, V. Subramanian, S. Gopu Kumar, et. al., *Electrochem. Commun.,* **2,** 18 (2000).
8. H. Kobayashi, M. Shigemura, H. Tabuchi, K. Sakaebe, H. Ado, A. Kageyama, R. Hirano, M. Kanno, S. Wakita, S. Morimoto, S. Nasu, *J. Electrochem. Soc*., **147**, 960 (2000).
9. M. Holzapfel, R. Schreiner, A. Ott, *Electrochim. Acta*, **46**, 1063 (2001).
10. R. Stoyanova, E. Zhecheva, L. Zarkova, *Solid State Ionics*, **73**, 233 (1994).
11. C. Delmas, I. Saadoune, A. Rougier, *J. Power Sources*, **44**, 595 (1993).
12. C. Julien, *Solid State Ionics*, **157**,57 (2003).
13. Ch. Julien, *Solid State Ionics*, **135**, 241 (2000).
14. G. G. Amatucci, J.M. Tarascon, L. Klein, *J. Electrochem. Soc*., **143**, 1114 (1996).
15. H. J. Orman, P. J. Wiseman, *Acta Crystallogr.*, **C 40**,12 (1984).
16. J. Akimoto, Y. Gotoh, Y. Oosawa, *J. Solid State Chem.*, **141**, 298 (1998).
17. A. Marini, V. Berbenni, V. Massarotti, D. Capsoni, E. Antolini, *J. Solid State Chem*., **116**, 23 (1995).
18. R. J. Gummow, M. M. Thackeray, W. I. F. David, S. Hull, *Mater. Res. Bull*., **27**, 327 (1992).
19. R. D. Shannon, Acta Crystallogr., **A32**, 751 (1976).
20. R. J. Gummow and M. M. Thackeray, *J. Electrochem. Soc.*, **140**, 3365 (1993).
21. P. Scherrer, GottingerNachrichtenGesell., 2 (1918) 98; A. L. Patterson, Phys. Rev., 56 (1939) 97
22. Ueda, T. Ohzuku, *J. Electrochem. Soc.,* **141**, 2013 (1994).
23. S. T. Myung, N. Kumagai, S. Komaba, H.T. Chung, *Solid State Ionics*, **139**, 47 (2001).
24. Chi-lin Li, W. Liu, Z. Fu, *Chinese J. of Chemical Physics*, **19,** 493 (2006).

ВИСОКО ВОЛТОВИ КАТОДНИ МАТЕРИАЛИ НА ОСНОВАТА ЛИТИЕВ КОБАЛТАТДОТИРАНИ С НИКЕЛ И МАНГАН

Кр. Банов[1,2], Т. Петков[2], Р. Букурещлиева[1], Д. Иванова[2],
Л. Фачиков[2], В. Котев[4], Бр. Банов[1,3*]

[1.] *Институт по електрохимия и енергийни системи, ИЕЕС, ул. "Акад. Г. Бончев" N:1, Бл. 10. 1113 София*
[2)] *Химико-технологичен и металургичен университет, бул. "Кл. Охридски" N:8, 1756 София*
[3)] *Европейски политехнически университет, ЕПУ, ул. "Св. Св. Кирил и Методи" N:23,*
2300 Перник
[4)] *Институт по механика, ул. "Акад. Г. Бончев" N:1, Бл. 4. 1113 София*

(Резюме)

Дотиран с никел и манган литиев кобалтат $LiCo_{1-y}M_yO_2$ (M = Mn, Ni, y = 0.1, 0.3, 0.5) е синтезиран успешно по твърдофазен метод. Получените проби са охарактеризирани с помощта на рентгеноструктурен анализ. Специфичната повърхност е определена с помощта на BET метода. Изготвените проби притежават ромбоедрична структура с изключение на $LiCo_{0.5}Mn_{0.5}O_2$, която кристализира в кубична шпинелна структура от пространствена група **Fd3m.** Електрохимичното поведение на синтезираните материали е изследвано в електрохимична клетка при галваностатичен режим във високо волтовата област с граници 3.0V до 4.8V спрямо Li/Li^+ сравнителен електрод. Проведените изследвания показват, че количеството на дотиращия елемент определят в голяма степен структурата, електрохимичното поведение, и живота на изследваното съединение. Литиев кобалтат дотиран с манган с формула $LiCo_{0.9}Mn_{0.1}O_2$ показа най-добрите резултати по отношение на циклируемост в сравнение с другите изследвани съединения.

Ключови думи: високо волтови катоди за литиево йонни батерии, кобалтат и никелат дотирани с манган, катоди на основата на литиран никел манган кобалтови смесен оксид

Electrochemical behaviour of LiMn$_2$O$_4$ and LiCoO$_2$ in water electrolyte

T. Petkov[1*], T. Stankulov[2], K. Banov[1,2], and A. Momchilov[2]

[1)]*University of Chemical Technology and Metallurgy – UCTM, bul. "Kl. Ohridski" N:8, 1756 Sofia*
[2)] *IEES, "Acad. E. Budevski" – BAS, "Acad. G. Bonchev" str. BL10, IEES-BAS, 1113 Sofia*

Li-Ion Batteries can afford quite large energy densities based on organic electrolytes with highly toxic and flammable solvents and its preparation is complicated and expensive, partly because the electrolyte is moisture and air sensitive. Utilization of aqueous electrolytes in rechargeable lithium batteries will increase their safety, economical, and environmental issues. The electrochemical properties of LiMn$_2$O$_4$ and LiCoO$_2$as positive electrode materials for Li-ion battery with water electrolytes against LiV$_3$O$_8$ as negative electrode were investigated. The used salts are 6M LiNO$_3$ and 2M Li$_2$SO$_4$ dissolved in distilled water. LiMn$_2$O$_4$ was prepared by conventional solid state reaction heating stoichiometric mixtures of LiNO$_3$ and MnO$_2$ at temperature under 650°C for 24 h. LiCoO$_2$ was obtained via sol-gel method with final thermal treatment at800^{o}Cfor 24 h. Lithium vanadate was prepared via solid state reaction. All materials are stable in the aqueous solution and intercalation/deintercalation of lithium ions occurs within the window of electrochemical stability of the water, which was determined using slow cycling voltammetry. Manganese spinel exhibit specific capacity of 99mAh.g^{-1} in 6M LiNO$_3$and 94mAh.g^{-1} in 2M Li$_2$SO$_4$water electrolyte, while its capacity in organic electrolyte is 135mAh.g^{-1}. The obtained capacities from lithium cobaltate in water electrolytes were 99mAh.g^{-1} and 79mAh.g^{-1}respectively while that in organic electrolyte is 145mAh.g^{-1}. The cycling behaviorand specific capacityof these active compounds in electrochemical cell with vanadate as a negative active mass is not as stable as in organic electrolytes.

Key words: Manganese spinel, Lithiumcobaltate,Water electrolyte, Li-ion Battery

INTRODUCTION

The present commercially available lithium ion batteries contain flammable organic liquid electrolyte, which are major safety problem [1]. In recent years, spinel LiMn$_2$O$_4$ has been intensively investigated as a promising candidate for positive materials for lithium-ion batteries (LIBs) due to its low cost, non-toxicity, environmental friendliness, easy preparation, excellent voltage profile, and operating safety characteristics[2,3]The LiCoO$_2$ has provided a good balance between high energy density and good cyclability. The specific capacity of LiCoO$_2$ remains 160mAh.g^{-1} or less when it is charged up to 4.2 V, which is 60% at of the theoretical capacity of 274mAh.g^{-1} for one electron reaction. Elevating the charging voltage beyond 4.2 V can be one promising approach to utilize more lithium ions in the LiCoO$_2$ and to increase the capacity and energy density of the lithium-ion batteries [4]. Aqueous Rechargeable Lithium Batteries (ARLB) can solve the safety problems in some extents, which can assemble the battery without gas protection and humidity control. The inorganic electrolyte is cheaper; the ion conductivity is two orders of magnitude higher than in the organic electrolyte. The capacity of LiCoO$_2$ and LiMn$_2$O$_4$ are well known and shown in our pervious papers [5-7]. Especially, the ARLB is the green environmental protection battery indeed[8-13].The manganese spinel LiMn$_2$O$_4$ is cited in the literature as suitable for application as active material in li-ion battery with LiNO$_3$ aqueous solution electrolyte [14-17] The lithium cobaltate LiCoO$_2$show also reversible Li intercalation in LiNO$_3$ water electrolyte [17]. In the literature LiNO$_3$ and Li$_2$SO$_4$ are cited as promising conducting salts for li-ion battery with water electrolyte [18, 19].

That preliminary information gives rise to the following questions:

-What is the better conducting salt for water electrolyte?

-What is the difference of capacity in water electrolyte and organic one?

-Is it possible to use LiMn$_2$O$_4$ as a negative active material?

The aim of the present work is to study the impact of synthesis methods, physicochemical characteristics, and electrochemical behaviour of LiMn$_2$O$_4$ and LiCoO$_2$ in LiNO$_3$ and Li$_2$SO$_4$ water electrolyte.

EXPERIMENTAL

Preparation of active compounds, electrodes and electrolyte

Samples studied of LiMn$_2$O$_4$ were prepared by heating of stoichiometric mixture of MnO$_2$ andLiNO$_3$ in a nickel crucible for 12 to 48 h in the temperature range of 450-850 ºC. The Li salt used is LiNO$_3$, commercial product of Fluka, the manganese dioxide is CMD Faradizer M supplied by Sedema. The precursors were mixed, dried at 80ºC for 12 h and milled. After that, the obtained mixture was preheated at 450ºC for 12h and then heated finally on 650ºC for 24h. The LiCoO$_2$ was prepared by sol-gel method by stoichiometric mixture of Co(NO$_3$)$_2$ and LiNO$_3$. Appropriated amount of lithium and cobalt nitrate (Fluka) salts with the cationic ratio of Li:Co 1:1 were dissolved in distilled water and mixed well with an aqueous solution of citric acid (Fluka). Citric acid was used as a chelating agent in making a gel. The resultant solution was evaporatedat 80°C with magnetic stirring untila transparent pink sol was formed. As water evaporated further, the sol turned into a viscous transparentpink gel. The gel obtained was heated at 800ºC for 8 h. The inorganic electrolyte, which was used, was neutral saturated solution of LiNO$_3$ or Li$_2$SO$_4$(Fluka) in distilled water.

Electrochemical measurements were performed in a three-electrode glass test cell containing 6 M LiNO$_3$ or 2M Li$_2$SO$_4$ water electrolyte. The active mass of the test electrodes was a mixture of tested active electrode materials studied and teflonized acetylene black at 1:1 ratio by weight. After that test, electrodes were formed by pressing 25 mg.cm^{-2} of thus prepared mixture onto an expanded nickel grid atapressure of 3t.cm^{-2}.

Characterization techniques

Cyclic voltammetry (CV) was performed with an Arbin 320 potentiostat/galvanostat (Arbin Instruments Co.) in a three-electrode glass cell at 200 and 50 µV s^{-1} scan rate in various voltage ranges, using LiMn$_2$O$_4$ or LiCoO$_2$ as working electrode, counter electrode were LiV$_3$O$_8$,LiCoO$_2$and LiMn$_2$O$_4$, and reference electrodes Ag/AgCl, respectively. X-ray analysis was carried out on a Philips APD 15 diffractometer with Cu Kα radiation.

RESULTS AND DISCUSSIONS

Fig. 1(a) shows the XRD patterns of LiMn$_2$O$_4$ samples having the spinel structure without any impurity phases, which belongs to Fd3m face cubic crystal system (ICSD, no. 087775). In this crystal structure, lithium atom occupies the tetragonal 8a position, manganese atom occupies 16d position, and oxygen atom is in the position of 32e.

In Fig. 1(b) X-ray diffraction patterns for LiCoO$_2$ obtained by nitrate gel treated at 800ºC for 24h as described above. The peaks marked as (#) correspond to Co$_3$O$_4$ impurity.

The diffraction pattern show clear (006)/(102) peaks and (018)/(110) split peaks indicating a perfect layered-structure for LiCoO$_2$ [19]. The pattern of LiCoO$_2$ prepared at 800ºC comprises a major LiCoO$_2$ phase crystallizing in rhombohedral structure with a small amount of Co$_3$O$_4$ as impurity.
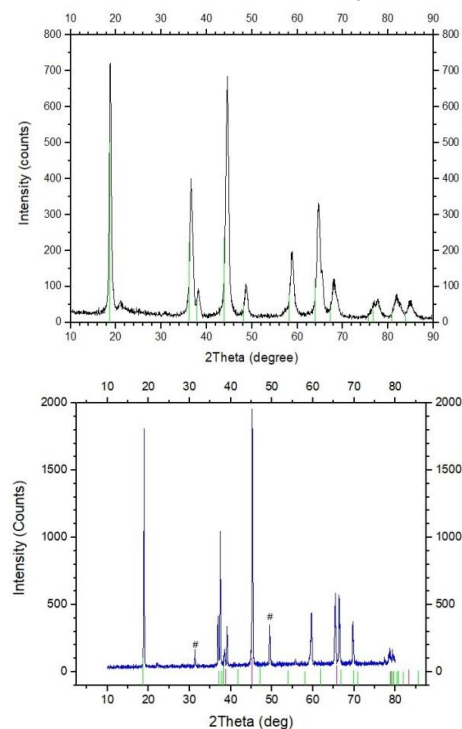
Fig. 1. The X-ray diffraction pattern of the materials. (a) LiMn$_2$O$_4$ and (b) LiCoO$_2$

Fig.2 shows the SEM micrographs of the LiMn$_2$O$_4$ sample synthesized by solid-state reaction from MnO$_2$ Faradizer M (CMD) and LiNO$_3$heated at 850ºC a) and b) and heated at 650ºC c) and d) for 24h. From Fig. 2a and 2b it is seen that the resultant LiMn$_2$O$_4$ sample mainly consists of large quantities of particles with a size about 1µm. Fig.2b gives a high-magnification image of several selected LiMn$_2$O$_4$ particles. It is found that the prepared LiMn$_2$O$_4$ sample is composed of particles with well-developed octahedral shapes [20, 21]. In addition, very few quasi-spherical particles can also be observed in Fig. 2c. However, a high-magnification micrograph in Fig. 2d indicates the outer part of this quasi-spherical LiMn$_2$O$_4$ particle has been evolved to many small polyhedral particles, suggesting better electrochemical performance.
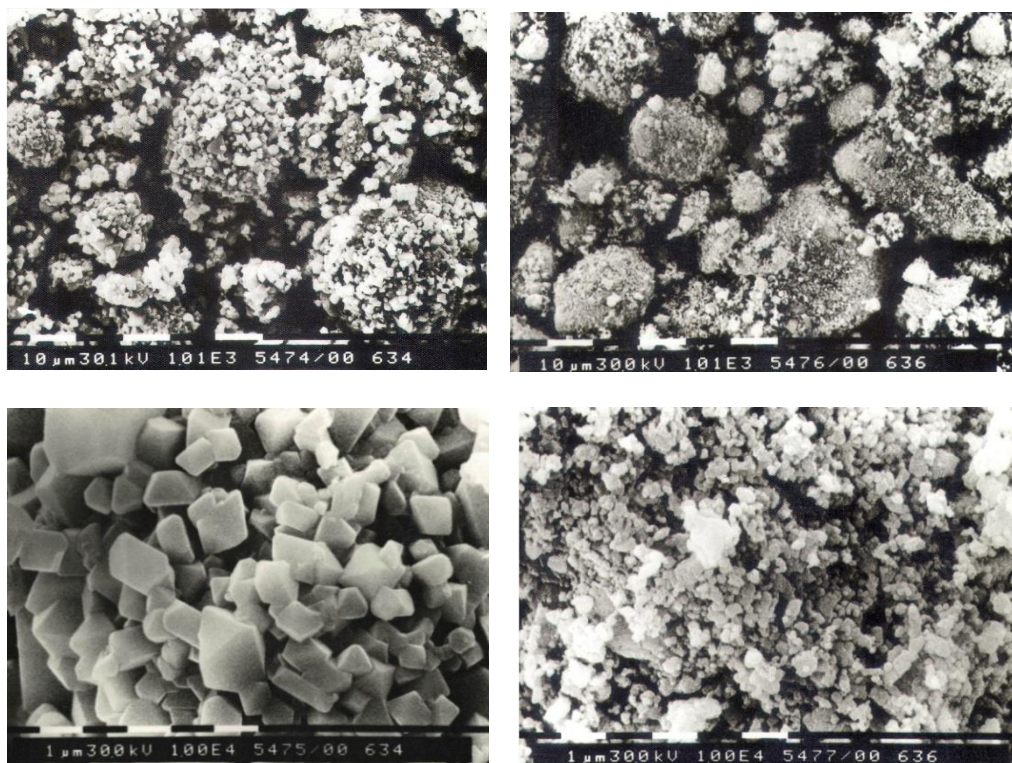
Fig.2 EM images of the LiMn$_2$O$_4$ synthesized by the solid-state reaction at 850ºC a), b) and at 650ºC c), d) for 24h

Fig.3 shows SEM images of the LiCoO$_2$ synthesized by sol-gel method a) and by solid stat reaction - SSR b). It is clear that both materials are characterized by good crystallinity and have similar morphology. As can be seen from Fig.3, the resulting materials are not monodispersed and consist of both particles of less than 1μm and agglomerates of about 1-2μm. Better

dispersion of the precursor particles in the sample sol-gel method results in particle size reduction (Figure 3b).

To understand the electrochemical behavior of LiCoO$_2$ and LiMn$_2$O$_4$ in aqueous solutions, we performed voltammograms from -0.2 to 1.6V and

from -0.6 to 0.02V vs.Ag/AgCl using two different aqueous electrolytes, 6M

LiNO$_3$ and 2M Li$_2$SO$_4$. This involved the use of a LiV$_3$O$_8$ as a counter electrode. The results are shown on Fig.4, Fig.5 and Fig.6. The scan rates were rather low, 50μV.s^{-1}. In all cases, an electrochemical process was clearly observed. The electrochemical behavior of LiMn$_2$O$_4$ in 6M LiNO$_3$ and in 2M Li$_2$SO$_4$ is very close. The specific capacities in two water electrolytes are almost the same as the nitrate is slightly higher, respectively, 99mAh.g^{-1} and 94mAh.g^{-1}, which correspond to 80% of the theoretical capacity of the material. The material works in the range of electrochemical stability of water, the evolution of O$_2$ starting after 1.15V (Fig.4).

Fig. 3. SEM images of the LiCoO$_2$ synthesized by sol-gel method treated at 800ºC a) and SSR at 650ºC b) for 24h

Using 6M LiNO$_3$ as electrolyte, Ag/AgCl as reference electrode and scan rate of 50 µVs^{-1} the first peak of Li$^+$ ions extraction appears at 0.92V and the corresponding insertion peak is located at 0.9V. The second peak of extraction, was at 1.05V and peak of insertion was at 1.01V and the spacific capacity of 99 mAh g^{-1}. Observed difference between both couple of peaks is only 20-30mV that means the processes are in quasi equilibrium (Fig.4a). The CV carried out in the same conditions but with 200 µV.s^{-1} shouwed difference of 50mV and almost the same specific capacity (95 mAh.g^{-1}) which indicate a fast electropchemical process for this material. On the Fig. 4b are shown the curves

of works of LiMn$_2$O$_4$ in Li$_2$SO$_4$ with scan rate 50 µV.s^{-1}. The specific capacity is 94 mAh g^{-1} and all peaks are shifted with 100 mV to the potential of reference electrode incomparison with this in LiNO$_3$, this is most probaly due to the nature of electrolyte. This shifting to the lower potentials reduces probability of O$_2$ evolution. The last electrochemical system realazedin real cell will work morestabile and safety. The capacity of delithiation (lithium extraction) is little higher usingLiNO$_3$ (in both rates) than those of delithiation in Li$_2$SO$_4$ cause of proximity of peaks to the evolution of O$_2$ in LiNO$_3$ electrolyte.
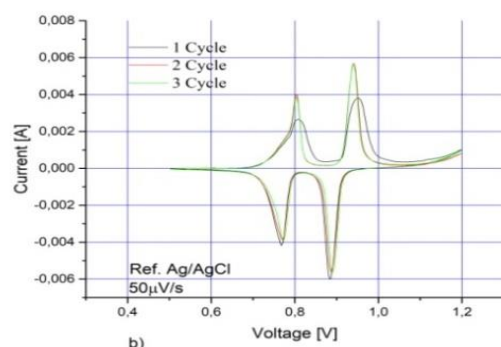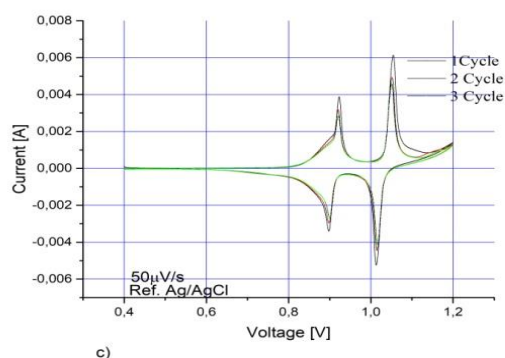
Fig.4. Cyclic voltammograms of LiMn$_2$O$_4$ synthesized by SSR method at 650°C in 6M saturated aqueous LiNO$_3$, a), in 2M Li$_2$SO$_4$ b) scan rate 50 µVs^{-1}.

Fig.5 shows cyclic voltammograms of LiCoO$_2$. In the first cycle of the sol-gel-synthesized LiCoO$_2$, a deintercalation peak at 0.92V and intercalation peak at 0.67V were observed (Fig.5a). These potency values are typical of the LiCoO$_2$ presented. In the second cycle, the peak potential values of deintercalation/intercalation are respectively 0.7 and 0.9V. The value of the second peak of the potential is higher than that of the first. This polarization difference is most likely due to rearrangement of the structure after the first cycle. The voltammogram in Li$_2$SO$_4$ shows that deintercalation peaks were at 0.76V and the intercalation were at 0.66V. The difference is about 50 mV. The process of extraction of Li$^+$ in Li$_2$SO$_4$ is easier compared to process in LiNO$_3$ (Fig.5b). The specific capacities in the two water electrolytes are 99mAh.g^{-1} and 79mAh.g^{-1} respectively for LiNO$_3$ and Li$_2$SO$_4$, which is 68% of the theoretical capacity of the material.

The manganese spinel LiMn$_2$O$_4$ has two voltage plateaus at 3 and 4 V vs. Li, both of them located in the electrochemical window of aqueous electrolyte.
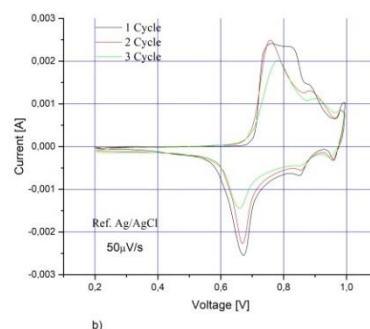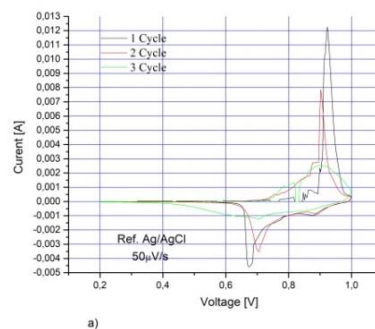
Fig.5 Cyclic voltammograms of LiCoO$_2$ as synthesized by sol-gel method and treated at temperature 800°C in 6M saturated aqueous LiNO$_3$ a) and 2M Li$_2$SO$_4$; scan rate was 50 µVs^{-1}.

Therefore, LiMnO₄ could be utilized as both the cathode and anode in such an aqueous cell.We focused on the performance of the aqueous negative active material. The results are shown in Fig. 6. We present voltammograms within 0.2 to -0.6V vs. Ag/AgCl in the lithium nitrate aqueous solutions. This include, the use of a LiCoO₂ (Fig.6 a)) and LiMn₂O₄ (Fig.6 b) as counter electrode.
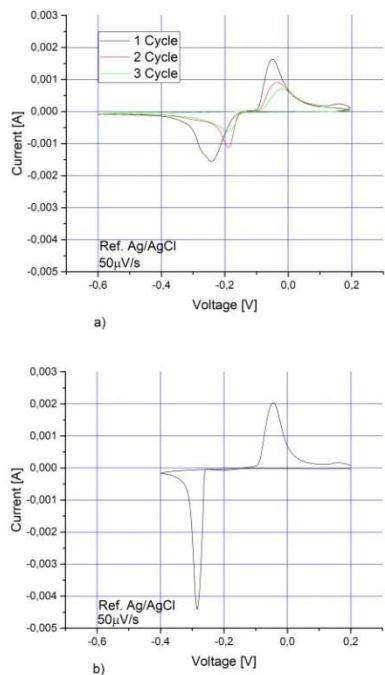
Fig. 6 Cyclic voltammograms of LiMn₂O₄ for negative electrode in 6M saturated aqueous LiNO₃ vs. LiCoO₂ as counter electrode a) and vs. LiMn₂O₄ as counter electrode b); scan rate was 50 μVs⁻¹

Fig.6 a) shows use of spinel LiMn₂O₄ as anode material. In the first cycle an intercalation peak at -0.25V and deintercalation peak at -0.048V were observed. In second cycle, the peaks are shifted to -0.19 and -0.035V and in the third cycle the peaks position were 0.19 and -0.14V. In the beginning is observed polarization of electrode, but in the next cycles the process of charge/discharge becomes stable. Charge capacity in the first cycle was 40mAh.g⁻¹ and the discharge capacity - 32mAh.g⁻¹. In second cycle the values were 26 mAh.g⁻¹ and 21 mAh.g⁻¹and in the third cycle - 21mAh.g⁻¹and 16mAh.g⁻¹. The efficiency is about 80% from the theoretical one that means the material is stable and work good.

Fig.6 b) shows the rechargeable lithium-ion cell with LiMn₂O₄ as a use of spinel LiMn₂O₄ as anode material, working and counter electrodes. In this way, we have fully symmetric cell with same active electrode materials as cathode and anode. The intercalation peak appears at -0.28 V and the deintercalation is at -0.043V. The charge capacity is

49 mAh.g⁻¹ and the discharge is 41 mAh.g⁻¹, values very close each other. In reality, the discharge capacity is exactly 84% from the charge capacity.

CONCLUSION

The electrochemical characteristics of LiMn₂O₄ and LiCoO₂ used as cathode were studied in aqueous electrolyte containing lithium nitrate or sulfate with respect to its use as a new kind of rechargeable battery system. Cyclic voltammetry showed that spinel LiMn₂O₄ and LiCoO₂ reversibly intercalated/deintercalated Li⁺ ions at potentials lower than the potentials of hydrogen or oxygen evolution in present aqueous solution with neutral pH.

The use of spinel and cobaltate as a positive active material for rechargeable battery delivers 95жmAh.g⁻¹ and 99жmAh.g⁻¹ discharge capacity. The capacity of cobaltate is lower in sulfate solution – 79 mAh.g⁻¹. The use of manganese spinel LiMn₂O₄ as anode were investigate against LiCoO₂ as counter electrode in nitrate solution. This electrochemical system is stabile but the discharge capacity was very low – 32 mAh.g⁻¹.

The experiments show that the capacity in lithium nitrate is higher but the process of extraction of Li⁺ is easier in sulfate. A symmetric electrochemical system based on manganese spinel in LiNO₃ electrolyte was tested for the first time and shows very promising results for large-scale energy storage and energy conversion.

The cost of the aqueous cell will be lower than that of conventional Li-ion battery cell, because electrode and electrolyte materials are not expensive and toxic compared with those used in conventional lithium ion batteries. The assembling process is simple, environmental friendly and trouble-free.

REFERENCES

1. R. Murugan, V. Thangadurai, W. Weppner, *Appl. Phys. A* **91**, 615, (2008).
2. J. M. Tarascon, E. Wang, F.K. Shokoohi, W.R. Mckinnon, S. Colson, *J. Electrochem.Soc.* **138**, 2859, (1991).
3. J. M. Tarascon, M. Armand, *Nature* **414**, 359, (2001).
4. Y. Takahashi, S. Tode, A. Kinoshita, H. Fujimoto, I. Nakane, and S. Fujitan, *Electrochem. Soc.,* **155 (7),** A537, (2008).
5. V. Manev, B. Banov, A. Momchilov, A. Nassalevska, *Journal of Power Sources* **57,** (1-2) 99, (1995).
6. L. Predoană, A. Barău (Szatvanyi), M. Zaharescu, H. Vasilchina, N. Velinova, B. Banov, A. Momchilov, *Journal of the European Ceramic Society*, **27**, 1137, (2007).

7. B. Banov, Y. Todorov, A. Trifonova, A. Momchilov, V. Manev, *Journal of Power Sources,* **68 (2),** 578, (1997).
8. H.B. Wang, K.L. Huang, Y.Q. Zeng, S. Yang, L.Q. Chen, *Electrochim. Acta* **52**, 3280, (2007).
9. J. Kohler, H. Makihara, H. Uegaito, H. Inoue, M. Toki, *Electrochim. Acta* **46**, 59 (2000).
10. A. Eftekhari, *Electrochim. Acta,* **47**, 495, (2001).
11. J. Lee, S. Pyun, *Electrochim. Acta,* **49**, 753, (2004).
12. M.M. Rao, M. Jayalakshmi, O. Schaf, H. Wuff, U. Guth, F. Scholz, *J. Solid State Electrochem.* **5**, 50, (2001).
13. K.S. Abou-El-Sherbini, M.H. Askar, *J. Solid State Electrochem.* **7**, 435, (2003).
14. M. Zhaoa, Q. Zheng, F. Wang, W. Dai, X. Song, *Electrochimica Acta* **56**, 3781(2011).
15. J. Yan, J.Wang, H. Liu, Z.y Bakenov, D. Gosselink, P. Chen, *Journal of Power Sources,* **216**, 222, (2012).
16. I. Stojkovi, N. Cvjeti´canin, M. Mitri, S. Mentusa, *Electrochimica Acta* **56**, 6469, (2011).
17. R. Ruffo, C. Wessells, R. A. Huggins, Y. Cui, *Electrochemistry Communications* 11, 247, (2009).
18. L. Suo, O. Borodin, T. Gao, M. Olguin, J. Ho, X. Fan, C. Luo, C. Wang, K. Xu, *Science* **350**, 938, (2015).
19. W. T. Jeong, J. Lee, *Alloys Comp.*, **322**, 205, (2001).
20. H.M. Wu, J.P. Tu, Y.F. Yuan, X.T. Chen, J.Y. Xiang, X.B. Zhao, G.S. Cao, *J. Power Sources* **161**, 1260 (2006).
21. C.H. Jiang, S.X. Dou, H.K. Liu, M. Ichihara, H.S. Zhou, *J. Power Sources* **172**, 410, (2007).

ЕЛЕКТРОХИМИЧНИ СВОЙСТВА НА LiMn₂O₄ И LiCoO₂ ВЪВ ВОДНИ ЕЛЕКТРОЛИТИ

Т. Петков[1*], Т. Станкулов[2], К. Банов[1,2], А. Момчилов[2]

[1]*Химикотехнологичен и металургичен университет, бул. "Климент Охридски" 8, 1756 София, България*
[2]*Институт по обща и неорганична химия, Българска академия на науките, ул. "Акад. Георги Бончев" бул. 11, 1113 София, България*

(Резюме)

Литиево-йонните батерии базирани на органичен електролит дават възможност за постигане на големи енергийни плътности. Тези електролити представляват силно токсични и запалими разтворители, а подготовка им е сложна и скъпа, отчасти защото са чувствителни към влагата от въздуха. Използването на водни електролити в акумулаторни литиево-йонни батерии ще увеличи безопасността, екологичността им и ще намали стойността им. Разгледани са електрохимичните свойства на LiMn₂O₄ и LiCoO₂ като положителни електроди за литиево-йонна батерия с воден електролит срещу LiV₃O₈ като отрицателен електрод. Използваните електролити са 6M LiNO₃ и 2M Li₂SO₄, разтворени в дестилирана вода. LiMn₂O₄ е получен чрез приготвяне на стехиометрична смес от LiNO₃ и MnO₂ в твърдо състояние и нагряване при температура 650°C в продължение на 24 часа. LiCoO₂ се получава чрез зол-гел метод с крайно термично третиране при 800°C в продължение на 24 часа. Литиевият ванадат се получава чрез твърдофазен синтез. Всички материали са стабилни във водния разтвор и интеркалацията/деинтеркалацията на литиевите йони се извършва в прозореца на електрохимична стабилност на водата, който се определя при използване на бавна циклична волтаметрия. Манганооксидният шпинел има специфичен капацитет от 99 mAh.g⁻¹ в 6M LiNO₃ и 94 mAh.g⁻¹ в 2M Li₂SO₄ воден електролит, докато неговият капацитет в органичния електролит е 135 mAh.g⁻¹. Полученият капацитет от литиев кобалтат във водните електролити е съответно 99 mAh.g⁻¹ и 92mAh.g⁻¹, докато този в органичния електролит е 145 mAh.g⁻¹. Цикличното поведение и специфичният капацитет на тези активни материали са изследвани в електрохимичните клетки и като отрицателна активна маса.

Ключови думи: манганов шпинел, лтиев кобалтат, воден електролит, литиево-йонна батерия

The electrochemical behavior of LiV$_3$O$_8$ obtained via different syntheses as negative active material in aqueous Li-ion battery

T. Petkov[1*], T. Stankulov[2], K. Banov[1,2], and A. Momchilov[2]

[1] *University of Chemical Technology and Metallurgy – UCTM, bul. "Kl. Ohridski"8, 1756 Sofia*
[2] *Institute of Electrochemistry and Energy Systems "Acad. E. Budevski", Bulgarian Academy of Sciences, Acad. Georgi Bonchev Str., bl. 10, 1113 Sofia, Bulgaria*

The electrochemical properties of the lithium trivanadate (LiV$_3$O$_8$, LVO) as a negative electrode material for aqueous Li-ion battery was studied. Two methods of synthesis were applied to prepare LiV$_3$O$_8$: sol-gel method followed by solid-state reaction (SSR) at 500 and 550 °C and melting process with subsequent hydrothermal treatment and drying. As a counter electrode was used LiMn$_2$O$_4$ (LMO) prepared by conventional SSR synthesis. The intercalation/de-intercalation of lithium ions occurs within the window of electrochemical stability of the water. LiV$_3$O$_8$ prepared by melting process, hydrothermally treated and dried (MP65DR), shows a poorer performance in galvanostatic mode compared to these obtained via sol-gel. The sample obtained via sol-gel followed by SSR at 550 °C (SG55) shows an initial specific capacities of ~75 (intercalation) and ~52 (de-intercalation) mAh.g^{-1} which is about 4-5 times less in comparison to the capacities delivered in non-aqueous electrolytes. Although the lower capacity (30-33 mAh.g^{-1}), the other sol-gel sample annealed at 500 °C (SG50) displays better capacity retention and coulombic efficiency throughout the cycles.

Keywords: Aqueous Li-ion Battery, anode active material, Lithium trivanadate

INTRODUCTION

Li-ion Batteries (LIBs) possess large energy densities but it employs organic electrolytes which consists highly toxic and flammable solvents. Furthermore the electrolyte manufacture is complicated and expensive, partly because it is sensitive to moisture and air. Incorporation of aqueous electrolytes in rechargeable lithium batteries will improve their safety and economical parameters as well as minimization of the environmental issues. Although the aqueous electrolytes are stable in narrower electrochemical window (0-2 V) than their organic counterparts (0-4.5 V), they are much safer, less toxic and easer to manufacture [1]. Dahn and co-workers were one of the first research groups that proposed an aqueous based type battery using b-VO$_2$ and LiMn$_2$O$_4$ (LMO) as negative and positive electrodes, respectively [2]. Another aqueous battery system with improved cycling stability that was recently presented is LiTi$_2$(PO$_4$)$_3$ | Li$_2$SO$_4$ | LiFePO$_4$[3]. G.J. Wang *et al.* studied electrochemical performance of a LiV$_3$O$_8$ (negative electrode) and LiCoO$_2$ (positive electrode) in saturated LiNO$_3$ aqueous electrolyte. These two electrode materials are stable in the aqueous solution and the obtained capacity of this cell system is about 55 mAh g^{-1} which is comparable to those of the lead acid and Ni–Cd batteries [4]. Lithium trivanadate (LiV$_3$O$_8$, LVO) is a compound with layered 2D structure, which was defined by Wadsley as a γ-LiV$_3$O$_8$ [5]. LVO is widely investigated as positive active materials for rechargeable non-aqueous Li batteries [6-11]. Its active working window is between 1.5 and 3.5 V vs Li/Li$^+$. Hydrothermal treatment of the active material leads to an increase of the interlayer distance due to the incorporation of water molecules into the structure [12]. This modification improves the initial electrochemical lithiation of the compound to 320 mAh g^{-1}, corresponding to ~3.5 Li per mol inserted in LVO. This result correlates with the assumption of Thackeray *et al.* that is possible up to 4 Li$^+$ to be inserted in LiV$_3$O$_8$[13]. Furthermore the reversible (de-intercalation) specific capacity increases to 280 mAh g^{-1}, which corresponds to 3 Li per mol LVO. After few cycles the reversible capacity fades to 250 mAh g^{-1}. Theoretically maximum potential difference of about 3V could be reached if LiV$_3$O$_8$ is paired with counter electrode of LiMn$_2$O$_4$. This fact prompts an interest to study such water based battery configuration and its Li$^+$ intercalation and de-intercalation processes. LVO possesses lower electrochemical potential than LMO thus appears to be negative electrode in the above mentioned system.

The aim of this work is to study the electrochemical properties of LiV$_3$O$_8$ obtained via different synthesis approaches and tested as negative

---

* To whom all correspondence should be sent.
E-mail: todorvp@abv.bg

active material for aqueous rechargeable lithium battery (ARLB).

EXPERIMENTAL
Samples preparation

Lithium trivanadate was synthesized via two ways. Two of the samples were prepared via sol-gel as follows: V_2O_5 (synthesized by decomposition of NH_4VO_3 (Fluka, >99 %) at 320 °C [14]) was added in preliminary prepared water solution of $H_2C_2O_4.2H_2O$ (Neuber GmbH, 99.5%). Separately $LiOH.H_2O$ (Neuber GmbH, 99%) was dissolved in distilled water and added to the main solution after completely dissolution of the vanadium oxide. The molar ratio between the initial compounds $LiOH/V_2O_5/H_2C_2O_4.2H_2O$ was 1/1.5/6. The final solution was constantly stirred and evaporated at ~80 °C until a dry precursor was formed. Then the precursor was annealed at 500 °C for16h under air atmosphere (sample SG50). Part of the product was annealed again at 550 °C for another 16h in air atmosphere (sample SG55). Alternatively, another LiV_3O_8 sample was prepared by mixing stoichiometric amounts of Li_2CO_3 and V_2O_5 and grinding them in a ball-mill for 30 min. Afterwards the homogenized mixture was melted at 650 °C [12]. After cooling down the smelt was ground in a ball-mill for 8h (sample MP65). Then a part of the product was sealed in autoclave and treated hydrothermally at 320 °C for 24h in order to expand the interlayer distances in the structure (sample MP65HT). Finally the powder was dried at 250 °C for 24h (sample MP65DR).

$LiMn_2O_4$ (LMO) was prepared via conventional solid state reaction (SSR) synthesis using stoichiometric amounts of $LiNO_3$ and MnO_2 and annealing temperature at 750 °C. The synthesis is described in details elsewhere [15].

Characterization techniques

Powder X-ray diffraction (XRD) was performed on a Philips APD 15 diffractometer with Cu Kα radiation. Thermogravimetric (TGA) and differential thermal (DTA) analyses of the sol-gel precursor were carried out in air on a Stanton Redcroft STA 780 thermal analyzer, in the range 20–570 °C at a heating rate of 5 K min⁻¹. The morphology of the powders was observed by Scanning Electron Microscopy (SEM) on JEOL 200-CX (MP65 and MP65DR) and Philips525/EDAX 9900 (SG50 and SG55). The evaluation of specific surface area (SSA) was conducted by the Brunauer-Emmett-Teller (BET) method on a Strohlein& Co. Area instrument.

Electrochemical testing

The ARLB system was fabricated in two (galvanostatic mode) and three (cyclic voltammetry) electrode cells. The working electrodes were prepared by mixing an active materials and teflonized acetylene black (TAB) [16] in ratio 1:1, then deposited onto Ni mesh and pressed at 3.0 tones per cm². The LiV_3O_8 active material loading was ~14 mg.cm⁻² and weight ratio between the positive and negative active materials was kept $LiMn_2O_4$:LiV_3O_8 = 3:1 in all cases based on their specific capacities obtained in non-water electrolytes. Ag/AgCl was used as a reference electrode. Saturated solution of 6M $LiNO_3$ (Chimtex Ltd., 99.8%) in distilled water was used as electrolyte for the electrochemical testing. The cycling voltammetry was carried out on Autolab PSTAT 10 instrument at sweep rate 50 μV s⁻¹ and voltage range -0.8 to 0V vs Ag/AgCl. The galvanostatic tests were performed on Arbin BT 2000 in the voltage range 0.7 –1.9 V vs. $LiMn_2O_4$, at C/10 (0.1C) and C/100 (0.01C) where C is the theoretical specific capacity for 3 moles of intercalated Li^+ in LiV_3O_8, i.e. ~279.4 mAh g⁻¹ and 10 or 100 are the theoretical charge or discharge time in hours.

RESULTS AND DISCUSSIONS

Thermogravimetric and differential thermal analyses were carried out for a precursor obtained after the first step of the sol-gel process, thus after drying (aging) the gel (Fig. 1).
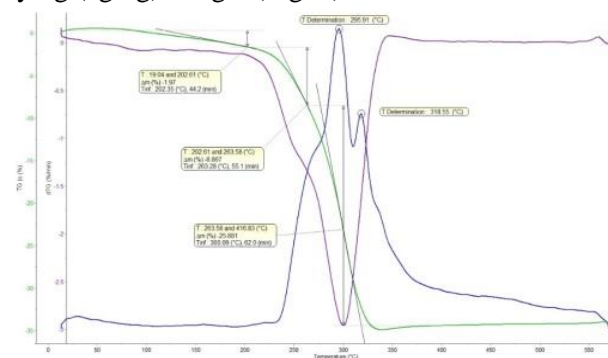
Fig. 1 TG-DTA of the precursor obtained via sol-gel.

The initial weight loss in the range 20-200 °C can be attributed to a small amount of crystal water and/or adsorbed moisture in the precursor. The large weight loss is due to the decomposition of oxalic acid and $LiHC_2O_4$[17]. The strong exothermal peaks in the differential thermogram at ~296 and ~319 °C are caused by the carbon combustion and most likely vanadium oxidation ($V^{4+} \rightarrow V^{5+}$). Heretofore the vanadium was reduced from V^{5+} to V^{4+} (forming VO^{2+} ion) by the oxalic acid during the sol-gel process, a phenomenon that is inevitable during the V_2O_5 dissolution. The small increase of the sample

weight after 330 °C could be associated with gaining of oxygen by the sample to complete the synthesis of the product (LiV_3O_8). The small peak at about 570 °C is most probably due to some initial melting of the sample. Thus two synthesis temperatures were chosen at 500°C (sample SG50) and 550°C (sample SG55).

The XRD patterns of samples prepared via sol-gel method followed by sintering at 500 °C (SG50) and 550 °C (SG55) as well as Wadsley's standard [5] are presented in Fig. 2. The formation of LiV_3O_8 is evident even at 500 °C. Better crystallinity was obtained at 550°C.
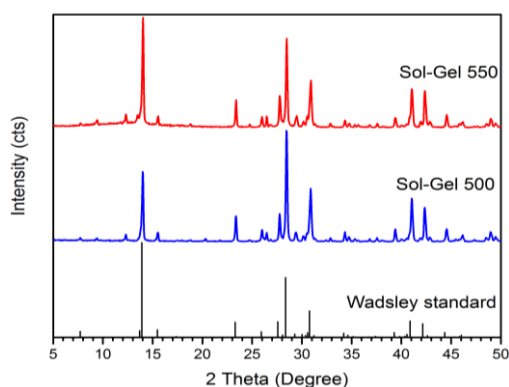
Fig. 2 XRD of the samples prepared via sol-gel method (SG50 and SG55).

There are two additional small peaks in both samples' patterns at 9.3° and 12.3° 2Θ which are not part of the Wadsley's standard. Based on our previous experience we suspect that these peaks are caused by small amount of absorbed water molecules (from the atmosphere) between the structure's layers [12]. This phenomenon is more evident in fig. 3 where such peaks appear at the same positions when the material obtained via meting process is hydrothermally treated (fig. 3b). These peaks vanish when the hydrothermally treated material is dried above 250 °C (Fig. 3c).
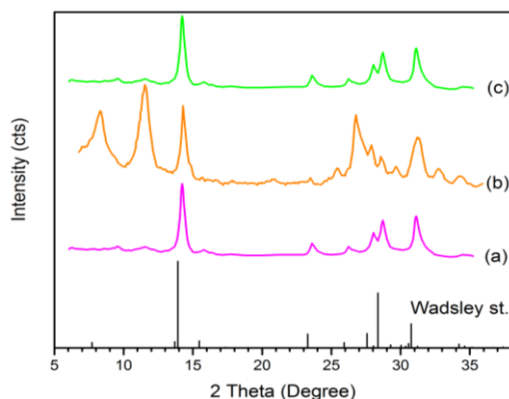
Fig. 3. XRD of samples obtained via melting process: (a) after synthesis (MP65), (b).

Scanning electron microscopy images of melted sample after 8h grinding in a ball-mill (MP65) and hydrothermally treated and dried (MP65DR) are illustrated in Fig. 4.
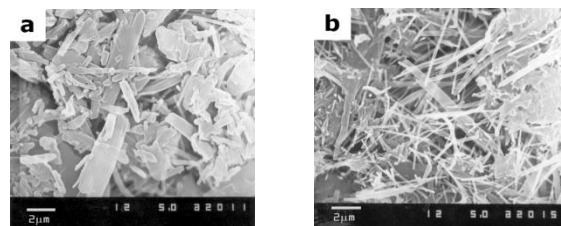
Fig. 4 Scanning electron microscopy of MP65 (a) and MP65DR (b).

The untreated sample shows flake-like type of morphology (fig. 4a). These flakes seem to become fractured into rod-like particles due to the high pressure of the water during the hydrothermal process (fig. 4b). Sample SG50 shows similar morphology of thin rods and flakes (fig. 5 a, c). These rods appear to grow during the additional 16h at 550 °C forming bigger block-like particles/agglomerates presented by SG55 (fig. 5 b, d).
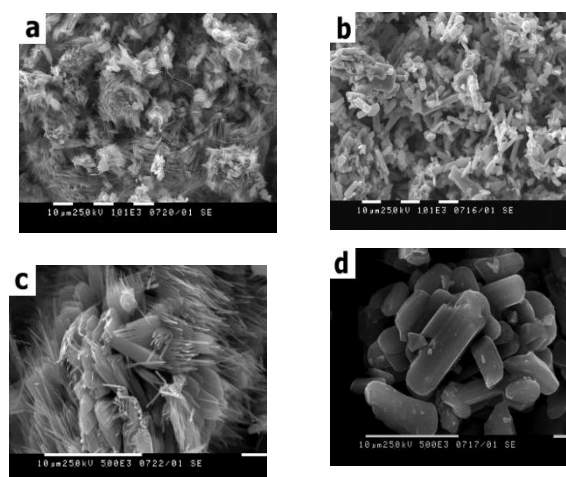
Fig. 5 Scanning electron microscopy of samples SG50 (a and c) and SG55 (b and d).

The specific surface area (SSA) of the materials was evaluated by Brunauer-Emmett-Teller (BET) method. The SSA of MP65 and MP65DR samples are 1.1 and 11 $m^2\ g^{-1}$, respectively, while sol-gel samples display 1.5$m^2\ g^{-1}$ (SG50) and 1.1 $m^2\ g^{-1}$ (SG55).

The cycling voltammetry (CV) of the materials is shown in Fig. 6. All Li⁺ insertion peaks of LiV_3O_8 observed in organic electrolyte [12] seem to be merged in one broad peak split into two apexes at -0.43 and -0.33 V vs Ag/AgCl when sample MP65DR is tested in aqueous electrolyte. Similarly SG50 display one broad cathodic peak (-0.34 V vs Ag/AgCl) in contrast to SG55 showing three distinguished peaks at -0.25, -0.31 and -0.47 V vs

185

Ag/AgCl. The oxidation curves of SG50 and MP65DR also appear to be similar in shape with two peaks for each sample at -0.35 and -0.19 V vs Ag/AgCl (SG50), and -0.39 and -0.25 V vs Ag/AgCl (MP65DR). SG55 shows three anodic peaks (-0.31, -0.27 and -0.23V vs Ag/AgCl) which are merged into one broad feature during the de-intercalation process. After integration of the areas, the initial delivered intercalation and following de-intercalation capacities are 64.35 and 55.43 mAh g⁻¹ (SG50), 92.68 and 67.48 mAh g⁻¹ (SG55), and 123.87 and 73.12 mAh g⁻¹ (MP65DR), respectively. These capacity values delivered in aqueous electrolyte are much lower in comparison to their organic counterparts (20-50% lower) [12].
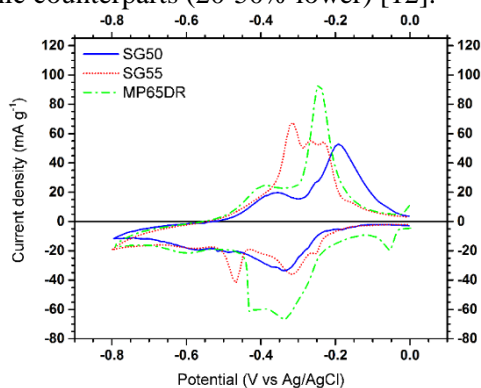
Fig. 6 Cyclic voltammetry of SG50, SG55 and MP65DR at a scan rate of 50 µV s⁻¹ in the voltage range of 0 and -0.8 V vs. Ag/AgCl.

Galvanostatic tests were conducted in order to investigate the electrochemical performance of the studied materials. Fig. 7a shows initial charge-discharge profiles of the samples at C/10 (0.1C) in the voltage range 0.7-1.9 V vs LiMn₂O₄ (LMO). Both SG50 and SG55 present solid-solution-type (shape) of the de/intercalation curves. These samples deliver 35.45 (SG50) and 75.23 (SG55) mAh g⁻¹ during the first lithiation, and 30.57 (SG50) and 51.50 (SG55) mAh g⁻¹ in the consecutive de-lithiation process. Although MP65DR delivers the highest capacities in potentiodynamic mode (fig. 6), it performs very poorly in galvanostatic mode, marking 4.2 and 0.3 mAh g⁻¹ during first intercalation (Int) and de-intercalation (Dei). Even when the current load is lowered as much as C/100 (fig. 7b), the delivered capacities are unsatisfactory: 47.77 (Int) and 9.8 (Dei) mAh g⁻¹, implying kinetic difficulties thus hindered diffusion.
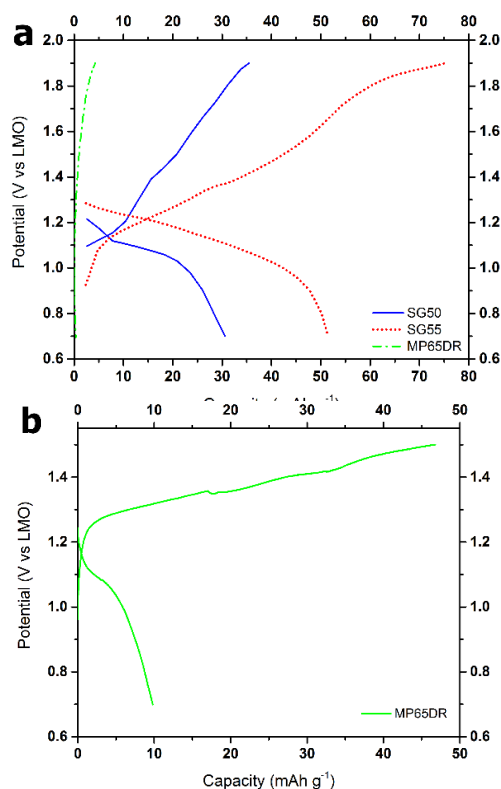
Fig. 7 Galvanostatic tests: (a) charge-discharge profiles of all materials at C/10 in the voltage range 0.7-1.9 V vs LMO; (b) charge-discharge profiles of MP65DR at C/100 in the voltage range 0.7-1.5 V vs LMO.

The de-intercalation specific capacity of the studied materials (discharge mode for the whole LVO-LMO system) as functions of the cycles at C/10 in the voltage range 0.7-1.9 V vs LMO are presented in fig. 8a. SG55 marks highest de-lithiation capacity of ~55 mAh g⁻¹ in the 4th cycle. After 10th cycle the materials becomes unstable expressed by fluctuations and rapid capacity loss of ~40% in the 30th cycle (fig. 8b). Although the capacity of SG50 is lower, this material display steady behavior with varying capacity of 30-33 mAh g⁻¹. The capacity retention (fig. 8b) in every cycle is calculated as follows:

$$CapRet = \frac{C_n}{C_1} * 100 \ [\%],$$

where C_n and C_1 are the capacities of the respective and first cycles, respectively. Therefore the capacity retention of sample SG50 (2-30 cycles) exceeds 100% due to the lowest capacity (30.57 mAh g⁻¹) is delivered in the first cycle. The coulombic efficiency (95-97% after 4th cycle) of this sample is also much better compared to SG55 (70-90%) (Fig. 8c).
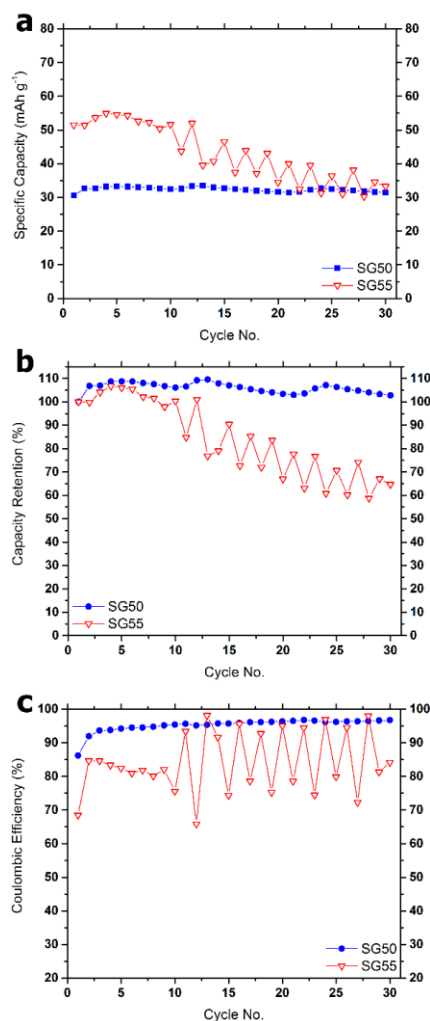
Fig. 8. Specific capacity (a), capacity retention (b) and coulombic efficiency (c) as functions of the cycles at C/10 in the voltage range 0.7-1.9 V vs LMO.

CONCLUSIONS

LiV$_3$O$_8$ active materials were synthesized via sol-gel followed by solid state reaction at 500 and 550 °C, and melting process at 650 °C with subsequent hydrothermal treatment and drying. X-ray diffraction patterns show that samples were successfully indexed as LiV$_3$O$_8$. However, there are additional small peaks at 9.3° and 12.3° 2Θ in the patterns of SG50 and SG55 which can be attributed to small amounts of absorbed water from the atmosphere. Among all samples SG55 delivers the highest capacities of 75.23 and 51.50 mAh g^{-1} during

the first lithiation and de-lithiation, respectively, in galvanostatic mode. However, SG50 appears to be more stable throughout the cycles. Although MP65DR shows highest intercalation and de-intercalation capacities (123.87 and 73.12 mAh g^{-1}) in potentiodynamic mode, this material performs very poorly in galvanostatic mode.

REFERENCES

1. J. Yan, J. Wang, H. Liu, Z. Bakenov, D. Gosselink, P. Chen, *Journal of Power Sources*, **216,** 222 (2012).
2. W. Li, J.R. Dahn, D.S. Wainwright, *Science*, **264**, 1115 (1994).
3. J.-Y. Luo, W.-J. Cui, P. He, Y.-Y. Xia, *Nature Chemistry*, **2**, 760, (2010).
4. G.J. Wang, N.H. Zhao, L.C. Yang, Y.P. Wu, H.Q. Wu, R. Holze, *Electrochimica Acta,* **52,** 4911 (2007).
5. A. Wadsley, *Acta Crystallographica*, **10,** 261 (1957).
6. D.G. Wickham, *Journal of Inorganic and Nuclear Chemistry*, **27,** 1939 (1965).
7. G. Pistola, M. Pasquali, M. Tocci, V. Manev, R.V. Moshtev, *Journal of Power Sources,* **15**, 13-25, (1985).
8. A. Hammou, A. Hammouche, *Electrochimica Acta*, **33(12)**, 1719 (1988).
9. G. Pistoia, M. Pasquali, G. Wang, L. Li, *Journal of The Electrochemical Society*, **137**, 2365 (1990).
10. T. Miyazaki, T. Ogino, Y. Masuda, H. Wada, T. Kawagoe, Patent US5013620A (1991).
11. A. Momchilov, V. Manev, A. Nassalevska, M. Pasquali, G. Pistoia, *Journal of Applied Electrochemistry*, **20**, 763 (1990).
12. V. Manev, A. Momchilov, A. Nassalevska, G. Pistoia, M. Pasquali, *Journal of Power Sources*, **54**, 501 (1995).
13. L. A. de Picciotto, K.T. Adendorff, D.C. Liles, M.M. Thackeray, *Solid State Ionics*, **62**, 297(1993).
14. V. L. Volkov, Sverdlovsk: Ural. Nauchn. Tsentr, Akad. Nauk SSSR, (1987).
15. A. Momchilov, V. Manev, A. Nassalevska, A. Kozawa, *Journal of Power Sources,* **41**, 305(1993).
16. V. Manev, A. Momchilov, K. Tagawa, A. Kozawa, *Progress in Batteries & Battery Materials*, **12**, 157, (1993).
17. D. Li, F. Lian, K.-C. Chou, *Rare Metals,* **31**, 615 (2012).

ЕЛЕКТРОХИМИЧНИ СВОЙСТВА НА LiV_3O_8, ПОЛУЧЕН ЧРЕЗ РАЗЛИЧНИ МЕТОДИ НА СИНТЕЗ, КАТО ОТРИЦАТЕЛЕН АКТИВЕН МАТЕРИАЛ В ЛИТИЕВО-ЙОННА БАТЕРИЯ С ВОДЕН ЕЛЕКТРОЛИТ

Т. Перков[1*], Т. Станкулов[2], К. Банов[1,2], А. Момчилов[2]

[1]Химикотехнологичен и металургичен университет, бул. "Климент Охридски" 8, 1756 София, България
[2]Институт по електрохимия и енергийни системи, Българска академия на науките, ул. "Акад. Георги Бончев" бул. 10, 1113 София, България

(Резюме)

Изследвани са електрохимичните свойства на литиевия триванадат (LiV_3O_8, LVO) като отрицателен електроден материал за литиево-йонна батерия с воден електролит. Два метода на синтез бяха приложени за подготовка на LiV_3O_8: метод зол-гел, последван от реакция в твърдофазен синтез (SSR) при 500 и 550°C и процес на топене с последващо хидротермично третиране и сушене. Като за противоелектрод беше използван $LiMn_2O_4$ (LMO), получен чрез конвенционален твърдофазен синтез. Интеркалирането / деинтеркалирането на литиевия йон се извършва в прозореца на електрохимичната стабилност на водата. LiV_3O_8, получен по метода на топене, третиран хидротермично и изсушен (MP65DR), показва по-лошо представяне в галваностатичен режим в сравнение с тези, получени чрез сол-гел. Пробата, получена чрез зол-гел, накалена при 550°C (SG55), показва първоначален специфичен капацитет от ~ 75 (интеркалация) и ~ 52 (де-интеркалация) mAh.g-1, който е около 4-5 пъти по-нисък в сравнение с капацитета, в неводни електролити. Въпреки че е с по-малък капацитет (30-33 mAh.g-1), другата проба от сол-гел, нагрята при 500 ° C (SG50), показва по-добро запазване на капацитета и ефективност при циклите.

Ключови думи: водна литиево-йонна батерия, аноден активен материал, литиев триванадат

Screening impedance analysis of Zn-air cells

Z. B. Stoynov[1†], D. E. Vladikova[1*], B. I. Abrashev[1], M. P. Slavova[1], B. G. Burdin[1],
E. S. Mihaylova-Dimitrova[1], L. C. Colmenares[2], A. R. Mainar[2], J. A. Blázquez[2]

[1]*Acad. Evgeni Budevski Institute of Electrochemistry and Energy Systems, Bulgarian Academy of Sciences, Acad. G. Bonchev Str., Bl. 10, Sofia 1113, Bulgaria*
[2]*CIDETEC Energy Storage, Pº Miramón 196, 20014 San Sebastián, Spain*

As a promising technology, zinc-air secondary batteries have gained considerable attention over the past few years. The presented work aims at application of Electrochemical Impedance Spectroscopy (EIS) as a tool to develop new nanostructured and environmentally friendly materials for rechargeable zinc-air cells. The results are obtained on both half- and full-cell configuration during cycling. They ensure electrochemical characterization of the cell and its components (electrodes and electrolyte) in similar state of charge. This offers experimental evidence to determine the rate limiting stages. The accumulated information will be used for further studies and optimization of the zinc-air cell.

Key words: Zn-air cell, Gas diffusion electrode, Zinc electrode, Impedance measurementss

INTRODUCTION

In principle the main advantage of metal-air cells is the use of oxygen from the atmospheric air as a reactant. The air gas-diffusion electrode possesses two advantages over the metal-oxide cathode: infinite charge capacity and low weight independent on capacity. Thus the capacity of metal-air battery is determined only by the amount of active metal, but not by the air electrode. As a result, the specific capacities like gravimetric (Ah/kg) and volumetric (Ah/l) are significantly higher than those for classical electrochemical systems with the same metal anode [1].

Developed zinc–air batteries are traditionally non-rechargeable. Therefore their transition to rechargeable ones is lately becoming a hot topic, due to the advantages of this system to ensure electrochemical storage with high energy density, high capacity and low price [2, 3]. However, there is still not well-performing (long-term) secondary Zn-air battery which makes this technology attractive for intensive research, especially on low-cost materials with improved reversibility and enhanced durability [4].

Battery capacity fading is recognized to happen due to the loss of material properties (for example morphological changes) during cycle life. For the Zn-electrode the shape or the morphology of the zinc particles is of great importance to assure good inter-particle contact and hence, to keep lower internal resistance which improves the electrochemical performance. However, as the electrode surface area increases, the corrosion rate of the zinc electrode generally becomes more significant. The combination of coarse and fine particles or agglomeration of nano-sized zinc/zinc alloyed particles in a meso-porous structure can be regarded as a compromise between high-rate electrochemical performance and self-corrosion [5]. Alloying zinc with other metals (e.g. lead, cadmium, bismuth, tin and indium), or coating the zinc metal with other materials as lithium boron oxide or aluminum oxide are effective approaches. Some additives such as silicates, surfactants and polymers can also efficiently suppress or reduce the rate of hydrogen generation.

In respect to the gas diffusion electrode (GDE) there are two challenges: development of non-precious bifunctional air electrocatalysts for both oxygen reduction and evolution [6, 7] and introduction of carbon-free gas diffusion layer for preventing carbon electrochemical oxidation/corrosion during battery charging (oxygen evolution) [8].

In order to improve the overall reversibility of the zinc-air battery, it is necessary to understand the current limitations, requirements and challenges for each cell component (viz. anode, electrolyte and cathode) and their interaction [9]. It can be achieved by performing electrochemical impedance spectroscopy (EIS) studies. EIS is regarded as one of the most powerful techniques for investigation of electrochemical systems due to its unique capability to separate the kinetics of different steps comprising the overall electrochemical

process [10]. Since impedance measurements are performed in a large frequency range (about 9 decades), processes with big difference in velocities and time-constants can be monitored, distinguished and evaluated – fast electronic conduction, fast electrochemical kinetics, diffusion and other types of transport limitations, as well as formation and growth of new phases [11, 12].

The aim of this work is to characterize electrochemically a rechargeable zinc-air cell by impedance spectroscopy. It is performed at cell level and to its electrodes during cycling. This feasibility study will be further used for deeper insight in the aging and degradation mechanisms and processes occurring during long-term operation. It will further support the optimization of the zinc-air system.

EXPERIMENTAL

The experiments were performed in a homemade 25 cm^2 test cell which has the possibility to be used as full cell and/or half-cell with three electrodes configuration having Hydrogen Reference Electrode (HRE) (Fig.1) [13].
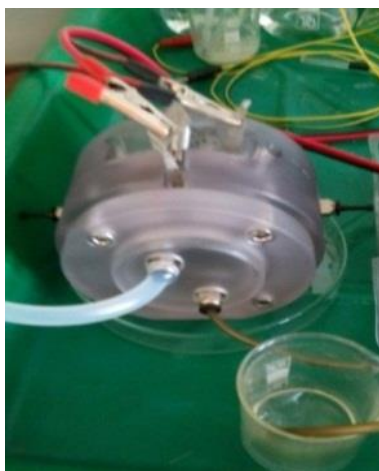
Fig. 1. Homemade Zn-Air test cell.

The Zn electrode was made from a paste prepared by mixing in an optimal ration commercial Zn battery-grade micrometric powder (containing traces of bismuth, indium and aluminum) and ZnO. Both materials are from UMICORE. For improvement of the electrode mechanical stability an improved procedure was introduced. The classical binder carboxymethyl cellulose (CMC) was replaced by PTFE. The discharge capacity of the first cycle in half-cell configuration was used as criterion to define the optimal ratio PTFE:Zn-paste which was found to be 1:5 (Fig. 2). Although it causes about 10 %

capacity losses (estimated from nominal and calculated discharge capacity), the PTFE enhances the mechanical stability of the Zn-electrode demonstrated by increasing the number of cycles from 20 when CMC was used to 120 (in full cell configuration). The Zn electrodes were fabricated to provide a capacity of 1000 mAh/g. The active Zn mass was deposited on 9 cm^2 stainless steel mesh and pressed at 250ºC with 300 kg/cm^2.
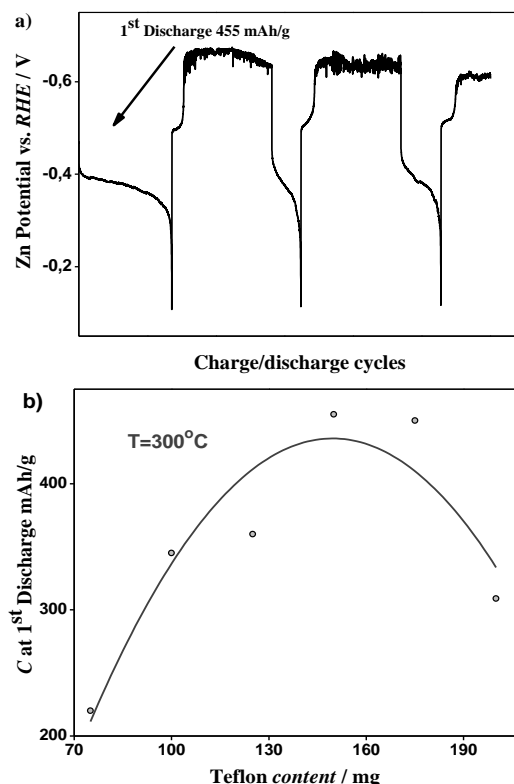
Fig. 2. Zn-electrode: a) voltage profile during charge/discharge cycling at 5 mA/cm^2; b) Initial cell capacity as a function of PTFE content.

An optimized bifunctional GDE which ensures 700 charge/discharge cycles in half cell configuration at current density of 10 mA/cm^2 was used. The GDL was produced from Vulcan XC-72 (Cabot Corp.) which was modified with 60 wt. % Teflon (Sigma Aldrich emulsion) through especially developed procedure. A mixed catalyst with optimized composition of 70 wt. % Ag, 20 wt. % Co$_3$O$_4$ and 10 wt. % PTFE which showed excellent performance (Fig. 3) was used as active catalyst layer [14]. The electrode was prepared by hot pressing at 250ºC with 300 kg/cm^2 for 3 minutes. The tests were carried out using an optimized formulation (CIDETEC) based on an alkaline electrolyte system [15].

190
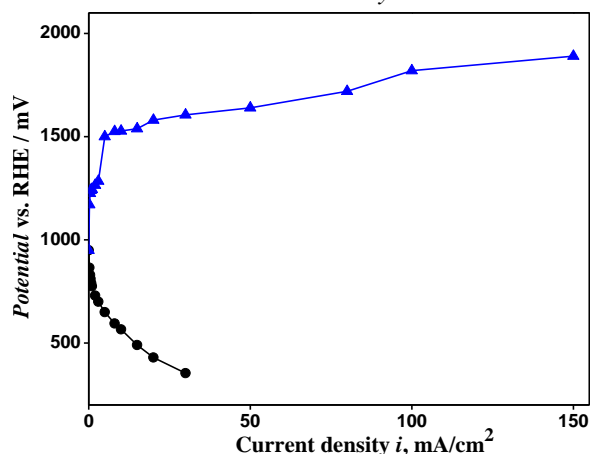
Fig. 3. Charge (▲) and discharge (●) voltages of an optimized bifunctional GDE at different current densities in a homemade 10 cm² cell.

The cycling test was performed applying a current density of ± 10 mA/cm² during 7 h of charge and 6 h of discharge. The cut-off voltages were set at 2.5 V at charge (C) and 0.5 V at discharge (D), respectively (Fig.4) after the first cycles where the C/D voltages were beyond these limits. This situation most likely induced Zn passivation reflected by the subsequent decrease in capacity.
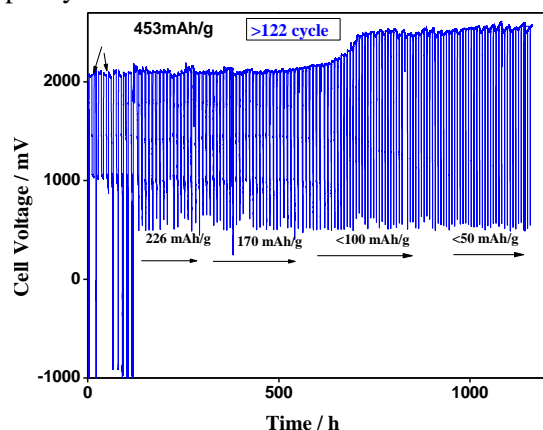
Fig. 4. Long-term cycling of homemade Zn/Air cell at 10 mA/cm²

The impedance measurements were carried out using a Solartron 1260 Frequency Response Analyzer in the frequency range 1 kHz – 10 mHz with density of 5 points per decade at applied DC current of 10 mA and amplitude of the AC signal of 2.5 mA during both charge and discharge modes. They were performed after the 20th cycle and at the end of the cell life at similar state of charge or discharge for characterization of both the electrodes and cell behavior. For convenience, the impedance measurements of the electrodes were related to the cell voltage, measured before the AC perturbation. Preliminary screening performed before and after the impedance experiments

registered insufficient voltage changes, which could be ignored.

RESULTS AND DISCUSSIONS

The volt-ampere characteristic (VAC) is a key feature of any electrochemical power source. It covers the entire operating range and reflects the set of dominant phenomena that govern a process. Thus, VAC gives the main fundamental and simplest description of the cell performance in a given moment of the test. VAC depends on the operating conditions and degradation state. For batteries the state of charge/discharge should be also taken into account. Therefore, at constant working conditions the changes in the VAC may serve as performance indicator to estimate the state of health (SoH) and the degradation rate. For deeper insight into the phenomena and mechanisms the VAC analysis is combined with impedance measurements in selected working points [16].

Fig. 5 represents VAC of the homemade Zn-air cell at a given state during discharge after 20 previous charge/discharge cycles. Generally, the volt-ampere curve has three distinct areas: (*i*) an activation zone at low current (segment I in Fig. 5), followed by (*ii*) a transport zone with linear behavior (segment II in Fig. 5) and (*iii*) a diffusion restriction zone at high current (not presented in Fig. 5). A working point (WP) at 10 mA was selected (triangle in Fig.5) to perform the impedance measurements of the Zn-Air cell in both full- and half-cell configuration. Due to its position in the kink of segments I and II in the voltage-current curve, the measured impedance can ensure information about both the charge transfer, which depends on the electrode catalytic activity, and the transport hindrances.
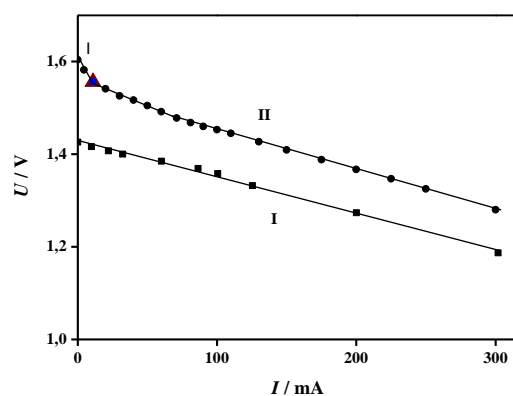
Fig. 5. Volt-ampere characteristic of a Zn-air cell in discharge regime: (●) full cell configuration; (■) half-cell configuration of gas diffusion electrode (GDE).

The VAC of the GDE recorded during discharge shows a linear behavior (Fig. 5.). This is

characteristic of electrodes operating under the domination of transport limitations. The VAC comparison with the full cell performance suggests that the activation losses come mainly from the Zn electrode. This hypothesis is confirmed by the impedance measurements presented in Fig. 6.
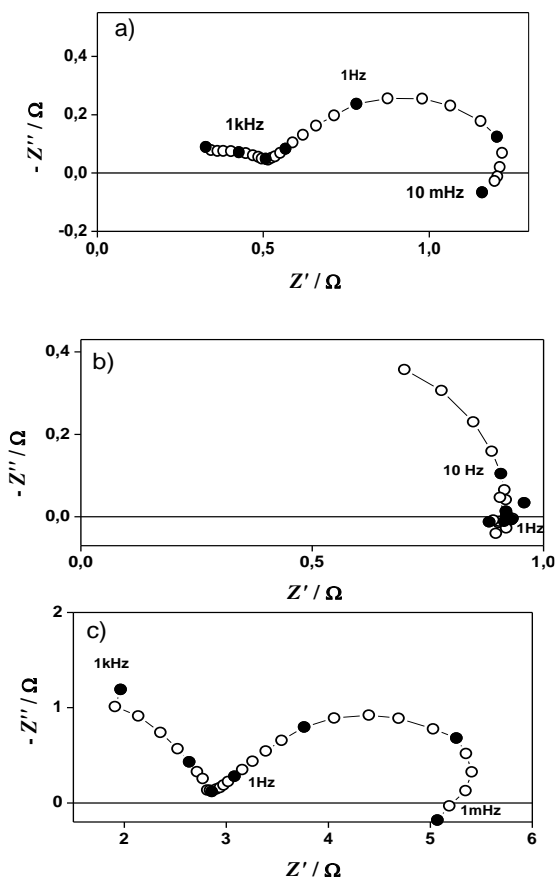
Fig. 6. Impedance diagrams for: a) GDE, b) Zn electrode and c) full-cell during discharge (1,6 V).

The impedance diagram of the GDE (Fig. 6a) is characterized by a well-defined low frequency arch corresponding to bounded transport limitations, while that for the Zn electrode (Fig. 6b) exhibits the domination of the charge transfer semicircle. The impedance of the full cell combines the two characteristic impedance shapes in the high and in the low frequency range, respectively. A significant increase of the resistance is also observed (Fig. 6c). The state of discharge (SoD) influences weakly the anode reaction. The inductive complicated shape in the low frequency range, which is typical for impedance of batteries, usually marks the formation of a new phase [17].

The impedance diagrams for the full cell and for the two electrodes during charge are also well defined (Fig. 7). The charge transfer resistance of the zinc electrode decreases about 3 times, which obviously influences also the cell resistance (Fig. 7b). This asymmetry during charge and

discharge may be due to the screening effect of the teflonized anode surface.

The volt-ampere characteristic and impedance measurements in full cell configuration performed at the end of the cell life (after 120 C/D cycles) showed strongly deteriorated behavior (Fig. 8). The resistance registered by impedance was about 10 times higher in comparison to that after the 20th C/D cycle.
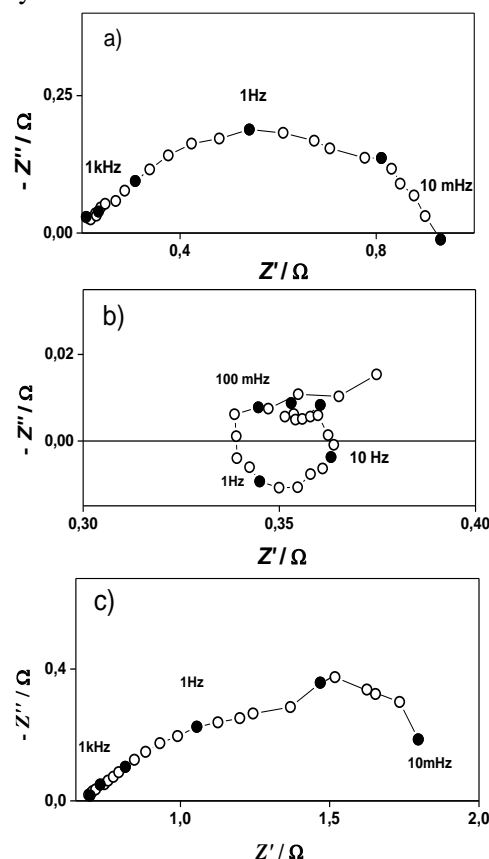
Fig. 7. Impedance diagrams for: a) GDE, b) Zn electrode and c) full-cell during charge (1,9 V).
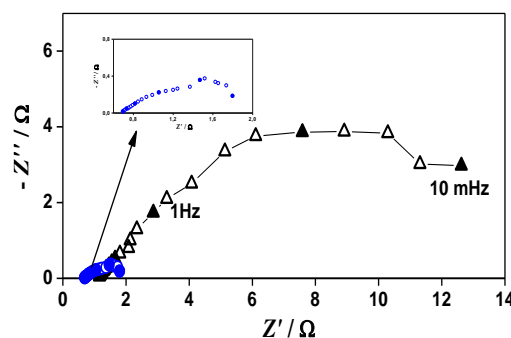
Fig. 8. Impedance characteristics of full cell during charge (about 1,8 V) after the 20th cycle (●) and after the last (120th) cycle (▲).

The subsequent measurement of the Zn electrode failed, due to obviously the entire Zn dissolution and total loss of contacts with the current collector (visually confirmed after opening the cell). It is interesting to note that a lower

resistance was registered for the measurements in full cell configuration after the failure of the Zn electrode (Fig. 9), which can be explained with a change of the system, since in practice the Zn electrode was replaced by the stainless steel current collector.
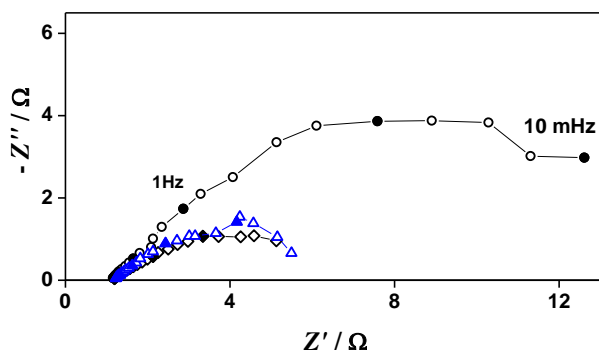
Fig. 9. Impedance of full cell during charge after the 120th discharge: before (●) and after (▲, ♦) the failure of the Zn electrode.

After opening the homemade cell, it could be seen that while the zinc electrode was totally dissolved, the GDE was in good condition (Fig. 10). The replacement of the damaged Zn electrode with a new one and refreshment of the electrolyte ensured more than 50 additional C/D cycles at 10 mA/cm^2.

Fig. 10. Gas diffusion electrode before and after 120 C/D cycles.

CONCLUSIONS

These preliminary results demonstrate the applicability of EIS for performance studies of Zinc-air rechargeable cells. The measurements can be carried out in half-cell and full-cell configuration during charge or discharge. This versatility ensures information about the behavior and influence of the cell components thus determining the rate limiting step and its position in the cell. Comparison of volt-ampere characteristics combined with periodic impedance measurements during battery cycling can bring to a deeper insight into the degradation mechanisms. Getting such knowledge, Zinc-air cells can be further optimized in terms of performance and cycle life.

REFERENCES

1. A. Kaisheva in: Z. Stoynov and D. Vladikova (Eds.), Portable and Emergency Energy Sources, Marin Drinov Academic Publishing House, Sofia, p. 301, (2006).
2. P. Gu, M. Zheng, Q. Zhao, X. Xiao, H. Xue, H. Pang, *J. Mater. Chem. A*, **5**, 7651 (2017) DOI: 10.1039/ C7TA01693J.
3. J. Fu, Z. P. Cano, M. G. Park, A. Yu, M. Fowler, Z. Chen, *Adv. Mater*. 29, **7** (2016). DOI: 10.1002/adma. 201604685.
4. EU funded H2020 project „Zinc-Air Secondary innovative nanotech based batteries for efficient energy storage" ZAS (GA 646186) (http://sintef.no/projectweb/zas/).
5. A. R. Mainar, L. C. Colmenares, J. A. Blázquez, I. Urdampilleta, Int. J. Energy Res., **42**, 903 (2018). doi.org/10.1002/er.3822.
6. A. R. Mainar, L. C. Colmenares, O. Leonet, F. Alcaide, J. Iruin, S. Weinberger, V. Hacker, E. Iruin, I. Urdanpilleta, J. A. Blazquez, *Electrochim.Acta,* **217,** 80 (2016). doi.org/10.1016/j.electacta.2016.09.052.
7. E. Davaria, D. Ivey, *Sustainable Energy Fuels*, **2**, 39, (2018).
8. S. Velraja, J. Zhua, ECS Meeting Abstracts, 232nd ECS Meeting, MA2017-02 National Harbor, Maryland (2017).
9. A. R. Mainar, L. C. Colmenares, M. Juel, E. Sheridan, J. A. Blázquez, I. Urdampilleta, Proc. II Metal-air Batteries International Congress, Santander (2016).
10. Z. Stoynov, D. Vladikova, Impedance Spectroscopy of Electrochemical Power Sources in: U. Garche (Ed.) Encyclopedia of Electrochemical Power Sources, Elsevier, p. 632, 2009.
11. D. Vladikova, Z. Stoynov, G. Raikova, A. Thorel, A. Chesnaud, J. Abreu, M. Viviani, A. Barbucci, Z. Ilhan, P. Carpanese, S. Presto, Proc. 15th European Fuel Cell Forum 2011, 28 June – 1 July 2011, Lucerne, Switzerland, Ch. 18/B1205, p. 1, (2011).
12. Z. Stoynov, D. Vladikova, E. Mladenova, *J. Solid State Electrochem*., **17**, 555, (2013). DOI: 10.1007/s10008-012-1916-z.
13. B. Abrashev, D. Uzun, H. Hristov, D. Nicheva, K. Petrov, Adv. Natural Science: Theory & Applications, **4**, 65 (2015)
14. H. M. A. Amin, H. Baltruschat, D. Wittmaier, K. A. Friedrich, *Electrochim.Acta*, **151**, 332 (2015). DOI: doi.org/10.1016/j.electacta.2014.11.017.

15. A. R. Mainar, E. Iruin, L. C. Colmenares R., J. A. Blázquez, *Energy Sci. Eng*., **3**, 174 (2018). doi.org/10.1002/ese3.191

16. Z. Stoynov, D. Vladikova, B. Burdin, J. Laurencin, D. Montinaro, A. Nakajo, P. Picardo, A. Thorel, M. Hubert, R. Spotorno, A. Chesnaud, *MRS Advances*, **2**, 3991 (2017). doi.org/10.1557/adv.2017.592.

17. D. Vladikova, Z. Stoynov, G. Raikova in: Z. Stoynov, D. Vladikova (Eds.), Marin Drinov Academic Publishing House, Sofia, p.441 (ISBN 954-322-133-2) (2006).

СКРИНИНГОВ ИМПЕДАНСЕН АНАЛИЗ НА ЦИНК-ВЪЗДУШНИ КЛЕТКИ

З. Б. Стойнов[1†], Д. Е. Владикова1*, Б. И. Абрашев[1], М. П. Славова[1], Б. Г. Бурдин[1], Е. С. Михайлова-Димитрова[1], Л. К. Коменарес[2], А. Р. Мейнар[2], Ж. А. Блазкес[2]

[1]Институт по електрохимия и енергийни системи, Българска академия на науките, ул. Акад. Г. Бончев, бл. 10, София 1113, България

[2]CIDETEC Съхранение на енергия, Pº Мирамон 196, 20014 Сан Себастиан, Испания

Като обещаваща технология, вторичните цинк-въздушни батерии спечелиха значително внимание през последните няколко години. Представената работа цели въвеждането на електрохимична импедансна спектроскопия (EIS) като инструмент за разработване на нови наноструктурирани и екологосъобразни материали, подходящи за внедряване в акумулаторна цинк-въздушна клетка. Първите резултати при циклиране са получени при измервания както в конфигурация на полу-клетка, така и на цяла клетка. Те осигуряват електрохимично охарактеризиране на клетката и нейните компоненти (електроди и електролит) при фиксирано състояние на заряд, което позволява експериментално дефиниране на скорост-определящия стадий. Получената информация ще бъде използвана за по-нататъшно проучване и оптимизиране на цинк-въздушната клетка.

Instructions about Preparation of Manuscripts

General remarks: Manuscripts are submitted in English by e-mail The text must be typed on A4 format paper using Times New Roman font size 11, normal character spacing. The manuscript should not exceed 15 pages (about 3500 words), including photographs, tables, drawings, formulae, etc. Authors are requested to use margins of 2 cm on all sides

Manuscripts should be subdivided into labelled sections, e.g. **Introduction, Experimental, Results and Discussion**, *etc*. **The title page** comprises headline, author's names and affiliations, abstract and key words. Attention is drawn to the following:

a) **The title** of the manuscript should reflect concisely the purpose and findings of the work. Abbreviations, symbols, chemical formulas, references and footnotes should be avoided. If indispensable, abbreviations and formulas should be givenin parentheses immediately after the respective full form.

b) **The author**'s first and middle name initials and family name in full should be given, followedby the address (or addresses) of the contributing laboratory (laboratories). **The affiliation** of the author(s) should be listed in detail by numers (no abbreviations!). The author to whom correspondence and/or inquiries should be sent should be indicated by asterisk (*) with e-mail address.

The abstract should be self-explanatory and intelligible without any references to the text andcontaining not more than 250 words. It should be followed by key words (not more than six).

References should be numbered sequentially in the order, in which they are cited in the text. The numbers in the text should be enclosed in brackets [2], [5, 6], [9−12], etc., set on the text line. References are to be listed in numerical order on a separate sheet. All references are to be given in Latin letters. The names of the authors are given without inversion. Titles of journals must be abbreviated according to Chemical Abstracts and given in italics, the volume is typed in bold, the initial page is given and the year in parentheses. Attention is drawn to the following conventions:a) The names of all authors of a certainpublications should be given. The use of "*et al*." inthe list of references is not acceptable.b) Only the initials of the first and middle names should be given. In the manuscripts, the reference to author(s) of cited works should be made without giving initials, e.g. "Bush and Smith [7] pioneered...". If the reference carries the names of three or more authors it should be quoted as "Bush *et al*. [7]", if Bush is the first author, or as "Bush and co-workers [7]", if Bush is the senior author.

Footnotes should be reduced to a minimum. Each footnote should be typed double-spaced at thebottom of the page, on which its subject is first mentioned.**Tables** are numbered with Arabic numerals on the left-hand top. Each table should be referred to inthe text. Column headings should be as short as possible but they must define units unambiguously.The units are to be separated from the preceding symbols by a comma or brackets. Note: The following format should be used when figures, equations, *etc*. are referred to the text (followed by the respective numbers): Fig., Eqns., Table, Scheme.

Schemes and figures. Each manuscript should contain or be accompanied by the respective illustrative material as well as by the respective figure captions in a separate file (sheet).As far as presentation of units is concerned, SI units are to be used. However, some non-SI units are also acceptable, such as °C, ml, l, etc.The author(s) name(s), the title of the manuscript, the number of drawings, photographs, diagrams, etc., should be written in black pencil on the back of the illustrative material (hard copies) inaccordance with the list enclosed. Avoid using more than 6 (12 for reviews, respectively) figures in the manuscript. Since most of the illustrative materials are to be presented as 8-cm wide pictures, attention should be paid that all axis titles, numerals, legend(s) and texts are legible.

The authors are required to submit the text with a list of three individuals and their e-mail addresses that can be considered by the Editors as potential reviewers. Please, note that the reviewers should be outside the authors' own institution or organization. The Editorial Board of the journal is not obliged to accept these proposals.

The authors are asked to submit **the final text** (after the manuscript has been accepted for publication) in electronic form by e-mail. The main text, list of references, tables and figure captions should be saved in separate files (as *.rtf or *.doc) with clearly identifiable file names. It is essential that the name and version of the word-processing program and the format of the text files is clearly indicated. It is recommended that the pictures are presented in *.tif, *.jpg, *.cdr or *.bmp format.

The equations are written using "Equation Editor" and chemical reaction schemes are written using ISIS Draw or ChemDraw programme.

EXAMPLES FOR PRESENTATION OF REFERENCES

REFERENCES
1. D. S. Newsome, *Catal. Rev.–Sci. Eng.*, **21**, 275 (1980).
2. C.-H. Lin, C.-Y. Hsu, *J. Chem. Soc. Chem. Commun.*, 1479 (1992).
3. R. G. Parr, W. Yang, Density Functional Theory of Atoms and Molecules, Oxford Univ. Press, New York, 1989.
4. V. Ponec, G. C. Bond, Catalysis by Metals and Alloys (Stud. Surf. Sci. Catal., vol. 95), Elsevier, Amsterdam, 1995.
5. G. Kadinov, S. Todorova, A. Palazov, in: New Frontiers in Catalysis (Proc. 10th Int. Congr. Catal., Budapest,(1992), L. Guczi, F. Solymosi, P. Tetenyi (eds.), Akademiai Kiado, Budapest, 1993, Part C, p. 2817.
6. G. L. C. Maire, F. Garin, in: Catalysis. Science and Technology, J. R. Anderson, M. Boudart (eds), vol. 6, SpringerVerlag, Berlin, 1984, p. 161.
7. D. Pocknell, *GB Patent* 2 207 355 (1949).
8. G. Angelov, PhD Thesis, UCTM, Sofia, 2001, pp. 121-126.
9 JCPDS International Center for Diffraction Data, Power Diffraction File, Swarthmore, PA, 1991.
10. CA **127**, 184 762q (1998).
11. P. Hou, H. Wise, *J. Catal.*, in press.
12. M. Sinev, private communication.
13. http://www.chemweb.com/alchem/articles/1051611477211.html.

Texts with references which do not match these requirements will not be considered for publication!!!

Selected papers presented on the "Sofia Electrochemical Days 2017" – National Conference with International Participation, May 10 – 13, 2017, Sofia, Bulgaria

CONTENTS

СЪДЪРЖАНИЕ